UNIVERSITÀ
DEGLI STUDI
DI PADOVA

Sede Amministrativa: Università degli Studi di Padova

Dipartimento di Biologia

SCUOLA DI DOTTORATO DI RICERCA IN BIOSCIENZE E BIOTECNOLOGIE

INDIRIZZO: BIOTECNOLOGIE

CICLO XXVI

HUMAN TISSUE-ON-A-CHIP DEVELOPMENT FOR TYPE 2 DIABETES STUDIES

Direttore della Scuola: Ch.mo Prof. Giuseppe Zanotti

Coordinatore d'indirizzo: Ch.mo Prof. Fiorella Lo Schiavo

Supervisore: Dr. Nicola Elvassore

Dottoranda: Alice Zoso

Table of content

Sommario ..... *v*

Summary ..... *vii*

Foreword ..... *ix*

Chapter 1

State of the Art and Motivation **1**

1.1 Type 2 Diabetes 1

1.1.1 Insulin Signaling Cascade and Insulin Resistance Mechanism 2

1.1.2 Multi-organ cross-talk in Type 2 Diabetes 3

1.1.3 In vitro models for the study of Type 2 Diabetes 4

1.2 Cell Microenvironment Engineering 5

1.2.1 Micropatterning 5

1.2.2 Microfluidic technology 6

1.3 Rational and Motivation for the Study of T2D through human Body-on-a-Chip 6

1.3.1 Aim of the thesis 8

Chapter 2

Micro-scaled Cell and Ex-Vivo Tissue Culture Models **11**

2.1 Introduction and Motivation 11

2.2 Microfluidic technology development 12

2.3 Micro-scaled cell cultures development and analyses 13

2.3.1 C2C12 cell culture in a microfluidic chip 13

2.3.2 Myoblasts derivation and integration within the microfluidic chip 13

2.3.3 Myoblasts differentiation driven by micro-patterning topology 16

2.3.4 Molecular biology analyses on micro-scaled cell cultures 18

2.3.5 Adipose tissue ex-vivo organ culture 18

Chapter 3

Determination of Glucose Flux Parameters in Living Cells **21**

3.1 Introduction and Motivation 21

3.2 High resolution glucose uptake measurements through extracellular medium concentration measurements 23

3.3 High resolution glucose uptake measurements through FRET nanosensor intracellular detection 26

3.4 Dissection of myoblast glucose handling mechanisms 27

3.5 Conclusions 30

Chapter 4

High Resolution Glucose Uptake Measurements in Adipose Tissue In Vitro Cultures **33**

4.1 Introduction and Motivation 33

4.2 Microfluidic adipose tissue organ culture validation 35

4.3 High resolution glucose uptake measurements in microfluidic adipose tissue cultures 36

4.4 Temporally controlled stimulation through microfluidic devices 38

4.4.1 Insulin stimulation: validation of the system and proof of concept experiments 39

4.5 Conclusions 41

Chapter 5

Development and Characterization of Human Skeletal Muscle on a Chip **43**

5.1 Introduction and Motivation 43

5.2 Micropattern topology affects myoblasts proliferation and differentiation 45

5.3 Micropattern integration in the microfluidic chip and C2C12 culture 49

5.4 Human skeletal muscle cells integration and characterization in the microfluidic chip 50

5.5 Conclusions 52

Chapter 6

Conclusions and Future Perspectives **55**

References **61**

Appendix A

CX3CL1 (fractalkine), a new myokine protecting beta-cell and skeletal muscle from TNF-alpha induced insulin resistance **61**

Appendix B

Micro-patterning topology on soft substrates affects myoblasts proliferation and differentiation **89**

Appendix C

Clinical trial on chip show human donor pericyte efficiency in restoring dystrophin in a DMD in vitro model **111**

Appendix D

Determination of glucose flux in live myoblasts by microfluidic nanosensing and mathematical modeling **127**

Appendix E

Methods and Experimental Protocols **159**

Foreword

The work of this PhD program was performed at the Department of Industrial Engineering of the University of Padova and at the VIMM (Venetian Institute of Molecular Medicine) of "Fondazione per la Ricerca Biomedica Avanzata onlus". Part of the experiments on human skeletal muscle cells integration within the microfluidic chip were performed at the Department of Genetic Medicine and Development in the Medical Centre (CMU) of the University of Geneva (Switzerland), under the supervision of Dr. Karim Bouzakri.

In this 3 year period, I could apply engineering tools to my biological background, having the possibility to explore new and unexpected frontiers in a multidisciplinary laboratory.
It is mandatory for me to thank Dr. Alessandro Zambon, for his scientific and human support during these years, and Prof. Philippe Halban and Dr. Karim Bouzakri for the great opportunity to work in their group at the CMU in Geneva. I also would like to thank Dr. Nicola Elvassore for giving me constructive chances and challenges.
I am also grateful to Università degli Studi di Padova, MIUR, Telethon, EASD-Roche for the financial support to the research activity and to EASD again, for awarding me with an "Albert Renold Fellowship Travel Grant" that financially supported my stay abroad.

All the material reported in this dissertation is original, unless explicit references to studies carried out by other people are indicated.

During the period of the PhD program the following publications have been produced:

1. Zambon A*, Zoso A*, Luni C, Frommer WB, Elvassore N. 2013. "Determination of glucose flux in live myoblasts by microfluidic nanosensing and mathematical modeling". *Integrative Biology*. In press. DOI: 10.1039/c3ib40204e (*equally contributing authors).

2. Zatti S, Zoso A, Serena E, Luni C, Cimetta E, Elvassore N. 2012. "Micropatterning topology on soft substrates affects myoblast proliferation and differentiation" *Langmuir* 28(5):2718-26.

3. Plomgaard P, Rutti S, Hansen J, Dusaulcy R, Arous C, Zoso A, Bianda V, Brandt C, Berney T, Elvassore N, Dermitzakis E, Donath M, Pedersen BK, Halban P, Bouzakri K. "CX3CL1 (fractalkine), a new myokine protecting beta-cell and skeletal muscle from TNF-alpha induced insulin resistance" Submitted to *Diabetes*.

4. Serena E, Zatti S, Zoso A, Lo Verso F, Tedesco FS, Cossu G, Elvassore N. "Clinical trial on chip show human donor pericyte efficiency in restoring dystrophin in a DMD *in vitro* model" Submitted to *Stem Cells Translational Medicine.*

5. Zambon A*, Zoso A*, Magrofuoco M, Flaibani M, Quake SR, Fadini GP, Elvassore N. "Diabetes on a chip". In writing.

Moreover, part of this work has been presented at the following national and international conferences:

1. Dissection of organ cross-talk through human body on-a-chip. *SAB visit Venetian Institute of Molecular Medicine*, Padova, Italy, November 22nd – 23rd 2013

2. Determination of glucose metabolic fluxes in live myoblasts by microfluidic nanosensing and data analysis. *49th EASD Annual Meeting* Barcelona, Spain, September 23rd – 27th 2013

3. Extrinsic clock-factors oscillatory dynamic on the circadian rhythm of peripheral tissues through microfluidic technology. *Chronobiology Gordon Conference*. Newport (Rhode Island, USA), July 14th – 19th 2013

4. Mesoangioblasts contribution to dystrophin restoration in a human DMD in vitro model. *International Society for Stem Cell Research 11th Annual Meeting ISSCR*. Boston (USA), June 12th – 15th 2013

5. Muscle tissue micro-engineering. *2013 Spring Padua Muscle Days. Skeletal muscle in denervation, aging and cancer*. Padova and Terme Euganee, Padova (Italy), March 15th – 17th 2013

6. Microfluidic chip for high-resolution glucose uptake measurements on patient-derived adipose tissue culture. *BMES 2012*, Atlanta, Georgia (USA), October 24th – 27th 2012.

7. Patient-specific insulin resistance investigation through in vitro microfluidic glucose uptake assay. *11th Annual VIMM meeting*. Marostica (VI), Italy, October 19th – 20th 2012.

8. Sviluppo di una piattaforma microfluidica automatizzata per la misura ad alta risoluzione del consumo di glucosio in tessuto adiposo e muscolare. *GRICU 2012*, Pescara, Italy, September 16th – 19th 2012.

9. Automazione e integrazione di piattaforme microfluidiche. *GRICU 2012*, Pescara, Italy, September 16th – 19th 2012.

10. Foto-pattern in situ per l'adesione e la coltura selettiva di cellule in microfluidica. *GRICU 2012*, Pescara, Italy, September 16th – 19th 2012.

11. Engineering an in vitro model of human muscle dystrophy for highthroughput screenings and development of therapeutic strategies. *XVI Telethon Scientific Convention*. Riva del Garda (TN), Italy. March 7th – 9th 2011.

12. Microfluidic technologies for biotechnology applications. *SAB visit. Venetian Institute of Molecular Medicine*, Padova, Italy. 20th – 21st February 2011.

Sommario

Il Diabete di tipo 2 insorge da una condizione di insulino-resistenza che colpisce soprattutto il tessuto muscolare e il tessuto adiposo, alterando il loro uptake di glucosio e portando a complicanze cliniche più gravi. È altresì noto che questi tessuti interagiscono tra loro con una comunicazione distruttiva che peggiora la patologia. A causa della sua complessità clinica, il Diabete di tipo 2 richiede spesso trattamenti paziente-specifici.
In questo scenario, nasce la necessità di sviluppare un un modello *in vitro* umano capace di fornire risposte biologiche rilevanti e che sia rappresentativo della patologia *in vivo* specifica del paziente.

L'obiettivo di questa tesi di dottorato è lo sviluppo e l'integrazione di modelli di tessuto umano derivati da pazienti affetti da Diabete di tipo 2 in una tecnologia microfluidica per svolgere screening di farmaci *in vitro*. Tale modello, permetterà di dissezionare, riprodurre e studiare le interazioni dei tessuti in patologie che coinvolgono più organi. In questo specifico caso, permetterà di investigare l'insulino-resistenza dei tessuti umani sottoposti a stimoli veloci, sia fisiologici che fisio-patologici.

Considerato il loro ruolo centrale nell'insorgenza del Diabete, in questa tesi è presentata l'integrazione in una tecnologia "Lab-on-a-chip" di tessuto muscolare e tessuto adiposo.

Un modello di mioblasti è stato utilizzato per lo studio delle dinamiche cellulari del glucosio. La tecnologia microfluidica in cui è stato integrato ha permesso di monitorare la concentrazione extracellulare di glucosio con un'alta risoluzione temporale, mantenendo integra nel contempo la coltura cellulare. Inoltre l'uso di un nanosensore intracellulare FRET specifico per il glucosio ha permesso di misurare la concentrazione citosolica del metabolita in mioblasti vivi. Avvalendosi di modellazione matematica e analitica dei dati sperimentali è stato possibile calcolare i parametri cinetici propri del glucosio in una cellula: nello specifico sono state calcolate le cinetiche del trasporto attraverso la membrana citosolica e della fosforilazione intracellulare.

Il tessuto adiposo è stato invece integrato come organo-coltura in un chip microfluidico automatizzato, il quale è in grado di fornire stimoli di insulina o farmaci controllati nel tempo, rendendo flessibile la possibilità di sperimentazione. Il tessuto adiposo da parte sua ha mostrato elevate vitalità e attività metabolica, un'alta sensibilità alla portata del medium durante le misure di uptake di glucosio e soprattutto una elevata ripetibilità sperimentale.

Infine, viene presentata l'integrazione in dispositivi microfluidici di tessuto muscolare umano accoppiando inoltre tecniche di micropattern per ottenere un migliore controllo della topologia cellulare *in vitro*. Innanzitutto è stato studiato l'effetto dovuto all'utilizzo di pattern a righe di diverse ampiezze sulla proliferazione e differenziamento dei mioblasti *in vitro*: maggiore è l'ampiezza delle righe del pattern, minore è la proliferazione e maggiore è il differenziamento. Il miglior pattern (composto da righe di 300 μm), è stato riprodotto all'interno di chip microfluidico. Mioblasti umani coltivati in questo sistema sono stati in grado di differenziare in miotubi caratterizzati da una elevata organizzazione sarcomerica. Inoltre è stato verificato il mantenimento dell'attivazione del pathway dell'insulina, risultato evidenziato adattando convenzionali tecniche di biologia molecolare ai piccoli volumi cellulari coinvolti. Il tessuto muscolare integrato in microfluidica è stato infine studiato sotto lo stimolo di medium condizionato da tessuto adiposo, mostrando l'insorgenza di insulino-resistenza.

Questi risultati mostrano un elevato potenziale nel futuro delle sperimentazioni cliniche e farmaceutiche grazie alla possibilità di poter riprodurre *in vitro* le interazioni multi-organo di patologie complesse. Con il supporto di tali strumenti sarà possibile superare le attuali limitazioni presenti nello sviluppo di nuove terapie. Sarà infatti possibile riprodurre *in vitro* la patologia, anche in una maniera paziente-specifica, permettendo quindi l'attuazione di terapie personalizzate.

Summary

Type 2 Diabetes (T2D) results from an insulin resistance condition that affects mainly adipose and skeletal muscle tissues by altering their glucose uptake and leading to major clinical complications. Moreover, it is known that these tissues interact each other with a negative cross-talk that worsen the pathology. Due to its clinical complexity, T2D would require patient-specific treatment. In this context it will be extremely helpful to have *in vitro* human tissue-based assays, able to provide biological responses representative of the *in vivo* patient-specific pathology.

The aim of this PhD thesis is the development and integration of human tissue models in a microfluidic technology, for *in vitro* T2D drug testing on patient-derived tissues. More specifically, to develop a new tool with the capability to dissect, reproduce and study tissue interactions in multi-organs derived pathologies, that allows to carry out biological investigations on human insulin-resistant tissue models which are exposed to fast physiological and pathological stimuli.

Integration "on-a-chip" of skeletal muscle and adipose tissues and their applications are presented in this thesis. These tissues were chosen for their involvement in T2D.

A myoblasts model integrated in a microfluidic technology and coupled with glucose FRET-based nanosensing is described. Through microfluidic technology it was possible to monitor extracellular glucose concentration with high temporal resolution with minimum disruption of cell culture condition, while glucose FRET nanosensing permitted to measure cytosolic glucose concentration in live cells. With the assistance of mathematical modeling and data analyses it was possible to derive from experimental data the kinetic parameters involved in glucose handling (glucose diffusion through plasma membrane and intracellular glucose phosphorylation).

On its side, adipose tissue organ cultures was integrated in an automated microfluidic chip which is able to provide temporally controlled stimulations (e.g. insulin or drugs), allowing significant flexibility of the experiments. This tissue model showed high viability and

metabolic activity, high flow rate sensitivity in high resolution glucose uptake measurements and robustness.

Finally, it is presented the integration of human skeletal muscle in a microfluidic device. For the development of this *in vitro* tissue, micropattern techniques were coupled and applied in order to have a better control on cell topology. It has been studied the effect of different-width of pattern lanes on myoblasts proliferation and differentiation. Wider lanes negatively affect cell proliferation, whereas they have a positive effect on myoblasts differentiation. Human myoblasts were successfully integrated and differentiated in the microfluidic chip with a 300-μm lanes pattern. Myotubes showed a high sarcomeric organization, outlining the obtainment of a tissue model very similar to the *in vivo* muscle. Moreover, it has been demonstrated that insulin pathway activation is conserved in physiological conditions, and that it can be deeply investigate through conventional molecular biology techniques.
The skeletal muscle model on-a-chip was finally studied for the insulin resistance onset after treatment with adipose tissue conditioned medium.

These results show a good potential in future pharmaceutical and clinical experimentation. In fact they give proofs that a new tool able to dissect and reproduce tissue interactions in multi-organs derived diseases, can be generated. With its support, it would be possible to overcome current limitation in therapy design, by reproducing *in vitro* models of the disease, even in a patient-specific way, in order to perform individual therapeutic development.

Chapter 1

State of the Art and Motivation

1.1 Type 2 Diabetes

Type 2 Diabetes (T2D) is a metabolic disorder characterized by chronic hyperglycemia with disturbance of carbohydrates, fat and protein metabolism(Alberti and Zimmet, 1998). This chronic disease arises from a condition of both insulin resistance and insulin secretion defect. In normal conditions, after glucose ingestion the increased glycemia in the blood stimulates pancreatic β-cells to secrete insulin. Circulating insulin promotes then glucose uptake by insulin sensitive tissues (liver, muscle and adipose tissue), contributing to the maintenance of glucose homeostasis(DeFronzo *et al.*, 1992). If a decrease of insulin action (insulin resistance) occurs, β-cells can upregulate insulin secretion. However, blood glycemia levels increase mildly over time, resulting damaging because of glucose toxicity, and this contribute to β-cells dysfunction(Stumvoll *et al.*, 2005). Defects on β-cells function and insulin resistance of liver and peripheral tissues lead to the development of glucose intolerance and overt diabetes. The long-term effects of T2D include long-term damage, dysfunction and failure of various other organs, such as kidney eye retina and peripheral nervous system and to general cardiovascular diseases(Alberti and Zimmet, 1998).

T2D has a multifactorial pathogenesis, which comprises alterations in several gene products and a change in lifestyle (physical inactivity) and overeating (obesity). In last decades this disease has become epidemic worldwide (Figure 1.1). According to the IDF (International

Diabetes Federation) estimations, 382 million people suffer of diabetes and by 2035 will rise to 592 million in the world. It usually occurs in adults, with the greatest number of people with diabetes comprises between age of 40 and 59, even if its diagnosis is increasing in children and adolescents. Along with this increase on number of people affected, in 2013 the global health expenditure for this disease is accounted for USD 548 billion dollars, the 11% of health-care spending for adults (International Diabetes Federation; Stumvoll *et al.*, 2005).

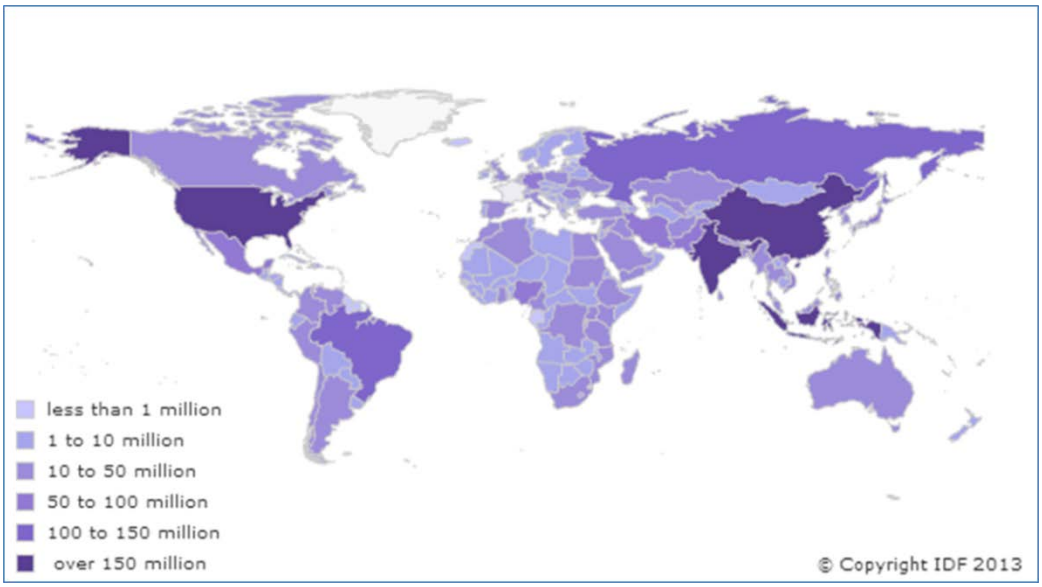

Figure 1.1 *Distribution of diabetes in the world. Data and map from: IDF – International Diabetes Federation- Atlas 2011*

1.1.1 Insulin Signaling Cascade and Insulin Resistance Mechanism

In the great majority of individuals, impaired tissue insulin sensitivity represents the primary defect. Numerous studies based on euglycemic insulin-clamp test, have demonstrated that insulin resistance initiate the process of T2DM in humans, by inducing hyperglycemia (DeFronzo *et al.*, 1992).

In normal conditions, insulin action starts by its binding to the proper receptor tyrosine kinase which lead to the phosphorylation of the Tyr residues in the cytoplasmic face. The active receptor recruits and phosphorylates on Tyr residues the substrate proteins, such as IRS1 (Insulin Receptor Substrate-1) or IRS2. The phosphorylated IRS recruits in turn, PI3K at the plasma membranes leading to the production of the second messenger PIP_3. PIP_3 then targets the signal by phosphorylating PDK1 whose target is PKB/Akt, which is activated after phosphorylation on Serine and Threonine residues. Activation of Akt finally leads to the phosphorylation and activation of AS160 (Akt Substrate of 160 kDa). This protein is the

last messenger that lead to the translocation of glucose transporter GLUT4 to the plasma membrane, resulting thus in increased glucose uptake (Figure 1.2).

In obesity and T2D, insulin resistance is characterized by defects at many levels of this pathway, from decreases in protein concentration (e.g. IRS1 expression) and kinase activity (e.g. phosphorylation of Akt) to translocation of GLUT4 (Saltiel and Kahn, 2001). Although the molecular defects that characterize this condition is very well known, the causes of insulin resistance are not well defined yet. Genetic and acquired factors (e.g. sedentary lifestyle and obesity) can deeply influence insulin sensitivity (Eckel *et al.*, 2005).

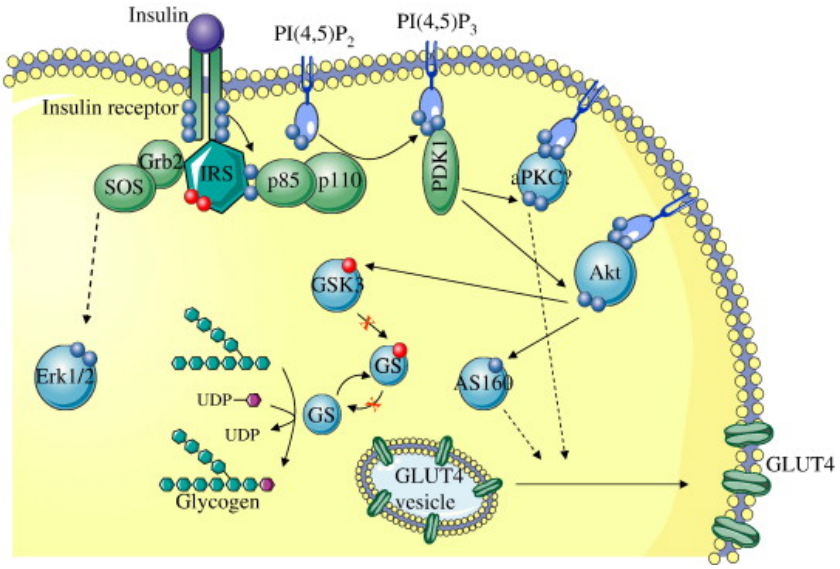

Figure 1.2 *Schematic of the insulin intracellular signal transduction cascade , reporting the signaling steps whose alterations have been studied in insulin resistant and T2D subjects (Source: Frojdo S et al., 2009).*

Since T2D is polygenic, it may comprises polymorphisms in multiple genes encoding the proteins involved in insulin signaling, secretion and intermediary metabolism (Saltiel and Kahn, 2001). Moreover, accumulation of lipidic metabolites, ER stress and activation of systemic inflammation are thought to play a role in the development of insulin resistance (Samuel and Shulman, 2012).

1.1.2 Multi-organ cross-talk in Type 2 Diabetes

As already mentioned above, T2D is far to be a pathology caused by a single triggering event. In recent years, it has become apparent that, beyond insulin resistance onset, inter-organ communication plays a pivotal role in the development of diabetes (Plomgaard *et al.*, 2012).

Adipose tissue is now largely recognized as a major endocrine and secretory organ of molecules such as free fatty acids, tumor necrosis factor (TNF-α), Interleukin-6 (IL-6), angiotensin, resistin and other adipokines and pro-inflammatory factors. All these factors can interfere with insulin sensitivity of peripheral tissues, such as skeletal muscle and liver (Dietze *et al.*, 2002, 2004; Sell *et al.*, 2008) and more generally with their normal activity, as it occurs with endothelial vessels.

By its side, also skeletal muscle has been shown to be a secretory organ, by secreting so-called myokines that can act on the muscle itself and on distant tissues, such as fat, liver and on pancreatic β-cells. Within these myokines, there are IL-6, IL-8, Irisin and a plethora of other molecules (Pedersen, 2011).

Along adipose and skeletal muscle tissue, also brain and the nervous system may be a key mediator by reacting to adipose tissue signals. Its role seems to interfere with fat mass and distribution, hepatic glucose production and inflammation state (Lee *et al.*, 2009).

1.1.3 *In vitro* models for the study of Type 2 Diabetes

In the study of molecular and biochemical mechanisms involved in diabetes, the most used *in vitro* models are skeletal muscle and adipose tissues. They result very advantageous, since skeletal muscle represents the principal tissue involved in insulin-stimulated glucose metabolism, whereas adipose tissue is easily available and highly insulin sensitive and responsive (Ciaraldi *et al.*, 1995).

In vitro cultures of human differentiated skeletal muscle cells are a widely diffuse and recognized model. It exhibits biochemical and molecular features of insulin-stimulated glucose metabolism comparable with the *in vivo* situation and it allows to study cells from different subjects under standardized and well-controlled experimental conditions. More importantly, skeletal muscle cells established from T2DM patients maintain the diabetic phenotype, including the decrease of insulin-dependent glucose uptake (Henry *et al.*, 1995; Thompson *et al.*, 1996).

Adipose tissue models are mainly based on culture of adipocytes isolated from biopsy or on organ-culture of whole adipose tissue explants. The major strength of this second method is the good maintenance of gene expression and adipocytes function within the adipose tissue for up to 2 weeks. Moreover, adipose tissue obtained from T2DM patients maintains the insulin resistance characteristics (Fried and Moustaid-Moussa, 2001; Phillips *et al.*, 2008; Trujillo *et al.*, 2006). Furthermore, few papers have been recently published on the *in vitro* tests of anti-diabetic drugs (van de Venter *et al.*, 2008; Alonso-Castro and Salazar-Olivo,

2008) for comparing their effects and studying their mechanism of action on murine and human cell lines.

1.2 Cell Microenvironment Engineering

In vitro models of biological tissues have been fundamental tool to understand human pathophysiology. By studying isolated cells in well-defined laboratory conditions, it is possible to have robust, predictable and repeatable results. Moreover, *in vitro* tissue models are fast, simple to use, and can mimic both healthy and diseased conditions, resulting thus an indispensable and complement tool to the *in vivo* studies. However their simplicity can't reflect the complexity of the human body. (van der Meer & van der Berg, 2012).

In the human body, cells are exposed to multiple signals that vary in space and time, including cytokines secreted by neighbor cells, direct contact with them and biochemical and mechanical interactions with the extracellular matrix. Standard *in vitro* cultures are not capable to closely mimic the cellular environment present in a whole organism: soluble factors are presents in abnormal concentrations, topological cues are absent and cell-cell interactions are randomly organized (El-Ali *et al.*, 2006).

When increasing the realism of the system by adding more cell type, the model become more complex: each part of the system interact with the other parts with an unpredictable behavior. The system consequently is more prone to deviations and less robust results due to small differences on the starting condition.

More realistic models can be reproduced by artificially engineering key features of the *in vivo* environment, such as geometrical, mechanical and biochemical factors.

Microfabricated systems (or "Lab-on-a-chip" technology) are an alternative tool that offers the capability to integrate to the *in vitro* tissue models these features in a controllable and reproducible way. These systems that integrate *in vitro* tissue cultures with engineered microenvironment are termed *Organs-on-chips.*

Organs-on-chips are based on bioMEMS (biological MicroElectroMechanical Systems) and on microfluidic technologies that allow high spatio-temporal control of the culture conditions. Furthermore with these technologies, the models have micrometric dimensions, permitting a small use of cells and reagents.

1.2.1 Micropatterning

One way to control cell environment is the use of micropattern of adhesion proteins on the *in vitro* tissue culture. Micropattern allows the precise control of the cells topology over the

culture surface. By patterning micrometer-sized geometries it is possible to control cell-cell interactions and cell-ECM interactions. A large variety of surface-patterning techniques are available, from photoreactive chemistry to soft lithography (e.g. microcontact printing) (El-Ali *et al.*, 2006), coupled with elastic surfaces or not (Engler *et al.*, 2004; Serena *et al.*, 2010).
It has already been shown that guide and control cell topology can help cell fusion into syncytium (as it happens for skeletal muscle cells *in vitro*) or to create gap junctions for communication in cardiomyocytes. Moreover, it is possible to control cell spreading or the location of focal adhesions (Cagnin *et al.*, 2012).

1.2.2 Microfluidic technology

Microfluidic technology is the science and technology of systems that manipulate small amount of fluids, using channels with dimensions of hundreds to tens of micrometers.
Microfluidics offers the capabilities to control the concentrations of molecules in space and time. This feature lead to the possibility of having a dynamic control over the cellular microenvironment in terms of providing nutrients, stimuli and gases.
A microfluidic system usually has a series of generic components: units for introducing reagents and samples and units for moving these fluids around on the chip, and for combining and mixing them. They are usually composed by glass, silicons and more frequently by elastomers such as PDMS (polydimethylsiloxane) which is optically transparent, soft and biocompatible. Moreover, microfluidic may be characterized by side benefits such as miniaturization, automation and parallelization. All these characteristic allow a spatiotemporally control of the culture microenvironment with higher resolution and accuracy (Whitesides, 2006; El-Ali *et al.*, 2006).

1.3 Rational and Motivation for the Study of Type 2 Diabetes through Human Body-on-a-Chip

Type 2 Diabetes is a complex pathology that need the utilization of different classes of drugs that act with different mechanism and targets and with effects that often change between patients. In last decades, significant changes in the ability to treat diseases have resulted by innovations in health sciences with a consequent improvement of the quality of life (DiMasi *et al.*, 2003).
New therapy screening and development demands robust, cheap and fast methods to test drug candidates (Dittrich and Manz, 2006).

Specific studies on human patients are possible but are tremendously expensive and require ethical and safety approvals. Moreover, *in vivo* studies often don't permit a deep evaluation at specific tissue level: their interplay complexity allow a very difficult outcome interpretation. Animal models are not ideal either because of the phenotypic and metabolic differences between humans and animal and for the raised ethical issues. On the other side, *in vitro* models are simple, but with their simplicity they fail to mimic key aspects of the human body; moreover the most relevant limitation of conventional single-cell-type-based assays is that they do not capture multi-organ interactions. For all these reasons, the interest in developing new models, able also to contain times and costs, is continuously increasing.

Lab on-a-chip technologies are powerful tools, whose increasing accessibility is leading them to become a diffuse support for cell culture, in order to better answer some fundamental biological questions (Figeys and Pinto, 2000).

Single organs on a chip, such as lung-on-a-chip (Tam *et al.*, 2011; Zhang *et al.*, 2010) or liver-on-a-chip (Khetani and Bhatia, 2008; van Midwoud *et al.*, 2011), have already been generated within microfluidic systems, in order to study human physiology and pathophysiology. These *in vitro* models are promising substitutes for human *in vivo* studies, and their small scale enables precise control of culture conditions and high-throughput experiments, which are not economically sustainable on a macroscopic level.

Cross-talk between tissues can be realized through technological mechanisms that mimic what occurs in the human body, i.e., through soluble agents. Moreover the possibility to integrate biosensor technology with microscopy-based readouts in combination with automated analyses systems, makes microfluidics a powerful tool for highly parallel, multiplexed and high-throughput assays (Neuži *et al.*, 2012; Hong *et al.*, 2009).

With this outlook, microfluidic technology seems to be a very good system for studying and treating complex and multifactorial diseases, such as Type 2 Diabetes.

To develop a good T2D *in vitro* model, the conservation of diabetic phenotype is a crucial point and an essential prerequisite for a reliable screening of anti-diabetic drugs and therapies with a perspective of translational medicine and testing of *ad hoc* treatments for each patient. In this perspective, the use of *in vitro* models of human patient-derived muscle and adipose tissue results to be a good tool, since the conservation of diabetic phenotype and insulin resistance characteristics are maintained (Ciaraldi *et al.*, 1995; Fried and Moustaid-Moussa, 2001).

In particular, by using microfluidic technology chips, it is possible to control the time evolution of the culture conditions through an accurate control of metabolites concentration (such as glucose), mimicking as close as possible the physio-pathological conditions.
In a prospective view, through *ad hoc* microfluidic devices, it will be possible to associate the response of even patient-derived tissue to specific dose-time drug stimulation, with the obtainment of useful information to create a patient-specific therapy. Through this technology, it will be possible to reproduce *in vitro* the pharmacokinetics and pharmacodynamics of patient specific pharmacological treatments.

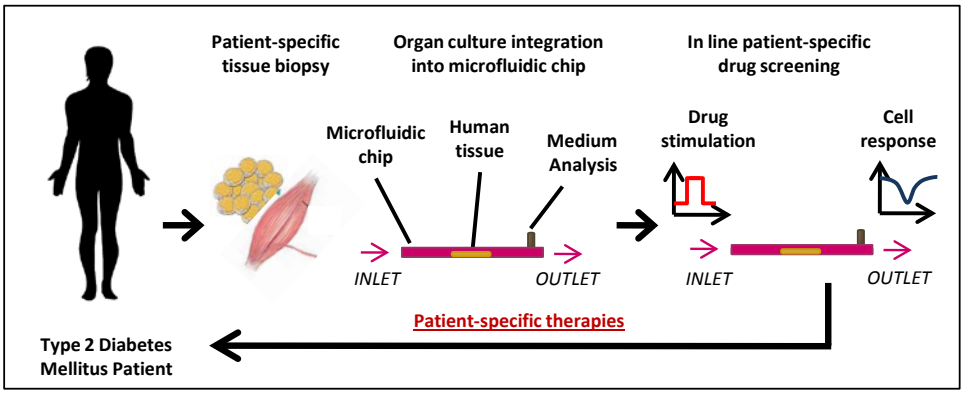

Figure 1.3 *Schematic view of microfluidic in vitro model strategy for the study of type 2 diabetes.*

The intrinsic property of microfluidic based on nano-volumes, will highly increase the aspect-ratio between volume of the living tissue and the net medium volume in culture chamber leading for example, to high sensitivity of measuring glucose uptake directly from the culture medium or enhancing the tissue response to small concentration variation of cytokines. Finally, it will be possible to re-create the connections that occurs between the organs that are more involved in the onset of the pathology, mimicking as close as possible the complexity of the human body.

1.3.1 Aim of the thesis

Considering all these cues, the aim of this PhD thesis is the development and integration of human tissue models in a microfluidic technology, for *in vitro* Type 2 Diabetes drug testing on patient-derived tissues. More specifically, the aim is to develop a new tool with the capability to dissect, reproduce and study tissue interactions in multi-organs derived pathologies and that allows to carry out biological investigations on human insulin-resistant tissue models exposed to fast physiological and pathological stimuli.
In details, to go after this goal two different type of tissues were integrated in a microfluidic technology, that are the peripheral tissues that mostly account for insulin-mediated glucose

uptake and homeostasis. On one side it was integrated skeletal muscle tissue, which accounts for the 80% of insulin-stimulated glucose uptake; on the other side adipose tissue was integrated, which contributes to the onset of Diabetes not only with blunted glucose uptake, but also by secreting cytokines which "communicate" with other tissues.
By its side, microfluidic technology were applied since it allows to obtain accurate time evolution control of the culture conditions. Moreover, thanks to the high ratio between tissue surface and culture medium volume it allows to enhance tissue's response with high overall changes in medium concentration of metabolites and cytokines.
Finally, micropattern techniques coupled with microfluidic technology facilitated to reproduce a more physiological microenvironment cell culture condition, more precisely, by controlling cell topology and cytokines accumulation.

In this thesis, the evolution to get to the development of reliable micro-scaled *in vitro* models of human muscle and adipose tissues has been divided in specific chapters.
In Chapter 2 the methods of cell and organ cultures and of micro-scaled technologies applied in this work are presented.
In Chapter 3 it is described a first application of skeletal muscle tissue integrated with microfluidic technology. Here glucose flux dynamics is dissected in living cells, thanks to the development of high temporal resolution extracellular and intracellular glucose uptake measurements obtained in microfluidics. Then mathematical modeling and data analysis were used to combined data and extrapolate the kinetic parameters of glucose flux.
Chapter 4 reports the integration and characterization of adipose tissue organ culture in a microfluidic technology. Also for this tissue high temporal resolution measurements were obtained. Moreover, an integrated and automated chip is presented here with proof of concept experiments of its application for insulin (or drug) stimulation.
Chapter 5 is focused on human skeletal muscle cells integrated with microfluidics. In the first part it's shown how engineering microenvironment can help to obtain a model that is more similar to the *in vivo* tissue. In the second part is highlighted the characterization of skeletal muscle integrated in the chip, both in a myogenic and in a Diabetes-related point of view.
Chapter 6 summarizes conclusions of the work, giving also perspectives of how the technology can be applied.
Appendixes will give more details about specific contents in the chapters.*in vitro*

Chapter 2

Micro-scaled Cell and *Ex-Vivo* Tissue Culture Models

2.1 Introduction and Motivation

Human physiology is a complex phenomenon which mechanisms are not easy to unravel. The most faithful model to study it's the human body itself. By the way, human studies does not permit a deep investigation at single tissue level, besides of being intrinsically low through-put for testing new therapies and drugs.

A reductionist approach based on *in vitro* tissue models have helped to dissect human functions both in healthy and diseased conditions, through robust and repeatable measurements. However *in vitro* models simplicity brings scientists to put aside physiologically relevant features of the cellular *in vivo* environment.

Within these considerations, it is necessary to develop *ad hoc in vitro* models capable to mimic the key aspects of *in vivo* physiology and also able to permit the complete control of microenvironment over the cell culture (van der Meer and van den Berg, 2012).

In this perspective microfluidic technology, which is based on small volumes, allows to tune the exchange rates of nutrients and create thus more controlled cell culture conditions. This characteristic combined with miniaturization and the possibility to have on-line measurements, prompt microfluidic to be an highthroughput tool in therapy development (Gómez-Sjöberg *et al.*, 2007). A more realistic microenvironment can be generated by

adding micropattern to the cell culture, in order to reproduce *in vitro* the geometrical stimuli to which cells are exposed *in vivo*.

To date, cell systems based on microfluidics are applied to many different situations, and a new era based on organs-on-a-chip has raised in recent years. The most diffuse model, is the integration of liver in microfluidic devices (liver on a chip) to perform hepatic metabolism and toxicity studies (van Midwoud *et al.*, 2011). Other organs on a chip developed are the lung and the blood vessels (Tam *et al.*, 2011; Raghavan *et al.*, 2010).

Focusing on the study of T2D, the only *in vitro* models coupled with microfluidic technology are mainly pancreatic cells. In these studies, microfluidics serve to mimic vascularization of the whole islets or to permit the on-line monitoring of hormones secrection (e.g. glucagon) (Sankar *et al.*, 2011; Shackman *et al.*, 2012).

By the way, few of these tissue models on a chip are based on human primary tissues: most are based on animal derived cells or on cell lines which can't truly mimicking the *in vivo* human behavior.

In this scenario, a reliable model to study T2D mechanisms in human peripheral tissues, based on high spatio-temporal control of the culture microenvironment and a highthroughput scalability perspective, is still missing.

In this work, attention has been put on those tissues that are mainly involved in blunted glucose uptake observed in T2D, skeletal muscle and adipose tissues. To integrate these tissues, *ad hoc* microfluidic chips were designed and developed in collaboration with Dr. Alessandro Zambon.

2.2 Microfluidic technology development

In this thesis different types of microfluidic chip are presented. Each one has been specifically designed to fulfill the requirements of the type of tissue that needs to be integrated. All chips mentioned in this methods section consist in a device composed by a large chamber to host the tissue or cells, with inlet/outlet channels that are needed for medium flowing. They are all prototype chips, designed on the base of a more complex chip, that will be presented in Chapter 4. It presents an injector system that can permit highly temporally controlled biochemical stimulations, and valves and micropumps for the automation of the technology. All these types of microfluidic devices are made of a PDMS layer built via soft-lithography techniques and bound to a cover glass slide (as done for cell cultures) or to another PDMS layer (as made for 3D organ culture).

The different chips are presented from time to time in the next sections.

2.3 Micro-scaled cell cultures development and analyses

2.3.1 C2C12 cell culture in a microfluidic chip

During the development of new technologies, great efforts must be spent in the optimization of the operative conditions, in order to have reliable models, comparable with the conventional "Petri-dish" models.

In this work, the first type of cells that were integrated in a microfluidic chip were C2C12, an immortalized cell line of murine myoblasts, precursor cells of skeletal muscle.

C2C12 present a morphology very similar to human skeletal muscle cells (which will be presented in the next section), but are easier to manage and are less precious then primary cultures of human-derived cells.

These cells were integrated in the chip shown in Figure 2.1. This chip has a surface area of 10 mm^2 and a total volume of 1 µL and usually is equipped with a reservoir for medium at the inlet. More details for C2C12 seeding and culture in the microfluidic chip are reported in the Appendix E

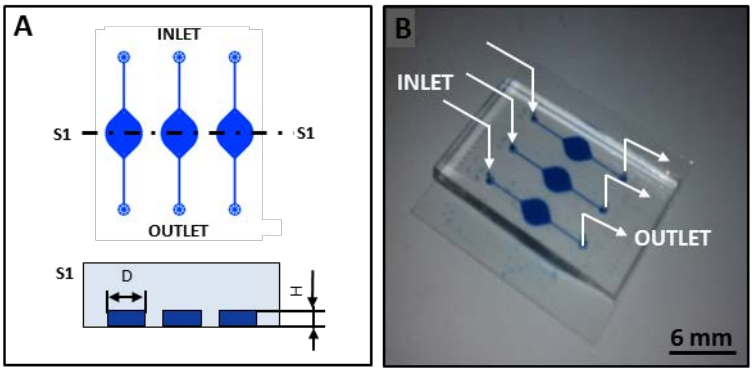

Figure 2.1 *Microfluidic chip prototype.* ***A)*** *Schematic of top view and section of the microfluidic cell culture chambers. D is equal to 3 mm, H is equal to 100 um.* ***B)*** *Picture of the microfluidic chip.*

C2C12 integration permitted to take practice with microfluidic culture system, to find out the tricky points of this type of culture (e.g. air bubble formation during medium management, water evaporation, medium refills) and to proceed with the integration of other cell types, in this case human myoblasts.

2.3.2 Myoblasts derivation and integration within the microfluidic chip

In the study of diabetes, *in vitro* cultures of human differentiated skeletal muscle cells (or myoblasts) is a widely diffuse model, since skeletal muscle represents the principal tissue

involved in insulin-stimulated glucose metabolism. This model exhibits biochemical and molecular features comparable with the *in vivo* situation, and more importantly, myoblasts established from T2DM patients maintain the diabetic phenotype, including the reduction of insulin-dependent glucose uptake (Henry *et al.*, 1995). In this contest, T2D skeletal muscle cells represent the ideal patient-derived tissue that can be integrated within the microfluidic chip for insulin-resistance detection.

To achieve this goal, the first cornerstone is to isolate myoblasts from human biopsies and to maintain them in the appropriate culture conditions. After that, myoblasts can be integrated in a microfluidic chip.

Primary human skeletal muscle cells are normally isolated from biopsies explanted after surgery. Myoblasts are ready to be passed after 10 days approximately (Figure 2.2). It is important to maintain these cells in the correct culture conditions in order to keep insulin sensitive or diseased phenotypes. To perform consistent experiments, myoblasts must be differentiated in myotubes (multinucleated cells derived by the fusion of single cell myoblasts), since myotubes are a more reliable model of muscle with the expression of all the proteins involved in insulin-mediated glucose uptake (e.g. IRS-1, GLUT4)(Bouzakri *et al.*, 2003; Al-Khalili *et al.*, 2003). Protocols referring to extraction, culture and differentiation of human skeletal muscle cells are reported in Appendix E .

In addition, Appendix A reports typical experiments on how human skeletal cells are usually analyzed in *in vitro* experiments.

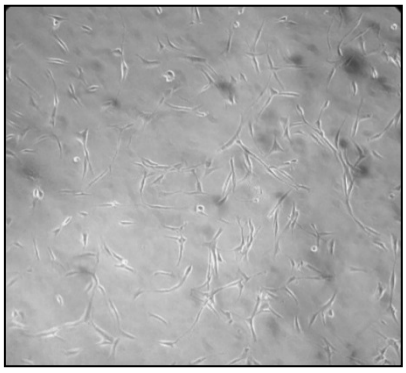

Figure 2.2 *Primary human skeletal muscle cells, 8 days after extraction.*

Once that myoblast cultures are established, they can be integrated in the microfluidic chip. For myoblasts cultures, the chip presented in Figure 2.1 was used, or a bigger version of 21 mm^2 area and a volume of 3 µL. The two types of chip can be used in the same way, without changing the protocol of management.

Since in this system cells are seeded on glass, first of all different coatings were tested in order to outline which one gives a better cell adhesion and cell proliferation. The coatings

tested were Poly-L-Lysine, matrix 804G, matrix Htb9 and gelatin. Among these, matrix 804G, matrix Htb9 and gelatin gave the best results with cell adhesion and proliferation (Figure 2.3), whereas, poly-L-Lysine was ineffective. The firsts three coatings, was after substituted by Matrigel® 2.5% in DMEM, since this matrix is easier to purchase but gives identical results.

Once the best coating was defined, different cell seeding densities were tested, in order to delineate the best starting point for the microfluidic cell cultures. The following cell density were tested: 25 cell/mm^2, 50 cell/mm^2, 100 cell/mm^2, 200 cell/mm^2, 400 cell/mm^2. The optimal density outlined was 200 cell/mm^2.

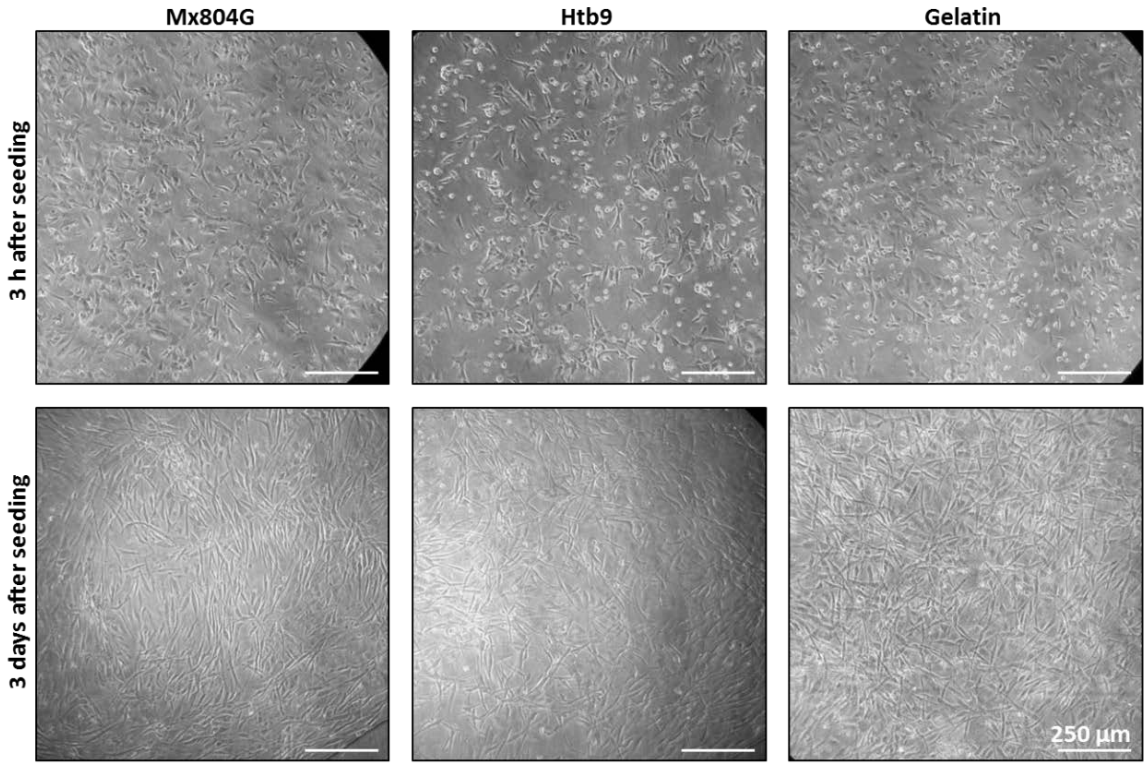

Figure 2.3 *Primary human skeletal muscle cells cultured in the microfluidic chip coated with 3 different coating: matrix 804G, matrix Htb9 and gelatin.*

After seeding, myoblasts cell cultures must be kept vital for long period. Different time rates for medium change were tested in order to have a good proliferation in the tiny volumes of the microfluidic chip. The best results were achieved by changing medium every 12 h during myoblasts proliferation until they reach confluence. Figure 2.4 shows myoblasts proliferation during the first days of culture.

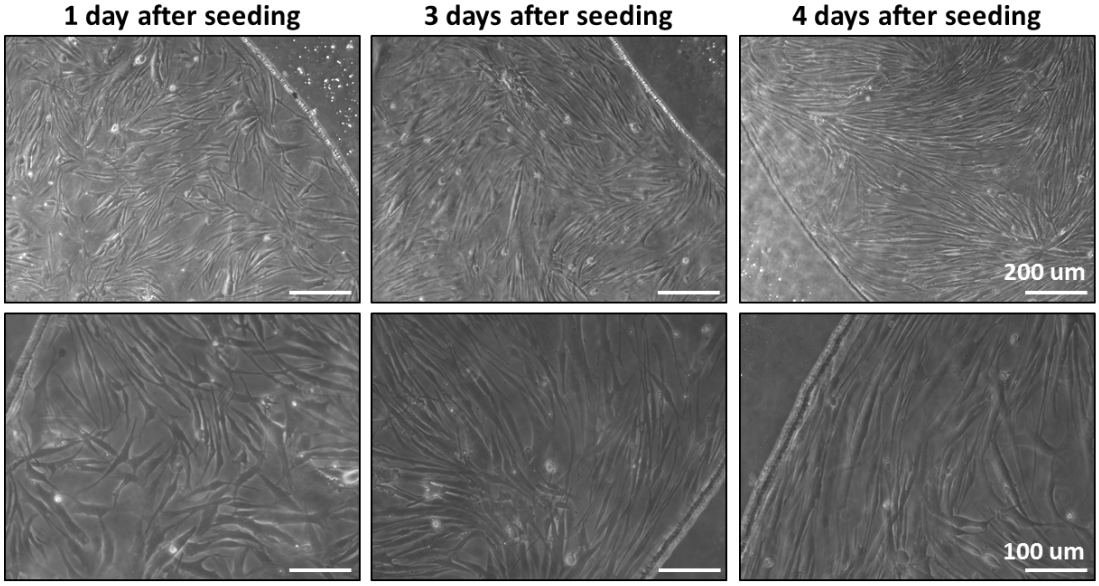

Figure 2.4 *Primary human skeletal muscle cells in the microfluidic chip, during the different days of cultures.*

2.3.3 Myoblasts differentiation driven by micro-patterning topology

Myoblasts differentiation is a very sensitive process and its completion is achieved once myoblasts are fused in multinucleated myotubes. Skeletal muscle differentiation *in vitro* is greatly influenced by microenvironmental culture conditions, as demonstrated in many previous works (Engler *et al.*, 2004; Serena *et al.*, 2010). Factors as myokines accumulation, mechanical properties of the substrate, geometry cues and extracellular matrix composition can intensely drive this process.

In the microfluidic chip myoblasts differentiation can be achieved by finely tuning medium change rates from 12 h to 24 h. By the way, myoblasts fusion can be boost and helped through the topological control of adhesion proteins and through the accumulation of soluble factors in the cell niche. Micropatterning techniques were used to organize myoblasts in parallel lanes of increasing width and interspacing size and by analyzing then how myoblasts proliferation and differentiation are influenced.

The study was carried out on elastic substrates, i.e. polyacrylamide hydrogels of 15 kPa, were micropattern can be achieved in a easy and fast way through microcontact-printing techniques.

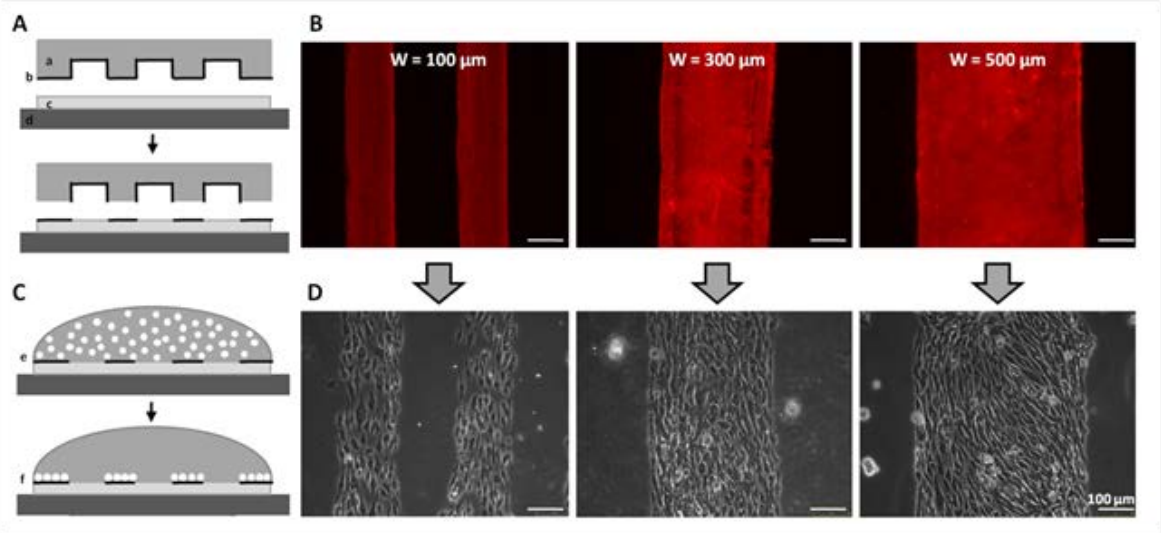

Figure 2.5 A) *Micro-contact printing sketch which outline how adhesion proteins (b) are patterned with a PDMS mold (a) onto the hydrogel surface (c) polymerized on a glass slide (d).* ***B)*** *Laminin immunofluorescence on micro-printed hydrogels. The indicated value of W represents both lane and inter-spacing widths, which are the same for these configurations.* ***C)*** *Cell seeding on the patterned hydrogel substrates: cell suspension is dropped over the micro-patterned hydrogel surface (e); after overnight incubation cells adhere only to the protein-patterned areas (f).* ***D)*** *Phase contrast images of myoblasts culture within the geometries shown in B.*

In details, extracellular proteins lanes of 100, 300 and 500 µm width were patterned over the hydrogel surface, as shown in Figure 2.5. Myoblasts proliferation in the different conditions was studied with BrdU assay, while myoblasts differentiation was evaluated with the calculation of myoblasts fusion index (Total nuclei / MHC+ nuclei). Results are reported in Chapter 5 and in Appendix B.

After having defined which geometry gives the best results, this was reproduced in the microfluidic chamber following the protocol reported in Appendix E .

In this case, a pattern of linear acrylamide is photo-polymerized inside the culture chamber (Figure 2.6). Acrylamide avoid cell adhesion on coated glass, guiding thus cell topology and alignment.

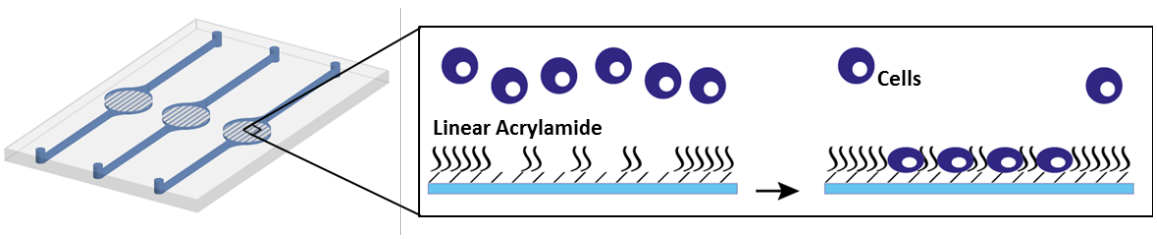

Figure 2.6 *Micro-Pattern in the microfluidic chip schematic and principle of working.*

2.3.4 Molecular biology analyses on micro-scaled cell cultures

Usually, insulin pathway regulation is investigated on myotubes, which are structurally more similar to the *in vivo* skeletal muscle fibers.

Myotubes differentiation is confirmed through the examination of myogenic proteins, such as Myosin Heavy Chain (MHC) or Dystrophin expression and their organization in the myotubes; on the other hand insulin pathway activation is studied through different readouts, like insulin pathway proteins phosphorylation or glucose uptake.

MHC expression and sarcomeric structures organization of myotubes integrated in the microfluidic chip were evaluated through immunofluorescence analysis performed directly inside the microfluidic chamber (protocol is reported in Appendix E), using channels to introduce reagents and antibodies. At the end of the sample preparation, since it can't be mount with a cover glass, they are maintain in PBS 1x and stock at 4 °C.

Expression and phosphorylation of the other proteins were instead analyzed through immunoblot analyses. When working with micro-scaled cultures, protein extraction is a delicate point since the amount of material is very limited.

Immunoblot protocols are reported in Appendix E and were optimized during the development of the work reported in the Appendix C, were the detection of awkward proteins (i.e. dystrophin) from micro-scaled tissue models is a crucial point for a reliable therapy test.

In microfluidic chip cultures, immunoblot can be adapted to the nanoliter volumes involved, giving consistent results as reported in Chapter 5.

2.3.5 Adipose tissue *ex-vivo* organ culture

Adipose tissue culture techniques offers the unique possibility to study the metabolism of human fat cells under basal conditions and under the influence of various stimuli (Nyberg *et al.*, 1976). This method of culture permits a long term maintenance of adipocytes functionality for up to 2 week. Moreover, adipose tissue ex vivo organ culture can preserve its diseased insulin resistance features.

In the past years, the common method to incubate ex vivo biopsies was to place them in well plates, filled with medium (Fried and Moustaid-Moussa, 2001). However, in this *in vitro* system the medium need to be refreshed every 24 hours because of the decrease of nutrient concentration and of metabolites and waste products accumulation. To avoid these factors oscillations, some systems use a different approach, consisting of a macroscopic perfused

bioreactor in which the biopsy is closely maintained in a perfused chamber (Sjöström *et al.*, 1977).

In order to have a trustworthy microscaled model of this type of tissue, the integration of ex vivo organ tissue into microfluidic chip requires specific characteristics. The integration of ex vivo tissue has first of all to ensure the maintenance of cell tissue viability and of cell tissue behavior. Moreover, the device has to guarantee the establishment of an *in vitro* microenvironment able to mimic as close as possible *in vivo* physiological conditions.

In this work, for the *ex vivo* adipose tissue organ culture, a microfluidic culture chamber was specifically designed to allocate the adipose tissue biopsy and create a physiological environment that is able to maintain tissue viability and metabolic activity for days. Figure 2.7 shows the microfluidic device fabricated for organ culture integration.

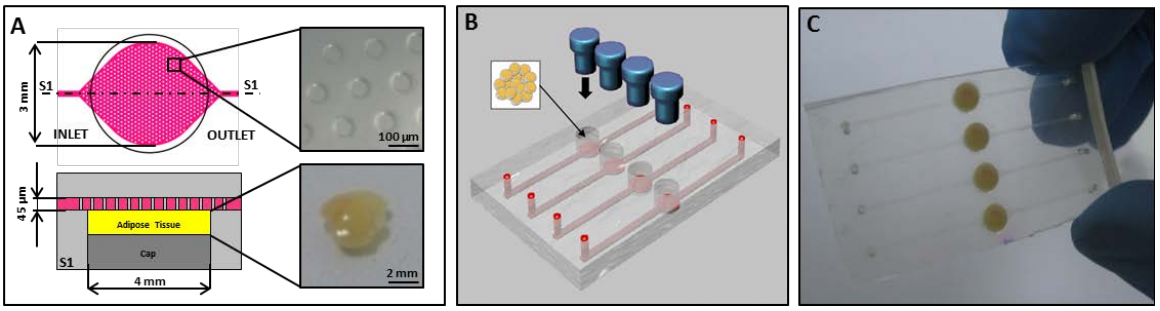

Figure 2.7 *Microfluidic chip for adipose tissue culture.* ***A)*** *Left: Schematic representation of culture chamber for adipose tissue culture (top view and section); Right: microposts and biopsy slice images.* ***B)*** *Schematic 3D platform with biocompatible cup.* ***C)*** *Picture of microfluidic chip with adipose tissue integrated. Cup are not shown.*

As shown in Figure 2.7 the chip is composed by a tridimensional chamber for tissue culture which comprise on the bottom a set of pillar. Pillars serve to avoid tissue collapse over medium flow. Viability of the tissue can be tested through MTT assay at the end of the culture (protocol is reported in Appendix E), while metabolic activity can be monitored during the whole culture through extracellular glucose measurements.

More details of this study are reported in Chapter 4 about adipose tissue integration into microfluidic chip and glucose uptake detection.

Chapter 3

Determination of Glucose Flux Parameters in Living Cells

3.1 Introduction and Motivation

Glucose is the primary source of energy for cells in human body and its blood concentration is tightly regulated in healthy individuals (3.9-6.1 mmol/L) (Frier, 2009; Laakso, 1999).
However, in diseases such as metabolic syndrome and diabetes, impaired blood glucose control is found. Diabetes is related to body's capability to use glucose, since tissue glucose uptake is reduced, event that leads to increasing hyperglycemia and at the end to serious consequences for patients (Cryer *et al.*, 2003; Rolo and Palmeira, 2006).
Identifying the components involved in the different steps of intracellular glucose processing is crucial to identify which mechanisms are disrupted under disease conditions. Glucose uptake represents the amount of glucose that enters cells from the extracellular environment through facilitate diffusion across glucose transporters (GLUTs). Once internalized by the cell, glucose is phosphorylated by the enzyme hexokinase, forming glucose-6-phosphate (G6P) which can't diffuse outside cell, continuing thus its metabolism through glycolysis. In insulin resistant patient, skeletal muscle cells show impaired glucose dynamics (Bird *et al.*, 2007). However, the defect could be related both to the mechanism of glucose uptake itself or to other downstream reactions that limit the overall rate of the process.

Measuring the rate of each single step is not an easy task to achieve in *in vitro* cultures. In a cell culture (as it happens in human body), three different phenomena are involved in glucose handling: extracellular mass transport, diffusion through plasma membrane and intracellular phosphorylation.

Conventionally, glucose uptake is measured in cell cultures by the utilization of non-metabolizable glucose analogs. The most widely used are radioactive hexoses, such as 2-[^{14}C]-deoxyglucose (2DG). They are molecules similar to glucose, able to cross cell membrane through GLUTs. However, on the contrary of glucose, they don't enter glycolysis process. Thus, it is possible to estimate the uptake rate of these glucose analogs by measuring cell radioactivity, since it is proportional to analogs intracellular concentration (Thorens and Mueckler, 2010). Since these radiolabeled hexoses require special training and equipment, other type of molecules were developed, such as fluorescent glucose analogs (Yoshioka *et al.*, 1996) or F-2-deoxy-2-fluoro-glucose (FDG) which are detectable by using fluorescence or positron emission tomography (PET) respectively. By the way, all these methods show many limitations. First, glucose analogs have slightly different kinetics compared to glucose because of the different interaction with the membrane GLUTs and because they are not handled by intracellular enzymes in the same way as glucose. Secondly, they can be toxic, even at low doses. Finally, isotopic techniques offer low spatio-temporal resolution, precluding the detection of rapid dynamics, since glucose uptake measurement is not derived from a viable cell culture.

On the other hands, hexokinase kinetics has been studied only after enzyme purification, therefore in an environment far from the cell cytoplasm, where usually hexokinase works.

In the next paragraphs, it will be described how glucose uptake can be analyzed in living cells first, taking advantages of microfluidic technology and secondly with FRET-based intracellular glucose nanosensing.

Microfluidic technology offers the capability to highly increase the ratio between the volume of the cell culture and the net volume of culture chamber, offering capabilities not achievable in other systems. Thus, thanks to this high cell/medium volumes ratio, small changes in glucose amounts result in detectable changes in the overall medium glucose concentrations. Moreover, microfluidic technology permits an accurate control of the extracellular environment, particularly in the immediate vicinity of cell membrane.

FRET nanosensors are able to measure dynamic changes in metabolites concentration with cellular and subcellular resolution. They consist of a recognition element for the metabolite (i.e. a member of the bacterial periplasmic-binding protein family MglB which recognize in a

specific way D-glucose (Kurtoglu *et al.*, 2007)) fused to a cyan fluorescent protein (eCYP) and a yellow fluorescent protein (eYFP), whose peculiarity is the overlapping emission spectra (Fehr *et al.*, 2003; Hou *et al.*, 2011). This characteristic of the two proteins permit the phenomenon called Forster Resonance Energy Transfer (FRET) between the two fluorescent dies if they are very close in space. In this specific case, glucose binds to the recognition element and induces a conformational change that lead the two protein to distance themselves bringing thus to a variation (diminution) in transferred excitation energy between eCFP and eYFP. FRET efficiency change can be directly correlated to intracellular glucose concentration (Kim *et al.*, 2012) and is visualized as a modification in intensity ratio Ia/Id (where Id and Ia are the fluorescence intensities in the donor (eCFP) and acceptor (eYFP) emission channels upon excitation of the donor). The FRET nanosensor used in this work is the FLIPglu-600μΔ13V, developed in the prof. Frommer lab (Deuschle *et al.*, 2006). It can be encoded within the cells by plasmidic DNA transfection through the plasmid pcDNA3.1-FLIPglu-600μΔ13V.

By using mathematical modeling and data analyses it can be possible to dissect the dynamics of the three processes involved in glucose handling (extracellular mass transport, glucose diffusion through the plasma membrane and hexokinase phosphorylation).

Experiments have been carried out in an easy-to-use cellular model, specifically C2C12 cell line, which are an immortalized line of murine myoblasts.

3.2 High resolution glucose uptake measurements through extracellular medium concentration measurements

Glucose concentration was detected in the extracellular environment through an non-invasive manner based on continuous sampling and analysis of downstream culture medium. Through these measurements it was possible to derive the overall glucose uptake of the culture chamber.

We developed an experimental system composed by a microfluidic chip for cell culture and a liquid handling apparatus that perfuse continuously medium across culture chamber at precise flow rates. More details are reported in Appendix D. The microfluidic chip is composed by 3 or more culture chambers where experiments are performed independently and in parallel and is the same presented in Paragraph 2.2, and shown in Figure 2.1. The measurement of glucose concentration was achieved during perfusion by sampling medium at the outlet of the microfluidic chip at multiple time points. In this manner an off-line

sensing of glucose concentration in the medium was obtained by measuring it via enzymatic assay.

To sample medium, a system to entrap medium drops was used: it was positioned downstream of the microfluidic culture chamber where it collects a small quantity of medium (<1 uL). The trap consisted in a luer-lock needle, closed with a PMMA male luer cup to avoid medium evaporation.

Then, sensing of glucose concentration was determined offline using enzymatic kit assays, more precisely a glucometer which can sample 0.3 uL of solution for a single measurements.

As already stated before, thanks to the high surface-to-volume ratio of chamber over cell culture, the difference between inlet and outlet resulted in a large variation in glucose concentration. Principle is clarified in Figure 3.1A.

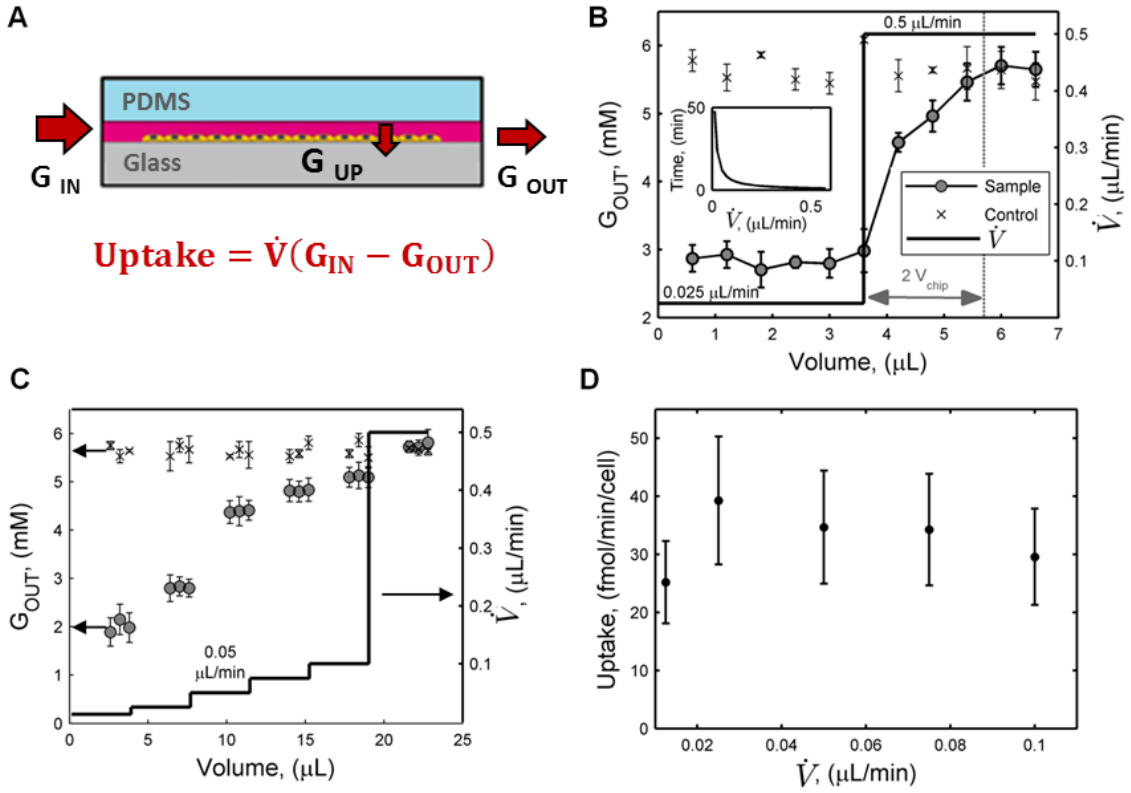

Figure 3.1 *Extracellular glucose measurements.* ***A)*** *Schematic representation of glucose uptake measurements principle.* ***B)*** *Experimental measurements of outlet glucose concentration after a step change in flow rate as a function of the eluted volume. Error bars represent standard deviation (n=3). Inset: computational simulation of the duration of sampling as a function of volumetric flow rate.* ***C)*** *Experimental steady-state measurements of outlet glucose concentration at increasing flow rates, as a function of the eluted volume. Error bars represent standard deviation (n=3).* ***D)*** *Mean single-cell glucose uptake rate as a function of flow rate, calculated from data in C).*

The overall glucose uptake in each cell culture chamber was finally derived through steady-state experiments performed at defined inlet glucose concentrations and calculated from the overall mass balance on the culture system (Equation is reported in Figure 3.1A).

Firstly, the sensitivity of the system was verified and parameters for glucose measurements were optimized, in order to establish times and flow rate for having reliable experiments. During all experiments, measurements of glucose concentration taken from a cell-empty chamber was kept as control, since evaporation of medium is a critical issue when working with tiny volumes.

The first experiment was performed to calculate and confirm the length of transient before a new steady state is established, fundamental requirement when performing dynamic experiments.

A rapid switch in flow rate was applied, by changing it from 0.025 to 0.5 μL/min, during the continuous sampling and measuring of medium every 0.6 uL eluted. As shown in Figure 3.1B the time needed to reach a new steady-state was assess to be approximately that needed for eluting 2-μL volume, that is 2-fold the total volume of the chip.

Moreover, all the measurements showed a high accuracy, since average data variability was approximately 30% both for samples from different culture chambers and for samples collected at different time points at the same steady-state.

The inlet of Figure 3.1B shows the inverse proportionality between flow rate and time needed to collect a 0.6 μL sample. For example, at 0.025 μL/min each sampling was performed every 24 min, while at 0.5 μL/min every 1.2 min. This condition states that flow rate also affects the maximum time resolution of the measurement: working at low flow rates decreases time resolution and vice versa.

On the other hand, the steady-state outlet concentration at 0.5 μL/min is not significantly different to the concentration of the control (perfusion through a chamber without cells) and the signal-to-noise ratio is too small for an accurate detection.

Since flow rate highly impact glucose concentration measured, in order to determine the optimal flow rate to use, a second experiment was performed by measuring outlet glucose concentration at steady-state for six different flow rates ranging between 0.0125 and 0.5 μL/min. The experimental results are shown in Figure 3.1C and they confirm that the smaller is the flow rate, the larger is the glucose concentration difference between inlet and outlet, and the higher is glucose uptake measurement sensitivity. However, as stated before, lower flow rates imply longer times for sample collection that is less temporal resolution during dynamic experiments. As a trade-off between these two requirements the optimal flow rate to use for glucose uptake measurements is 0.05 μL/min.

Data reported in Fig 3.1C, permitted to calculate single cell glucose uptake (G_{up}) through the following mass balance equation:

$$G_{up} = \frac{\dot{V} \times (G_{in} - G_{out})}{N\ cells}$$

where $\dot{V}$ is medium flow rate, G_{IN} and G_{OUT} are glucose concentrations at the inlet and outlet of the chamber, respectively and N_{cells} is the total number of the cells in the culture chamber. As shown in Figure 3.1D, uptake was approximately independent from the flow rate. This is not verified for low flow rates (0.0125 uL/min), in order words, when glucose gets to cell surface more slowly than it is consumed. It's important to notice that the single-cell uptake calculated (~30 fmol min^{-1} per cell) is of the same order of magnitude of a previous study on myoblasts (Kotliar and Pilch, 1992) (17±3 fmol min^{-1} per cell), obtained from radioactivity measurements, if assuming a total protein content of 120±18 pg/cell (as experimentally measured, data not shown).

3.3 High resolution glucose uptake measurements through FRET nanosensor intracellular detection

Also the intracellular glucose detection by the FRET-based nanosensor FLIPglu-600μΔ13V need to be validated in microfluidic experimental system. Myoblasts were seeded within the microfluidic chamber and transfected with the nanosensor plasmid. A high flow rate (4μL/min) was used in these experiments so that glucose concentration on cell membrane, was approximately equal to its concentration in the inlet. Cells were dynamically stimulated by alternating glucose-free and 1.5-mM concentration buffer solution and each concentration was kept constant for 4 min during repeated pulses. Repeated pulses were achieved by the use of a microfluidic multi-inlet system. More details are reported in Appendix D.

Live cell imaging for FRET detection was performed (Figure 3.2A), and the images were analyzed as previously reported(Hou *et al.*, 2011), to obtain the FRET index (Figure 3.2B). As seen in Figure 3.2A a decrease in this index represents an increase in cytosolic glucose concentration. The results show the accuracy of our measurements, with a consistent return to the FRET index baseline after each stimulation pulse. After 4 min of stimulus, FRET signal approximately reaches a new steady state.

FRET results at steady-state were used to determine cytosolic glucose concentration. For using the nanosensor to determine non-steady-state concentrations, the nanosensor-

glucose binding needs to be faster than the other intracellular processes involving glucose (membrane transport, phosphorylation, and maybe others), so that a quasi-steady-state approximation holds and online FRET detection is directly correlated to cytosol glucose concentration. However, we will show later that this condition is not satisfied in our system.

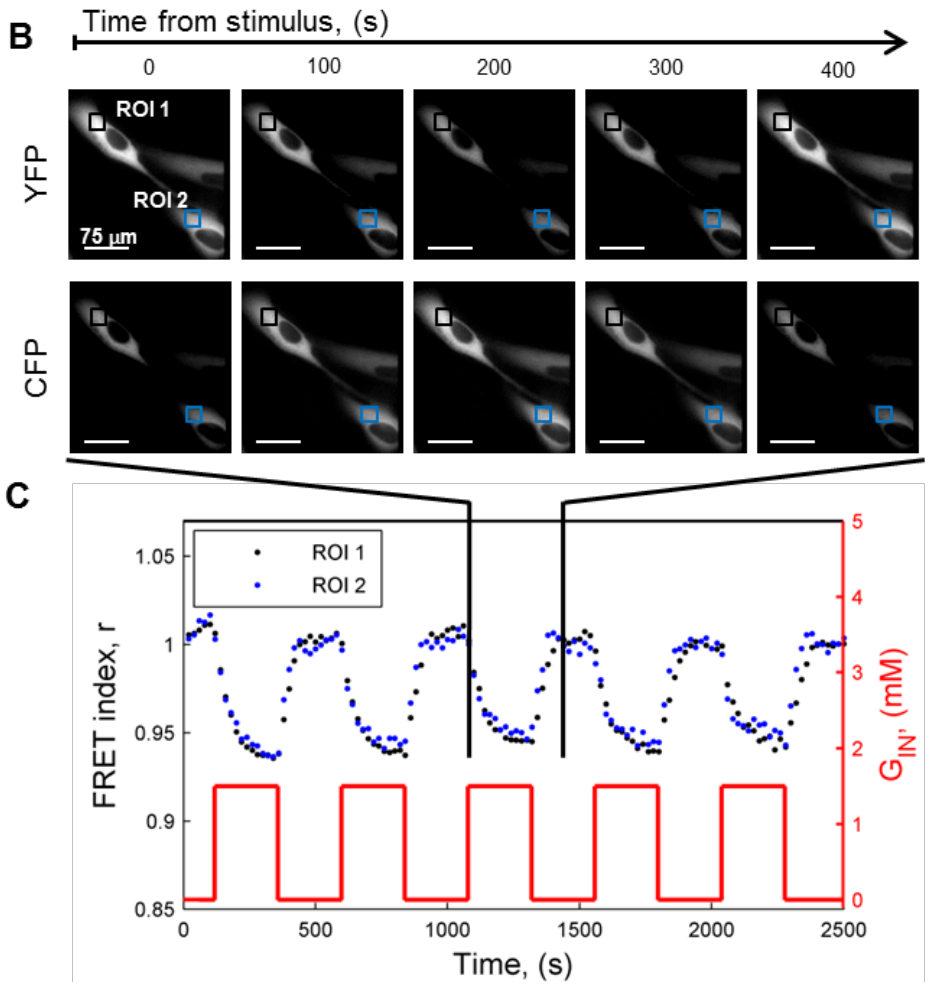

Figure 3.2 *Dynamic measurements of intracellular glucose concentration via FRET nanosensor.* ***A)*** *Sequence of images, obtained by fluorescence microscopy, of cyan (CFP) and yellow (YFP) fluorescent signals during pulse perfusion at 1.5 mM glucose concentration.* ***B)*** *Normalized baseline-corrected FRET index, r, during an experiment of 4-min cyclic pulses of 1.5-mM glucose concentration. Blue and black dots refer to the two regions of interest (ROIs) shown in A).*

3.4 Dissection of myoblast glucose handling mechanisms

Once glucose measurements were set up and technology validates, glucose uptake rate changes was studied as a function of extracellular glucose concentration in a physiological range of concentrations (3-13 mM).

To this aim, the outlet glucose concentration was measured for different inlet conditions, using a flow rate constant and equal to 0.05 µL/min, as stated during validation. Experimental data are reported in Figure 3.3 and show a linear relationship between inlet and measured outlet glucose concentration, with the second being the 74% of the former.

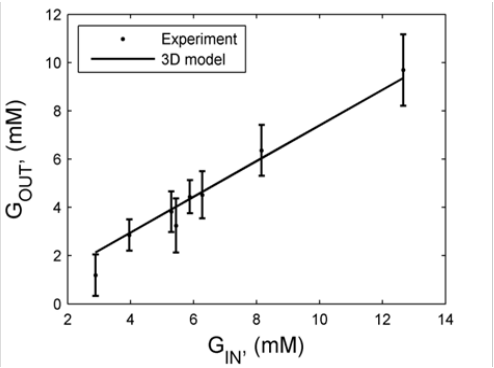

Figure 3.3 *Data of steady-state glucose concentration at the outlet of the culture chamber, obtained from off-line enzymatic measurements, as a function of different inlet glucose concentrations. Error bars: standard deviations (n=3).*

In the same way, also intracellular glucose concentration was analyzed under different inlet conditions. Flow rate was fixed at approximately 4 µL/min, and pulses of increasing glucose concentrations (from 0.5 to 5 mM) were applied, separated by 4 min of glucose-free inlet condition. Figure 3.4A shows that the FRET index has larger amplitude of oscillation for pulses of higher glucose concentration. Measurement noise was relevant at low concentrations, but the sensor response showed a good signal-to-noise ratio for concentrations larger than 1 mM. Approximating FRET response at the end of each pulse as a steady state, it is possible to derive steady-state cytosolic glucose concentration, G_{cyt} as a function of inlet concentration, G_m (Figure 3.4B).

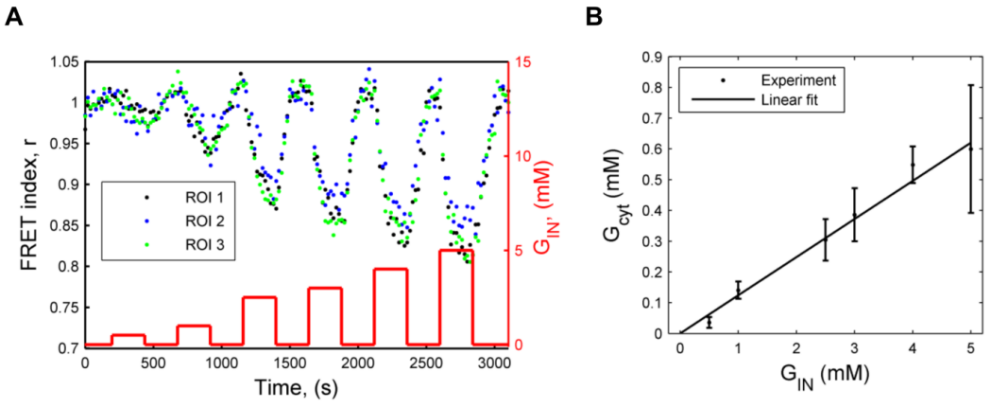

Figure 3.4 *Effect of glucose concentration on FRET nanosensor response.* ***A)*** *Normalized baseline-corrected FRET index, r, as a function of time during repeated pulses of increasing inlet glucose concentrations (0.5, 1, 2.5, 3, 4, and 5 mM). Black, blue and green dots refer to the signal from 3 different cells.* ***B)*** *Relationship between steady-state cytosolic and inlet glucose concentrations, derived from data in A). Linear fit slope: 0.12.*

From experimental data the following linear relationship was found:

$$G_{cyt} = 0.12 \cdot G_m$$

that is characteristic of myoblasts stimulated with glucose concentrations up to 5 mM (and maybe even higher).

After, the system was perturbed with Verapamil (150 µM), an inhibitor that is known to affect glucose transport(Louters *et al.*, 2010). As shown in Figure 5C and D a reduction in cytosolic glucose concentration of about 26% was found, reducing thus the constant in the equation reported above, to 0.065 (Figure 3.5B). This result is consistent with a 30% decrease in glucose uptake obtained in L929 fibroblasts using radiolabeled 2-deoxyglucose (Louters *et al.*, 2010), and shows how impairments can be precisely detected by our system.

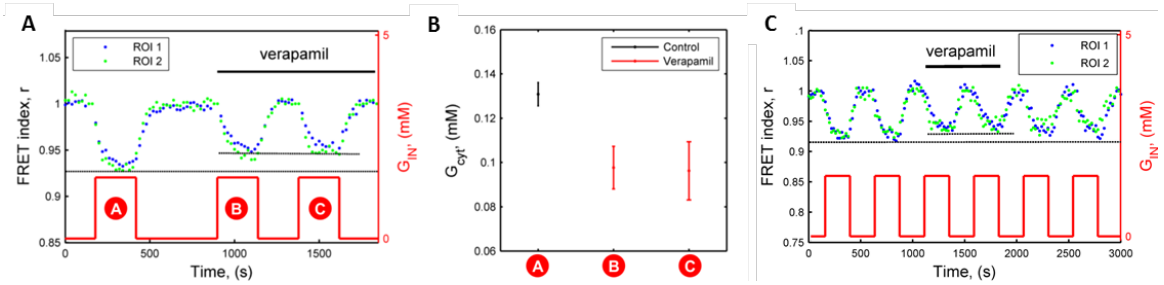

Figure 3.5 *Effect of verapamil on FRET nanosensor response.* ***A)*** *Repeated pulses of inlet glucose concentration (1.5 mM), in presence or absence of verapamil, as indicated. Blue and green dots refer to the signal from 2 different cells.* ***B)*** *Decrease of steady-state cytosolic glucose concentration, for G_{IN} = 1.5 mM, in presence of the inhibitor, calculated from the data in A. p-value is < 0.05.* ***C)*** *Removal of verapamil after 2 glucose pulses shows the inhibitory effect is reversible. Blue and green dots refer to the signal from 2 different cells.*

Through this approach, it was also verified the reversibility of Verapamil inhibitory mechanism: Figure 3.5C shows cyclic pulses of glucose in presence or not of the inhibitor: during of Verapamil stimulation, FRET index decreases its amplitude but it is restored at the basal values after drug removal.

As previously mentioned, the steady-state measurements of glucose uptake and cytosolic glucose concentration can be coupled in order to quantitatively dissect the contribution of the two phenomena of glucose transport through cell membrane and glucose phosphorylation.

Details of the analytical model established are reported in Appendix D, and where developed in collaboration with Dr. Camilla Luni and Dr. Alessandro Zambon.

The characteristic times derived from this model of glucose transport and phosphorylation are summarize in Figure 3.6. They are 3.7 s and 0.5 s, respectively, and they are equal to the reciprocal of the kinetic constants of these phenomena. Thus, the latter process is 7.4 times

faster than the former, making transport the limiting step of glucose handling process, as already well-known.

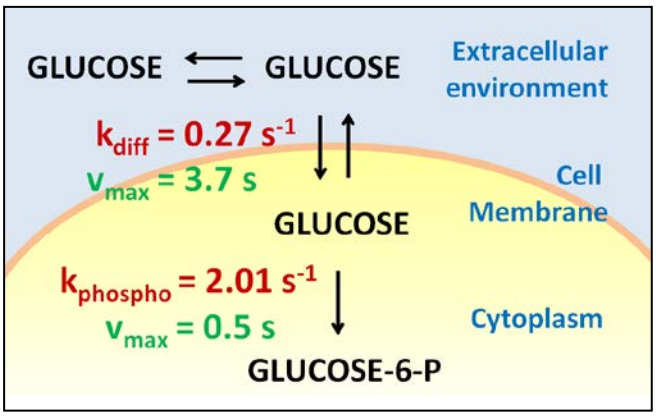

Figure 3.6 *Schematic representation of glucose handling. Kinetic parameters and characteristic times calculated are reported.*

3.5 Conclusions

In this chapter it has been presented a new methodology developed to quantitatively dissect the kinetics of glucose intracellular transport, single-cell uptake and phosphorylation kinetics in live myoblasts. Multiple technologies were exploited, from microfluidic technology to FRET nanosensing.

Microfluidic system in particular can enhances cell microenvironment dynamic control and measurement sensitivity. On the other hand, FRET-based nanosensor measures cytosolic glucose in live cells with high spatial resolution.

The results obtained provide means to experimentally measure precise metabolic fluxes within the cellular environment. The direct detection of glucose uptake in a microfluidic system offers accuracy at high time resolution and minimal disruption of culture conditions. As far as it is known, the determination of hexokinase phosphorylation rate has never been achieved previously in living cells and under physiological conditions. These results are particularly relevant in the context of studies on glucose handling processes, involved in the development of dramatic diseases, such as diabetes, but are not restricted to the particular cell system we analyzed.

Thus, a relevant perspective of this work is the extension of the dissection of glucose-related processes to other biological systems involved in metabolic impairments, such as differentiated myotubes which are a model more similar to skeletal muscle *in vivo*. As a demonstration for this perspective, Figure 3.7 shows that myoblasts can efficiently differentiated within the microfluidic culture chamber, obtaining myotubes that show high

sarcomeric organization. Currently, direct transfection of myotubes with the FRET nanosensor plasmid resulted too inefficient for reliable measurements. However, transfection with different vectors for constitutive expression, such as a lentivirus, could overcome this limitation and extend the applicability of the methodology.

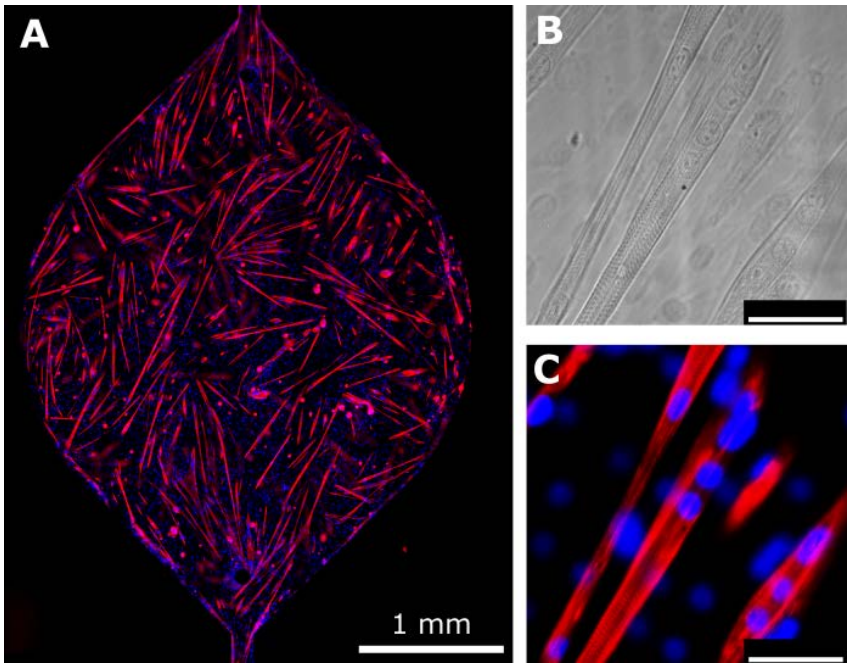

Figure 3.7 *Differentiated C2C12 myotubes within the microfluidic culture chamber.* ***A)*** *Immunofluorescence analysis of myotubes derived from murine myoblasts after 7 days of differentiation Red: myosin heavy chain, blue: Hoechst staining for nuclei.* ***B-C)*** *Magnification of myotubes in A), bright field and fluorescence images highlighting the sarcomeric structure. Scale bar: 50 µm.*

Chapter 4

High Resolution Glucose Uptake Measurements in Adipose Tissue *In Vitro* Cultures

4.1 Introduction and Motivation

Along with myocytes, adipocytes are also highly insulin-responsive cells. During diabetes onset, even in this tissue insulin responsiveness is dramatically blunted, with reduced glucose uptake and reduced capability to produce storage triglycerides (Virtanen *et al.*, 2002).

Due to its involvement, studying glucose uptake dynamics in adipose tissue can help to clarify how glycemia is managed in diseased conditions.

Moreover, adipose tissue can results as another eligible target tissue for therapy development and glucose uptake can be an interesting readout, that can be monitored continuously, giving thus a new way of investigation of tissue responsiveness to drugs.

Even for adipose tissue in a microfluidic device it is possible to monitor glucose uptake in a direct and continuous way, by measuring glucose depletion from the medium, without perturbing the culture viability.

By the way, for three-dimensional organ culture, the intracellular glucose detection is not an easy matter: plasmid transfection for FRET expression within adipocytes is not feasible in adipose tissues slices. Moreover three-dimensional tissues display intrinsic limitations for the application of optical fluorescence analysis. For these reasons the evaluation of glucose

concentration in adipose tissue integrated in a microfluidic chip is limited to off line measurements.

Microfluidic technology offers supplementary capabilities, relevant for *in vitro* drug testing. As outlined in the introduction, in drug development spatial and temporal resolved delivery of soluble factors is a key feature to take into account. Standard biochemical stimulation techniques require a partial or a complete change of cell culture medium. Disadvantages of these protocols are the unknown kinetic of the interaction between molecules and cells, and the rapid variation that is induced within the cellular environment. Moreover, these stimulation protocols lack of defined spatio-temporal control and are demanding in terms of reagents consumption and costs (Biffi *et al.*, 2012).

In this perspective, microfluidics can be used for locally stimulate cells or to create dynamic concentration gradients. Microfluidics can precisely define the biochemical cell microenvironment, allowing the delivery of microscale volumes of drugs, especially in temporal defined manner (Biffi *et al.*, 2012).

In order to give a stimulus that is temporally controlled, an *ad hoc* integrated microfluidic chip was designed by Dr. Zambon, and presented in his PhD thesis (Zambon, 2013) and showed in Figure 4.1. It is composed by a set of 8 independent culture chambers that can be controlled in parallel and it comprises a set of valves and micropumps that permit the automation of fluids movimentation for medium changes. In addition, in the microfluidic circuit an injection system for each culture chamber has been inserted in order to permit controlled biochemical stimulations.

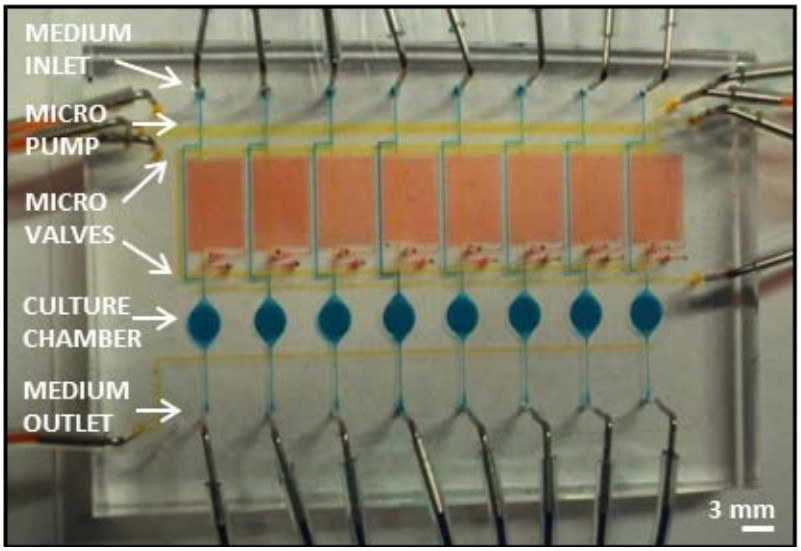

Figure 4.1 *Integrated microfluidic chip. It comprises 8 independent culture chambers and can be automated thanks to the presence of microvalves and micropumps that can direct fluid motion.*

Through this microfluidic chip it's possible to perform long-term culture of organ culture, and at the same time continuously monitoring glucose consumption, both in basal condition and after precise insulin/drug stimulations, without perturbing the system.

4.2 Microfluidic adipose tissue organ culture validation

When setting up the integration of a novel culture in a microfluidic technology, the confirm that this unusual tissue culture method can sustain tissue viability and appropriate phenotype is a fundamental requirements. For these earliest data, a prototype chip (already presented in Paragraph 2.3.5) was used. In this chip, medium is perfused in the culture chamber by connecting the device with syringes that are moved for medium injection with an automated syringe pump.

Usually adipose tissue as organ culture is cultured in well-plate filled with medium, that is changed every 24-48 h. For culture in the microfluidic chip, adipose tissue is integrated one day after surgery, after 24 h of static culture. The organ culture is inserted through a thick chamber placed over the microfluidic medium distribution system. The array of circular microposts (see Paragraph 2.5) ensures a constant medium volume at the biopsy surface, reducing the formation of dead volumes due to biopsy leaking from the PDMS bottom chamber and to avoid obstruction of the medium circuit.

In order to determine adipose tissue viability, MTT assay has been performed after 1 week of dynamic microfluidic culture and values were compared with static cultures (conventional organ culture in wells, medium replaced every day) and with MTT values obtained from the same biopsy preparation, right after processing. In the three cases, there were no substantial differences between static and microfluidic cultures (Figure 4.2) nor with fresh isolated tissue. These data confirm that long term dynamic culture in the microfluidic chip does not affect tissue viability.

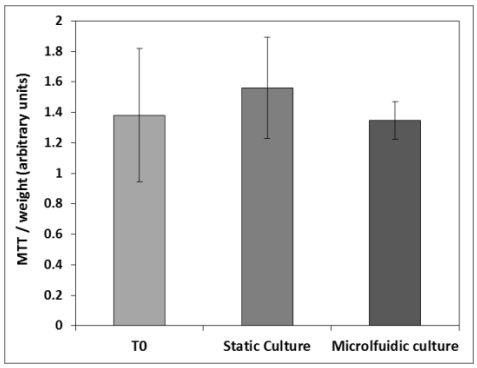

Figure 4.2 *MTT analyses performed on adipose tissue in three conditions: right after surgery, after 8 days in traditional static condition and after 8 days in microfluidic culture condition.*

Histological analyses has also been performed on AT right after explant, after static culture and after microfluidic culture. in order to verify that the proper morphology is maintained during the culture, with no major alterations. Hematoxylin & Eosin analyses does not show significant differences between the 3 conditions (Figure 4.3).

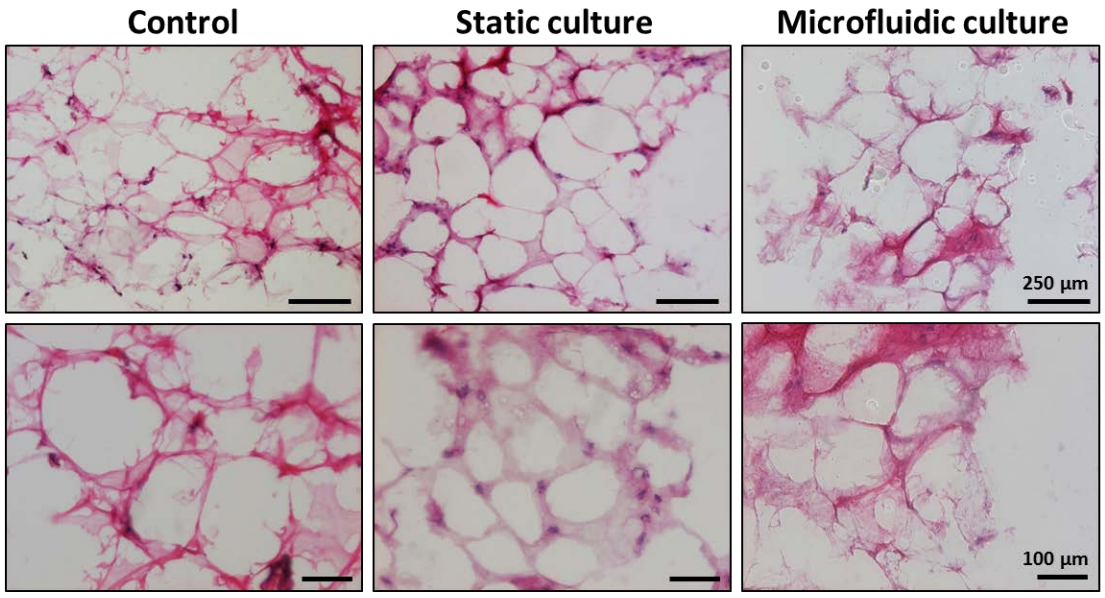

Figure 4.3 *Hematoxylin & Eosin staining on adipose tissue performed on tissue right after explant (Control), after 8 days of culture in Petri dish (Static culture) and after 8 days of culture in microfluidic (Microfluidic culture).*

4.3 High resolution glucose uptake measurements in microfluidic adipose tissue cultures

As described for skeletal muscle cell in Paragraph 3.3, also for long term culture of adipose tissue in microfluidic, it is possible to examine its glucose consumption by monitoring glucose depletion from flowing medium.

First of all, the effect of flow rate on glucose concentration was investigated. More precisely, They were performed starting from low flow rates (0.025 uL/min) and scaling gradually to higher rates (0.6 uL/min), at the maximum time resolution possible, in other words by continuously collecting and analyzing medium every 0.6 µL eluded. In this way, increasing flow rate has the effect in higher temporal resolution, up to 1 minute for the highest flow rate investigated (Figure 4.4).

Figure 4.4 shows a continuous glucose profile during time at increasing flow rates, referred to 4 samples coming from the same patient. As outline by the graph, glucose concentration measured in the medium, increase with increasing flow rates, up to washout rate, where

glucose concentration measured is equal to the control. Moreover, glucose concentration profiles were maintained with low variability for the different samples.

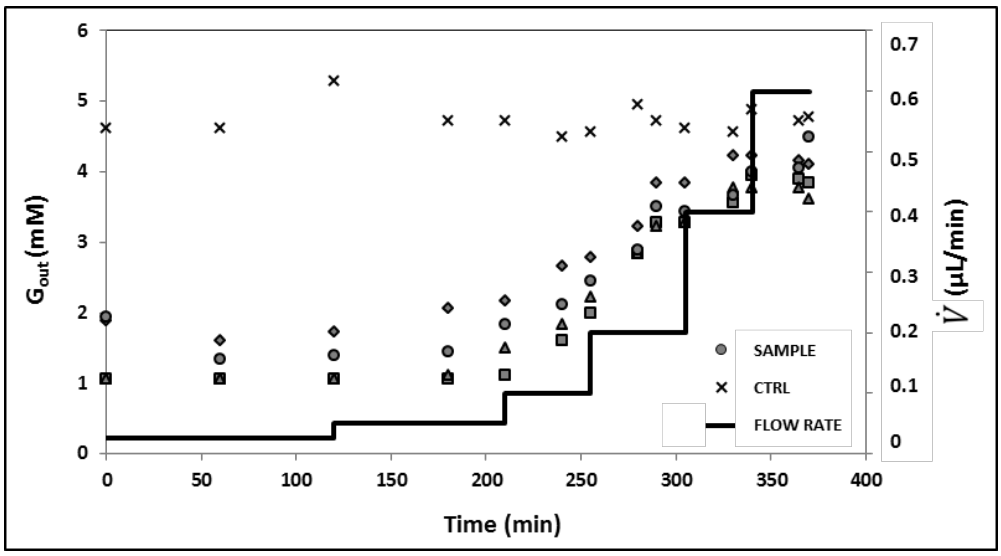

Figure 4.4 *Outlet medium glucose concentration measurements as a function of time, at different flow rates. Graph report measurements from 4 different samples and control.*

The robustness of the data collect and of the tissue model system were tested in different ways as shown in Figure 4.5.

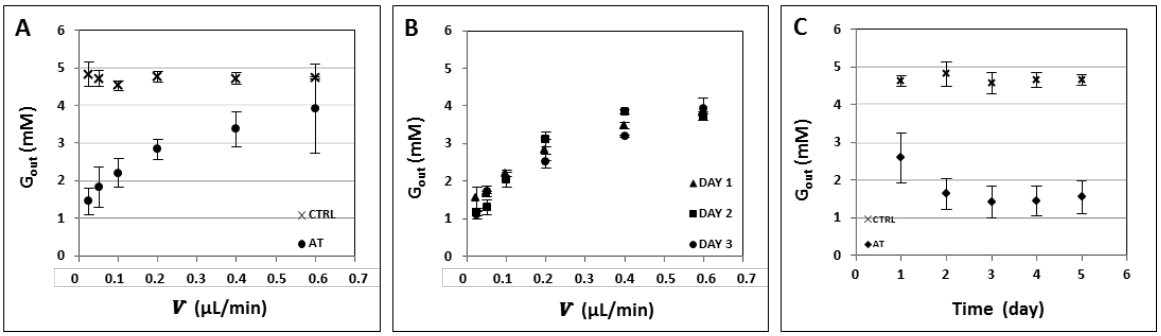

Figure 4.5 *Glucose concentration measurements.* ***A)*** *Means of different sample measurements as a function of flow rate.* ***B)*** *Means of different measurement of the same biopsy during different days of culture as a function of flow rate.* ***C)*** *Means of different measurement of the same sample as a function of days (Flow rate = 0.025 uL/min). For all data, n=4.*

Figure 4.5A evidences through the mean of different samples (n=4), the obtainment of consistent data from analyses at different flow rates after the establishment of the new steady state.

Figure 4.5B compares glucose profile obtained from the same experiment repeated for several days. As the figure shows, high measurement reproducibility of data repeated for 3 following days in the same biopsy sample were obtained.

Figure 4.5C shows the maintenance of metabolic activity during different days. In this experiments glucose concentration was measured at 0.025 µl/min flow rate perfusion during 5 days of culture. Glucose concentration is maintained pretty constant for the entire period of investigation. Higher glucose values in the medium in the first day of culture (that is lower glucose consumption by the biopsy) seems to be correlated to biopsy adaptation to the new culture condition, as also seen in static conditions (data not shown). Data refer to 4 samples derived from the same patient.

These important considerations, have a positive feedback in robustness and in experimental feasibility, which are key parameters for a robust *in vitro* drug screening test. In regard of glucose uptake calculations and measurement, the complexity of three-dimensional adipose tissue has a negative effect on the obtainment of reliable data to date. Further modeling and other experiments need to be performed and are still pursued.

4.4 Temporally controlled stimulation through microfluidic devices

As outline in the introduction of this chapter, the total control of the biochemical stimulations is an important cue for improving the reliability of *in vitro* tissue model studies. In the integrated chip shown in Figure 4.1 an injector system has been introduced and it permit to temporally control the delivery of biochemical compounds. In Figure 4.6 its shown a schematic representation of a single microfluidic chamber and its connection with the injection system. It has been designed as a 16 cm long serpentine channel, 100 µm wide and 50 µm high, that is able to contain up to 1.5 folds the total chamber volume (0.7 uL). It presents also independent inlet and outlet, permitting thus to insert easily the solution, right before the stimulation and avoiding in this manner the possible deterioration of delicate compounds. This integrated system can be used both for short or long term stimulations, since the fast reloading permits to repeat quickly the injection procedure. In this way, the duration of stimulus can be adapted as required, repeating the stimulation process.

Microvalves and micropumps permits to isolate the culture chamber for the injection system during conventional culture operation (coating, seeding and medium changes) and to move automatically the fluids in the chip.

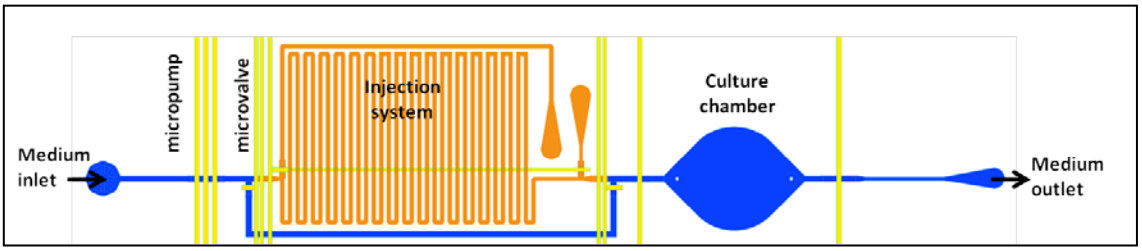

Figure 4.6 *Schematic representation of a single unit composing the integrated microfluidic chip. A unit is composed of medium distribution channels and culture channel (blue), injection system (orange) and pneumatic control (yellow).*

4.4.1 Insulin stimulation: validation of the system and proof of concept experiments

First step in using injection system, is the confirmation that the stimulus can uniformly distribute over the surface of the chamber. To validate this element, a fluorescent tracer (i.e. fluorescein sodium) has been added in the reservoir loop channels (Figure 4.7A) and its route was followed by fluorescence fluoroscopy. An uniform distribution of fluorescent tracer was observed inside the chamber (Figure 4.7B) and biopsy has been completely covered by the tracer (Figure 4.7C).

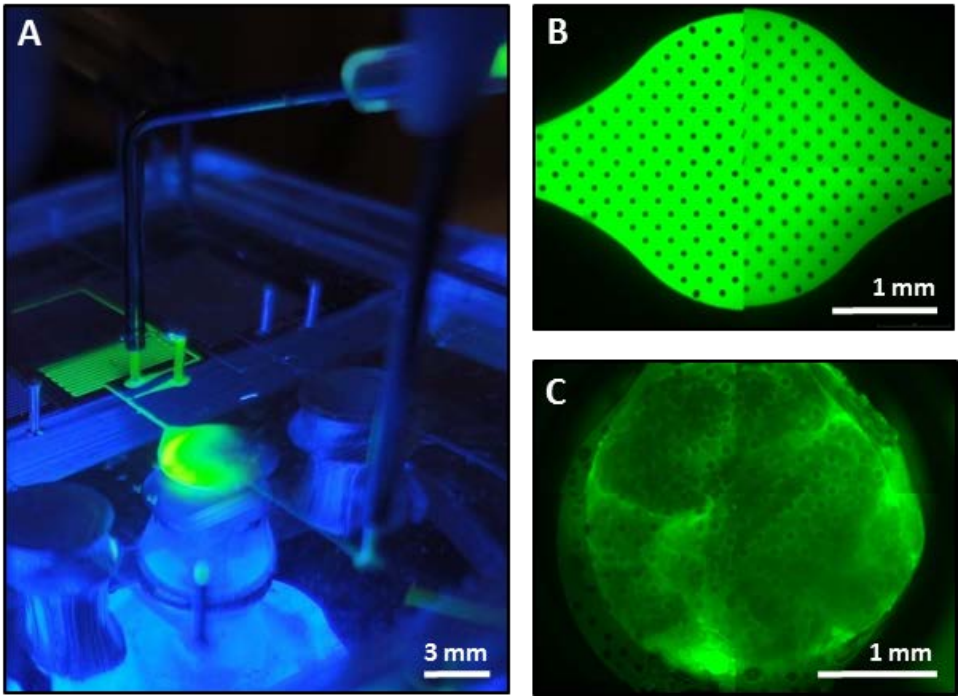

Figure 4.7 *Insulin delivery validation.* ***A)*** *Insulin stimulation with automated injection system is shown through addiction of fluorescein as a tracer.* ***B)*** *Image of empty culture chamber tracer distribution after stimulus with fluorescein.* ***C)*** *Image of adipose tissue within a culture chamber perfused with fluorescent tracer.*

Insulin step effects was then assessed in preliminary experiments. Precisely, outlet glucose concentration was measured in biopsies coming both from diabetic and non-diabetic patients. The strategy is to determine differences in glucose outlet concentrations from insulin stimulated and controls (non-stimulated) biopsies, in order to outline different profiles in diabetic and healthy patients. Two set of experiments were performed: in the first step of experiments, healthy and diabetic samples were stimulated at basal glucose concentration (4 mM) with 100 nM insulin, maintaining a constant basal glucose concentration during the total length of experiment (Figures 4.8A, 4.8B); in the second set of experiments, post-prandial phase were simulated by stimulating biopsies with 100 nM insulin, during a step change in extracellular glucose concentration from basal (4 mM) to higher glucose level (7 mM) (Figures 4.8C, 4.8D).

In the first experimental conditions, changes in glucose outlet concentration both in healthy (Figure 4.8A) and diabetic (Figure 4.8B) patients were not observed.

In the second experimental conditions, in healthy patients the combined effect of insulin and increased glucose concentration appears to be related to a decrease in outlet glucose concentration (that is an increase in glucose consumption), with a substantial difference from control samples (Figure 4.8C). On the other hand for the diabetic patient (Figure 4.8D) there were no differences in glucose concentration between the stimulated and control samples, stating a non-effectiveness of insulin stimulus for the entire length of experiment. These data, derived from preliminary results, give the proof of concept of how tissue insulin response can be evaluated in *in vitro* experiments taking advantages of microfluidic capabilities and how experiments can be adapted to different requirements.

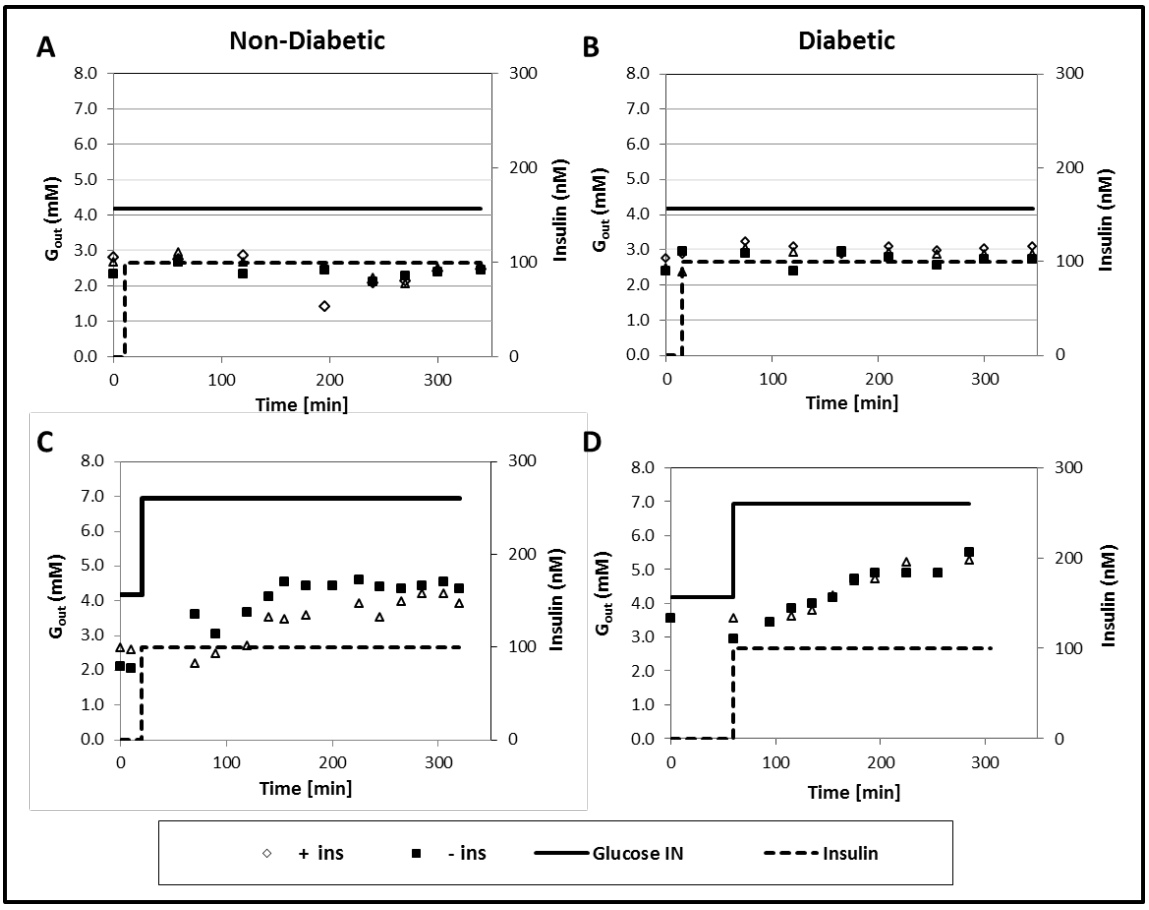

Figure 4.8 *Insulin step effects on sample from non-diabetic (left) and diabetic (right) patients.* ***A,B)*** *Effect of insulin step stimulus (dotted line) on glucose outlet concentration.* ***C,D)*** *Effect of insulin step stimulus on glucose outlet concentration with the simultaneous increment of glucose inlet concentration (solid line). Experiments were performed at 0.1 µL/min at the third day of microfluidic culture.*

4.5 Conclusions

In this chapter has been reported results from adipose tissue organ culture integration on a microfluidic technology. Long term viability and metabolic activity has been confirmed within microfluidic culture conditions. High temporal resolved glucose concentration has been monitored for days with the obtainment of consistent profiles during different days.

Moreover a multilayer microfluidic chip for type 2 diabetes studies has been developed and tested. Microfluidic automated technology can improve throughput, sensitivity and dynamic range with a low expenditure in biological instrumentation. In line microvalves and micropump comprise in this chip allow to increase the pliancy in the studying of cells under simulated microenvironments *ex vivo*. The chip is able to precisely control the culture microenvironment by accurate delivery of culture medium. Insulin and other drugs can be

easily inserted into the chamber with minimum dispersion and temporal stimulus pulse evolution can be modulated specifically for each experiment.

Preliminary experiments of insulin sensitivity have been performed with this automated device. The high variability is due to the complexity of the tissue and further investigation is still pursued. By the way, High temporal and control evolution of insulin stimulation have been achieved, with adaptable and flexible automated operations.

These data are promising for further insulin responsiveness experiments from healthy and diabetic patients in order to define the insulin response dynamic with high temporal resolution.

Chapter 5

Development and Characterization of Human Skeletal Muscle on a Chip

5.1 Introduction and Motivation

Skeletal muscle represents the principal tissue involved in insulin-stimulated glucose uptake and contributes considerably to the whole body glucose homeostasis (Henry *et al.*, 1995; Ciaraldi *et al.*, 1995).

For this reason, its involvement in Type 2 Diabetes onset and development is central, since it is a principal site for insulin resistance upcoming (Fröjdö *et al.*, 2009).

The firsts studies reporting alterations that occurs in Type 2 Diabetes were performed *in vivo*, by studying molecular alterations in biopsy taken from healthy and diseased patients after euglycaemic hyperinsulinaemic clamp, a technique that consist in a constant infusion of insulin and glucose with the concomitant monitoring their blood levels. By the way, a number of differences regarding the origin of the tissue (that is the location of the biopsy or the way biopsy is used) may complicate the interpretation of the results (Fröjdö *et al.*, 2009). Moreover interpretation of clinical studies are complicated by the inability to accurately control the multiple metabolic variables involved(Henry *et al.*, 1995).

A largely used model to study Type 2 Diabetes is *in vitro* cultures of human primary skeletal muscle cells (also called myoblasts). These cells are easily established in primary culture and most importantly they retain both insulin responsiveness or defects in glucose

utilization present in the original donor (Ciaraldi *et al.*, 1995; Henry *et al.*, 1995; Perriott *et al.*, 2001)(4, 13).

Indeed, after myoblasts fusion and differentiation into myotubes, this model exhibits both basal and insulin-stimulated glucose signaling and transport similar to the *in vivo* situation. Moreover, cells established from Type 2 Diabetes patients retain the molecular defects in glucose handling.

In vitro cultures of human skeletal muscle cells has been established from years and they have been fundamentals in the deep investigation of pathological mechanisms at the basis of Type 2 Diabetes. However, conventional cell culture techniques consist of growing cells on a homogeneous large surface immersed in a homogeneous bath, whereas *in vivo* cells respond to spatially and temporally organized signals in the surrounding microenvironment. (Tourovskaia *et al.*, 2005). In this scenario, the physiological realism of such isolated *in vitro* models can potentially be increased by optimizing the culture microenvironment in terms of spatio-temporal control of stimuli, cell confinement, etc. (van der Meer and van den Berg, 2012).

A key point in *in vitro* skeletal muscle model is that its differentiation is greatly influenced by microenvironmental culture conditions. More specifically previous studies have demonstrated that elements like mechanical and topological stimuli and composition of adhesion proteins can highly influence differentiation of skeletal muscle cells *in vitro* (Serena *et al.*, 2010). For this reason, numbers of study has been carried out with the goal of optimizing cell microenvironment in order to properly enhance myoblasts differentiation using elastic substrates for mechanical stimuli, micro-patterns that guide cell alignment and specific coatings of adhesion proteins.

On the other hand, the possibility of having a dynamic control both in space and in time over the cellular microenvironment in terms of providing nutrients, stimuli and gases becomes relevant especially in the study of those process where rapid stimuli appears *in vivo*. One of this case is control of total glycemia and Diabetes where insulin can drive glucose uptake with fast dynamics and where the crosstalk between the different tissues involved plays a pivotal role in the onset of the pathology.

Microfluidics offers the capabilities to control the concentrations of molecules in space and time: in fact microfluidic systems have been developed with the purpose to create greater physiological relevant microenvironments, giving also the opportunity to create highthroughput chips for cell behavior analysis.

Torouvskaia *et al.* developed a microfluidic chip presenting a linear pattern, where C2C12 integration and differentiation where achieved. Apart from this work that integrate a non-

human cell line of myoblasts, since now none has never reported before the integration of human primary skeletal muscle cells within a microfluidic device.

In the following paragraphs it will be reported the study of an ad hoc pattern of lanes capable to guide myoblasts alignment, while having the best results of proliferation and differentiation and the following integration of human primary myoblasts in a microfluidic chip which present the most beneficial pattern of lanes outlined before. Human skeletal muscle tissue integrated were also characterized for its phenotype and functionality.

5.2 Micropattern topology affects myoblasts proliferation and differentiation

Micropattern topology effects on proliferation and differentiation were evaluated on human myoblasts cultured on hydrogels with a stiffness of 15 kPa. More details on these studies are reported in Appendix B.

Hydrogels were used as a support for the culture since in these substrates pattern production is easy and fast to achieve and it was an already established technique in the lab.

Proliferation was evaluated with BrdU assay both on C2C12 and in human myoblasts cultured over patterns of different width lanes. In the specific 100, 300 and 500 μm lane widths were evaluated (Figure 5.1A); interspace between lanes were equal to the lane width.

Figure 5.1B shows results obtained from proliferation assays obtained in C2C12 seeded at two different initial seeding density. C2C12 cultured in 100 μm lanes geometry showed a highest percentage of proliferating cells for both the seeding density. The percentage of proliferating cells significantly decreased using the 300 and 500 μm lanes geometry.

As expected, the proliferation rate was negatively influenced by an increased seeding density in all of the patterning geometries. More importantly, micro-patterning lane width strongly affects cell proliferation, for the same seeding density: the smaller the lane width, the higher is cell proliferation. However, cell seeding density and pattern geometry do not act synergistically in affecting proliferation (p-value > 0.01).

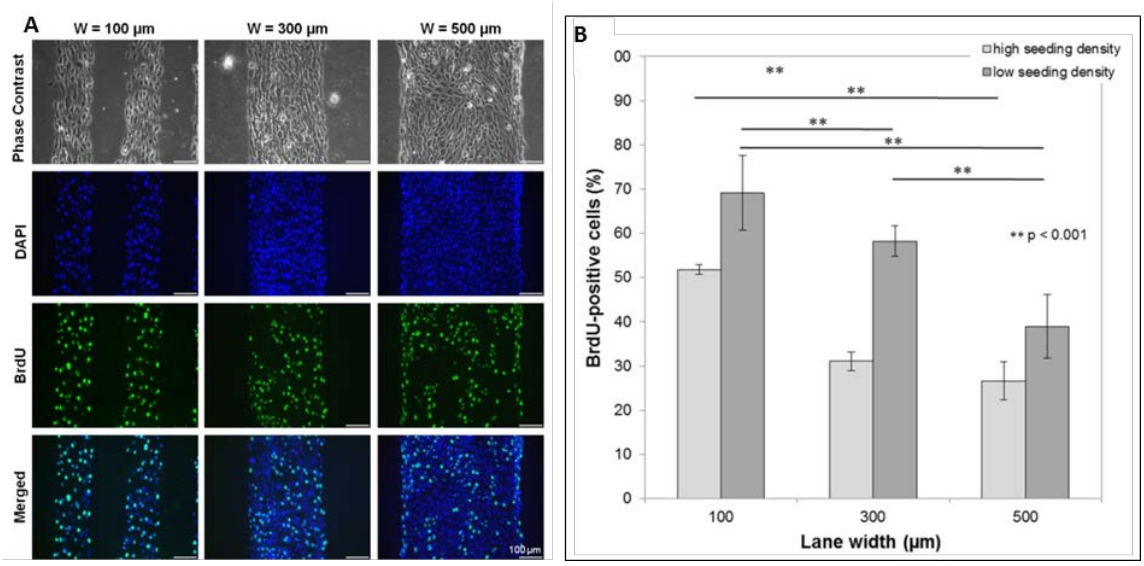

Figure 5.1 *C2C12 proliferation on pattern of different width lanes.* ***A)*** *BrdU immunofluorescence on micro-structured C2C12 cultures, 48 h after seeding on 100, 300 and 500 µm width lanes.* ***B)*** *Percentage of BrdU-positive C2C12 cells for each micro-patterning lanes width and for two different seeding densities.*

Different lane interspace effect on C2C12 proliferation was also investigated. 100 µm lanes were interspaced of 50, 100 and 200 µm respectively (Figure 5.2A). In this case no differences were highlighted between the different conditions (Figure 5.2B).

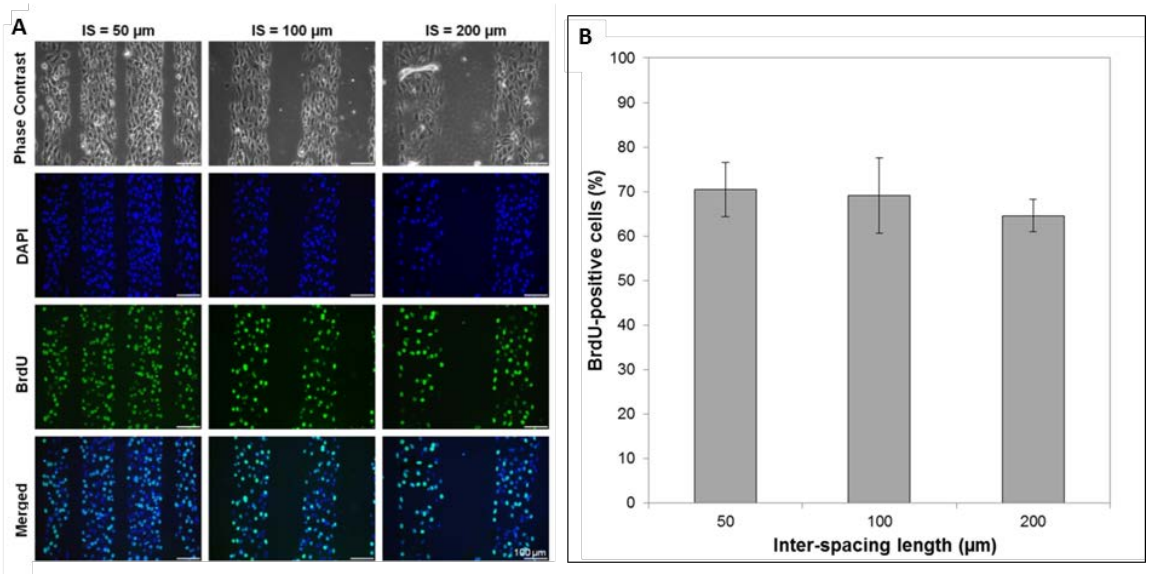

Figure 5.2 *C2C12 proliferation on pattern of different inter-spaced lanes.* ***A)*** *BrdU immunofluorescence on micro-structured C2C12 cultures, 48 h after seeding on with 100 µm width and 50, 100 and 200 µm inter-spacing length lanes.* ***B)*** *Percentage of BrdU-positive C2C12 cells for each micro-patterning lanes inter-space*

Thereafter, human primary myoblasts proliferation was evaluated. These cells were cultured on the same different micro-patterned surfaces (100, 300 and 500 μm lanes) using a seeding density of 400 cells/mm^2.

Unexpectedly, human myoblasts proliferation was the same in all the micropatterning width (Figure 5.3A). The divergence between C2C12 and human myoblast behavior may be dependent on the different proliferation medium used for cell cultures. In fact, human primary myoblasts medium contains add-ons such as mitogenic factors (β-FGF and EGF), insulin and a double amount of serum. This hypothesis was confirmed by the results shown in Figure 5.3B where C2C12 shows an increased proliferation when grown with primary myoblasts medium.

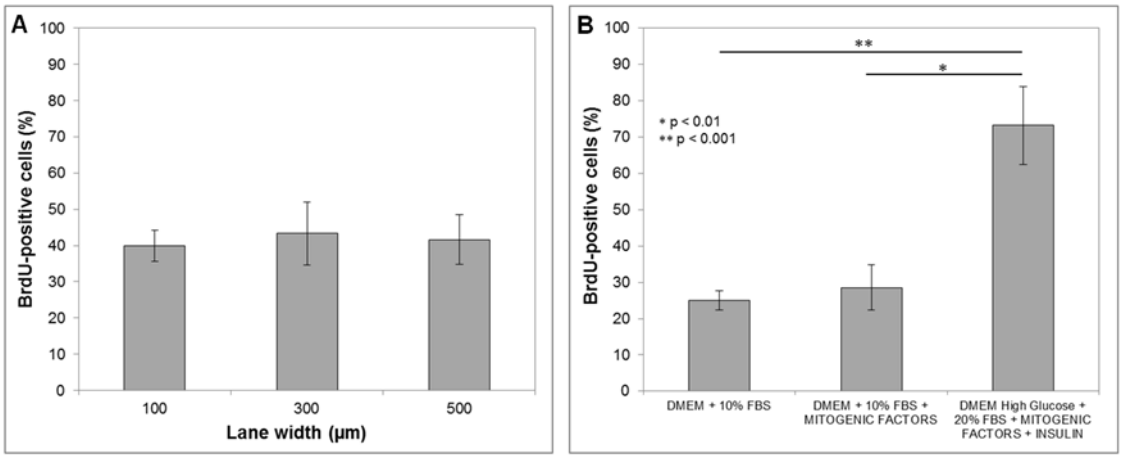

Figure 5.3 *Human primary myoblasts proliferation on pattern of different width lanes.* ***A)*** *Percentage of BrdU-positive human myoblasts for different micro-patterning lanes width.* ***B)*** *Effect of serum mitogens on C2C12 proliferation. The histogram reports the percentage of BrdU-positive C2C12 cells on micro-structured cultures characterized by 500 μm lanes width, treated with different media.*

Once that proliferation was examined, also effects of lane width on myoblast differentiation was evaluated. C2C12 cells were cultured on micro-patterned surfaces characterized by 100, 300 and 500 μm lane widths using a high seeding density (400 cells/mm^2). Confluent cells is the *condicio sine qua non* to have a proper differentiation in myotubes. Moreover, for all myoblasts type fusion is prompt with a switch in culture medium composition, using a medium with low serum content (2%).

First of all, in all geometries a remarkable formation of myotubes arranged in independent parallel bundles was observed and Myosin Heavy Chain (MHC) immunofluorescence analyses highlighted the sarcomeric organization of myosin (Figure 5.3A). Fusion index was evaluated as percentage of nuclei comprise into multinucleated structures expressing MHC over total number of nuclei. Figure 5.3B shows how C2C12 fusion index increased along

with patterning lanes width. As expected, myoblasts differentiation showed an opposite trend compared to proliferation rate.

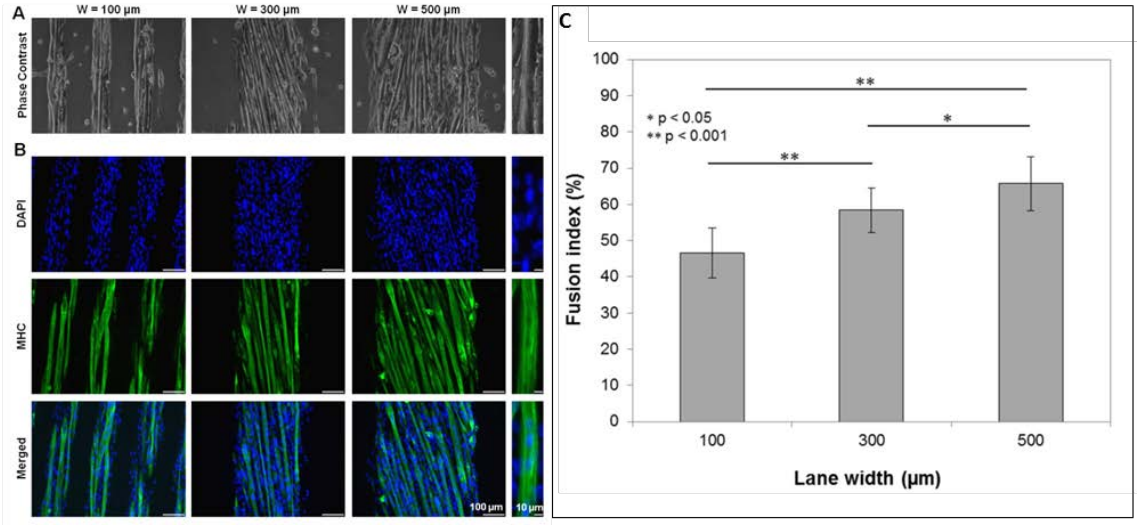

Figure 5.3 *C2C12 fusion index on pattern of different width lanes.* ***A)*** *MHC immunofluorescence on micro-structured C2C12 cultures, 48 h after seeding on 100, 300 and 500 µm width lanes.* ***B)*** *C2C12 fusion index for each micro-patterning lanes width.*

Fusion index on the three different micro-structures was evaluated also on human myoblasts. With these cells the positive trend obtained for C2C12 was confirmed. In this case, a more relevant increase of fusion index was observed in wider patterning lanes, (Figure 5.4).

All these data are consistent with myogenic differentiation process, in which secreted factors self-regulated myoblasts differentiation (Bajaj *et al.*, 2011).

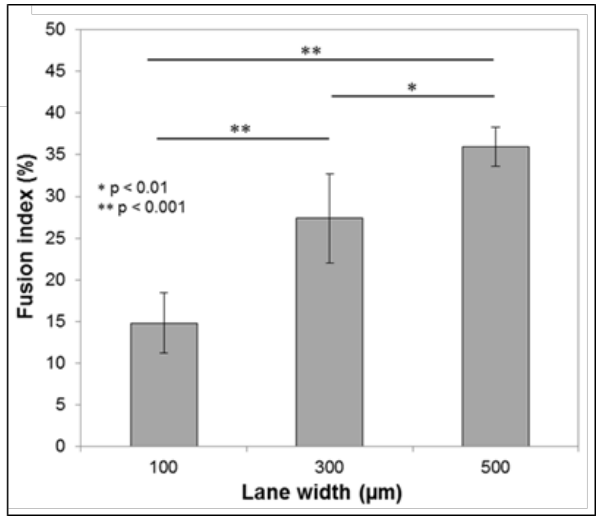

Figure 5.4 *Human myoblasts fusion index obtained for different micro-patterning lanes width.*

On the basis of all these results, the best pattern geometry outlined for myoblasts proliferation and differentiation is the 300 um width lanes. In fact, this geometry is a good compromise between having an effective proliferation and an efficient differentiation of myoblasts.

5.3 Micropattern integration in the microfluidic chip and C2C12 culture

The geometry of 300 μm width lanes was subsequently reproduced in the microfluidic chip presented in Figure 2.1. Since the microfluidic chip used is a closed system were PDMS cover cell culture surface, here it is not possible to carry out micro-contact printing as done on hydrogels. To produce a pattern inside the microfluidic chip, it was used another technique based on photo-pattern and optimized for this system, which protocol is reported in Appendix E.

A pattern of 300 μm width lanes, made of linear acrylamide, was created inside the microfluidic chip. In order to evaluate feasibility of cell culture in this system, first of all were integrated C1C12 cells, since they are a less precious source of myoblasts compared to human primary cells.

Figure 5.5 shows C2C12 after integration in the patterned microfluidic chip. C2C12 can outline the pattern defined by linear acrylamide few hours after seeding. After adhesion on Matrigel-coated glass they were able to grow and reach confluence.

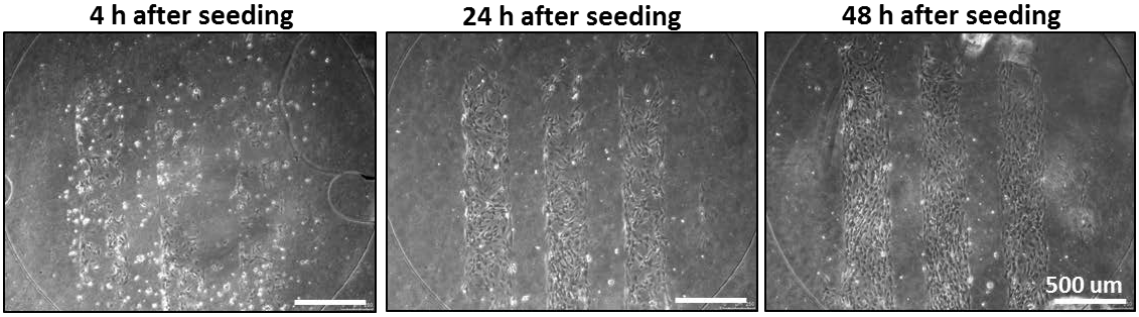

Figure 5.5 *C2C12 in the patterned microfluidic chip during different days of culture.*

After myoblasts reached confluence, they spontaneously undergone differentiation in the microfluidic chip. MHC immunofluorescence shown in Figure 5.6 confirmed the formation of multinucleated myotubes, expressing the myogenic marker myosin which also present sarcomeric organization.

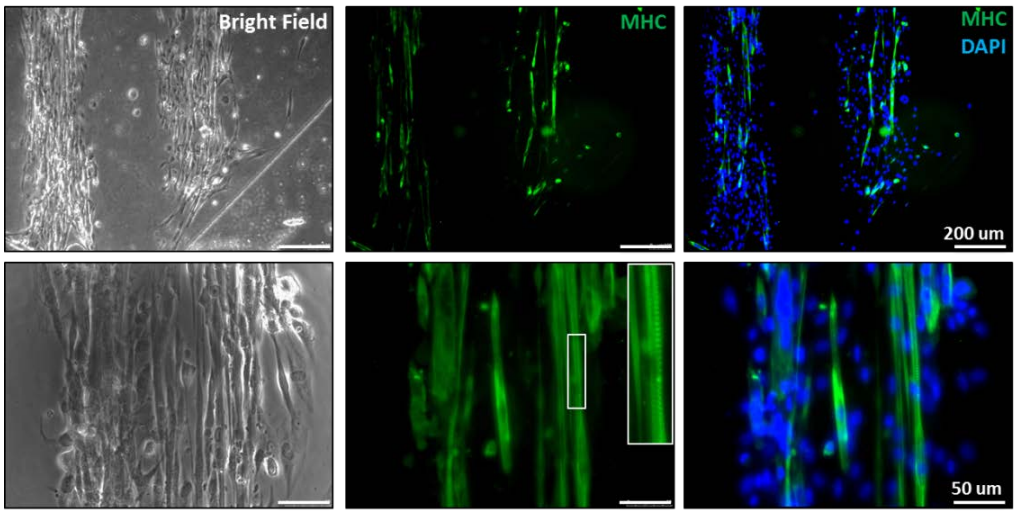

Figure 5.6 *Immunofluorescence for MHC on C2C12 cultured in the patterned microfluidic chip.*

C2C12 myotubes showed high spatial organization in space since they derived from highly aligned myoblasts, beyond a great degree of differentiation which confer a deeper similarity to *in vivo* skeletal muscle phenotype.

5.4 Human skeletal muscle cells integration and characterization in the microfluidic chip

After defining protocol for micropattern reproduction in the microfluidic device and optimization of culture condition with C2C12 cells, human primary myoblasts were integrated inside the chip after glass coating with Matrigel® 2.5% in DMEM. As shown in Figure 5.7 human myoblasts adhered in the chip following the topology pointed out by the pattern of 300 µm lanes and where able to proliferate during the different days of culture.

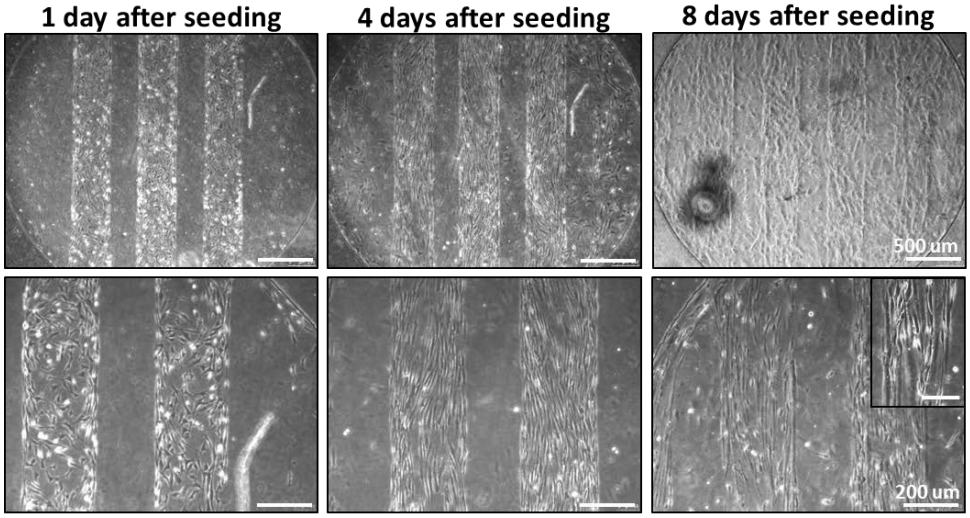

Figure 5.7 *Human primary myoblasts in the patterned microfluidic chip during different days of culture.*

Human myoblasts integrated in the patterned chip were then induced to differentiate into myotubes after they reached confluence. Results are shown in Figure 5.8. Myoblasts were able to form myotubes after 8 days of culture. Immunofluorescence analyses shows proper expression of MHC. MHC also shows to be highly organized into sarcomeric structure, the fundamental unit of skeletal muscle. This indicate a prompt maturation of myotubes.

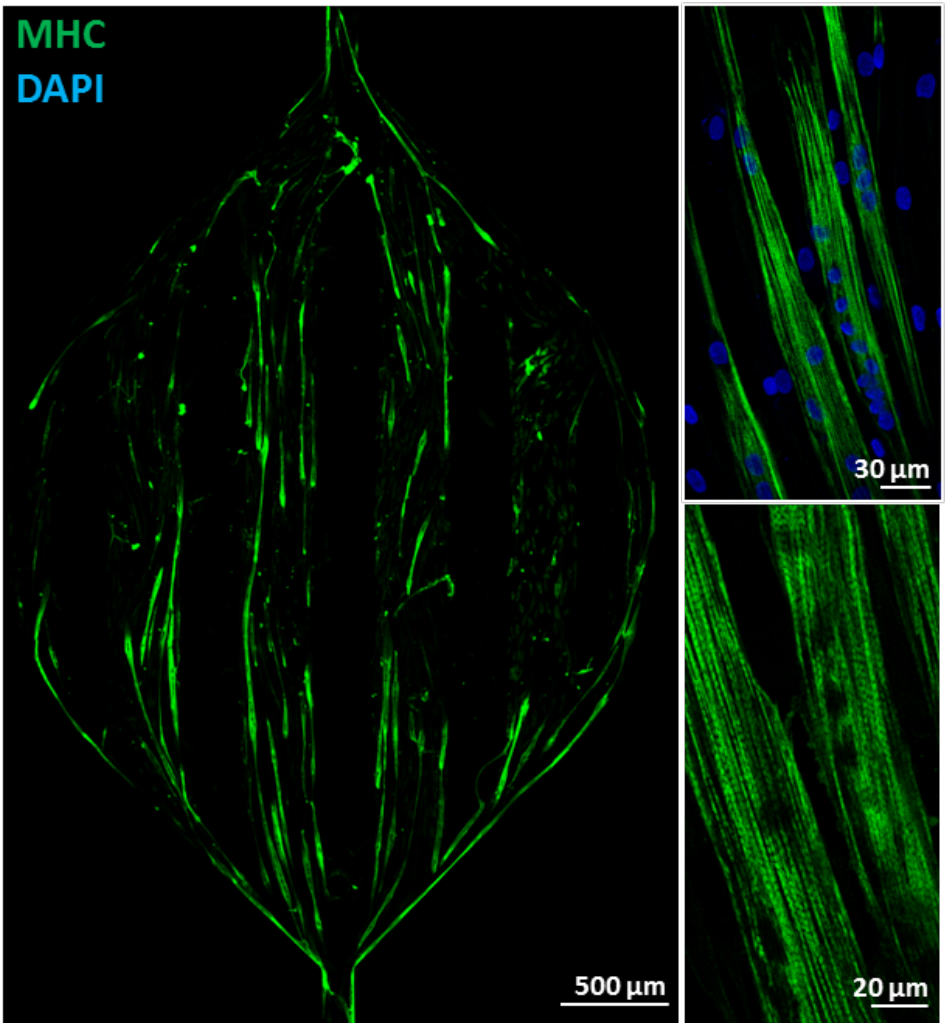

Figure 5.8 *Immunofluorescence for MHC on human primary myotubes cultured in the patterned microfluidic chip. Myotubes obtained show MHC sarcomeric organization as highlighted in the magnified images.*

Thereafter, human myotubes where tested also for the molecular features that characterize and insulin responsive tissue. For this purpose, myotubes where analyzed through western blot analyses in order to verify the activation of insulin signaling pathway.
Western blot analysis derived from skeletal muscle cells cultured in the microfluidic chip is shown in Figure 5.9.

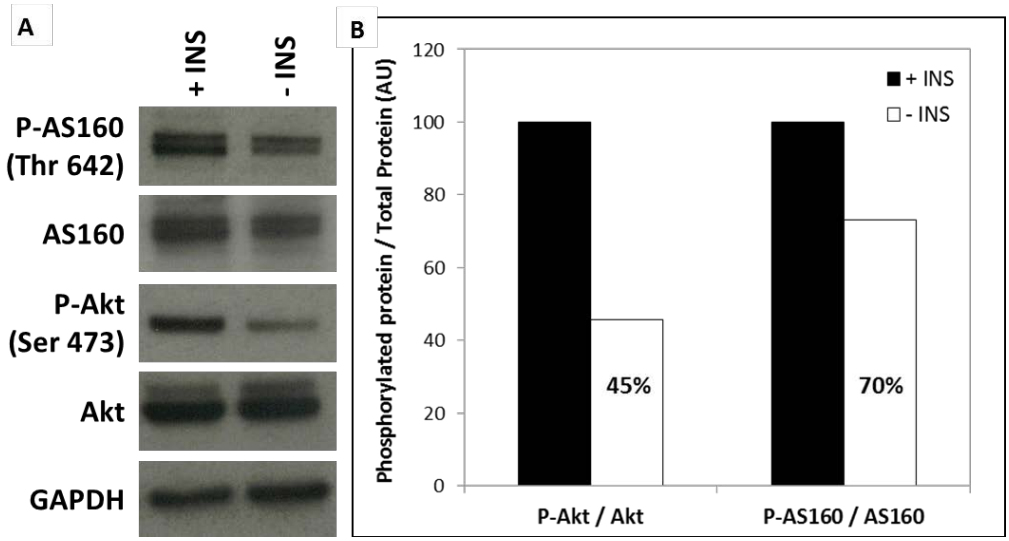

Figure 5.9 *Immunoblot analyses performed on human myotubes cultured in the microfluidic chip stimulated (closed bars) or not (open bars) with insulin.* ***A)*** *Representative western blot.* ***B)*** *Quantification of bands reported in A). Data represent the ratio between the phosphorylated form and the total amount of protein and are reported in Arbitrary Units (AU).*

In Figure 5.9 are reported 2 key proteins of the insulin pathway, Akt and AS160 (Akt Substrate of 160 kDa) which are phosphorylated respectively in a Serine (Ser 473) and a Threonine (Thr 642) residue in healthy individuals, after insulin binding to its membrane receptor. Microfluidic cultures of myotubes were stimulated with insulin 100 nM for 10 min and subsequently lysed. Lysates of stimulated cells show higher content of both Akt and AS160 in their phosphorylated forms compared with controls (myotubes not stimulated). Phosphorylation of these two proteins is a clear indicator of the proper activation of insulin signaling pathway, the most involved and disrupted pathway involved in muscle insulin resistance onset and overt Diabetes.

5.5 Conclusions

In this chapter it has been presented how the culture microenvironment can be optimized in order to improve cell similarity to the *in vivo* situation. In the specific, here it was study how the pattern geometry of parallel lanes can influence myoblasts proliferation and differentiation. It has been shown that lanes of different width bring to different percentage of proliferating and differentiating cells with the first one decreasing with higher lane width, while differentiation is enhance with larger lanes. It's clear that larger lanes promote the local accumulation of myokines. These results can be explained taking into account the key role of myokines secreted by myogenic cells in promoting myoblasts differentiation. These soluble secreted factors can act in an auto/paracrine manner mediating the interaction

between fusion partner cells, as well as the direct contact of neighboring cell membrane proteins.

Once outlined which is the best pattern for myoblasts proliferation and differentiation, the same geometry was introduced in the microfluidic chip. Here both murine and human primary myoblasts were able to grow, align and differentiate into myotubes with high sarcomeric organization. Moreover, human myotubes showed to express properly the insulin signaling pathway also in the microfluidic technology.

The characterizations done highlight the obtainment of a human skeletal muscle tissue integrated in a microfluidic chip. The integration with microfluidic technology will permit to perform deeper studies concerning insulin or drug stimulation and metabolites utilization as demonstrate in the previous chapters.

Finally, results of myogenic differentiation and insulin pathway activation were obtained through conventional molecular biology techniques (immunofluorescence and immunoblot). These results point out the capability to perform reliable biological analyses in a non-conventional system of culture. In fact microfluidic cell culture technology is intrinsically characterized by tiny amount of biological material. The possibility to perform biological relevant analyses gives an added value to this technology translating it into a complementary tool for biomedical studies.

Chapter 6

Conclusions and Future Perspectives

Type 2 Diabetes is a metabolic disorder characterized by chronic hyperglycemia with disturbance of carbohydrates, fat and protein metabolism which involves different organs and mechanism.

Its treatment is never straightforward and univocal and a huge effort in terms of therapy development and personalization must be promote to treat this disease in different patients.

In vitro human models based on automated and highthroughput systems and which can reproduce the complex pathophysiology of the disease can be advantageous in the development and screening of new drugs and therapy for Type 2 Diabetes.

In this thesis, human tissues integrated on-a-chip have been developed, more specifically skeletal muscle and adipose tissues were integrated within a microfluidic technology. Microfluidic permits to have a fine control over culture conditions and biochemical stimulation both in space and in time. Moreover, the tiny volumes permit to have high ratio between tissue surface and medium volume, feature that enhances small variation in medium composition. Finally microfluidic technology is suitable to be applied for automated and highthroughput analyses.

Skeletal muscle and adipose tissues were chosen for their involvement in Type 2 Diabetes when insulin resistance and glucose uptake impairment overcome, and their integration "on-a-chip" and their application were presented in this thesis.

In Chapter 3 it has been presented a model of myoblasts integrated in a microfluidic technology and coupled with glucose FRET-based nanosensing. Microfluidic technology permitted to monitor extracellular glucose concentration with high temporal resolution and derive precise value of glucose uptake with minimum disruption of cell culture condition. On the other hand glucose FRET nanosensing permitted to measure cytosolic glucose concentration in live cells, with high spatial resolution and at a single cell level. With the assistance of mathematical modeling and data analyses it was possible to derive from experimental data the kinetic parameters involved in glucose handling, i.e. glucose diffusion through plasma membrane and intracellular glucose phosphorylation. As far as it is known, the determination of these parameters has never been achieved previously in living cells and under physiological conditions.

In Chapter 4 is has been presented the integration in a microfluidic technology of another tissue involved in Type 2 Diabetes, that is adipose tissue. Adipose tissue organ cultures in the microfluidic chip showed high viability and metabolic activity, up to 8 days long cultures. This tissue model also showed high flow rate sensitivity in high resolution glucose uptake measurements and robustness in experiments. In this chapter it was also presented an integrated chip for temporally controlled stimulations (insulin, drug or other relevant biochemicals). This microfluidic device permit automation of the procedures and more importantly the modulation of the stimulus given. Proof of concept experiments of glucose uptake measurements after insulin stimulation were performed, highlighting the feasibility and flexibility of the system.

Finally, in Chapter 5 is presented the integration of human skeletal muscle in a microfluidic device. For the development of this in vitro tissue, micropattern techniques were also applied in order to have a better control on cell microenvironment, in the specific of their topology. In details, the effect on myoblasts proliferation and differentiation into myotubes of a pattern of different width lanes was studied. Wider lanes negatively affect cell proliferation, whereas they have a positive effect on myoblasts differentiation. This outline that larger lanes promotes the local accumulation of myokines whose key role is acting in an auto/paracrine manner that mediates the interaction between fusion partner cells, promoting thus myoblasts differentiation. To have the best compromise between cell proliferation and differentiation, a pattern of 300 μm width lanes was subsequently integrated in a microfluidic chip. Here human myoblasts were successfully integrated, cultured and differentiated. Myotubes showed a high sarcomeric organization, outlining the obtainment of a tissue model very similar to the in vivo muscle phenotype. Moreover, it was given proof that in this system insulin pathway activation is conserved in physiological

conditions and that it can be deeply investigate through conventional molecular biology techniques.

These last findings open the possibility to deeply investigate diabetes mechanisms in the well-controlled culture conditions offered by microfluidic technology. Moreover, Microfluidics open also a new opportunity to study the pathology not only in a classical single-tissue model view, but also by integrating different kind of tissue in the same system.
It is very well know that organs involved in Type 2 Diabetes communicate and influence each other their behavior, as demonstrate also in the Appendix A which reports the pancreas/skeletal muscle intercommunication.
Another example is the crosstalk between adipose tissue and skeletal muscle. In vitro studies carried out by others (Dietze *et al.*, 2002, 2004; Kraegen and Cooney, 2008), demonstrates that adipose tissue from diseased individuals secretes cytokines (adipokines) and free fatty acids that can induce insulin resistance in skeletal muscle cells. By the way the in vitro experiments of these previous works doesn't modulate the ratios and times of exposure of biochemical. Also, they are performed in a discontinuous system that does not resemble the human body were different organs are in a continuous connection through circulatory system. Preliminary experiments of insulin resistance induced by adipose tissue-conditioned medium (CM) in myotubes cultured in the microfluidic chip were performed and are shown in Figure 6.1.

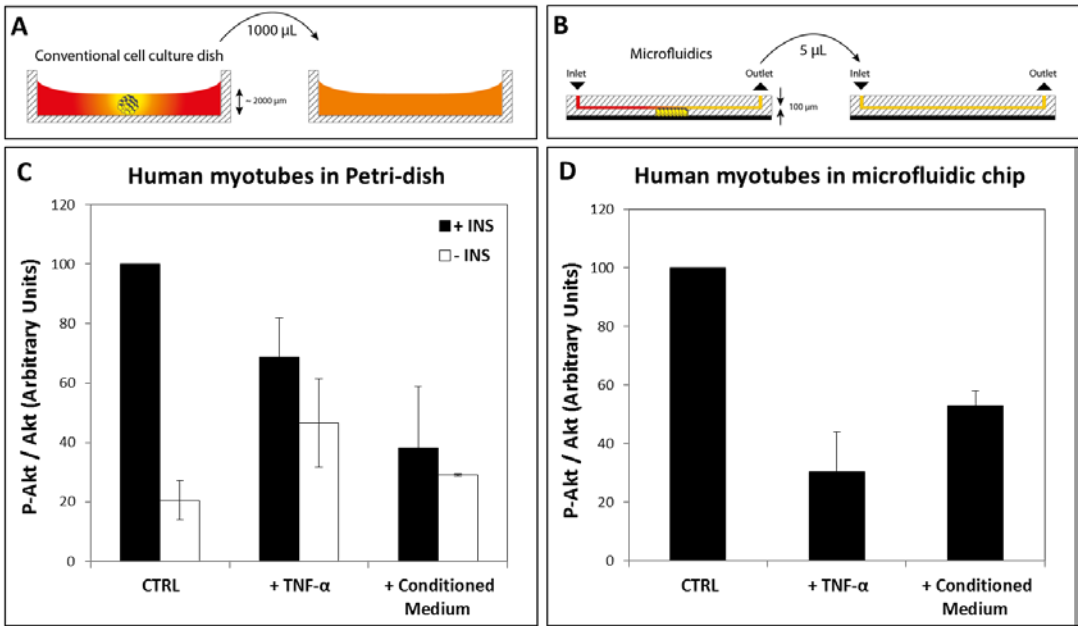

Figure 6.1 *Adipose tissue-induced insulin resistance evaluation.* ***A-B)*** *Schematic of volumes involved in the two types of experiments, conventional Petri dish (A) and microfluidic culture (B).* ***C-D)*** *Quantification of immunoblot analyses performed on human myotubes cultured in conventional Petri dish (C) or in the microfluidic chip (D). Data represent the ratio between the phosphorylated form of Akt (Ser 473) and the total amount of Akt.*

In Figure 6.1 is shown quantification of phosphorylated Akt (Ser 473) normalized to total Akt in human myotubes cultured both in conventional Petri dish cultures and in microfluidic cultures in the presence or not of TNF-α (a well-known in vitro insulin resistance inducer) or of CM of adipose tissue cultures. Petri dish experiments (Figure 6.1A) confirm the data reported in literature where insulin-stimulated Akt phosphorylation is suppressed after 24 h incubation with TNF-α or with CM. As reported in Figure 6.1B these data are confirmed also in myotubes cultures performed in a microfluidic chip. In this system is possible to reproduce insulin resistance induction through various factors. In microfluidic condition the volumes involved are very tiny, feature that can enhance tissue response to small variation on its extracellular environment.

These results release new perspectives in the use of these tissue-on-a-chip models and on the feasibility of performing organs cross-talk studies. In fact, different tissues can be connected through a microfluidic device that can reproduce in vitro the complex physiology of human body (Figure 6.2).

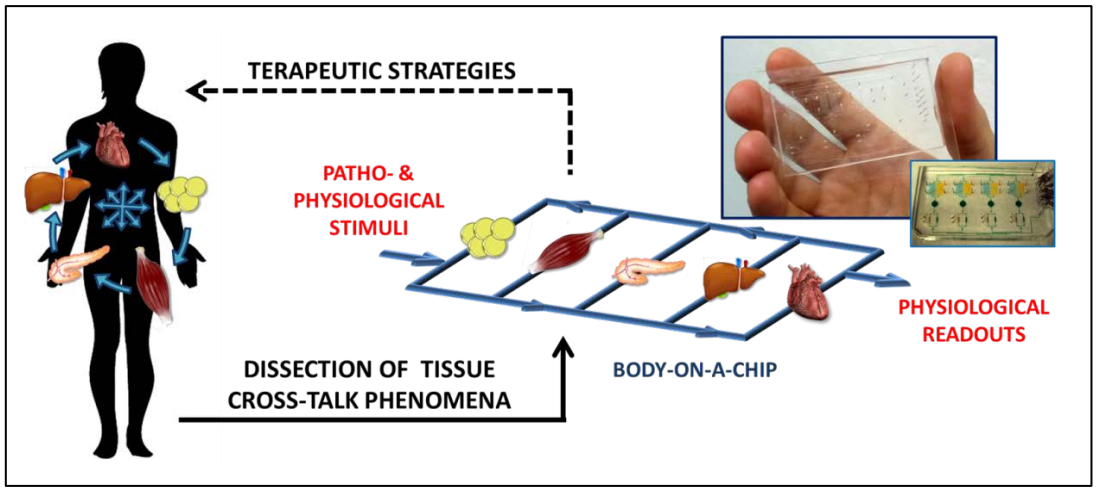

Figure 6.2 *Schematic view of organs-on- chip idea, for tissue cross-talk dissection.*

In this way, it can be generated a new tool able to dissect, reproduce and study tissue interactions in multi-organs derived diseases, suitable for drug testing and pathophysiological studies. This human in vitro model will be characterized by a small scale that enables precise control of culture conditions and gives the possibility to perform high-throughput experiments, which are not economically sustainable on a macroscopic level and that can be shaped even in a patient-specific way.

Concluding, in this thesis it is reported the development of human tissue models “on-a-chip”. These models can be successfully applied for the investigation of glucose management in

living cells, permits to have a better control over culture conditions and biochemical stimulations and in the meantime to explore different types of readout.

By the use of microfluidic technologies in a perspective view, it will be possible to overcome current limitation in therapy design, by reproducing in vitro models of the disease for a targeted drug investigation, even in a patient-specific way in order to perform individual therapeutic development.

References

Alberti, K.G., and Zimmet, P.Z. (1998). Definition, diagnosis and classification of diabetes mellitus and its complications. Part 1: diagnosis and classification of diabetes mellitus provisional report of a WHO consultation. Diabet. Med. J. Br. Diabet. Assoc. *15*, 539–553.

Alonso-Castro, A.J., and Salazar-Olivo, L.A. (2008). The anti-diabetic properties of Guazuma ulmifolia Lam are mediated by the stimulation of glucose uptake in normal and diabetic adipocytes without inducing adipogenesis. J. Ethnopharmacol. *118*, 252–256.

Bajaj, P., Reddy, B., Jr, Millet, L., Wei, C., Zorlutuna, P., Bao, G., and Bashir, R. (2011). Patterning the differentiation of C2C12 skeletal myoblasts. Integr. Biol. Quant. Biosci. Nano Macro *3*, 897–909.

Biffi, E., Piraino, F., Pedrocchi, A., Fiore, G.B., Ferrigno, G., Redaelli, A., Menegon, A., and Rasponi, M. (2012). A microfluidic platform for controlled biochemical stimulation of twin neuronal networks. Biomicrofluidics *6*, 24106–2410610.

Bird, R.B., Stewart, W.E., and Lightfoot, E.N. (2007). Transport Phenomena (John Wiley & Sons).

Bouzakri, K., Roques, M., Gual, P., Espinosa, S., Guebre-Egziabher, F., Riou, J.-P., Laville, M., Le Marchand-Brustel, Y., Tanti, J.-F., and Vidal, H. (2003). Reduced activation of phosphatidylinositol-3 kinase and increased serine 636 phosphorylation of insulin receptor substrate-1 in primary culture of skeletal muscle cells from patients with type 2 diabetes. Diabetes *52*, 1319–1325.

Cagnin, S., Cimetta, E., Guiducci, C., Martini, P., and Lanfranchi, G. (2012). Overview of micro- and nano-technology tools for stem cell applications: Micropatterned and microelectronic devices. Sens. Switz. *12*, 15947–15982.

Ciaraldi, T.P., Abrams, L., Nikoulina, S., Mudaliar, S., and Henry, R.R. (1995). Glucose transport in cultured human skeletal muscle cells. Regulation by insulin and glucose in nondiabetic and non-insulin-dependent diabetes mellitus subjects. J. Clin. Invest. *96*, 2820–2827.

Cryer, P.E., Davis, S.N., and Shamoon, H. (2003). Hypoglycemia in diabetes. Diabetes Care *26*, 1902–1912.

DeFronzo, R.A., Bonadonna, R.C., and Ferrannini, E. (1992). Pathogenesis of NIDDM. A balanced overview. Diabetes Care *15*, 318–368.

Deuschle, K., Chaudhuri, B., Okumoto, S., Lager, I., Lalonde, S., and Frommer, W.B. (2006). Rapid metabolism of glucose detected with FRET glucose nanosensors in epidermal cells and intact roots of Arabidopsis RNA-silencing mutants. Plant Cell *18*, 2314–2325.

Dietze, D., Koenen, M., Röhrig, K., Horikoshi, H., Hauner, H., and Eckel, J. (2002). Impairment of insulin signaling in human skeletal muscle cells by co-culture with human adipocytes. Diabetes *51*, 2369–2376.

Dietze, D., Ramrath, S., Ritzeler, O., Tennagels, N., Hauner, H., and Eckel, J. (2004). Inhibitor kappaB kinase is involved in the paracrine crosstalk between human fat and muscle cells. Int. J. Obes. Relat. Metab. Disord. J. Int. Assoc. Study Obes. *28*, 985–992.

DiMasi, J., Hansen, R.W., and Grabowski, H.G. (2003). The price of innovation: new estimates of drug development costs. J. Health Econ. *22*, 151–158.

Dittrich, P.S., and Manz, A. (2006). Lab-on-a-chip: microfluidics in drug discovery. Nat. Rev. Drug Discov. *5*, 210–218.

Eckel, R.H., Grundy, S.M., and Zimmet, P.Z. (2005). The metabolic syndrome. Lancet *365*, 1415–1428.

El-Ali, J., Sorger, P.K., and Jensen, K.F. (2006). Cells on chips. Nature *442*, 403–411.

Elliott, N.T., and Yuan, F. (2011). A review of three-dimensional in vitro tissue models for drug discovery and transport studies. J. Pharm. Sci. *100*, 59–74.

Engler, A.J., Griffin, M.A., Sen, S., Bönnemann, C.G., Sweeney, H.L., and Discher, D.E. (2004). Myotubes differentiate optimally on substrates with tissue-like stiffness: pathological implications for soft or stiff microenvironments. J. Cell Biol. *166*, 877–887.

Fehr, M., Lalonde, S., Lager, I., Wolff, M.W., and Frommer, W.B. (2003). In vivo imaging of the dynamics of glucose uptake in the cytosol of COS-7 cells by fluorescent nanosensors. J. Biol. Chem. *278*, 19127–19133.

Figeys, and Pinto (2000). Lab-on-a-chip: a revolution in biological and medical sciences. Anal. Chem. *72*, 330A–335A.

Fried, S.K., and Moustaid-Moussa, N. (2001). Culture of adipose tissue and isolated adipocytes. Methods Mol. Biol. Clifton NJ *155*, 197–212.

Frier, B.M. (2009). Defining hypoglycaemia: what level has clinical relevance? Diabetologia *52*, 31–34.

Fröjdö, S., Vidal, H., and Pirola, L. (2009a). Alterations of insulin signaling in type 2 diabetes: a review of the current evidence from humans. Biochim. Biophys. Acta *1792*, 83–92.

Fröjdö, S., Vidal, H., and Pirola, L. (2009b). Alterations of insulin signaling in type 2 diabetes: A review of the current evidence from humans. Biochim. Biophys. Acta BBA - Mol. Basis Dis. *1792*, 83–92.

Gómez-Sjöberg, R., Leyrat, A.A., Pirone, D.M., Chen, C.S., and Quake, S.R. (2007). Versatile, fully automated, microfluidic cell culture system. Anal. Chem. *79*, 8557–8563.

Henry, R.R., Abrams, L., Nikoulina, S., and Ciaraldi, T.P. (1995). Insulin action and glucose metabolism in nondiabetic control and NIDDM subjects. Comparison using human skeletal muscle cell cultures. Diabetes *44*, 936–946.

Hong, J., Edel, J.B., and deMello, A.J. (2009). Micro- and nanofluidic systems for high-throughput biological screening. Drug Discov. Today *14*, 134–146.

Hou, B.-H., Takanaga, H., Grossmann, G., Chen, L.-Q., Qu, X.-Q., Jones, A.M., Lalonde, S., Schweissgut, O., Wiechert, W., and Frommer, W.B. (2011). Optical sensors for monitoring dynamic changes of intracellular metabolite levels in mammalian cells. Nat. Protoc. *6*, 1818–1833.

International Diabetes Federation IDF Diabetes Atlas, 6th edn.

Al-Khalili, L., Chibalin, A.V., Kannisto, K., Zhang, B.B., Permert, J., Holman, G.D., Ehrenborg, E., Ding, V.D.H., Zierath, J.R., and Krook, A. (2003). Insulin action in cultured human skeletal muscle cells during differentiation: assessment of cell surface GLUT4 and GLUT1 content. Cell. Mol. Life Sci. CMLS *60*, 991–998.

Khetani, S.R., and Bhatia, S.N. (2008a). Microscale culture of human liver cells for drug development. Nat. Biotechnol. *26*, 120–126.

Khetani, S.R., and Bhatia, S.N. (2008b). Microscale culture of human liver cells for drug development. Nat. Biotechnol. *26*, 120–126.

Kim, W.H., Lee, J., Jung, D.-W., and Williams, D.R. (2012). Visualizing sweetness: increasingly diverse applications for fluorescent-tagged glucose bioprobes and their recent structural modifications. Sensors *12*, 5005–5027.

Kotliar, N., and Pilch, P.F. (1992). Expression of the glucose transporter isoform GLUT 4 is insufficient to confer insulin-regulatable hexose uptake to cultured muscle cells. Mol. Endocrinol. Baltim. Md *6*, 337–345.

Kraegen, E.W., and Cooney, G.J. (2008). Free fatty acids and skeletal muscle insulin resistance. Curr. Opin. Lipidol. *19*, 235–241.

Kurtoglu, M., Maher, J.C., and Lampidis, T.J. (2007). Differential toxic mechanisms of 2-deoxy-D-glucose versus 2-fluorodeoxy-D-glucose in hypoxic and normoxic tumor cells. Antioxid. Redox Signal. *9*, 1383–1390.

Laakso, M. (1999). Hyperglycemia as a risk factor for cardiovascular disease in type 2 diabetes. Prim. Care *26*, 829–839.

Louters, L.L., Stehouwer, N., Rekman, J., Tidball, A., Cok, A., and Holstege, C.P. (2010). Verapamil inhibits the glucose transport activity of GLUT1. J. Med. Toxicol. Off. J. Am. Coll. Med. Toxicol. *6*, 100–105.

Van der Meer, A.D., and van den Berg, A. (2012a). Organs-on-chips: breaking the in vitro impasse. Integr. Biol. Quant. Biosci. Nano Macro *4*, 461–470.

Van der Meer, A.D., and van den Berg, A. (2012b). Organs-on-chips: breaking the in vitro impasse. Integr. Biol. Quant. Biosci. Nano Macro *4*, 461–470.

Van Midwoud, P.M., Verpoorte, E., and Groothuis, G.M.M. (2011a). Microfluidic devices for in vitro studies on liver drug metabolism and toxicity. Integr. Biol. Quant. Biosci. Nano Macro *3*, 509–521.

Van Midwoud, P.M., Verpoorte, E., and Groothuis, G.M.M. (2011b). Microfluidic devices for in vitro studies on liver drug metabolism and toxicity. Integr. Biol. Quant. Biosci. Nano Macro *3*, 509–521.

Neuži, P., Giselbrecht, S., Länge, K., Huang, T.J., and Manz, A. (2012). Revisiting lab-on-a-chip technology for drug discovery. Nat. Rev. Drug Discov. *11*, 620–632.

Nyberg, G., Mellgren, G., and Smith, U. (1976). Human adipose tissue in culture. VI. Effect of age on cell size and lipolysis. Acta Paediatr. Scand. *65*, 313–318.

Pedersen, B.K. (2011). Muscles and their myokines. J. Exp. Biol. *214*, 337–346.

Perriott, L.M., Kono, T., Whitesell, R.R., Knobel, S.M., Piston, D.W., Granner, D.K., Powers, A.C., and May, J.M. (2001). Glucose uptake and metabolism by cultured human skeletal muscle cells: rate-limiting steps. Am. J. Physiol. Endocrinol. Metab. *281*, E72–80.

Phillips, S.A., Ciaraldi, T.P., Oh, D.K., Savu, M.K., and Henry, R.R. (2008). Adiponectin secretion and response to pioglitazone is depot dependent in cultured human adipose tissue. Am. J. Physiol. Endocrinol. Metab. *295*, E842–850.

Plomgaard, P., Halban, P.A., and Bouzakri, K. (2012). Bimodal impact of skeletal muscle on pancreatic β-cell function in health and disease. Diabetes Obes. Metab. *14 Suppl 3*, 78–84.

Raghavan, S., Nelson, C.M., Baranski, J.D., Lim, E., and Chen, C.S. (2010). Geometrically controlled endothelial tubulogenesis in micropatterned gels. Tissue Eng. Part A *16*, 2255–2263.

Rolo, A.P., and Palmeira, C.M. (2006). Diabetes and mitochondrial function: role of hyperglycemia and oxidative stress. Toxicol. Appl. Pharmacol. *212*, 167–178.

Saltiel, A.R., and Kahn, C.R. (2001). Insulin signalling and the regulation of glucose and lipid metabolism. Nature *414*, 799–806.

Samuel, V.T., and Shulman, G.I. (2012). Mechanisms for insulin resistance: common threads and missing links. Cell *148*, 852–871.

Sankar, K.S., Green, B.J., Crocker, A.R., Verity, J.E., Altamentova, S.M., and Rocheleau, J.V. (2011). Culturing pancreatic islets in microfluidic flow enhances morphology of the associated endothelial cells. PloS One *6*, e24904.

Sell, H., Eckardt, K., Taube, A., Tews, D., Gurgui, M., Van Echten-Deckert, G., and Eckel, J. (2008). Skeletal muscle insulin resistance induced by adipocyte-conditioned medium: underlying mechanisms and reversibility. Am. J. Physiol. Endocrinol. Metab. *294*, E1070–1077.

Serena, E., Zatti, S., Reghelin, E., Pasut, A., Cimetta, E., and Elvassore, N. (2010). Soft substrates drive optimal differentiation of human healthy and dystrophic myotubes. Integr. Biol. Quant. Biosci. Nano Macro *2*, 193–201.

Shackman, J.G., Reid, K.R., Dugan, C.E., and Kennedy, R.T. (2012). Dynamic monitoring of glucagon secretion from living cells on a microfluidic chip. Anal. Bioanal. Chem. *402*, 2797–2803.

Sjöström, L., Smith, U., Björntorp, P., Jacobsson, B., and Hallgren, P. (1977). Human adipose tissue maintained in a continuous flow system. Kinetic studies of glycerol release in response to noradrenaline and evidence for the formation of a hormone antagonist. J. Biol. Chem. *252*, 8833–8839.

Stumvoll, M., Goldstein, B.J., and van Haeften, T.W. (2005). Type 2 diabetes: principles of pathogenesis and therapy. Lancet *365*, 1333–1346.

Tam, A., Wadsworth, S., Dorscheid, D., Man, S.F.P., and Sin, D.D. (2011). The airway epithelium: more than just a structural barrier. Ther. Adv. Respir. Dis. *5*, 255–273.

Thompson, D.B., Pratley, R., and Ossowski, V. (1996). Human primary myoblast cell cultures from non-diabetic insulin resistant subjects retain defects in insulin action. J. Clin. Invest. *98*, 2346–2350.

Thorens, B., and Mueckler, M. (2010). Glucose transporters in the 21st Century. Am. J. Physiol. Endocrinol. Metab. *298*, E141–145.

Tourovskaia, A., Figueroa-Masot, X., and Folch, A. (2005). Differentiation-on-a-chip: a microfluidic platform for long-term cell culture studies. Lab. Chip *5*, 14–19.

Trujillo, M.E., Lee, M.-J., Sullivan, S., Feng, J., Schneider, S.H., Greenberg, A.S., and Fried, S.K. (2006). Tumor necrosis factor alpha and glucocorticoid synergistically increase leptin production in human adipose tissue: role for p38 mitogen-activated protein kinase. J. Clin. Endocrinol. Metab. *91*, 1484–1490.

Van de Venter, M., Roux, S., Bungu, L.C., Louw, J., Crouch, N.R., Grace, O.M., Maharaj, V., Pillay, P., Sewnarian, P., Bhagwandin, N., et al. (2008). Antidiabetic screening and scoring of 11 plants traditionally used in South Africa. J. Ethnopharmacol. *119*, 81–86.

Virtanen, K.A., Lönnroth, P., Parkkola, R., Peltoniemi, P., Asola, M., Viljanen, T., Tolvanen, T., Knuuti, J., Rönnemaa, T., Huupponen, R., et al. (2002). Glucose uptake and perfusion in subcutaneous and visceral adipose tissue during insulin stimulation in nonobese and obese humans. J. Clin. Endocrinol. Metab. *87*, 3902–3910.

Whitesides, G.M. (2006). The origins and the future of microfluidics. Nature *442*, 368–373.

Yoshioka, K., Takahashi, H., Homma, T., Saito, M., Oh, K.B., Nemoto, Y., and Matsuoka, H. (1996). A novel fluorescent derivative of glucose applicable to the assessment of glucose uptake activity of Escherichia coli. Biochim. Biophys. Acta *1289*, 5–9.

Zambon, A. (2013). Development of microfluidic cell culture technology for the study of type 2 Diabetes. Università degli Studi di Padova.

Zhang, L., Wang, J., Zhao, L., Meng, Q., and Wang, Q. (2010). Analysis of chemoresistance in lung cancer with a simple microfluidic device. Electrophoresis *31*, 3763–3770.

Appendix A

CX3CL1 (fractalkine), a new myokine protecting beta-cell and skeletal muscle from TNF-alpha induced insulin resistance

Peter Plomgaard[2,3,], Sabine Rutti[1,*], Jakob Hansen [2,3] ,Rodolphe Dusaulcy[1], Caroline Arous[1,] Alice Zoso[4]; Vanessa Bianda[1], Claus Brandt2,3, Thierry Berney[1], Nicola Elvassore[4], Emmanouil Dermitzakis[1], Marc Donath[5], Bente K. Pedersen[2], Philippe A. Halban[1] and Karim Bouzakri[1]**

[1]Department of Genetic Medicine and Development, Medical Centre, Geneva University, Geneva, Switzerland. [2]Centre of Inflammation and Metabolism and Department of infectious Diseases, Rigshospitalet, Copenhagen, Denmark. [3]Department of Clinical Biochemistry, Rigshospitalet, Copenhagen, Denmark. [4]Department of Industrial Engineering, Padova, Italia. [5]Endocrinology, Diabetes & Metabolism University Hospital Basel, Switzerland. [6]Medicine Faculty, UMR INSERM 1060, Lyon University France.*

Corresponding author: Dr Karim Bouzakri, University Medical Center, Department of Genetic Medicine and Development, 1 rue Michel-Servet, CH-1211 Geneva 4, Switzerland, Phone: +41 22 379 52 78, FAX: +41 22 379 55 28, E-mail: karim.bouzakri@unige.ch

Diabetes
Submitted

Abstract

Fractalkine (CX3CL1) is a membrane bound chemokine with a soluble form generated by enzymatic shedding. Biological actions of fractalkine are mediated through a specific G-protein coupled-receptor, CX3CR1. CX3CL1 mRNA expression is increased in human skeletal muscle cells (HSMC) treated with TNF-α. We have identified the existence of a muscle-pancreas intercommunication axis in which fractalkine produced by HSMC could be implicated. The aim of the study was to explore the autocrine impact of CX3CL1 on HSMC and its paracrine effects on islets and sorted beta-cells. Here we identify CX3CL1 as a new myokine regulated by exercise and TNF-α infusion in humans. Moreover, CX3CL1 takes part in the physiological process of exercise and is a protective factor against TNF-α adverse effects on skeletal muscle insulin sensitivity and beta-cell glucose-stimulated-insulin-secretion, suggesting a specific interaction between TNF-α and CX3CL1 signaling pathways. CX3CL1 represents a potential therapeutic target for the treatment of insulin-resistance and type-2-diabetes.

Introduction

Type 2 diabetes (T2D) pathophysiology is a complex process combining 2 major mechanisms: insulin resistance and beta-cell failure. During the prediabetic period, characterized by peripheral insulin resistance, euglycemia is maintained by a compensatory increase of insulin secretion. However, the addition to this prediabetic state of beta-cell failure, affecting both cell function and survival, leads to hyperglycemia and clinically manifest T2D (Bergman, 2013). This is exacerbated by abnormal alpha-cell function resulting in pathologically elevated levels of glucagon (Muller et al., 1970). The pathophysiology of T2D from peripheral insulin resistance to beta-cell failure shows the interdependence of insulin sensitive organs (muscle, adipose tissue, and liver) and the insulin producing organ (endocrine pancreas) in the control of glucose metabolism. Following the example of adipokines linking adipocytes to islets (Wijesekara et al., 2010), muscle derived cytokines are new actors in the communication axis between muscle and pancreas (Bouzakri et al., 2011; Handschin et al., 2007). Indeed, since it has been shown that muscle cells are able to express, produce, and actively release cytokines, they are considered as a new secretory organ. Muscle derived cytokines, also named myokines, can act locally on muscle itself or on distant organs (Pedersen et al., 2004; Pedersen et al., 2001). IL-6 was the first myokine to be described (Pedersen et al., 2004). During the last decade, the increasing

number of myokines (e.g.: myostatin, LIF, IL-7, BDNF, IGF-1, FGF-2, FSTL-1, Irisin…) and of their target organs (e.g.: adipose tissue, liver, blood vessels, bone and pancreas) attests to the importance of these factors in physiology (Pedersen and Febbraio, 2012; Plomgaard et al., 2012). We have previously shown that the insulin sensitivity status of muscle cells can impact their myokine expression profiles and function in vitro (Bouzakri et al., 2011). Moreover, conditioned medium from control muscle cells is able to increase rat primary beta-cell proliferation and glucose induced insulin secretion (GSIS) in rat and human primary beta-cells, whereas conditioned medium from insulin resistant muscle cells (following TNF-α treatment) has a negative impact on beta-cell survival and GSIS (Bouzakri et al., 2011). This illustrates the functional heterogeneity of myokines.

We have observed that fractalkine expression is dramatically increased in primary human skeletal muscle cells treated with TNF-α (Bouzakri et al., 2011). Fractalkine, also named CX3CL1, is the only member of the CX3C chemokine family. It is first synthesized in a plasma membrane bound form and a soluble form is shed through enzymatic cleavage by Adam 10 and Adam 17 (Garton et al., 2001; Hundhausen et al., 2003). CX3CL1 is the specific ligand for a G protein coupled receptor (GPCR) named CX3CR1. Upon binding to its receptor, CX3CL1 is implicated in chemotaxis, cellular adhesion and in increased cell survival during hemostasis and inflammatory episodes (Aoyama et al., 2010). Reporter gene studies have shown that CX3CL1 is principally expressed in neurons, lung epithelial cells, kidney and in the intestine (Aoyama et al., 2010; Cardona et al., 2006; Haskell et al., 1999), whereas CX3CR1 is mainly expressed in monocytes, natural killer cells and T cells (Haskell et al., 1999; Zernecke et al., 2008). Intriguingly, CX3CL1 has recently been described as a novel adipokine positively regulated by obesity and diabetes (Shah et al., 2011). Several studies strongly suggest that CX3CL1 could be implicated in the low-grade inflammation status of adipose tissue associated with obesity and T2D development. Indeed, CX3CL1 is involved in monocyte adhesion to adipocytes in vitro and its expression in adipocytes is stimulated by inflammatory cytokines (Shah et al., 2011). The CX3CL1/CX3CR1 system could also be implicated in some diabetes-associated pathologies such as painful neuropathy or extracellular matrix accumulation in diabetic nephropathy (Navarro-Gonzalez et al., 2011).

Interestingly, it has recently been shown that CX3CL1 could have beneficial metabolic effects (Lee et al., 2013). It was thus observed that in CX3CR1 KO mice, GSIS was decreased. CX3CL1 itself could increase insulin secretion during glucose tolerance tests in vivo and GSIS on *ex-vivo* isolated islets. These acute actions of CX3CL1, mediated by a MEK dependent pathway, were associated to chronic effects maintaining the expression of genes necessary to preserve fully functional beta-cells. This study also showed that T2D risk factors such as

aging and obesity are associated with a decrease in CX3CL1 expression within the islets (Lee et al., 2013).

In the present study, we provide for the first time evidence that CX3CL1 is a new myokine regulated by exercise and TNF-α infusion in human. Our data demonstrate that CX3CL1 is a protective factor against the adverse effects of TNF-α on skeletal muscle insulin sensitivity and beta-cell GSIS, suggesting a specific interaction between TNF-α and CX3CL1 signalling pathways. We also show here that CX3CL1 can directly regulate glucagon secretion in islets.

Results

CX3CL1 a new myokine regulated by exercise and TNF-alpha

We hypothesized that CX3CL1 could be regulated by exercise in skeletal muscle and classified as a new myokine. We therefore assessed whether circulating CX3CL1 was regulated by an exercise bout. Healthy young males performed 3 h of bicycling at 50% of VO_2max. As it appears in Figure 1A, performing exercise at a moderate intensity increased the plasma CX3CL1 concentration up to 3-fold. After cessation of bicycling, the concentration of plasma CX3CL1 decreased, returning to basal levels by the next morning. To demonstrate directly that CX3CL1 expression was regulated by exercise in the muscle, we performed a protocol of one-legged knee-extensor exercise for 2 h. This model allows a direct comparison between the resting leg and the exercising leg of the same individual. A marked increase of CX3CL1 mRNA was observed immediately after exercise only in the exercising leg. After 3 h of rest, the CX3CL1 mRNA content had returned to basal levels, comparable to levels measured in the resting leg (Figure 1B). Interestingly, CX3CL1 protein level was reduced after exercise, only in the exercising leg. This could coincide with secretion (or shedding) of the molecule (Figure 1C).

Our group and others have shown that CX3CL1 is regulated by TNF-α *in vitro* and in rodent models (Bouzakri et al., 2011; Turner et al., 2010). Therefore, we investigated the effect of acute TNF-α administration on plasma CX3CL1 in healthy young male subjects. Plasma TNF-α has been shown by us to be increased from (mean ± SEM) 0.7 ± 0.04 pg/ml to a plateau of 16.7 ± 1.8 pg/ml during a 4 hour infusion of human recombinant TNF-α (Plomgaard et al., 2008). Using the same protocol, plasma levels of CX3CL1 started to increase after 2 h of TNF-α infusion and reached a maximal level after 4 h (Figure 1D). No change was observed in the placebo treated group. The concentration obtained after TNF-α infusion was higher than the one obtained by exercise itself.

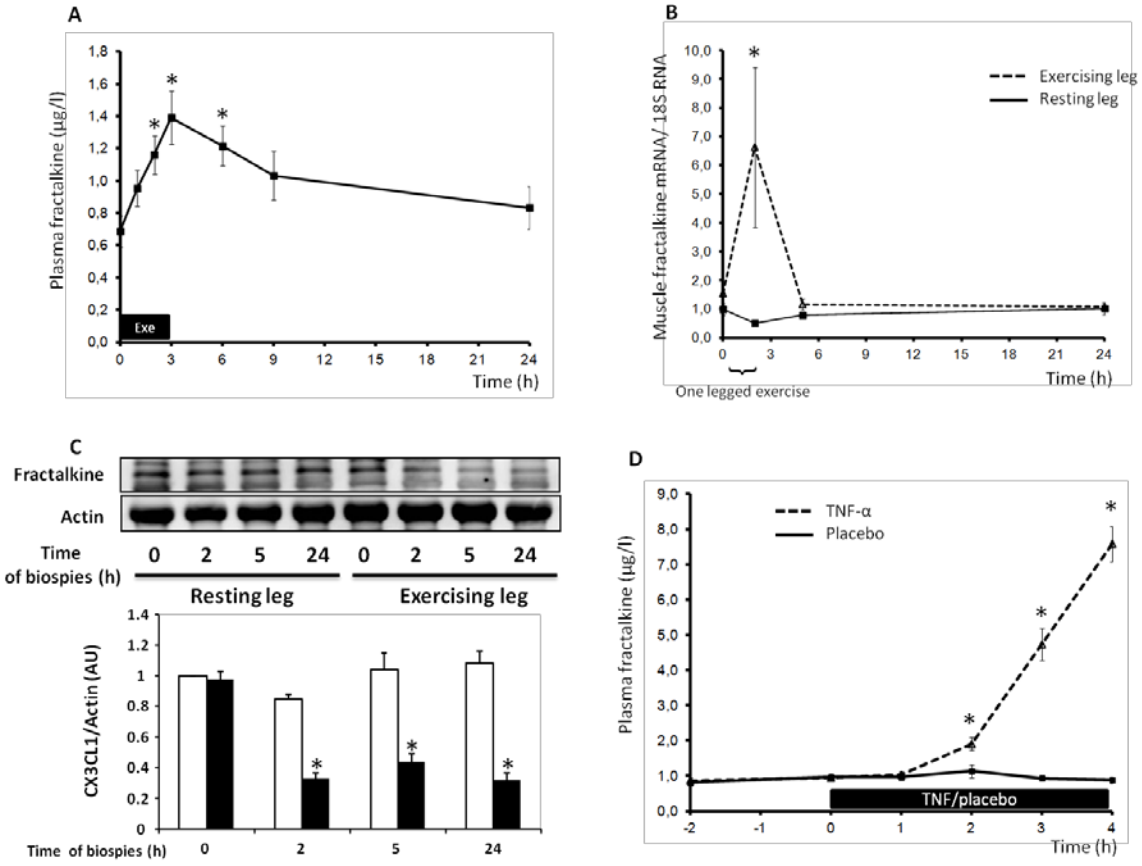

Figure 1: CX3CL1 is regulated by exercise and TNF-α in muscles.
*A: Plasma CX3CL1. 5 healthy males performed 3 h of bicycling exercise at 50% of VO2 max. * denotes significant difference from 0 h P < 0.05. B and C: Muscle mRNA content (B) and protein expression (C) of CX3CL1. 9 healthy subjects performed 2 h of one legged knee extensor exercise and muscle biopsies were obtained at 0, 2, 5 and 24 h from both resting and exercising legs. * denotes significant difference from 0 h P < 0.05. D: Plasma CX3CL1. 10 healthy males recieved 4 h of TNF-α infusion and placebo on two different experimental days. Plasma CX3CL1 was measured . * denotes significant difference from -2 h P < 0.05.*

CX3CL1 treatment protects human skeletal muscle cells against the effects of TNF-alpha on glucose uptake and insulin signaling

We have shown in the past that TNF-α injection induces skeletal muscle insulin resistance in healthy volunteers (Plomgaard et al., 2005). Therefore, we wanted here to investigate the role of CX3CL1 on glucose uptake in differentiated myotubes. Glucose uptake was assessed under basal and insulin stimulated conditions before or after 24 h TNF-α treatment in control conditions or after 48 h CX3CL1 exposure. In control conditions, insulin increased glucose uptake while TNF-α treatment prevented this. Basal glucose transport was increased in cells treated with CX3CL1 while insulin stimulated glucose uptake was unchanged. Importantly, TNF-α-induced insulin resistance (of glucose uptake) was rescued by CX3CL1 pretreatment (Figure 2A).

We then studied the impact of CX3CL1 on key proteins of the insulin signaling pathway involved in glucose uptake (Bouzakri et al., 2006). In myotubes treated with TNF-α for 24 h, insulin-stimulated Akt Ser473 and AS160 phosphorylation was completely prevented (Figure 2B-C). By contrast, in cells pretreated 48 h with CX3CL1, there was an increase in basal AS160 phosphorylation and insulin induced Akt and AS160 phosphorylation was unaltered by TNF-α exposure (Figure 2B-C). IRS-1 protein expression was increased by 48 h CX3CL1 treatment. Furthermore, in this condition, IRS-1 protein degradation induced by TNF-α was prevented (Figure 2D). IRS-2 protein expression was unchanged by TNF-α and/or CX3CL1 exposure (Figure 2E).

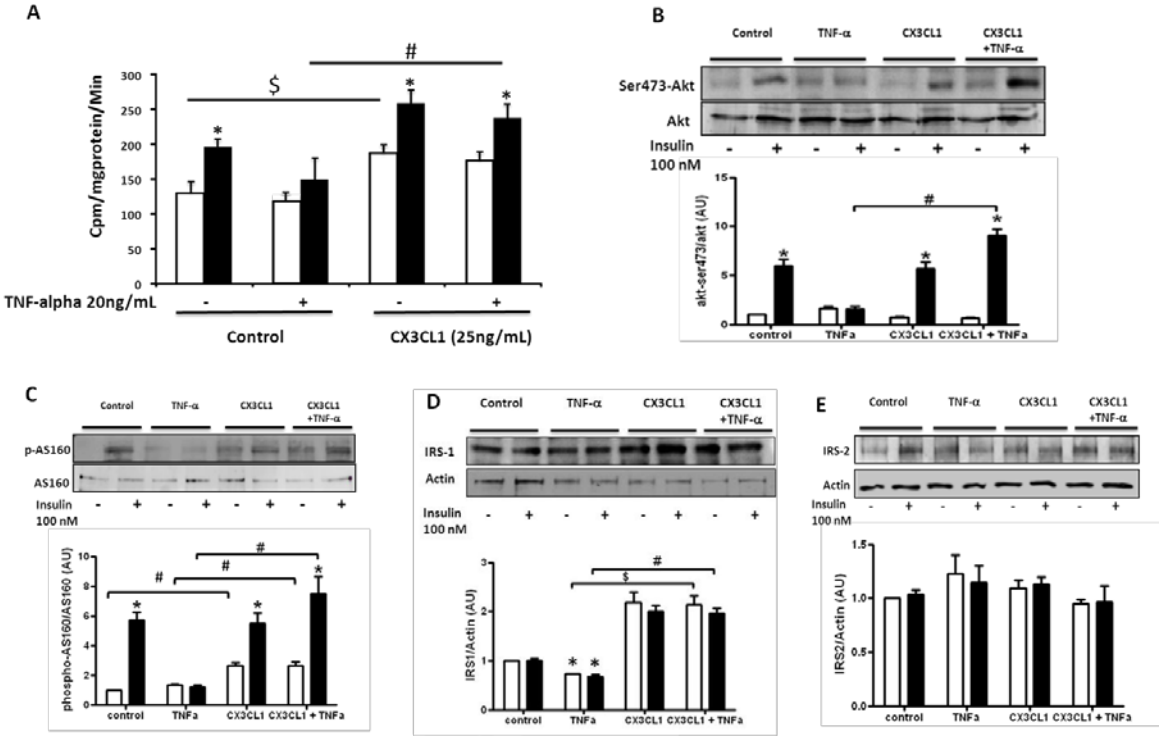

Figure 2: CX3CL1 treatment prevents TNF-α impact on glucose uptake and the insulin signaling pathway in primary human skeletal muscle cells. *Human skeletal muscle cells were treated 48 h with CX3CL1 (25 ng/ml) in presence or not of TNF-α (20 ng/ml) for the last 24 h in order to induce insulin resistance. A: glucose uptake in basal (open bars: without insulin) or insulin-stimulated conditions (closed bars: 100 nM insulin). Results are reported as cpm/milligram total protein/min (n=5). B and C: Representative Western blots and quantification showing Akt Ser-473 (B) or AS160 (C) phosphorylation in human skeletal muscle cells without insulin (open bars) or after 10 min stimulation with 100 nmol/l insulin (closed bars) (n=5). D and E: Representative Western blots and quantification showing IRS-1 (D) or IRS-2 (E) protein expression in human skeletal muscle cells without insulin (open bars) or after 10 min stimulation with 100 nM insulin (closed bars) (n=5). *: p<0.05 versus no insulin condition; $: p<0.05 versus no insulin TNF-α condition; #: p<0.05 versus 100 nM insulin TNF-α condition as tested by ANOVA followed by Bonferroni post hoc test.*

CX3CL1 treatment prevents TNF-α action on mTOR, NFκB and ERK-1/2 in human primary skeletal muscle cells

The impact of CX3CL1 on TNF-α induced mTOR, NFκB (p65) and ERK-1/2 signaling was explored as these targets are implicated in the negative regulation of the insulin signaling cascade and of glucose uptake. Insulin increased mTOR and ERK-1/2 phosphorylation in the control condition and in cells treated with CX3CL1, whereas there was no impact on NFκB phosphorylation. TNF-α increased basal mTOR, NFκB and ERK-1/2 phosphorylation (Figure 3). CX3CL1 treatment had no effect on protein expression and/or phosphorylation of mTOR, NFκB and ERK1/2. Interestingly, cells pretreated with CX3CL1 were resistant to the impact of TNF-α on the phosphorylation of these proteins (Figure 3). mTOR protein expression was reduced in the cells pretreated to CX3CL1 and exposed to TNF-α (Figure 3A).

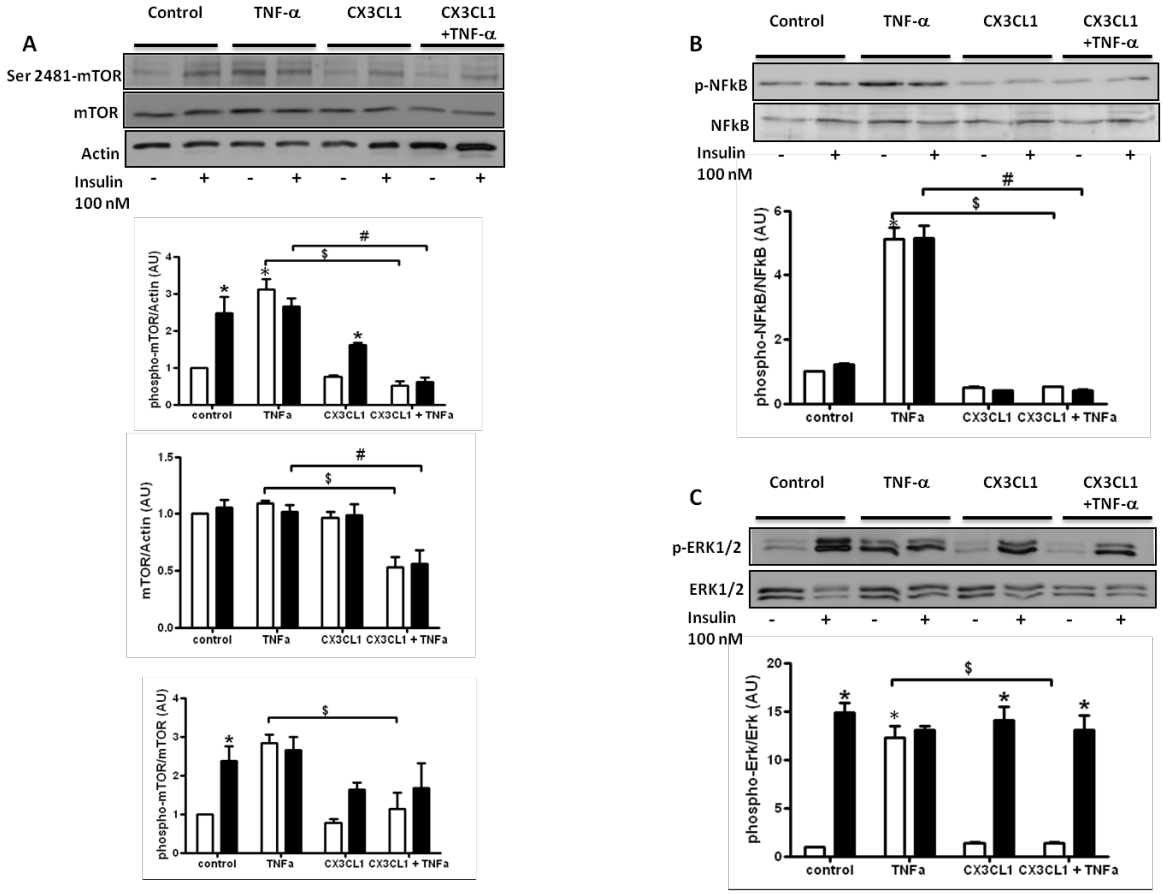

Figure 3: CX3CL1 treatment prevents TNF-α action on mTOR, NFκB and ERK-1/2 in human skeletal muscle cells: *A-C: Representative Western blots and quantifications showing mTOR Ser-2481 (A), NFκB (B) or ERK1/2 (C) phosphorylation in human skeletal muscle cells in response to CX3CL1 treatment (48 h, 25 ng/ml) and/or TNF-α (for the last 24 h, 20 ng/ml) without insulin (open bars) or after 10 min stimulation with 100 nmol/l insulin (closed bars) (n=5). *: p<0.05 versus no insulin condition; $: p<0.05 versus no insulin TNF-α condition; #: p<0.05 versus 100 nM insulin TNF-α condition as tested by ANOVA followed by Bonferroni post hoc test.*

CX3CL1 decreases human beta-cell apoptosis and alpha-cell glucagon secretion

Using immuno-staining and RNA sequencing, we report for the first time that CX3CL1 and its receptor CX3CR1 are differently expressed in human islets cells (Figure 4C and 4D). CX3CL1 is more expressed in the non-beta cell population (composed of 60% alpha-cells) than in beta-cells. As well, immunofluorescence staining of dispersed human islet cells, confirmed that CX3CL1 is present in both beta-cells and alpha-cells (Figure 4A and 4B). The receptor CX3CR1 is expressed in human beta-cells and in non-beta-cells, though at a lower level compared to the ligand (Figure 4C and 4D). To investigate the potential impact of CX3CL1 on human beta-cell survival, cell death was quantified using TUNEL assay on dispersed human islet cells. After 48 h treatment, CX3CL1 decreased human beta-cell apoptosis. This decrease in apoptosis was concentration dependent and could only be observed with 5 and 10 nM CX3CL1 (Figure 4E). When cell death of purified rat beta-cells cultured with CX3CL1 was quantified, no difference could be observed between the different concentrations and the control (Figure 4F). These results suggest that the positive impact of CX3CL1 on human beta-cells might be either species specific or mediated by the other islet cells that were present in the human dispersed islet cells population studied. We investigated also the impact of CX3CL1 on rat beta-cell proliferation (note that this was not possible using adult human beta cells since they do not replicate to any meaningful extent in vitro (Rutti et al., 2012). The replication was assessed by BrdU incorporation over 48 h. As for the survival, CX3CL1 did not affect rat beta-cell proliferation (Figure 4G).

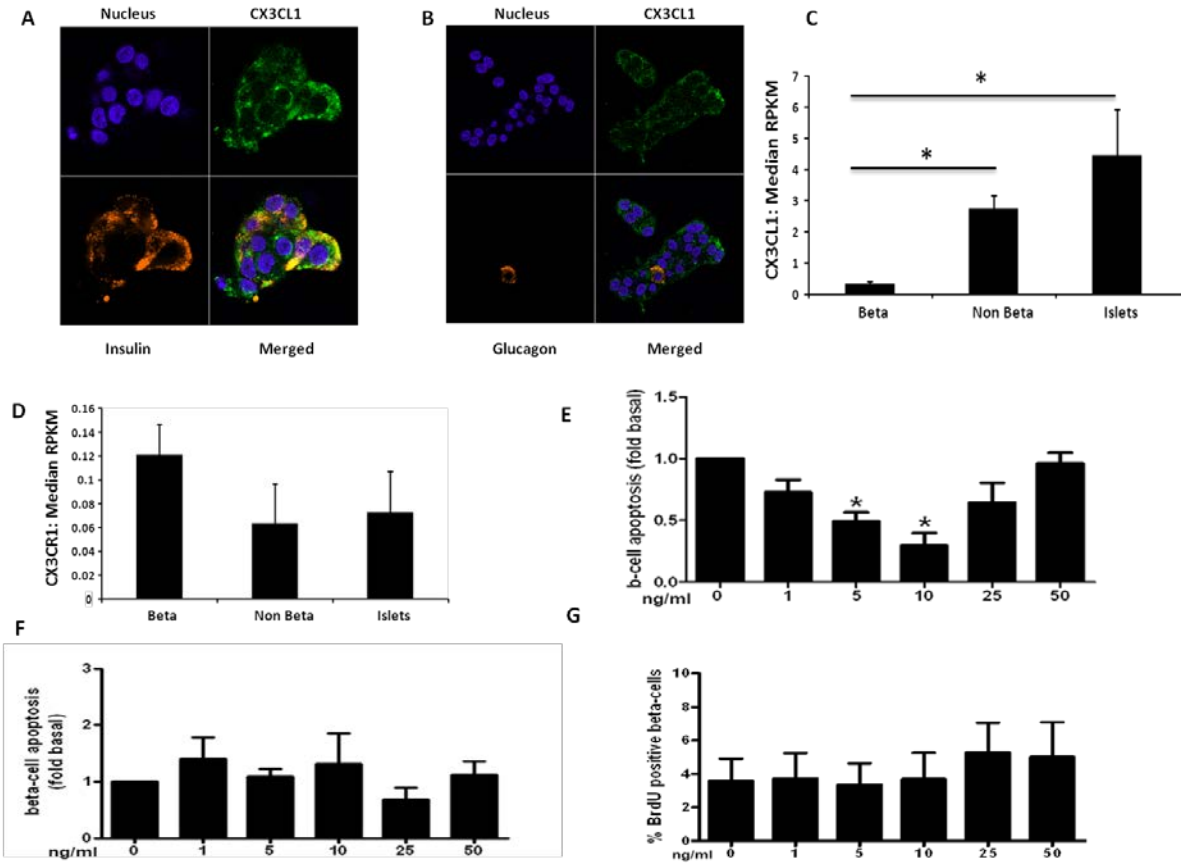

Figure 4: CX3CL1 and its receptor are expressed in human beta-cells and decreases beta-cell apoptosis*. A-B: Representative images of human non-sorted islet cells co-stained for CX3CL1 (red), insulin (A: green) or glucagon (B: green) and DAPI (blue). C: CX3CL1 mRNA expression in human islets (n=11), sorted beta-cells (n=6) and non beta-cells (n=6) presented as reads per kilobase per million mapped reads (RPKM). D: CX3CR1 mRNA expression in human islets (n=11), sorted beta-cells (n=6) and non beta-cells (n=6) presented as reads per kilobase per million mapped reads (RPKM). E: TUNEL-positive human beta-cells/total cells (n=3). Human islets were dispersed into single cells and cultured (not sorted) on 804G matrix-coated dishes for 48 h in the presence of increasing concentrations of CX3CL1. F: TUNEL-positive rat beta-cells/total cells (n=4). Sorted rat primary beta-cells were cultured on 804G matrix-coated dishes for 48 h in the presence of increasing concentrations of CX3CL1. G: BrdU-positive rat beta-cells. Sorted rat primary beta-cells were cultured on 804G matrix-coated dishes for 48 h in the presence of increasing concentrations of CX3CL1. Proliferation was measured by BrdU incorporation over 48 h (n=4). * p<0.05 as tested by ANOVA followed by Bonferroni post hoc test.*

We next analyzed the impact of increasing concentrations of CX3CL1 on human islet insulin and glucagon secretion and on purified rat beta-cell insulin secretion. Human islet insulin secretion as well as rat beta-cell insulin secretion was not influenced by the presence of CX3CL1, even if our highest concentration (50 ng/ml) seems to increase GSIS when compare to untreated cells (Control: 3.356 +/- 0.68 vs. CX3CL1: 4.557 +/-1.054 % of insulin content) it does not reach the statistical significance (Figure 5A and 5E). Total insulin content of human islets and of rat beta-cells was not affected by CX3CL1 (Figure 5B and 5F). In contrast, already low dose of CX3CL1 impaired human islet glucagon secretion (Figure 5C),

without affecting total glucagon content (Figure 5D), suggesting that CX3CL1 impacts directly on alpha-cells to decrease the amount of glucagon secreted in response to low glucose.

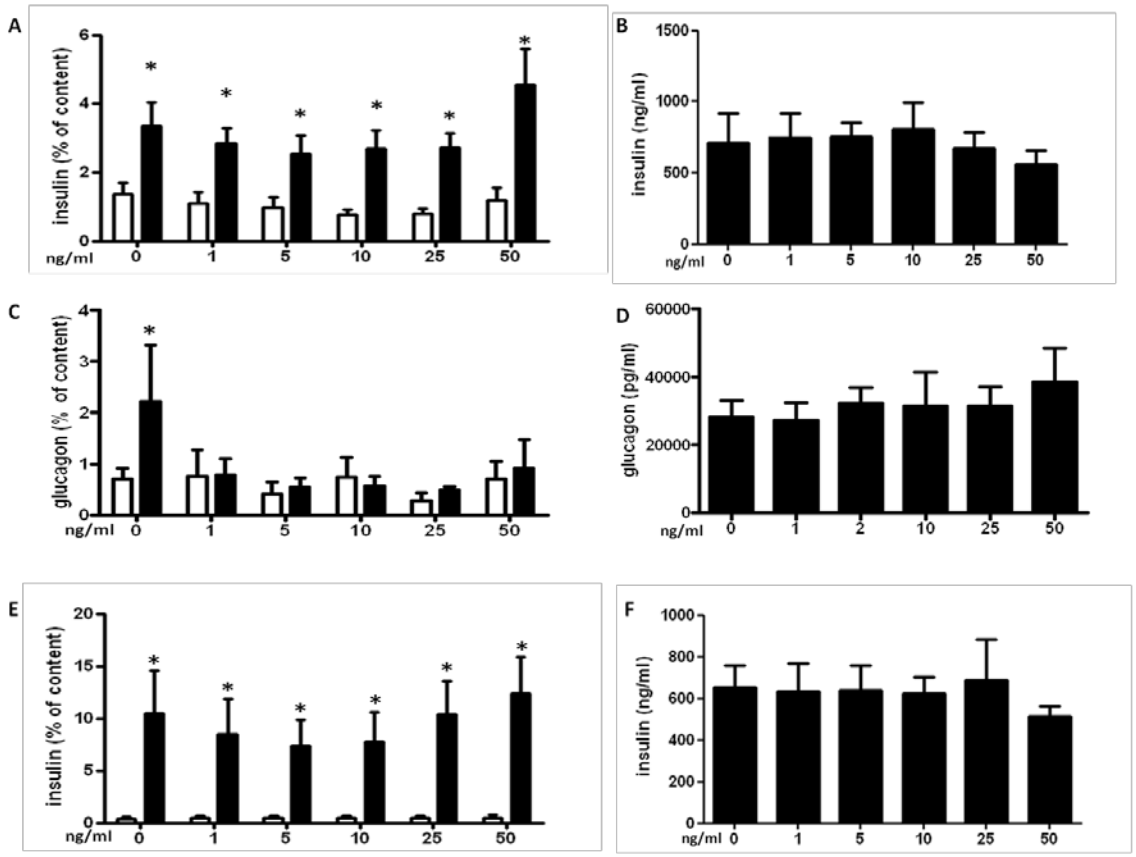

Figure 5: CX3CL1 decreases human islet glucagon secretion without affecting insulin secretion. *Human islets (A-D) and sorted rat primary beta-cells (E-F) were cultured for 48 h on 804G matrix-coated dishes in the presence of increasing concentrations of CX3CL1. A: Insulin secretion and B: Insulin content. Human islets were incubated for 60 min at 2.8 mmol/l glucose (open bars) followed by 60 min at 16.7 mmol/l glucose (closed bars) (n=8). C: Glucagon secretion and D: Glucagon content. Human islets were incubated for 60 min at 16.7 mmol/l glucose (open bars) followed by 60 min at 2.8 mmol/l glucose (closed bars) (n=5). E: Insulin and F: Insulin content. Rat sorted beta-cells were incubated for 60 min at 2.8 mmol/l glucose (open bars) followed by 60 min at 16.7 mmol/l glucose (closed bars) (n=5). F: Impact of CX3CL1 on rat beta-cells total (n=5). * $p<0.05$ as tested by ANOVA followed by Bonferroni post hoc test.*

CX3CL1 treatment prevents the impact of TNF-α on glucose-stimulated insulin secretion and the insulin signaling pathway in rat primary beta-cells.

The impact of CX3CL1 on glucose-stimulated insulin secretion (GSIS) was further investigated in primary rat sorted beta-cells following 24 h of treatment with TNF-α. In the basal condition (2.8 mM glucose) neither CX3CL1 (48 h pre-treatment) nor TNF-α (24 h pre-treatment) had an impact on insulin secretion, whereas TNF-α treatment dramatically reduced GSIS (16.7 mM glucose) and this was prevented by CX3CL1 (Figure 6A). As observed previously for TNF-α (Bouzakri et al., 2009), the total insulin content was not influenced by the different conditions (data not shown). We have shown that several proteins from the canonical insulin signaling pathway are involved in GSIS in primary beta-cells (Bouzakri et al., 2008). Therefore, we next explored the impact of CX3CL1 and/or TNF-α on Akt, AS160, IRS-1 and IRS-2 in the basal condition (2.8 mM glucose) or after glucose stimulation (16.7 mM glucose). In rat primary sorted beta-cells treated with TNF-α for 24 h, glucose action on Akt Ser473 and AS160 phosphorylation was completely prevented (Figure 6B-C). In contrast, in cells pretreated with CX3CL1, glucose-induced Akt and AS160 phosphorylation was unaltered by TNF-α exposure (Figure 6B-C). IRS-1 protein expression was unchanged by TNF-α or CX3CL1 exposure whereas its expression increased when cells were treated with TNF-α and CX3CL1 together (Figure 6D). IRS-2 protein expression was increased by 48 h CX3CL1 treatment. In that condition IRS-2 protein degradation induced by TNF-α was prevented (Figure 6E).

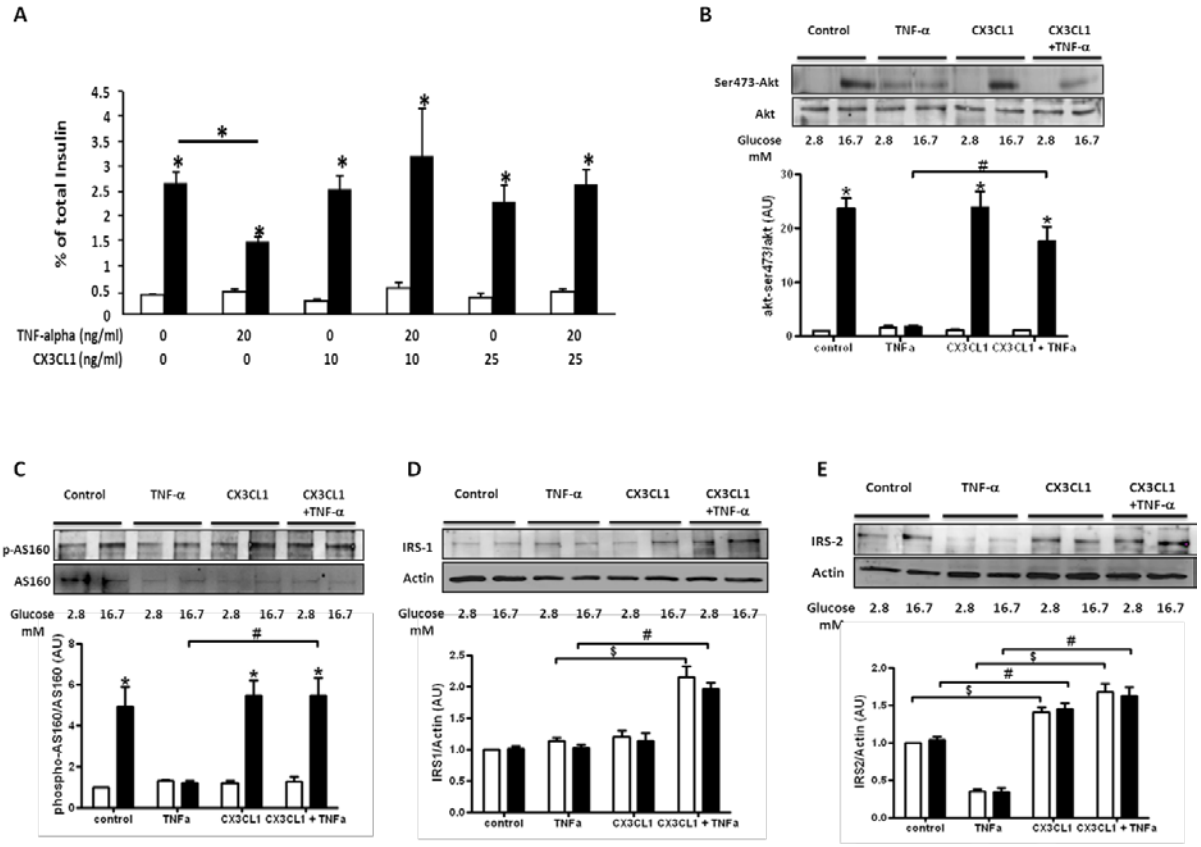

Figure 6: CX3CL1 treatment prevents the impact of TNF-α on glucose-stimulated insulin secretion and the insulin signaling pathway in rat primary beta-cells. *Rat primary beta-cells were cultured in the presence of CX3CL1 (48 h, 25 ng/ml) and/or TNF-α (for the last 24 h, 20 ng/ml) A: Insulin secretion measured for 60 min at 2.8 mmol/l glucose (open bars) followed by 60 min at 16.7 mmol/l glucose (closed bars) (n=5). B and C: Representative Western blots and quantifications showing Akt Ser-473 (B) or AS160 (C) phosphorylation at 2.8 mmol/l glucose (open bars) or after 60 min stimulation with 16.7 mmol/l glucose (closed bars) (n=5). D and E: Representative Western blots and quantifications showing IRS-1 (D) or IRS-2 (E) protein expression in rat primary beta-cells at 2.8 mmol/l glucose (open bars) or after 60 min stimulation with 16.7 mmol/l glucose (closed bars) (n=5). *: p<0.05 versus 2.8 mM glucose condition; $: p<0.05 versus 2.8 mM glucose TNF-α condition; #: p<0.05 versus 16.7 mM glucose TNF-α condition as tested by ANOVA followed by Bonferroni post hoc test.*

CX3CL1 treatment prevents TNF-α action on mTOR, and NFκB but has no effect on ERK-1/2 in primary sorted rat beta-cells.

Several pathways have been implicated in the negative impact of TNF-α on the insulin signaling pathway in beta-cells (Bouzakri and Zierath, 2007; Plomgaard et al., 2005). Therefore we have explored the impact of CX3CL1 in TNF-α induced mTOR, NFκB and ERK-1/2 signaling. Glucose stimulation increased mTOR, NFκB and ERK-1/2 phosphorylation in the control condition (Figure 7). TNF-α increased basal mTOR, NFκB and ERK-1/2 phosphorylation (Figure 7). In cells treated with CX3CL1, mTOR expression was reduced, glucose-induced mTOR and NFκB phosphorylation was prevented, whereas ERK-1/2

phosphorylation was increased (Figure 7). There was no change in total NFkB or ERK-1/2 (Figure 7B and 7C). As we observed in human skeletal muscle cells (Figure 3), primary rat beta-cells pre-treated with CX3CL1 were resistant to TNF-α action on the phosphorylation of mTOR and NFκB (Figure 7). Interestingly, CX3CL1 pretreatment had no impact on TNF-α induced ERK-1/2 phosphorylation (Figure 7C). mTOR protein expression was reduced in cells pretreated to CX3CL1 and exposed to TNF-α (Figure 7A).

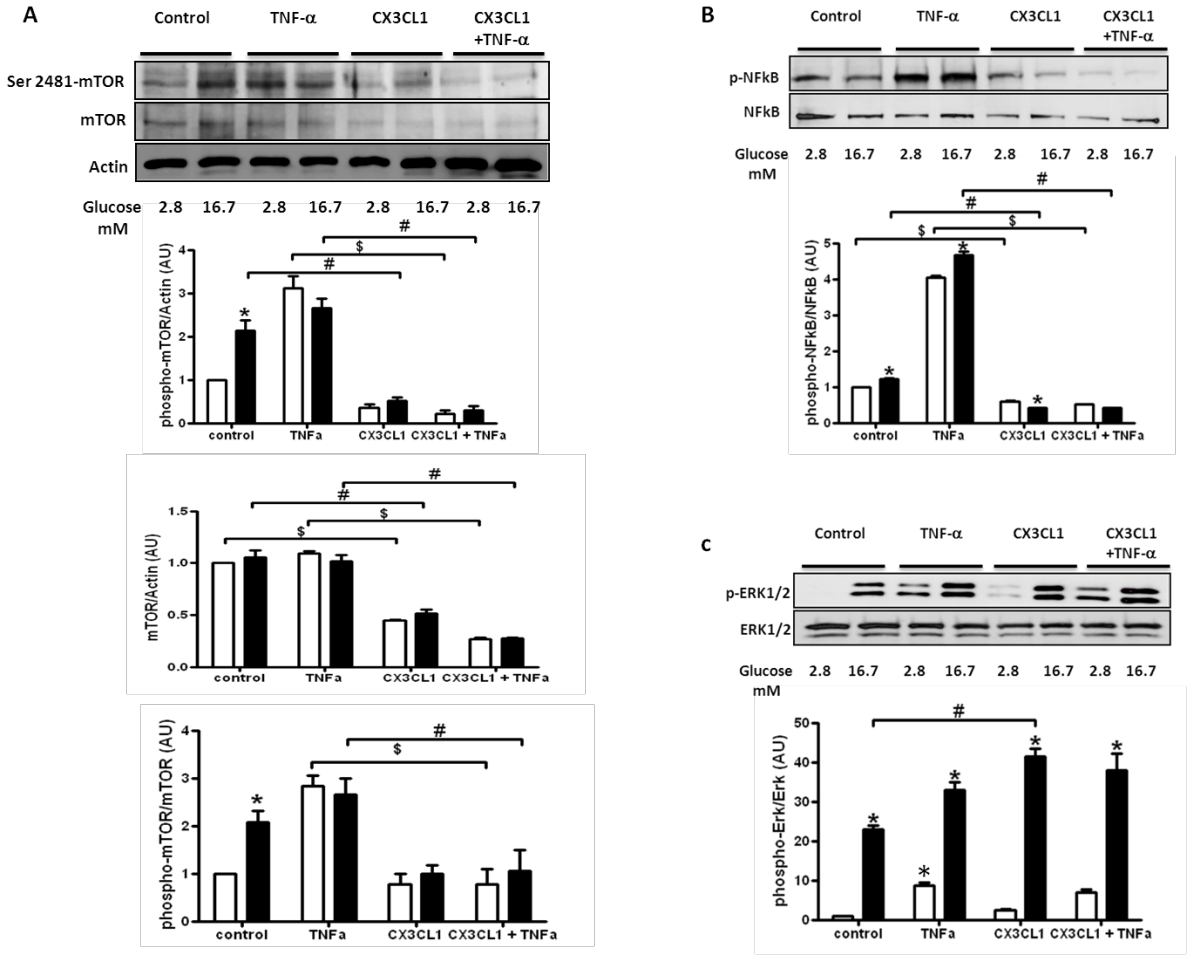

Figure 7: CX3CL1 treatment prevents TNF-α action on mTOR, and NFκB but not ERK-1/2 in primary sorted rat beta-cells. *A-C: Representative Western blots and quantifications showing mTOR Ser-2481 (A), NFkB (B) or ERK1/2 (C) phosphorylation in primary rat beta-cells in response to CX3CL1 (48 h, 25 ng/ml) and/or TNF-α treatment (for the last 24 h, 20 ng/ml) at 2.8 mmol/l glucose (open bars) or after 60 min stimulation with 16.7 mmol/l glucose (closed bars) (n=5). *: p<0.05 versus 2.8 mM glucose condition; $: p<0.05 versus 2.8 mM glucose TNF-α condition; #: p<0.05 versus 16.7 mM glucose TNF-α condition as tested by ANOVA followed by Bonferroni post hoc test.*

Discussion

Recently, we have shown that human skeletal muscle cells with different insulin sensitivity secrete different myokines, that have a bimodal impact on beta-cell insulin secretion, proliferation and survival (Bouzakri et al., 2011). The identification and functions of these

myokines remain a major goal of our studies. In our previous study, we found CX3CL1 as one of the major cytokines regulated by TNF-α in human skeletal muscle cells. Here, we have identified for the first time CX3CL1 as a myokine. We show, using healthy young volunteers that exercise up-regulates CX3CL1 mRNA expression in skeletal muscle biopsies and increases its serum concentration. In parallel, using the one leg exercising model, we have found that exercising skeletal muscles have a reduced level of CX3CL1 protein. Since this occurs within 2 hour of exercise, it is likely due to cleavage and shedding from muscle cells, in turning suggesting that Adam 10 and/or Adam 17 activity, the enzymes responsible for CX3CL1 cleavage, could be regulated by exercise. Moreover, we have shown that TNF-α infusion in healthy patient induces CX3CL1 up-regulation at the plasma level *in vivo*. Following on from these observations in human subjects, we studied the impact of CX3CL1 on primary human skeletal muscle cells, primary beta-cells and islets under basal conditions or after induction of insulin resistance by TNF-α treatment.

CX3CL1 is a unique member of the CX3C subclass of the chemokine superfamily and signals only via one receptor, which is a G protein-coupled receptor named CX3CR1 (Liu and Jiang, 2011). CX3CL1 is synthesized in a membrane-bound form and is processed by Adam 10 and Adam 17 at its exposed N-terminus to generate the soluble form (Haskell et al., 1999; Jones et al., 2010). CX3CL1 interacts with its receptor either bound to the membrane to facilitate cell-cell interaction and communication or in its cleaved soluble form to exert paracrine and endocrine effect on different tissues (Garton et al., 2001; Haskell et al., 1999; Hundhausen et al., 2003; Shah et al., 2011; Zernecke et al., 2008).

We first studied the potential autocrine impact of CX3CL1 in human primary skeletal muscle cells. CX3CL1 treatment (25 ng/ml; 48 h) induces an increase of basal glucose uptake and IRS-1 protein expression when compared to untreated cells. IRS-1 up regulation can explain the basal increase of glucose uptake following CX3CL1 treatment as we have demonstrated previously that IRS-1 controls glucose metabolism in skeletal muscle (Bouzakri et al., 2006). Our data indicate that CX3CL1 could be involved in part in the increase of glucose uptake observed during exercise (Egan and Zierath, 2013). Indeed, besides the increase of glucose uptake under basal condition, CX3CL1 increased AS160 phosphorylation. Several studies have demonstrated that AS160 is phosphorylated either by Akt after insulin stimulation or by AMPK after exercise (Long and Zierath, 2006). Therefore, CX3CL1 might impact on a different pathway, such as AMPK. However, further studies that are beyond the scope of the present study are necessary to address this. Surprisingly, human skeletal muscle cells

treated with CX3CL1 for 48 h were resistant to TNF-α induced insulin resistance. Moreover, CX3CL1 prevents the activation of mTOR, NFκB and ERK-1/2 that are known TNF-α targets implicated in the negative regulation of the insulin signaling cascade and glucose uptake (Bouzakri and Zierath, 2007; Plomgaard et al., 2005). The protective effect of CX3CL1 on skeletal muscle cells is supported by the literature, where different studies have shown that mutations on CX3CR1 are associated with an increase of T2D and metabolic syndrome (Shah et al., 2011; Sirois-Gagnon et al., 2011). In these patients, CX3CL1 affinity with its receptor was diminished, which is in line with the beneficial function of CX3CL1/CX3CR1 observed in our study. Nevertheless, CX3CL1 levels are increased in T2D patients, who are insulin resistant by definition (Shah et al., 2011). We have to mention here that our study involved exposure of skeletal muscle cells to CX3CL1 for a relatively short period of time (48 h), whereas the increase of CX3CL1 in T2D patients is chronic. Our hypothesis is that T2D patients develop a CX3CL1 resistance as observed for IL-6 (Jiang et al., 2013; Raschke and Eckel, 2013; Scheele et al., 2012). Moreover, T2D is characterized by low-grade systemic inflammation with the up-regulation of several known and yet unknown cytokines which can probably perhaps interact with the CX3CL1/CX3CR1 pathway (Dandona et al., 2004).

CX3CL1 can exert an endocrine effect on different tissues (Garton et al., 2001; Haskell et al., 1999; Hundhausen et al., 2003; Shah et al., 2011; Zernecke et al., 2008). The main propose of our ongoing work is to identify myokines which can impact on pancreatic beta-cells. Therefore we have tested the impact of CX3CL1 on islet cells under control condition or after TNF-α treatment, shown previously to decrease GSIS (Bouzakri et al., 2009). We have shown, using RNA sequencing in human islet cells and sorted beta-cells, that CX3CL1 is expressed in islet cells with a higher level in non-beta-cells compared to beta-cells. CX3CR1 receptor mRNA is expressed at comparable levels in all islet cells. Our data extend previous findings by others showing by immunofluorescence that CX3CL1 and its receptor are expressed in human beta cells (Lee et al., 2013). CX3CR1 RNA is expressed at comparable but extremely low levels in (non-sorted) human islet cells, and sorted beta cells or non-beta cells. Perhaps these low levels in alpha cells prevented detection of the receptor protein by immunofluorescence in the earlier study (Lee et al., 2013). Nevertheless, using lower concentrations than the one used by Lee et al (Lee et al., 2013) (1-50 ng/ml vs. 100 ng/ml), CX3CL1 did not potentiate GSIS in human islets or rat sorted beta-cells. In agreement with their findings, we also conclude that CX3CL1 is not a direct insulin secretagogue as it does not impact insulin secretion under low glucose concentration. Nevertheless, in our experimental condition (islets cells on extra cellular matrix, and 48 h CX3CL1 stimulation

and lower concentration) we found a small but not significant impact of CX3CL1 on GSIS Interestingly, CX3CL1 treatment blocks low glucose stimulation of glucagon secretion. This effect can be seen as a feedback loop regulation of glucagon secretion during and after exercise. Indeed, glucagon levels increase during exercise in order to stimulate hepatic glucose production and decrease rapidly after the training period (Wasserman et al., 1989a; Wasserman et al., 1989b) similarly to what we observed with CX3CL1 treatment.

As we have observed in human skeletal muscle cells, CX3CL1 treatment protects sorted beta-cells from the effect of TNF-α. Our data are in agreement with the improvement of glucose tolerance in mice injected with CX3CL1 and the results obtained in mice lacking CX3CR1 (Lee et al., 2013). However, we have demonstrated that the protective effect of CX3CL1 against TNF-α was lost when beta-cells were exposed to IL-1□, Interferon-□and TNF-α (data not shown). Despite our hypothesis of CX3CL1 resistance in T2D, our data could explain in part why an increase in CX3CL1 is not sufficient to protect beta-cell mass and function in T2D patients as a cytokine mixture abolishes the protecting impact of CX3CL1.

Taken together, our data demonstrate that CX3CL1 is a new myokine regulated by exercise and TNF-α infusion in human. Moreover, our study demonstrates that CX3CL1 takes part in the physiological process of exercise and is a protective factor against the adverse effects of TNF-α on skeletal muscle insulin sensitivity and beta-cell GSIS, suggesting a specific interaction between TNF-α and CX3CL1 signaling pathways. CX3CL1-based therapy could be a potential approach to prevent insulin resistance and beta-cell dysfunction in T2D.

Experimental Procedures

Human experimental studies

Bicycling exercise: 5 healthy males performed an exercise bout consisting of 3 h of bicycling. The study has previously been published in Hansen et al (trial 1), where a detailed description of the protocol is presented (Hansen et al., 2011). The obtained EDTA plasma samples were stored at -80 degrees until analysed.

One-legged knee exercise: 9 healthy males performed 2 h of one-legged knee extensor exercise. The study has previously been published and described in detail (trial 4) (Hansen et al., 2011). Biopsies were obtained from the skeletal muscle of both resting and exercising legs prior, immediately after exercise, and 3, and 24 h, into recovery after exercise. Total RNA was extracted and qPCR performed as previously described (Hansen et al.). The primer sequences for CX3CL1 were predesigned from Applied Biosystems (cat. No.: Hs00171086_m1).

TNF-α infusion in human volunteers: 10 healthy males received an intravenous infusion of human recombinant TNF-α for 4 h or placebo on two separate days. The study has previously been published (Plomgaard et al., 2008).

Plasma CX3CL1 measurement: Plasma CX3CL1 was measured using the Quantikine Human CX3CL1/CX3CL1 Immunoassay cat. no.: DCX310 from R&D Systems Inc. Minneapolis, USA. Samples were run in duplicates inter- and intra CV < 5%.

Human skeletal muscle cells

Human skeletal muscle cells isolated from muscle biopsies by trypsin digestion, were grown to confluent myoblasts, and then differentiated into myotubes as previously described (Bouzakri et al., 2003). Glucose uptake and western blots were performed as previously described for primary human muscle cells (Bouzakri et al., 2003).

Human islets and sorted beta-cells

Human islets were provided by the Islet Cell Resource Centers of Milan (Italy) and Geneva (Switzerland) with support from the Juvenile Diabetes Research Foundation (JDRF) European islet distribution program. Human beta-cells were sorted by FACS after labelling with Newport Green using a FACSVantage (Becton Dickinson, USA) as described before (Parnaud et al., 2008).

RNA extraction, Library preparation and sequencing and read mapping

Sorted beta-cells and islets were centrifuged, the supernatant was removed and the pellet disrupted in RLT buffer (RNeasy, Qiagen, Valencia, CA). Total RNA was prepared according to the standard RNeasy protocol. Total RNA and genomic DNA libraries were constructed

following customary Illumina TruSeq protocols for next-generation sequencing, as described elsewhere (Nica et al., Genome Research in press). Paired-end reads were mapped to the human genome (assembly version GRCh37/hg19) using BWA and allowing a maximum insert size of 500 kb (for instances when not enough good alignments could be used to infer the insert size distribution). RNA-seq reads were subsequently filtered for correct orientation of the mapped mate pairs with an insert size < 500 kb and a minimum mapping quality score of 10. **Immunofluorescence**

CX3CL1 and CX3CR1 were detected with specific antibodies according to standard procedures for fixation and confocal fluorescence microscopic observation (Tomas et al 2010).

Insulin secretion

Acute insulin release was measured as previously described (Bouzakri et al., 2009).

Detection of apoptosis and proliferation

Cell death was measured by TUNEL assay and proliferation was assessed by BrdU incorporation (Bouzakri et al., 2009).

Rat sorted beta-cells

Islets of Langerhans were isolated by collagenase digestion of pancreas from adult male Wistar rats followed by Ficoll (Histopaque-1077, Sigma-Aldrich, St. Louis, MO) purification (Rouillet et al). Rat beta-cells were sorted to measure insulin secretion, apoptosis, proliferation and western blot as previously described (Bouzakri et al., 2009).

Acknowledgments

Human islets were kindly provided by the Islet for Basic Research program through the European Consortium for Islet Transplantation, supported by the Juvenile Diabetes Research Foundation (JDRF award 31-2008-413). This work was supported by the Swiss National Science Foundation (Grant No. 31-135645 to KB). We thank Melanie Cornut, Katharina Rickenbach and Stéphane Dupuis for expert technical assistance.

References

Aoyama, T., Inokuchi, S., Brenner, D.A., and Seki, E. (2010). CX3CL1-CX3CR1 interaction prevents carbon tetrachloride-induced liver inflammation and fibrosis in mice. Hepatology *52*, 1390-1400.

Bergman, M. (2013). Pathophysiology of prediabetes and treatment implications for the prevention of type 2 diabetes mellitus. Endocrine *43*, 504-513.

Bouzakri, K., Plomgaard, P., Berney, T., Donath, M.Y., Pedersen, B.K., and Halban, P.A. (2011). Bimodal effect on pancreatic beta-cells of secretory products from normal or insulin-resistant human skeletal muscle. Diabetes *60*, 1111-1121.

Bouzakri, K., Ribaux, P., and Halban, P.A. (2009). Silencing mitogen-activated protein 4 kinase 4 (MAP4K4) protects beta-cells from TNF-alpha induced decrease of IRS2 and inhibition of glucose-stimulated insulin secretion. J Biol Chem.

Bouzakri, K., Ribaux, P., Tomas, A., Parnaud, G., Rickenbach, K., and Halban, P.A. (2008). Rab GTPase-activating protein AS160 is a major downstream effector of protein kinase B/Akt signaling in pancreatic beta-cells. Diabetes *57*, 1195-1204.

Bouzakri, K., Roques, M., Gual, P., Espinosa, S., Guebre-Egziabher, F., Riou, J.P., Laville, M., Le Marchand-Brustel, Y., Tanti, J.F., and Vidal, H. (2003). Reduced activation of phosphatidylinositol-3 kinase and increased serine 636 phosphorylation of insulin receptor substrate-1 in primary culture of skeletal muscle cells from patients with type 2 diabetes. Diabetes *52*, 1319-1325.

Bouzakri, K., Zachrisson, A., Al-Khalili, L., Zhang, B.B., Koistinen, H.A., Krook, A., and Zierath, J.R. (2006). siRNA-based gene silencing reveals specialized roles of IRS-1/Akt2 and IRS-2/Akt1 in glucose and lipid metabolism in human skeletal muscle. Cell Metab *4*, 89-96.

Bouzakri, K., and Zierath, J.R. (2007). MAP4K4 gene silencing in human skeletal muscle prevents tumor necrosis factor-alpha-induced insulin resistance. J Biol Chem *282*, 7783-7789.

Cardona, A.E., Pioro, E.P., Sasse, M.E., Kostenko, V., Cardona, S.M., Dijkstra, I.M., Huang, D., Kidd, G., Dombrowski, S., Dutta, R., et al. (2006). Control of microglial neurotoxicity by the fractalkine receptor. Nat Neurosci *9*, 917-924.

Dandona, P., Aljada, A., and Bandyopadhyay, A. (2004). Inflammation: the link between insulin resistance, obesity and diabetes. Trends in immunology *25*, 4-7.

Egan, B., and Zierath, J.R. (2013). Exercise metabolism and the molecular regulation of skeletal muscle adaptation. Cell Metab *17*, 162-184.

Garton, K.J., Gough, P.J., Blobel, C.P., Murphy, G., Greaves, D.R., Dempsey, P.J., and Raines, E.W. (2001). Tumor necrosis factor-alpha-converting enzyme (ADAM17) mediates the cleavage and shedding of fractalkine (CX3CL1). J Biol Chem *276*, 37993-38001.

Handschin, C., Choi, C.S., Chin, S., Kim, S., Kawamori, D., Kurpad, A.J., Neubauer, N., Hu, J., Mootha, V.K., Kim, Y.B., et al. (2007). Abnormal glucose homeostasis in skeletal muscle-specific PGC-1alpha knockout mice reveals skeletal muscle-pancreatic beta cell crosstalk. J Clin Invest *117*, 3463-3474.

Hansen, J., Brandt, C., Nielsen, A.R., Hojman, P., Whitham, M., Febbraio, M.A., Pedersen, B.K., and Plomgaard, P. (2011). Exercise induces a marked increase in plasma follistatin: evidence that follistatin is a contraction-induced hepatokine. Endocrinology *152*, 164-171.

Haskell, C.A., Cleary, M.D., and Charo, I.F. (1999). Molecular uncoupling of fractalkine-mediated cell adhesion and signal transduction. Rapid flow arrest of CX3CR1-expressing cells is independent of G-protein activation. J Biol Chem *274*, 10053-10058.

Hundhausen, C., Misztela, D., Berkhout, T.A., Broadway, N., Saftig, P., Reiss, K., Hartmann, D., Fahrenholz, F., Postina, R., Matthews, V., et al. (2003). The disintegrin-like metalloproteinase ADAM10 is involved in constitutive cleavage of CX3CL1 (fractalkine) and regulates CX3CL1-mediated cell-cell adhesion. Blood *102*, 1186-1195.

Jiang, L.Q., Duque-Guimaraes, D.E., Machado, U.F., Zierath, J.R., and Krook, A. (2013). Altered response of skeletal muscle to IL-6 in type 2 diabetic patients. Diabetes *62*, 355-361.

Jones, B.A., Beamer, M., and Ahmed, S. (2010). Fractalkine/CX3CL1: a potential new target for inflammatory diseases. Molecular interventions *10*, 263-270.

Lee, Y.S., Morinaga, H., Kim, J.J., Lagakos, W., Taylor, S., Keshwani, M., Perkins, G., Dong, H., Kayali, A.G., Sweet, I.R., et al. (2013). The fractalkine/CX3CR1 system regulates beta cell function and insulin secretion. Cell *153*, 413-425.

Liu, H., and Jiang, D. (2011). Fractalkine/CX3CR1 and atherosclerosis. Clin Chim Acta *412*, 1180-1186.

Long, Y.C., and Zierath, J.R. (2006). AMP-activated protein kinase signaling in metabolic regulation. J Clin Invest *116*, 1776-1783.

Muller, W.A., Faloona, G.R., Aguilar-Parada, E., and Unger, R.H. (1970). Abnormal alpha-cell function in diabetes. Response to carbohydrate and protein ingestion. N Engl J Med *283*, 109-115.

Navarro-Gonzalez, J.F., Mora-Fernandez, C., Muros de Fuentes, M., and Garcia-Perez, J. (2011). Inflammatory molecules and pathways in the pathogenesis of diabetic nephropathy. Nature reviews. Nephrology *7*, 327-340.

Parnaud, G., Bosco, D., Berney, T., Pattou, F., Kerr-Conte, J., Donath, M.Y., Bruun, C., Mandrup-Poulsen, T., Billestrup, N., and Halban, P.A. (2008). Proliferation of sorted human and rat beta cells. Diabetologia *51*, 91-100.

Pedersen, B.K., and Febbraio, M.A. (2012). Muscles, exercise and obesity: skeletal muscle as a secretory organ. Nat Rev Endocrinol *8*, 457-465.

Pedersen, B.K., Steensberg, A., Fischer, C., Keller, C., Keller, P., Plomgaard, P., Wolsk-Petersen, E., and Febbraio, M. (2004). The metabolic role of IL-6 produced during exercise: is IL-6 an exercise factor? Proc Nutr Soc *63*, 263-267.

Pedersen, B.K., Steensberg, A., and Schjerling, P. (2001). Muscle-derived interleukin-6: possible biological effects. J Physiol *536*, 329-337.

Plomgaard, P., Bouzakri, K., Krogh-Madsen, R., Mittendorfer, B., Zierath, J.R., and Pedersen, B.K. (2005). Tumor necrosis factor-alpha induces skeletal muscle insulin resistance in healthy human subjects via inhibition of Akt substrate 160 phosphorylation. Diabetes *54*, 2939-2945.

Plomgaard, P., Fischer, C.P., Ibfelt, T., Pedersen, B.K., and van Hall, G. (2008). Tumor necrosis factor-alpha modulates human in vivo lipolysis. J Clin Endocrinol Metab *93*, 543-549.

Plomgaard, P., Halban, P.A., and Bouzakri, K. (2012). Bimodal impact of skeletal muscle on pancreatic beta-cell function in health and disease. Diabetes Obes Metab *14 Suppl 3*, 78-84.

Raschke, S., and Eckel, J. (2013). Adipo-myokines: two sides of the same coin-mediators of inflammation and mediators of exercise. Mediators Inflamm *2013*, 320724.

Rutti, S., Sauter, N.S., Bouzakri, K., Prazak, R., Halban, P.A., and Donath, M.Y. (2012). In vitro proliferation of adult human beta-cells. PLoS One *7*, e35801.

Scheele, C., Nielsen, S., Kelly, M., Broholm, C., Nielsen, A.R., Taudorf, S., Pedersen, M., Fischer, C.P., and Pedersen, B.K. (2012). Satellite cells derived from obese humans with type 2 diabetes and differentiated into myocytes in vitro exhibit abnormal response to IL-6. PLoS One *7*, e39657.

Shah, R., Hinkle, C.C., Ferguson, J.F., Mehta, N.N., Li, M., Qu, L., Lu, Y., Putt, M.E., Ahima, R.S., and Reilly, M.P. (2011). Fractalkine is a novel human adipochemokine associated with type 2 diabetes. Diabetes *60*, 1512-1518.

Sirois-Gagnon, D., Chamberland, A., Perron, S., Brisson, D., Gaudet, D., and Laprise, C. (2011). Association of common polymorphisms in the fractalkine receptor (CX3CR1) with obesity. Obesity (Silver Spring) *19*, 222-227.

Turner, S.L., Mangnall, D., Bird, N.C., Blair-Zajdel, M.E., and Bunning, R.A. (2010). Effects of pro-inflammatory cytokines on the production of soluble fractalkine and ADAM17 by HepG2 cells. Journal of gastrointestinal and liver diseases : JGLD *19*, 265-271.

Wasserman, D.H., Lacy, D.B., Goldstein, R.E., Williams, P.E., and Cherrington, A.D. (1989a). Exercise-induced fall in insulin and increase in fat metabolism during prolonged muscular work. Diabetes *38*, 484-490.

Wasserman, D.H., Spalding, J.A., Lacy, D.B., Colburn, C.A., Goldstein, R.E., and Cherrington, A.D. (1989b). Glucagon is a primary controller of hepatic glycogenolysis and gluconeogenesis during muscular work. Am J Physiol *257*, E108-117.

Wijesekara, N., Krishnamurthy, M., Bhattacharjee, A., Suhail, A., Sweeney, G., and Wheeler, M.B. (2010). Adiponectin-induced ERK and Akt Phosphorylation Protects against Pancreatic Beta Cell Apoptosis and Increases Insulin Gene Expression and Secretion. J Biol Chem *285*, 33623-33631.

Zernecke, A., Shagdarsuren, E., and Weber, C. (2008). Chemokines in atherosclerosis: an update. Arterioscler Thromb Vasc Biol *28*, 1897-1908.

Appendix B

Micro-patterning topology on soft substrates affects myoblasts proliferation and differentiation

Susi Zatti[a,b], *Alice Zoso*[a,b], *Elena Serena*[a,b], *Camilla Luni*[a], *Elisa Cimetta*[a] *and Nicola Elvassore*[a,b,*]

[a] Department of Industrial Engineering, University of Padova, via Marzolo 9, 35131 Padova, Italy.

[b] Venetian Institute of Molecular Medicine (VIMM), via Orus 2, 35129 Padova, Italy.

* Author to whom correspondence should be addressed. Tel.: +39 049 827 5469 Fax: +39 049 827 5461 E-mail address: nicola.elvassore@unipd.it

Langmuir

Volume 28 (2012), pagg. 2718 – 2726

dx.doi.org/10.1021/la204776e

Abstract

Micro-patterning techniques and substrate engineering are becoming useful tools to investigate several aspects of cell-cell interaction biology. In this work, we rationally study how different micro-patterning geometries can affect myoblast behavior in the early stage of in vitro myogenesis. Soft hydrogels with physiological elastic modulus (E = 15 kPa) were micro-patterned in parallel lanes (100, 300 and 500 μm width) resulting in different local and global myoblast densities. Proliferation and differentiation into multinucleated myotubes were evaluated for murine and human myoblasts. Wider lanes showed a decrease in murine myoblast proliferation: (69 ± 8) % in 100 μm wide lanes compared to (39 ± 7) % in 500 μm lanes. Conversely, fusion index increased in wider lanes: from (46 ± 7) % to (66 ± 7) % for murine myoblasts, and from (15 ± 3) % to (36 ± 2) % for human primary myoblasts, using a patterning width of 100 and 500 μm respectively. These results are consistent with both computational modeling data and conditioned medium experiments, which demonstrated that wider lanes favor the accumulation of endogenous secreted factors. Interestingly, human primary myoblast proliferation is not affected by patterning width, which may be because the high-serum content of their culture medium overrides the effect of secreted factors.

These data highlight the role of micro-patterning in shaping the cellular niche through secreted factor accumulation and are of paramount importance in rationally understanding myogenesis *in vitro* for the correct design of *in vitro* skeletal muscle models.

KEYWORDS: stiffness, hydrogel; micro-contact printing; pattern geometry; laminin; micro-environment; myogenesis.

Introduction

The realization of functionally-differentiated skeletal muscle *in vitro* is one of the major challenges in tissue engineering and regenerative medicine[1]. Engineered substitutes for skeletal muscle tissue hold promise for the *in vivo* treatment of a variety of muscle defects and diseases[2]. Furthermore, micro-engineered muscles could represent a powerful tool suitable for the investigation of complex physiological processes[3], for drug-screening applications[4] and for testing new gene and cell therapy approaches, lowering the costs and time required to develop widely available personalized treatments for larger numbers of patients[5]. Knowing the factors that influence myogenesis *in vitro* is of paramount importance in order to engineer a skeletal muscle tissue.

In vivo skeletal muscle development is a process characterized by a defined series of events that includes myoblast proliferation, alignment and fusion into multinucleated myotubes[6], and their further differentiation into functional myofibers[7]. Simulating myogenesis *in vitro* requires the consideration of several key factors: cell-cell interaction, extracellular matrix composition and architecture, mechanotransduction signals, medium composition and electrical stimulation[7,8]. Early studies demonstrated that myoblasts need to interact with their fusion partner cells to differentiate into myotubes[9]. This interaction could occur either by direct contact of neighboring cell membrane proteins (such as members of the cadherin family and Ig superfamily)[10], or mediated by myokines[6], which are soluble factors secreted by myoblasts and acting in an auto/paracrine manner. To our knowledge, an experimental investigation of how these two aspects individually affect myogenesis has not yet been reported. Direct cell-cell interaction could be relatively simple to study, by changing myoblast density in culture, whereas the effect of secreted soluble factors may be more experimentally complex to investigate, because it requires a fine control of the cell culture topology and of the local accumulation of secreted soluble factors.

However, notwithstanding this experimental complexity, it is well-known that myokines maintain a balance between growth and differentiation of muscle cells[6]. A recent work by Griffin[11] demonstrated by quantitative proteomics approaches that a large number of chemokines, chemokine receptors and signaling molecules are expressed *in vitro* by muscle cells. This recent result shows that these endogenous secreted proteins may have a greater role in influencing the extracellular milieu and in myogenesis than previously appreciated[11]. On the other hand, besides myoblast-secreted factors, the extracellular soluble environment also includes exogenous mitogens from the serum fraction of the culture medium that normally promote proliferation and act as inhibitors of myogenic differentiation via the down-regulation of myogenic determination factors[12,13,14,15].

In order to decouple the effect of the cell-cell contact from the secretoma-derived auto/paracrine signaling on early myogenesis *in vitro*, we envisioned controlling cell topology and cell pattern by independently changing the local cell density (and, consequently, the cell-cell contact probability) and the size of the cell cluster which may influence the local accumulation of soluble secreted factors.

In this scenario, micro-technologies can be a powerful tool in studying the role of myoblasts soluble niche in myogenesis *in vitro*. Currently, recent works investigating myoblasts topology and myogenesis were either focused on the effect of substrate stiffness[16], on the effect of different topology geometries[17] or on the elongation of C2C12 myoblasts in 3D micro-channels[18]. However, experimental evidence, which isolates the role of myoblasts secreted factors from all other phenomena, has not yet been reported.

Therefore, in this work we aimed at studying the effects of myokines accumulation produced by myoblasts, on their proliferation and differentiation. We exploited micro-patterning techniques to organize myoblasts in parallel lanes of increasing width and inter-spacing size. We used a permeable and soft culture substrate. In particular, a permeable substrate absorbs cell secreted molecules, enhancing the local accumulation of secreted factors, whereas a soft substrate with a physiological elastic modulus (15 kPa) promotes skeletal muscle functional differentiation, in terms of sarcomeric striations of myotubes, and skeletal muscle stem cell self-renewal in culture[19,16,20].

The patterned geometries have been designed in order to change local and global cell density. We defined the local cell density as the specific number of cells within the micro-patterned area and it refers to the cell density at local level. The global cell density is defined as the ratio between the number of counted cells and the total area (which is the area including both micro-patterned lanes and inter-spacing). This parameter refers to the overall cell density of the whole culture surface. In this way we could rationally investigate how the imposed micropattern constraints could be associated with an accumulation, at local level, of cell secreted factors produced by cells and how they could compete with the exogenous mitogens provided by medium.

2. Experimental Methods

2.1. Cell culture

2.1.1. C2C12 cultures expansion

The murine skeletal muscle immortalized cell line C2C12 (ATCC) was expanded in standard conditions with proliferation medium: Dulbecco's modified Eagle's medium (DMEM, Sigma-Aldrich) supplemented with 10% foetal bovine serum (FBS, Gibco-Invitrogen) and 1% Penicillin-Streptomycin mix solution (Gibco-Invitrogen). C2C12 were induced to form myotubes in differentiating medium: DMEM supplemented with 2% horse serum (Gibco-Invitrogen) and 1% Penicillin-Streptomycin mix solution.

2.1.2. Human primary myoblasts cultures expansion

Human primary myoblasts were provided by the ''Telethon BioBank'' (Telethon Research Service, Istituto Nazionale Neurologico ''Carlo Besta'', Milano, Italy). Myoblasts were expanded with proliferation medium: 60% High-Glucose Dulbecco's Modified Eagle's Medium (DMEM Glutamax, Gibco-Invitrogen), 20% Medium M199 (Sigma-Aldrich), 20% foetal bovine serum (FBS, Gibco-Invitrogen), 10 ng/ml EGF (PeproTech), 2 ng/ml β-FGF (PeproTech), 10 μg/ml insulin (insulin from bovine pancreas, Sigma-Aldrich) and 1% Penicillin-Streptomycin-Glutamine mix solution (Invitrogen); on standard 100 mm tissue culture Petri dishes previously coated with 0.5% gelatin solution (gelatin from porcine skin, Sigma-Aldrich). Human primary myoblasts were induced to form myotubes in differentiating medium: 98% DMEM Glutamax, 2% horse serum (Gibco-Invitrogen), 30 mg/mL insulin and 1% Penicillin-Streptomycin-Glutamine mix solution.

2.2. Micro-structured culture engineering

2.2.1. Hydrogel film preparation

Micro-contact printing of adhesion proteins was performed onto the non-fouling surface of poly-acrylamide hydrogel films with an average thickness of 100 μm, which elastic modulus (15,00 ± 0,75 kPa) reproduces the stiffness of native skeletal muscle[19]. Hydrogel films were prepared as previously described[16] on chemically modified glass slides 25 mm in diameter. Briefly, 20 μl of the liquid prepolymer solution, composed of Acrylamide/bisacrylamide 29:1 40% solution (Sigma-Aldrich) diluted in phosphate-buffered saline (PBS, Gibco-Invitrogen) to the final concentration of 10% and supplemented with 20 mg/ml photoinitiator (Irgacure 2959; Ciba Specialty Chemicals), was polymerized by UV light exposure for 3 min (high-pressure mercury vapor lamp (Philips HPR 125 W) emitting at 365 nm. Glass slides with

covalently bound hydrogel films were immersed in ultra-pure distilled water for 48 h to ensure complete removal of the un-reacted monomeric units or photoinitiator. After rinsing with ultra-pure distilled water, hydrogels were allowed to dry completely for 1 h and then sterilized by exposure to UV light for 20 minutes under a sterile hood.

2.2.2. Micro-contact printing

A micro-pattern of adhesion proteins was performed onto the hydrogels surface as previously described using an elastomeric PDMS stamp reproducing the desired geometry in relief[16,21]. Briefly, the PDMS stamp was inked in the protein solution (mouse-laminin 100 µg/ml in PBS, Sigma-Aldrich) for a few seconds and the excess solution was removed. Conformal contact between the dry hydrogel surface and the stamp was then achieved by applying a gentle pressure, thus transferring the protein micro-pattern onto the substrate. Micro-contact printed hydrogels were then transferred into 35 mm Petri dishes for cell seeding.

2.2.3. Cell seeding and culture maintenance

Two different seeding densities were used: 200 cell/mm^2 (low seeding density) and 400 cell/mm^2 (high seeding density) (Table 1). 300 µL of cell suspension were dropped over the hydrogel and cells were allowed to adhere overnight to the laminin micro-pattern. The day after, 3 ml of proliferation medium were gently added and then cultures were kept in a 95% humidified and 5% CO_2 atmosphere at 37°C. After 2 days under proliferating conditions, cultures were used for BrdU pulse and chase analyses or switched to differentiating condition with the appropriate medium. Proliferation data reported in Table 1 were evaluated 48 h after seeding by image analysis. For each value, a minimum of 3 to a maximum of 8 independent images were analyzed.

2.3. Evaluation of cell proliferation

BrdU pulse and chase experiments were performed on the micro-structured cultures 48 h after seeding. Cell cultures were incubated with 10 µM BrdU (Sigma-Aldrich) for 3 h (C2C12) and 5 h (human primary myoblasts) and fixed with PBS-70% EtOH (Sigma-Aldrich) for 30 min at -20°C. Cultures were then incubated with HCl 2N for 45 min at 37°C in order to denature DNA and rinsed twice in borate buffer 0.1 M pH 8.5 for 5 min. Mouse primary antibody against BrdU (Roche) 5 µg/ml in PBS-0.1% BSA (Sigma-Aldrich) was then applied for 1 h at 37°C. Alexa488 fluorescence-conjugated anti-mouse IgG secondary antibody (Invitrogen) was applied for 45 min at 37°C. Finally, nuclei were counterstained with DAPI

(Sigma Aldrich). Samples were mounted with Elvanol and viewed under a fluorescence microscope. The fraction of proliferating cells was calculated as the number of BrdU-positive nuclei on total nuclei. Collected data were analyzed through one-way and two-way analyses of variance (ANOVA), using MatLab software, with a p-value of 0.01 as a threshold for significance. All data values reported are means ± standard deviation of the mean. For each group, a minimum of 3 to a maximum of 8 independent images were analyzed.

2.4. Evaluation of cell differentiation

Micro-structured cultures maintained for 6 days (for C2C12) or 8 days (for human primary myoblasts) in differentiating medium were then analyzed for the expression of myosin heavy chain. Mouse monoclonal primary antibody against myosin heavy chain II (MHC, Sigma-Aldrich) was applied for 1 h at 37°C, while the Alexa488 fluorescence-conjugated anti-mouse IgG secondary antibody (Invitrogen) for 45 min at 37°C. Nuclei were counterstained with DAPI. Samples were mounted with Elvanol and viewed under a fluorescence microscope. Fusion index was calculated as the percentage of nuclei inside MHC-positive myotubes of all nuclei, by images analyses. Collected data were analyzed through one-way ANOVA, using MatLab software, with a p-value of 0.01 as a threshold for significance. All data values reported are means ± standard deviation of the mean. For each group, a minimum of 3 to a maximum of 8 independent images were analyzed.

2.5. Computational model

A computational model was developed and solved in quasi-steady-state conditions. The system geometry includes hydrogel and medium volumes, whose heights are 100 μm and 3 mm, respectively. At their interface, a cell layer of negligible volume, reproducing various patterns (parallel lanes of different sizes, triangular shape), constitutes a homogeneous source of a representative exogenous factor. We neglected cell division and assumed a constant secretion of soluble factor, taking advantage of mathematical modeling capability of studying a phenomenon without the overlap of other physical and biological processes. The concentration field of the exogenous factor was obtained solving its equation of continuity. The diffusivity in the hydrogel was assumed 1/10 of its value in the medium (10^{-6} cm^2/s). The model was implemented in Comsol Multiphysics V3.4 (COMSOL, Inc, Stockholm, Sweden) using a relative tolerance of 10^{-6} for the solution. Coarsening and refining the mesh space grid ensured that the results were independent of the spatial discretization.

3. Results and Discussion

3.1. Rational design of micro-patterning and computational analyses of secreted factor concentrations

Micro-patterning allows a precise control over the shape of the area of cell adhesion. We designed a pattern geometry that is organized in 12 mm-long parallel lanes, over a total area of 144 mm^2. Cells attach on lanes, adsorbed with adhesion proteins, with micrometric spatial resolution; while the inter-spacing between the lanes is cell-repellent (Figure 1). In the following, we will refer to cell density within the lanes as local cell density, and to that averaged on the whole surface as global.

We designed five configurations differing in lane and inter-spacing widths. In three of them, lane and inter-spacing widths are the same (100, 300, and 500 μm) (Figure 1). Thus, when two configurations have equal local cell density, they also have equal global cell density (Table 1). On the contrary, in the other two configurations, lane width is maintained fixed (100 μm), while the inter-spacing varies (50 and 200 μm). Thus, even for the same local cell density, the global density is still different. Table 1 summarizes the geometric parameters and the local cell density of seeding used in the experiments.

With this setup, we aimed at studying how different micro-structured cultures and conditions of local and global cell density can affect myoblasts proliferation and differentiation. Analyses of different conditions of local and global densities could be important for decoupling the role of cell-cell interaction from the role of soluble secreted factors on myoblast behavior.

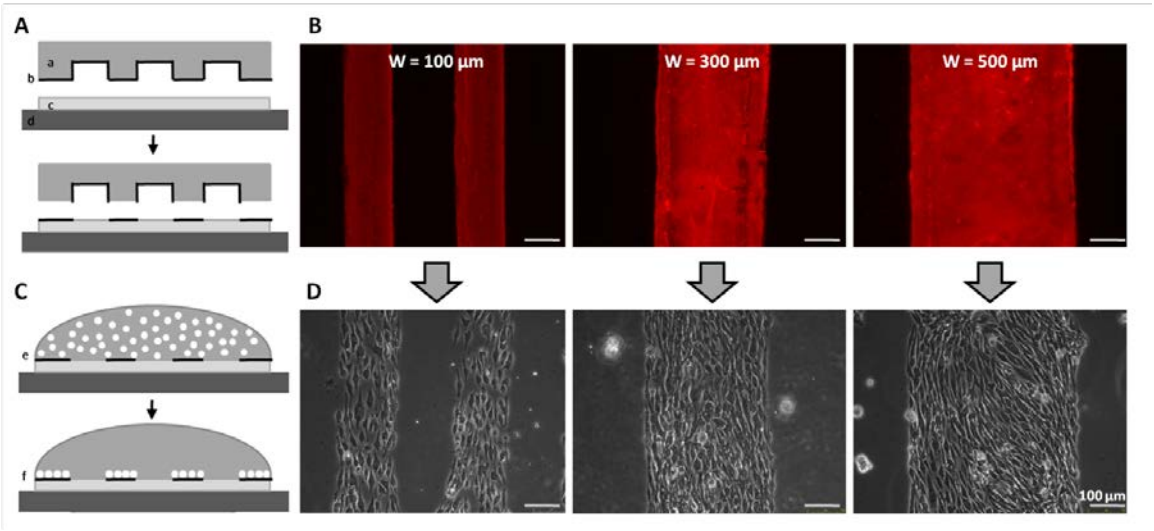

Figure 1. Micrometric control of cell culture topology by adhesion protein micro-patterning on hydrogel surfaces. (A) *Micro-contact printing. Adhesion proteins (b) are patterned with a PDMS mold (a), carrying a geometry of parallel lanes, onto the hydrogel surface (c) polymerized on a glass slide (d).* ***(B)*** *Laminin immunofluorescence on micro-printed hydrogels. The indicated value of W represents both lane and inter-spacing widths, which are the same for each configuration.* ***(C)*** *Cell seeding on the patterned hydrogel substrates. Cell suspension is dropped over the micro-patterned hydrogel surface forming a droplet-like structure (e). After overnight incubation cells adhere only to the protein-patterned areas (f).* ***(D)*** *Phase contrast images of C2C12 cultures within the geometries shown in B.*

Table 1. Summary of the parameters characterizing each micro-structured culture. *Local cell density is the ratio between the number of counted cells and the cell patterning area. Global cell density is the ratio between the number of counted cells and the total area. All data values reported are means ± standard deviation of the mean.*

lane – inter-spacing widths [µm]	**one-lane area [mm²] (ratio of lane to inter-spacing areas)**	**local seeding density [cell/mm²]**	**experimental local cell density [cell/mm²]** mean ± SD	**experimental global cell density [cell/mm²]** mean ± SD
100 – 100	72 (1/2 total area)	400	3300 ± 500	1700 ± 200
		200	1500 ± 200	800 ± 100
300 – 300	72 (1/2 total area)	400	3100 ± 500	1600 ± 200
		200	2000 ± 300	1000 ± 200
500 – 500	72 (1/2 total area)	400	3200 ± 500	1600 ± 200
		200	2300 ± 400	1200 ± 200
100 – 50	96 (2/3 total area)	200	1700 ± 300	1200 ± 200
100 – 200	48 (1/3 total area)	200	1900 ± 400	700 ± 100

First, we performed a computational study to simulate how the soluble extracellular environment is affected by the different patterning geometries. Specifically, we evaluated the concentration profile of a representative factor secreted by the cells (Figure 2). Because of the simplified structure of the model, the simulated results give only a qualitative understanding of the processes involved; nonetheless, they assist the interpretation of the experimental data.

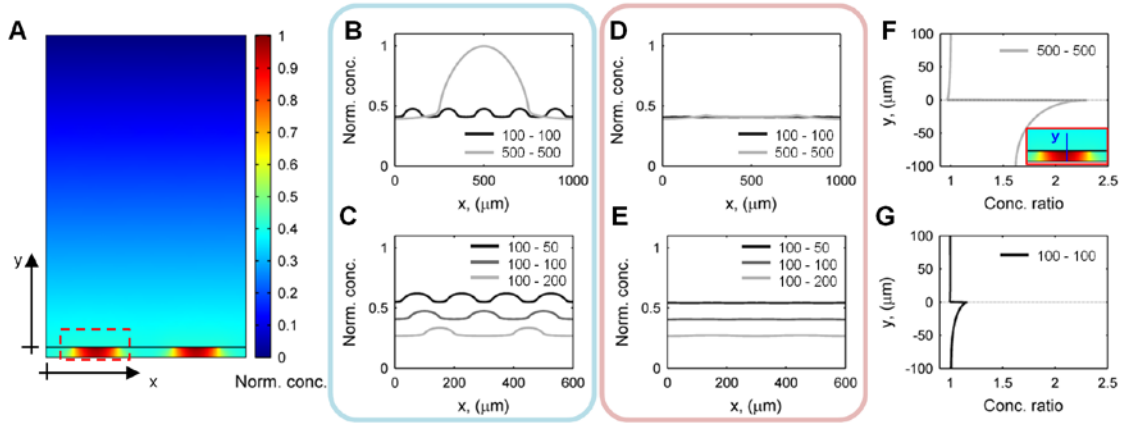

Figure 2. Concentration profiles of a representative secreted factor resulting from numerical simulations for different micro-patterning sizes. (A) *Transversal section of a two-lane cell culture on hydrogel. The coordinate system used in Figures B-G is also indicated. The plane y=0 represents the interface between hydrogel and medium. Normalized concentration in Figures A-E refers to the ratio of concentration to its maximum value in Figure A, where lane and inter-spacing widths are 500 μm.* ***(B)*** *Comparison between two different lane/inter-spacing widths at 5 μm below the medium-hydrogel interface (y=−5μm). Five 100-μm lanes and one 500-μm lane are shown. Legend: first number indicates lane width, second number inter-spacing size.* ***(C)*** *Comparison between two different inter-spacing widths at 5 μm below the medium-hydrogel interface (y=−5μm). Four, three, and two 100-μm lanes are shown, interspaced by 50, 100, and 200 μm, respectively.* ***(D)*** *Same as B, above medium-hydrogel interface (y=5μm).* ***(E)*** *Same as C, above medium-hydrogel interface (y=5μm).* ***(F-G)*** *Ratios of the concentration at the center of the lane to that at the edge, plotted along the y-direction (as indicated in the inset figure), for the micro-patterning sizes indicated in the respective legends.*

Figure 2A shows a color map indicating the concentration of the secreted factor within the whole volume of culture, included the hydrogel underneath the cells. A higher concentration is reached in the proximity of the cell-patterned area, in particular within the hydrogel domain, where the secreted factor diffuses more slowly and accumulates.

We studied the effect of lane width, keeping constant the global cell density (Figures 2B). The accumulation of secreted factor for 500 μm-wide lanes is significantly larger, with a maximum concentration at the lane center which is approximately double the concentration for 100 μm-wide lanes. Furthermore, wider lanes show a larger concentration change between the center and the lateral edge of the lane, producing a more heterogeneous environment for the cells therein (Figure 2F and G). On the contrary, the pattern size has

negligible effect in the medium above the cells, because of the fast diffusion that homogenizes secreted factor concentration (Figure 2D).

We also evaluated the effect of the inter-lane width when the lane size is kept constant and the local cell density is the same. The results show a less remarkable influence on factor accumulation in this case, not only in medium above the cells (Figure 2C), but also below the cells in the hydrogel (Figure 2E).

Thus, the different accumulation of secreted factors is highly influenced by the presence of a substrate, the hydrogel, having low diffusion coefficient and then acting as a reservoir. However, for this same substrate, the extent of this accumulation can be tuned by changing the width of the lanes where cells attach, allowing the study of the effect of secreted factors on cell behavior.

3.2. Micro-patterning affects C2C12 proliferation

C2C12 proliferation was investigated in the three geometries with equal lanes width and inter-spacing. We observed that C2C12 cultures in 100 μm lanes geometry showed the highest percentage of proliferating cells ((52 ± 1) % for the higher seeding density and (69 ± 8) % for the lower seeding density) (Figure 3C). BrdU-positive and negative cells were uniformly distributed inside the 100 μm patterning lanes (Figure 3A, left panel). The percentage of proliferating cells significantly decreased using the 300 and 500 μm lanes geometry ((31 ± 2) % and (27 ± 4) % respectively for the higher seeding density; (58 ± 3) % and (39 ± 7) % respectively for the lower seeding density) (Figure 3C) and BrdU immunofluorescence analyses revealed negative regions inside these wider patterning lanes (Figure 3A, middle and right panels).

As expected, the proliferation rate was negatively influenced by an increased seeding density (p-value < 0.01, two-way ANOVA), regardless of the patterning geometry. We also observed that micro-patterning lane width strongly affects cell proliferation, for the same seeding density (p-value < 0.01). However, cell seeding density and pattern geometry do not act synergistically in affecting proliferation (p-value > 0.01).

We then investigated how the global density influences myoblast proliferation, using the geometry that induces the highest percentage of proliferating cells (lanes width: 100 μm; inter spacing 50, 100 and 200 μm; see Table 1). We observed that the percentage of proliferating cells remained unchanged on the three micro-structured cultures, despite a different global cell density (Figure 3D).

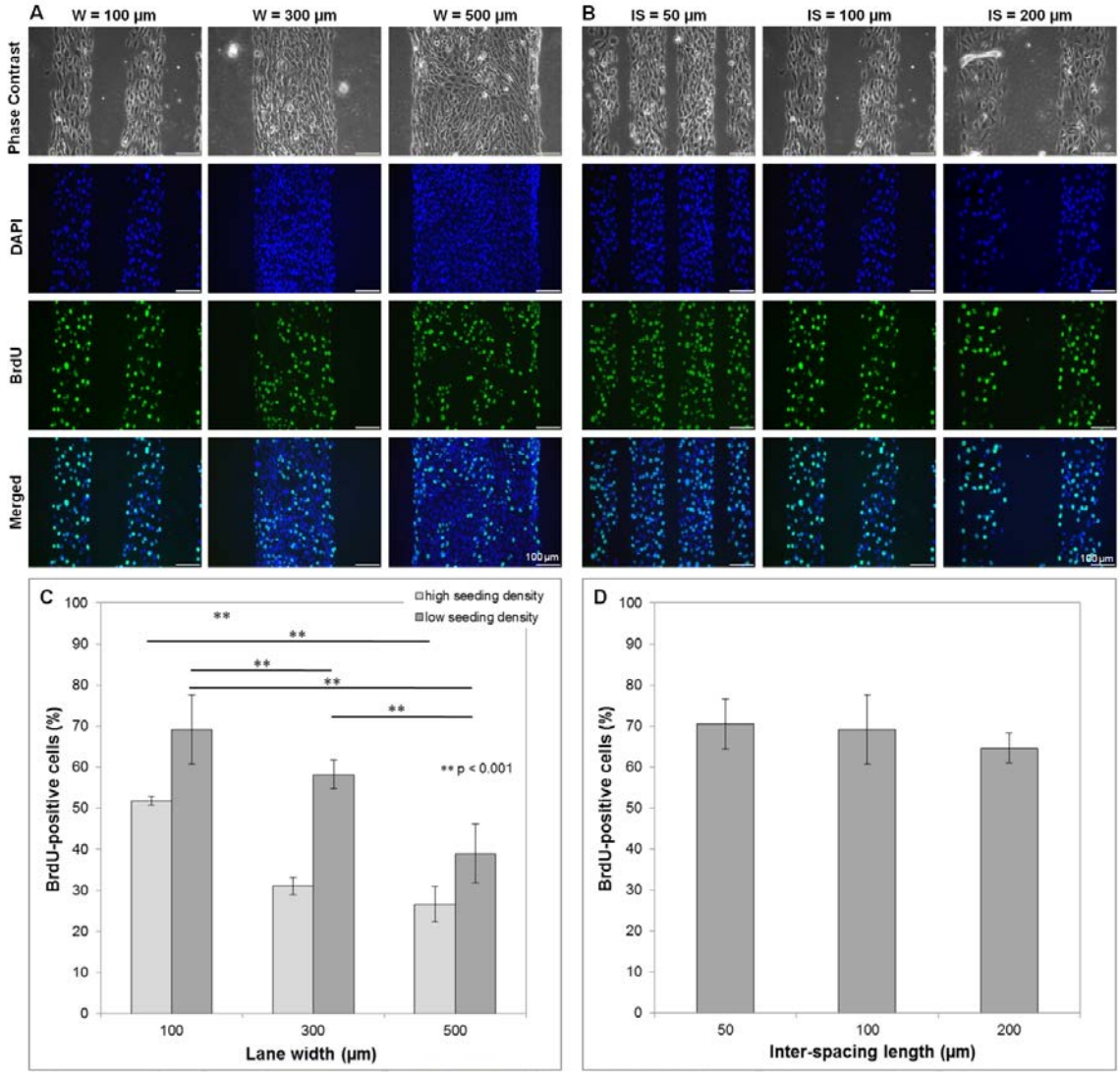

Figure 3. Effect of micro-patterning on C2C12 proliferation. A-B) *BrdU immunofluorescence on micro-structured C2C12 cultures 48 h after seeding on micro-patterning lanes (A) with 100, 300 and 500 µm width and with 100 µm width and (B) 50, 100 and 200 µm inter-spacing length. Nuclei are counterstained with DAPI.* ***C)*** *Histogram reporting the percentage of BrdU-positive C2C12 cells for each micro-patterning lanes width and for two different seeding densities. The number of proliferating cells decreases in micro-structured cultures with wider lanes geometries.* ***(D)*** *Histogram reporting the percentage of BrdU-positive C2C12 cells for each micro-patterning inter-spacing length. The number of proliferating cells is the same for micro-structured cultures with wider inter-spacing length geometries. Reported p-values were obtained by one-way ANOVA analyses of 5 (B) and 3 (D) independent images. Error bars represent standard deviations.*

A great number of studies have shown that cell behavior, in terms of differentiation fate, can be influenced by modulating the culture topology and the cell shape by micro-patterning techniques[22,23]. Human embryonic stem cells (hESC) were induced to different fate through colonies micro-patterning[24]

These results show that: *i*) cell density and micro-patterning width affect myoblast proliferation; *ii*) the effect of micro-patterning width is predominant; *iii*) the inter-spacing length does not affect myoblasts proliferation. They are fully consistent with the computational model, showing that accumulation of secreted factor increases when wider lanes are used (Figure 2B), whereas there is less significant accumulation of the secreted factor when varying the interspacing size (Figure 2D).

3.3. Micro-patterning lanes width positively influences C2C12 differentiation into myotubes

During early myogenesis *in vitro*, myoblast fusion into multinucleated myotubes is preceded by cell withdrawal from cell cycle. This is usually induced by reduction of the serum concentration in the culture medium.

C2C12 cells were cultured on micro-patterned surfaces characterized by 100, 300 and 500 μm lane widths using a high seeding density (400 cells/mm^2), which is required for an efficient muscle differentiation. In all the micro-structured cultures a remarkable formation of myotubes, arranged in independent parallel bundles, was observed, (Figure 4A,B). Myotubes were similar in size, with a characteristic width of about 30 μm, and a length ranging from 300 to 800 μm. MHC immunofluorescence analyses showed the sarcomeric organization of MHC (Figure 4A,B - magnifications), in agreement with our previously reported data[16].

We observed that C2C12 fusion index increased with patterning lanes width, from a minimum of (46 ± 8) % for 100 μm wide lanes to a maximum of (66 ± 7) % for 500 μm wide lanes (Figure 4C).

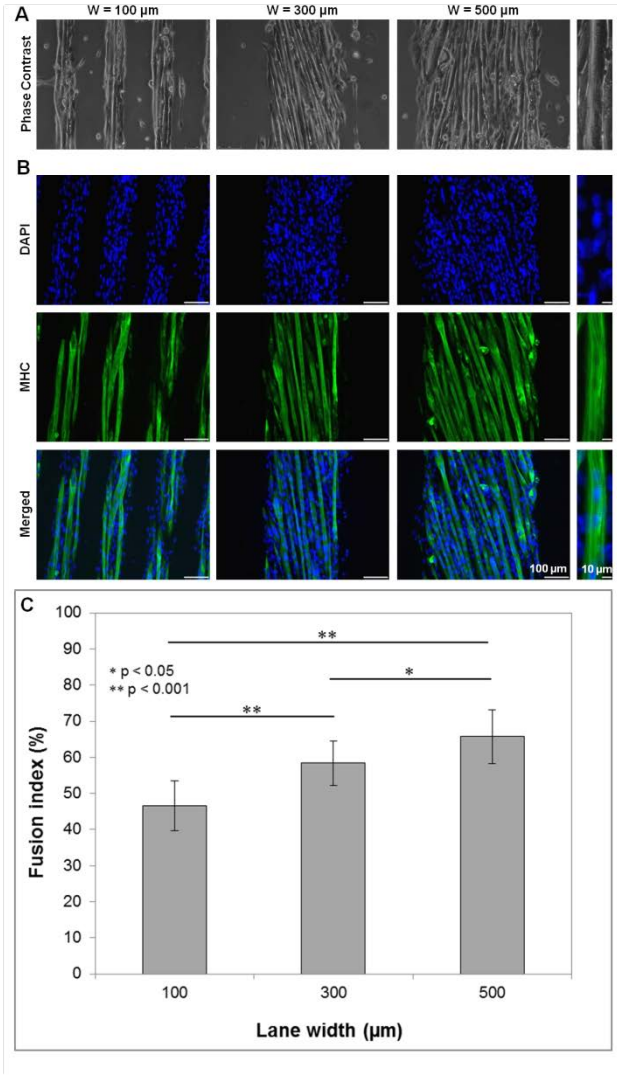

Figure 4. Effect of micro-patterning lanes width on C2C12 differentiation. (A) *Phase contrast of live C2C12 myotubes on the different micro-structured cultures characterized by 100, 300 and 500 µm lanes width, 8 days after seeding (2 days on proliferating conditions and 6 days on differentiating conditions).* ***(B)*** *Myosin heavy chain (MHC) immunofluorescence on C2C12 myotubes obtained in the same conditions. Nuclei are counterstained with DAPI. Right column reports magnification showing MHC sarcomeric organization.* ***(C)*** *Histogram reporting C2C12 fusion index for each micro-patterning lanes width. Fusion index increase for micro-structured cultures with wider lanes geometries. Reported p-values were obtained by one-way ANOVA analyses of 8 independent images. Error bars represents standard deviations.*

As expected, myoblasts differentiation showed an opposite trend compared to proliferation rate. The wider the micro-patterning lanes are, the more the effect on myoblasts withdrawal from cell cycle and consequent fusion into myotubes is relevant. These data are consistent with myogenic differentiation process, in which secreted factors self regulated myoblasts differentiation, as reported in a recent work published during the revision of this paper[17].

3.4. Myokine-containing conditioned medium negatively affect C2C12 proliferation

The results showed so far, both experimental and computational, suggest the hypothesis that there is a correlation between accumulation of secreted factors on different patterning geometries and myoblasts proliferation and differentiation.

In order to test if soluble secreted factors have an autocrine/paracrine influence on myoblast behavior, we performed the same proliferation experiment using a pre-conditioned medium (Figure 5). In particular, we compared C2C12 proliferation on micro-patterned surfaces characterized by 500 μm lanes cultured using (i) fresh medium (CTRL), (ii) medium pre-conditioned by a confluent culture of C2C12 myoblasts (MCM), (iii) medium pre-conditioned by a confluent culture of human foreskin fibroblasts (FCM), (iv) a mix of C2C12 conditioned medium and fresh medium in a 1:1 ratio (MCM: fresh medium = 1:1) (seeding density: 400 cells/mm^2).

The results showed that C2C12 conditioned medium remarkably decreases myoblasts proliferation, if compared to myoblasts cultured with fresh medium. On the other hand, medium pre-conditioned by fibroblasts do not have any effect on cells proliferation, meaning that: (a) the observed differences are not due to an exhausted medium; (b) the solely soluble secreted factors specifically produced by myoblasts (myokines) remarkably affect C2C12 behavior. Consistent with this, using the mixed medium (1:1 ratio) we observed only a partial decrease in myoblasts proliferation.

These results strengthen the hypothesis that an increase in myokines concentration, which is likely to happen in wider patterning, negatively affects cell proliferation and enhances cell differentiation, regardless of the cell density and, consequently, from cell-cell cross-talking through cell adhesion molecules

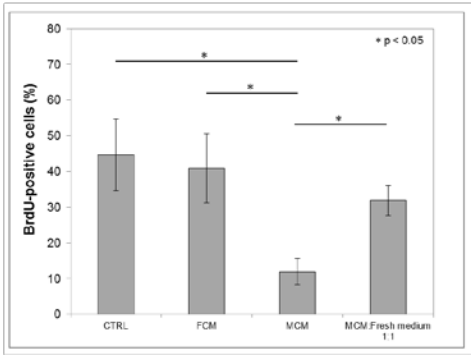

Figure 5. Effect of conditioned medium on C2C12 proliferation. *Histogram reporting the percentage of BrdU-positive C2C12 cells on micro-patterned surfaces characterized by 500 μm lanes cultured with freshly prepared medium, as control (CTRL), HFF fibroblasts conditioned medium (FCM); C2C12 myoblasts conditioned medium (MCM); medium obtained by mixing in a 1:1 ratio MCM and fresh medium. Reported p-values were obtained by one-way ANOVA analyses of 5 independent images. Error bars represent standard deviations.*

It could be important to underline that the hydrogel underneath the cells could have a major role in accumulating secreted factors, as reported in figure 2 F,G. This hypothesis is consistent with the results published by Bajaj and colleagues that report no difference when increasing patterning width. Since they used glass as myoblast substrate, they could not observe any significant accumulation[17]. Nevertheless, a direct comparison between these two substrates is difficult, because hydrogels create a myogenic environment also in terms of elastic modulus and favor myoblast differentiation through protein micro-patterning, as reported in our recent work[16].

Another important consideration concerns the role of secreted factors when translating from a two-dimensional to a three-dimensional model[25,18,26,27], which can better mimic the features of the *in vivo* cell micro-environment. In this latter case, the system is confined and the accumulation of secreted factors could be even higher than in a 2D system. Therefore, in a 3D system, it is likely that the matrix of encapsulated cells can act as a reservoir of soluble molecules, shaping local cell niche composition. This issue is extremely relevant when translating conventional 2D culture to 3D cell culture system.

3.5. Establishment of a gradient in C2C12 proliferation by *ad-hoc* patterning design

It would be interesting to understand if there is a threshold of patterning width that distinguishes between proliferating and non proliferating myoblasts. For this reason we developed a "sunrays-like" structure, in which a single ray shows a continuous gradient of width (Figure 6A). These geometries were made of circles with 7 rays. Each ray in the circle was a triangle characterized by 1 mm height and a base width of 500 μm. C2C12 myoblasts were cultured on these micro-patterned surfaces (Figure 6B) using a seeding density of 400 cells/mm^2.

First, we observed that BrdU-positive cells were uniformly distributed inside the thinner region of the rays, whereas BrdU-negative regions appeared in the wider portion. A similar phenomenon was previously observed for the 300 and 500 μm lanes geometry (Figure 3A). For the proliferation analysis, we divided the ray area in ten segments (Figure 6C) and we evaluated the percentage of proliferating cells inside each one. The reported data result from the analyses of 4 repeated experiments. The results show that myoblast proliferation decreases moving from the inner to the outer edge (Figure 6D), confirming the trend previously obtained with the discrete values of patterning width.

These results are consistent with the outcome of the computational model (Figure 6E, F). Figure 6E shows the concentration field of a representative factor secreted by the cells

cultured within a triangular geometry. The factor is accumulated in the hydrogel below the cells with a quasi-linear dependence on the width of the triangle (Figure 6F). The decrease in the last segments (9-10 in Figure 6F) is due to the boundary effect.

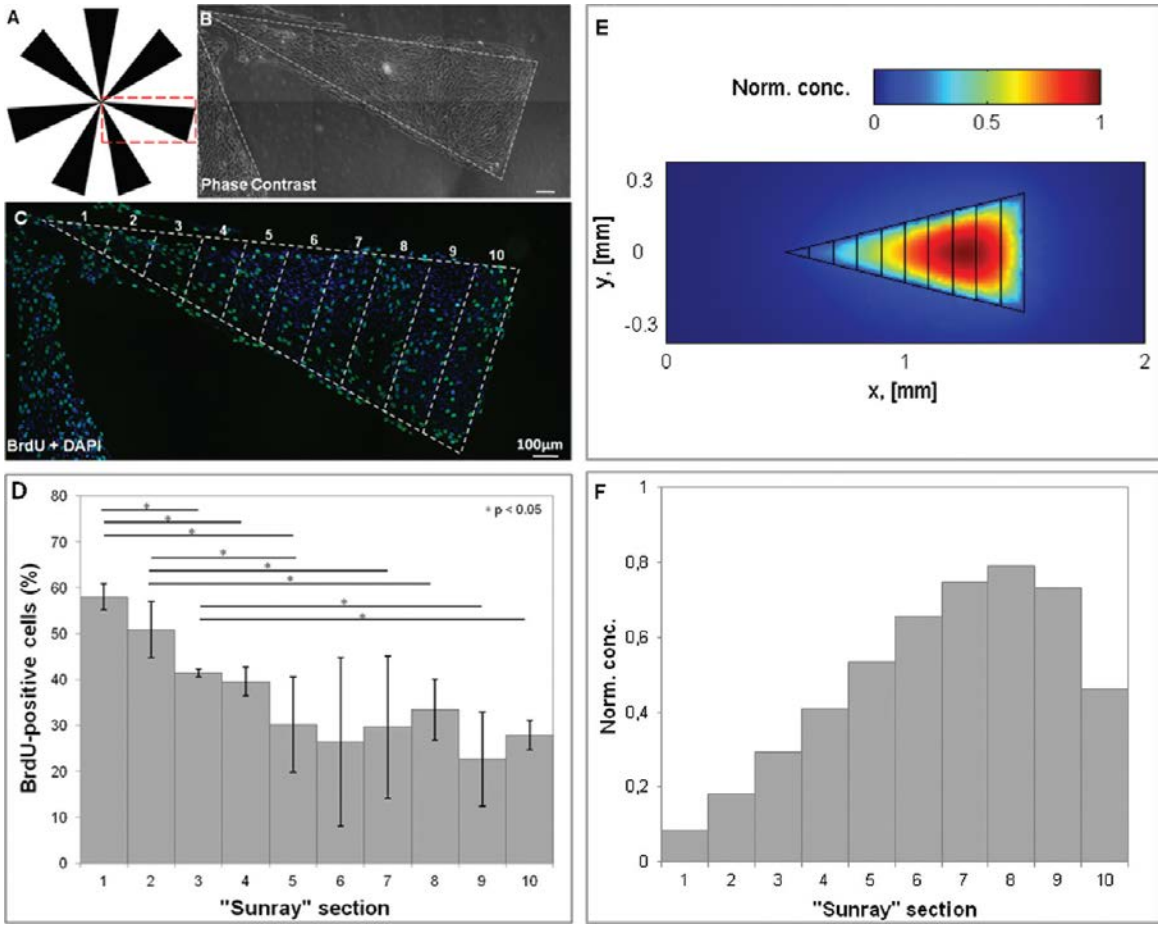

Figure 6. Establishment of a gradient in C2C12 proliferation by micro-patterning lane gradual enlargement. ***(A)*** *Schematic representation of the "sunrays-like" patterning geometry.* ***(B)*** *Phase contrast of C2C12 cultured in the micro-structured cultures.* ***(C)*** *BrdU immunofluorescence on micro-structured C2C12 cultures 48 h after seeding. Nuclei are counterstained with DAPI. The "sunray" area was divided in 10 portions as shown here.* ***(D)*** *Histogram reporting the percentage of BrdU-positive C2C12 cells in each of the 10 portions, mediated for 4 different "sunrays". Reported p-values were obtained by one-way ANOVA analyses of the 4 independent data. Error bars represent standard deviations.* ***(E)*** *Surface plot of the normalized concentration of a representative exogenous factor, as indicated by the color map, on the plane below the cells.* ***(F)*** *Mean concentration of the exogenous factor in each sector of the sunray indicated in E.*

3.6. Effect of micro-patterning lanes width on human myoblasts behavior

We replicated the experiments using human primary myoblasts. These cells were cultured on the three different micro-patterned surfaces (100, 300 and 500 μm lanes) using a seeding density of 400 cells/mm^2.

We observed that human myoblasts proliferation was the same in all micro-patterning width (about 40 % BrdU positive cells, independently from patterning width) (Figure 7A). The discrepancy between C2C12 (Figure 3C) and human myoblast behavior may be dependent on the different proliferation medium used for cell cultures. Human primary myoblasts medium contains mitogenic factors (β-FGF and EGF) and a double amount of serum.

We thus hypothesized that the proliferation of human myoblasts could be mainly affected by medium composition (high serum and growth factors) rather than by myokines, secreted factors. To test this hypothesis C2C12 were cultured in human myoblast medium, on 500 μm lanes and with a seeding density of 400 cells/mm^2. In particular, C2C12 were treated with three different media: 1) DMEM supplemented with 10% FBS (conventional medium for C2C12 proliferation); 2) DMEM supplemented with 10% FBS and the mitogenic factors β-FGF and EGF (2 and 10 ng/ml respectively); 3) DMEM High Glucose supplemented with 20% FBS, the mitogenic factors β-FGF and EGF (2 and 10 ng/ml respectively) and insulin (10 μg/ml) (medium reproducing the conditions used for human myoblasts proliferation). Figure 2B showed that C2C12 proliferation is highly increased by the presence of serum and mitogenic factors.

Concerning differentiation, the evaluation of human myoblasts fusion index on the three different micro-structured cultures confirmed the positive trend previously obtained for C2C12. In this case, a more relevant increase of fusion index was observed in wider patterning lanes, from a minimum of (15 ± 4) % for 100 μm lanes micro-structured cultures to a maximum of (36 ± 2) % for 500 μm lanes micro-structured cultures (Figure 7C). The values of fusion index for human primary myoblasts obtained in this work were consistent with the data reported in our recent work[16].

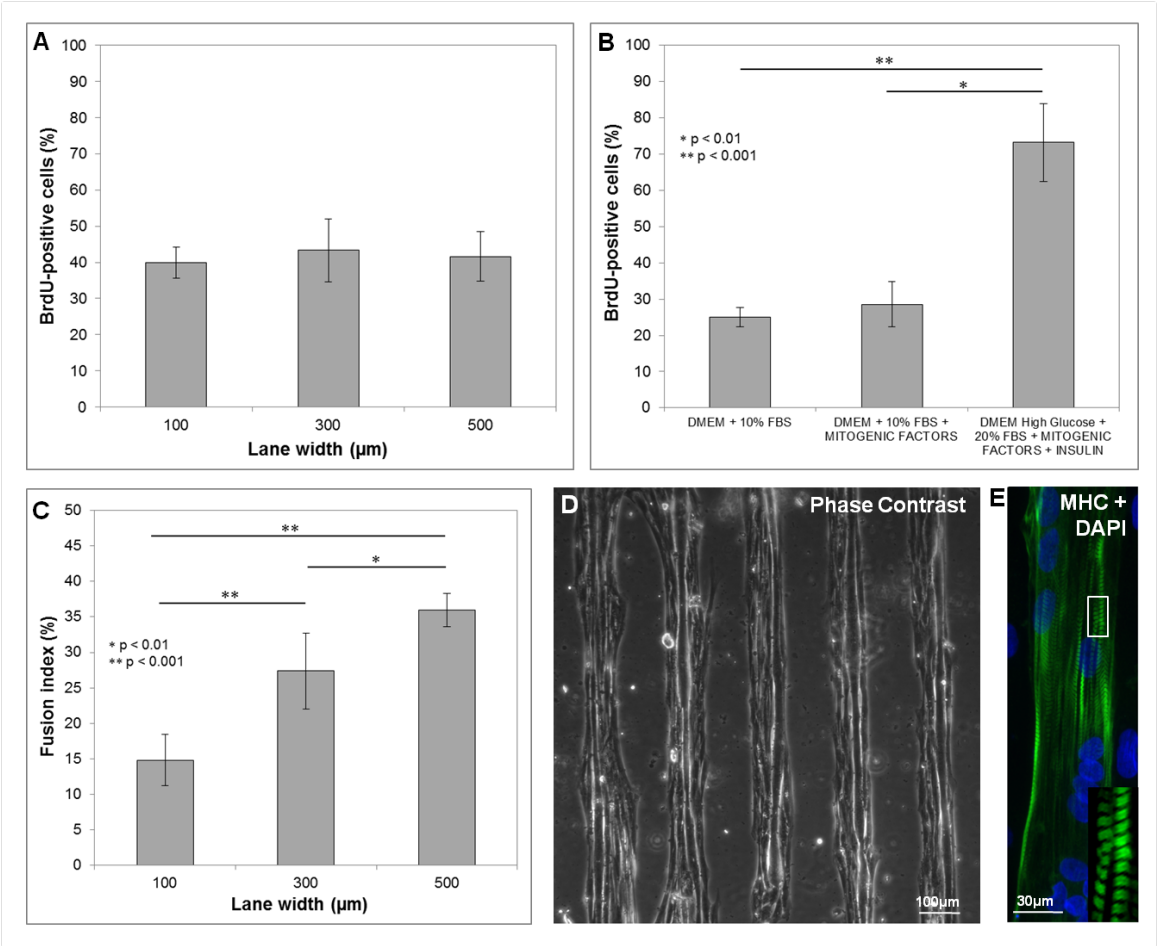

Figure 7. Effect of micro-patterning lanes width on human myoblasts proliferation and differentiation. ***(A)*** *Histogram reporting the percentage of BrdU-positive human myoblasts for different micro-patterning lanes width. The number of proliferating cells is the same for micro-structured cultures with wider lanes geometries.* ***(B)*** *Effect of serum mitogens on C2C12 proliferation. The histogram reports the percentage of BrdU-positive C2C12 cells on micro-structured cultures characterized by 500 μm lanes width, treated with different media. Human myoblasts proliferation medium, containing a double amount of serum, causes a significant increase in C2C12 proliferation.* ***(C)*** *Histogram reporting human myoblasts fusion index for different micro-patterning lanes width. Fusion index increases for micro-structured cultures with wider lanes geometries.* ***(D)*** *Myotubes formation on a micro-structured culture characterized by a 100 μm lanes geometry, after 8 days of differentiation.* ***(E)*** *Myosin heavy chain (MHC) immunofluorescence on human myotubes obtained on the micro-structured cultures after 8 days of differentiation. Sarcomeric organization indicating functional differentiation was revealed in each patterning condition. For each histogram, reported p-values were obtained by one-way ANOVA analyses of 5 independent images. Error bars represent standard deviations.*

Human myotubes obtained in all the micro-structured cultures (with a characteristic width of about 30 μm and a length ranging from 500 μm to 1 mm) revealed a remarkable level of sarcomeric organization. Again, MHC immunofluorescence analyses showed myotubes sarcomeric striations on portions or on their entire length (Figure 7D,E).

4. Conclusions

In conclusion, we demonstrated that: (i) micro-patterning affects myoblasts proliferation and differentiation; (ii) micro-patterning width, but not inter-spacing length, can affect myoblasts behavior in terms of both proliferation and differentiation; (iii) these effects can be due to an accumulation of secreted factors, as demonstrated by both the computational analysis and the experiments performed with conditioned medium; (iv) the accumulation of soluble secreted factors could be due to the presence of the hydrogel; (v) the same effect concerning myoblasts differentiation are true for human myoblasts, while concerning their proliferation the exogenous factors (medium composition) override the accumulation of endogenous secreted factors; (vi) studies conducted varying micro-patterning geometry and myoblasts behavior can give useful information for translating from 2D to 3D model of skeletal muscle in order to obtain *in vitro* model, which highly recapitulates the myogenesis *in vitro*.

Acknowledgment

This work was supported by Telethon (grant n. GGP08140); Città della Speranza; Fondazione CARIPARO and Regione Veneto (Azione Biotech II/III).

References

(1) Liao, H.; Zhou, G.-Q. *Tissue Eng Part B Rev* **2009**, *15*, 319-331.

(2) Bach, A. D.; Beier, J. P.; Stern-Staeter, J.; Horch, R. E. *J. Cell. Mol. Med* **2004**, *8*, 413-422.

(3) Baar, K. *Exp. Physiol* **2005**, *90*, 799-806.

(4) Vandenburgh, H. *Tissue Eng Part B Rev* **2010**, *16*, 55-64.

(5) Cossu, G.; Sampaolesi, M. *Trends Mol Med* **2007**, *13*, 520-526.

(6) Chargé, S. B. P.; Rudnicki, M. A. *Physiol. Rev* **2004**, *84*, 209-238.

(7) Sanger, J. W.; Kang, S.; Siebrands, C. C.; Freeman, N.; Du, A.; Wang, J.; Stout, A. L.; Sanger, J. M. *J. Muscle Res. Cell. Motil* **2005**, *26*, 343-354.

(8) Dupont, S.; Morsut, L.; Aragona, M.; Enzo, E.; Giulitti, S.; Cordenonsi, M.; Zanconato, F.; Le Digabel, J.; Forcato, M.; Bicciato, S.; Elvassore, N.; Piccolo, S. *Nature* **2011**, *474*, 179-183.

(9) Gurdon, J. B.; Tiller, E.; Roberts, J.; Kato, K. *Curr. Biol* **1993**, *3*, 1-11.

(10) Krauss, R. S.; Cole, F.; Gaio, U.; Takaesu, G.; Zhang, W.; Kang, J.-S. *J. Cell. Sci* **2005**, *118*, 2355-2362.

(11) Griffin, C. A.; Apponi, L. H.; Long, K. K.; Pavlath, G. K. *J. Cell. Sci* **2010**, *123*, 3052-3060.

(12) Li, L.; Zhou, J.; James, G.; Heller-Harrison, R.; Czech, M. P.; Olson, E. N. *Cell* **1992**, *71*, 1181-1194.

(13) Olwin, B. B.; Rapraeger, A. *J. Cell Biol* **1992**, *118*, 631-639.

(14) Szalay, K.; Rázga, Z.; Duda, E. *Eur. J. Cell Biol* **1997**, *74*, 391-398.

(15) De Angelis, L.; Borghi, S.; Melchionna, R.; Berghella, L.; Baccarani-Contri, M.; Parise, F.; Ferrari, S.; Cossu, G. *Proc. Natl. Acad. Sci. U.S.A* **1998**, *95*, 12358-12363.

(16) Serena, E.; Zatti, S.; Reghelin, E.; Pasut, A.; Cimetta, E.; Elvassore, N. *Integr Biol (Camb)* **2010**, *2*, 193-201.

(17) Bajaj, P.; Reddy, B., Jr; Millet, L.; Wei, C.; Zorlutuna, P.; Bao, G.; Bashir, R. *Integr Biol (Camb)* **2011**, *3*, 897-909.

(18) Aubin, H.; Nichol, J. W.; Hutson, C. B.; Bae, H.; Sieminski, A. L.; Cropek, D. M.; Akhyari, P.; Khademhosseini, A. *Biomaterials* **2010**, *31*, 6941-6951.

(19) Engler, A. J.; Griffin, M. A.; Sen, S.; Bönnemann, C. G.; Sweeney, H. L.; Discher, D. E. *J. Cell Biol* **2004**, *166*, 877-887.

(20) Gilbert, P. M.; Havenstrite, K. L.; Magnusson, K. E. G.; Sacco, A.; Leonardi, N. A.; Kraft, P.; Nguyen, N. K.; Thrun, S.; Lutolf, M. P.; Blau, H. M. *Science* **2010**, *329*, 1078-1081.

(21) Cimetta, E.; Pizzato, S.; Bollini, S.; Serena, E.; De Coppi, P.; Elvassore, N. *Biomed Microdevices* **2009**, *11*, 389-400.

(22) McBeath, R.; Pirone, D. M.; Nelson, C. M.; Bhadriraju, K.; Chen, C. S. *Dev. Cell* **2004**, *6*, 483-495.

(23) Li, F.; Li, B.; Wang, Q.-M.; Wang, J. H.-C. *Cell Motil. Cytoskeleton* **2008**, *65*, 332-341.

(24) Lee, L. H.; Peerani, R.; Ungrin, M.; Joshi, C.; Kumacheva, E.; Zandstra, P. *Stem Cell Res* **2009**, *2*, 155-162.

(25) Engler, A. J.; Humbert, P. O.; Wehrle-Haller, B.; Weaver, V. M. *Science* **2009**, *324*, 208-212.

(26) Bian, W.; Liau, B.; Badie, N.; Bursac, N. *Nat Protoc* **2009**, *4*, 1522-1534.

(27) Vandenburgh, H.; Shansky, J.; Benesch-Lee, F.; Skelly, K.; Spinazzola, J. M.; Saponjian, Y.; Tseng, B. S. *FASEB J.* **2009**, *23*, 3325-3334.

Appendix C

Clinical trial on chip show human donor pericyte efficiency in restoring dystrophin in a DMD *in vitro* model

E. Serena[1,2], S. Zatti[1,2], A. Zoso[1,2], F. Lo Verso[1,2], F. S. Tedesco[3], G. Cossu[3], N. Elvassore[1,2]

[1] Industrial Engineering Department, University of Padova, Padova, Italy

[2] Venetian Institute of Molecular Medicine, Padova, Italy

[3] Department of Cell and Developmental Biology, University College London, London, United Kingdom

Correspondence information: Elvassore Nicola. via Marzolo 9, 35131 Padova, Italy
Telephone: +39 049 827 5469, +39, fax: 049 827 5461, nicola.elvassore@unipd.it,
http://www.bioera.dipic.unipd.it

Stem Cells Translational Medicine

Submitted

Abstract

Restoration of the protein dystrophin on muscle membrane is the goal of many research lines aimed at curing Duchenne muscular dystrophy (DMD). From ongoing pre-clinical and clinical trials it emerges that restoration at least of 20% of dystrophin might be sufficient to protect muscles from damage. Pericytes are good candidates for the cell therapy of muscular dystrophies and have already entered clinical experimentation.

Our study aims at providing *in vitro* quantitative evidence of the ability of pericytes to restore dystrophin, in terms of protein accumulation and distribution within myotubes derived from DMD patients, using a micro-engineered model.

We designed an experimental strategy based on the co-culture, at different ratios, of human dystrophin^{+} myogenic progenitors and dystrophin^{-} myoblasts in a substrate with muscle-like physiological stiffness and cell micropatterns. Results showed that both healthy primary myoblasts and pericytes restore dystrophin expression in DMD myotubes derived in co-culture with DMD myoblasts. However, pericytes showed unexpected efficiency with respect to myoblasts in dystrophin production both in terms of amount of protein produced (40% vs 15% of wt at the same ratio) and length of the dystrophin membrane domain (210-240 μm vs 40-70 μm).

These results show that our microscaled *in vitro* model of human DMD skeletal muscle validate previous *in vivo* pre-clinical work and may be used to predict efficacy of new methods aimed at enhancing dystrophin accumulation and distribution before they are tested *in vivo*, thus reducing time, costs and variability.

Introduction

Duchenne muscular dystrophy (DMD) is a genetic disease caused by mutations in the gene encoding the protein dystrophin [1]. Dystrophin is a critical component of the dystrophin-glycoprotein complex (DGC) in muscle that links the actin cytoskeleton to the extracellular matrix of myofibers. The lack of a functional dystrophin protein causes loss of proper localization of many of the DGC components at the sarcolemma of muscle fibers leading to membrane instability and myofiber degeneration [2]. DMD primarily affects skeletal muscles and results in progressive paralysis and premature death. At the moment, no successful treatments are available, but new drug, gene and cell therapy strategies are under clinical investigation [3, 4].

Most of the therapeutic strategies and research lines for DMD are focused on the restoration of the protein dystrophin. In particular, in mice it has been shown that dystrophin levels

around 15% can improve pathology and performance, but levels of 20% are needed to fully protect muscle fibers from exercise-induced damage. Patients with Becker muscular dystrophy, which have a mild phenotype, express dystrophin at 40% of control. In addition, recently completed clinical trials showed that 15%[5] and 18%[6] of normal levels of dystrophin resulted in a moderate but significant clinical benefit during a 12 weeks study[7]. From these data a therapeutic strategy able to rescue the 20% of dystrophin could be considered a first successful step.

In this scenario, the cell therapy has good potentiality. In particular, strategies able to restore the compartment of muscle stem cells are amongst the most promising, since they would not require continuous injections to sustain the muscle regeneration. However, cell therapy is a complex regenerative process which includes intra-arterial (or intramuscular) cell delivery, crossing the blood vessel wall, survival, migration and contribution to skeletal muscle regeneration by fusion with regenerating muscle fibers and by entering the satellite cell compartment[8, 9]. In this perspective, pericytes are a promising cell source because of their peculiar characteristics: these cells surround the endothelium of small vessels and can differentiate into different mesoderm cell types, including skeletal muscle[8],[10]. When delivered into the arterial circulation, mouse pericytes, termed mesoangioblasts after *in vitro* expansion, cross the blood vessel wall and participate in skeletal muscle regeneration, ameliorating signs of muscular dystrophy in animal models such as the α-sarcoglycan–null (Sgca-null)[11] and mdx[8] mice and the golden retriever muscular dystrophy (GRMD) dog[12]. When cells similar to mouse mesoangioblasts were isolated from human adult skeletal muscle they were shown to correspond to a subset of pericytes, expressing alkaline phosphatase[13]. Pericytes are currently being transplanted in DMD patients in a phase I/II clinical trial (EudraCT no. 2011-000176-33).

Clinical trials are expensive and time-consuming processes required before drugs and therapies reach the market and the clinics, however many drugs are withdrawn and many therapies fail during clinical trial. In order to overcome this problem, the concept of “clinical trial on dish” or “clinical trial on chip” has been recently proposed[14]. Such complementary approaches could provide therapy safety and efficiency information at early stage of therapy development. For instance, Liang and colleagues validate the capacity of a library of human induced pluripotent stem cell–derived cardiomyocytes (hiPSC-CMs) to be used as a clinical trial in a dish model for accurate detection of patient-specific drug responses and drug-induced cardiotoxicity profiles[15]. The concept of “clinical trial on chip” emerged from the advances in micro-technology, microfluidics and development of physiologically relevant 3D organs or tissues at the microscale. The attempt is giving a cheaper, faster and more

accurate way to screen drugs or therapies for efficacy and toxicity. For a review of the potential of this approach see [14, 16, 17].

So far no study reports the use of skeletal muscle for clinical evaluation of therapy in a dish. However, the derivation of physiologically relevant skeletal muscle tissues *in vitro* is not straightforward. Physiological stimuli and interactions must be reproduced and finely controlled. In particular, the development of skeletal muscle model and a DMD assay requires the formation of a mature tissue with a high degree of differentiation and a proper expression of dystrophin, which is a late marker, not commonly detected in standard *in vitro* cultures. For this reason, primary myoblasts freshly isolated from patient should be used, since they can be expanded and successfully differentiated into mature myotubes, the functional unit of skeletal muscle. The major drawback of this cell source, the low number of derived cells, could be overcame with the design of micro-scaled assay able to maintain physiological relevance.

In this scenario, we propose a human-based skeletal muscle tissue-on-chip derived from healthy and DMD donors [20, 21]. We engineered the culture substrate, in terms of mechanical and topological properties, for optimizing human myoblasts differentiation and obtaining the expression of dystrophin *in vitro*[20].

The aim of this work is proving a skeletal muscle tissue on a chip able to assist the clinical trial phase with patient biology and physiologically relevant assays which can drive to potentially safer and more efficacious stem cell therapies. In particular, we aim at providing evidences of the ability of pericytes in restoring dystrophin, in terms of protein yield and protein distribution along myotubes derived from DMD patients, using a micro-engineered DMD model.

In order to simulate the natural process of cell fusion occurring during cell delivery, we designed an experimental strategy based on the co-culture, at different ratios, of Dys^+ and Dys^- human cells in a micro-engineered *in vitro* model of human DMD skeletal muscle (Fig. 1). We used primary myoblasts and primary pericytes derived from healthy subjects as Dys^+ cells. It is worth to underline that the pericytes used were harvested from three healthy donors, that are participating to a phase I/II clinical trial (EudraCT no. 2011-000176-33). The Dys^- cells were primary myoblasts derived from DMD patients. The co-culture of Dys^+ and Dys^- cells induced the formation of myotubes containing nuclei encoding for dystrophin and DMD nuclei not encoding for this protein. The functional maturation of these myotubes was achieved through a micro-engineered culture system, developed in our laboratory, that promotes the optimal maturation of human myoblasts[20, 21]. The obtained myotubes-on-chip showed a remarkable sarcomeric organization of MHC and dystrophin expression.

In this study, we report the ability of Dys+ nuclei in restoring dystrophin in terms of protein localization and yield.

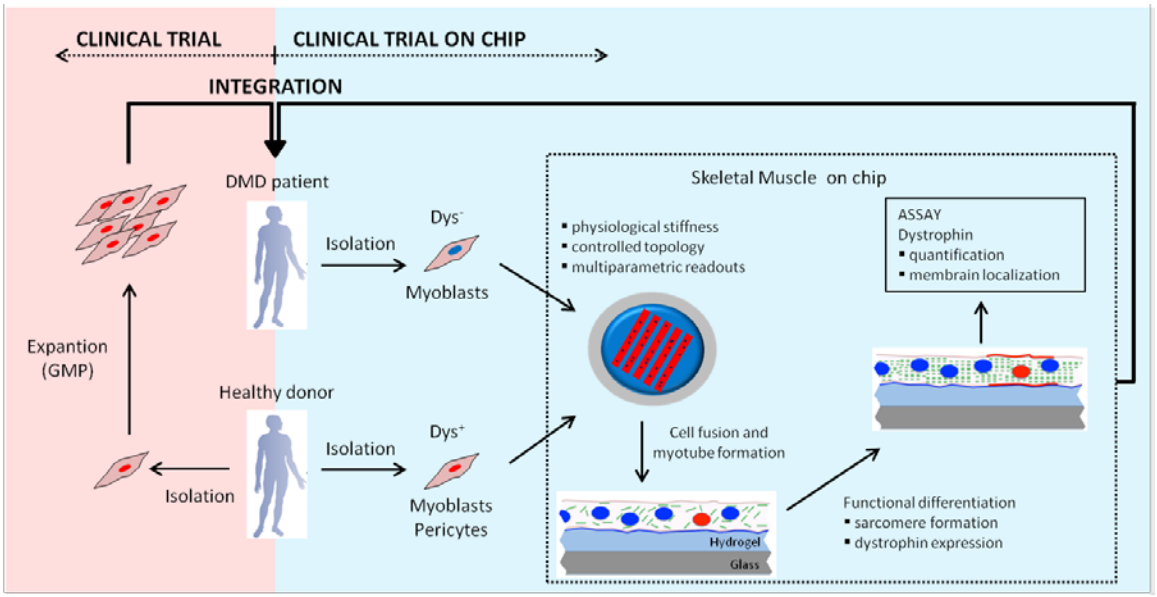

Figure 1. *Experimental strategy. Clinical trial (light red box) on stem cell therapies are based on the isolation and expansion of sFiguretem cells from a healthy donor following GMP guidelines. These cells are then injected into the DMD patient. Clinical trial on chip (light blue box) is based on the exploitation of the skeletal muscle on a chip, which allow to perform multiparametric and highthroughput experiments in vitro. Dys⁺ and Dys⁻ cells are co-cultured at different ratio within the skeletal muscle on chip. The proportion used for the core set of experiments was 1 Dys⁺ and 9 Dys⁻ cells (1:9). Dys⁺ and Dys⁻ fuse and result in myotubes composed of Dys⁺ and Dys⁻ nuclei. The micro-engineered model induces the functional maturation of the myotubes, promoting MHC sarcomeric organization and dystrophin expression within 8 days. The co-cultures are analyzed in terms of dystrophin accumulation and localization within the membrane. The knowledge acquired is then integrated within the clinical trial process.*

2. Materials and Methods

2.1 Cell Culture

Human primary myoblasts were provided by the ‘‘Telethon BioBank’’ (Telethon Research Service, Istituto Nazionale Neurologico ‘‘Carlo Besta’’, Milano, Italy). They are derived from healthy donors (dystrophin-positive, Dys⁺) and from DMD affected donors (dystrophin-negative, Dys⁻). Myoblasts were expanded with proliferation medium: 60% High-Glucose Dulbecco’s Modified Eagle’s Medium (DMEM Glutamax, Gibco-Invitrogen), 20% Medium M199 (Sigma-Aldrich), 20% fetal bovine serum (FBS, Gibco-Invitrogen), 10 ng/mL EGF (PeproTech), 2 ng/mL β-FGF (PeproTech), 10 µg/mL insulin (insulin from bovine pancreas, Sigma-Aldrich) and 1% penicillin– streptomycin–glutamine mix solution (Invitrogen); on

standard 100 mm tissue culture Petri dishes previously coated with 0.5% gelatin solution (gelatin from porcine skin, Sigma-Aldrich).

Human pericytes derived from healthy donors (Dys^+) were expanded in gelatin-coated dish with proliferation medium composed of MegaCell™ DMEM (Sigma-Aldrich) supplemented with 5% heat inactivated fetal bovine serum (Invitrogen), 2 mM L-Glutamine (Invitrogen), 1% non-essential aminoacids (Invitrogen), 0,1 mM β-mercaptoethanol (Invitrogen), 5 ng/ml β-FGF (PeproTech), 1% penicilin-streptomicin (Invitrogen). Pericytes were induced to differentiate into myotubes by changing proliferation medium with the same differentiating medium used for human primary myoblasts. Human primary myoblasts and pericytes were induced to form myotubes in differentiating medium: 98% DMEM Glutamax, 2% horse serum (Gibco-Invitrogen), 30 mg/ mL insulin and 1% penicillin–streptomycin–glutamine mix solution.

2.2 Dys^+ and Dys^- co-culture on micro-patterned substrate

The engineered culture system was prepared as previously described[20, 21]. Briefly, hydrogel with muscle-like stiffness were fabricated with acrylamide/bisacrylamide 29:1 40% solution (Sigma-Aldrich). The pre-polymer was diluted in phosphate buffered saline (PBS, Sigma-Aldrich) to the final concentrations of 10%. The photoinitiator (Irgacure 2959; Ciba Specialty Chemicals) was added to the acrylamide/bis-acrylamide solution with a final concentration of 20 mg/ml, and mixed thoroughly. Hydrogel polymerization occurred by exposing the prepolymer solution to UV light for 3 min (high-pressure mercury vapor lamp (Philips HPR 125 W) emitting at 365 nm with an incident light intensity of 20 mW/cm^2). Non-polymerized acrylamide was removed using distilled water. Hydrogel films were immersed in ultra-pure distilled water for 48 h to ensure complete removal of the unreacted monomeric units or photoinitiator and final sterilization occurred after 20 min exposure to UV light under a sterile hood.

Matrigel (2.5% v/v in DMEM) was used for the micropattern. Micropatterning geometry (parallel lanes) was optimized for myoblasts and pericytes, according to our previous work[21]. Dys^+ and Dys^- cells were co-cultured with the following ratio: 1:1, 1:2 and 1:9, respectively. 300 µL of the cell suspension (1×10^5 cells/mL) were dropped over the micropatterned hydrogel and the cultures kept at 37 °C, 5% CO_2. Co-cultures were maintained in a 1:1 mix of each specific proliferation medium for 1 or 2 days, followed by 8 days of culture in differentiating medium.

2.3 Western Blot

The cultures were treated ice-cold with 50 µl of lysis buffer: 50 mM Tris-HCl pH 7.5, 150 mM NaCl, 0.5 mM DTT, 10% Glycerol, 1 mM EDTA, 10 mM MgCl2, 2% SDS, 1% Triton X-100 1 mM PMSF, 1 mM NaV, 5 mM NaF, 3 mM β-glycerol (all Sigma), and Complete EDTA-free protease inhibitor cocktail (Roche). Lysis buffer were dropped directly onto the hydrogel surfaces and incubated at 4°C for 1 h. After 1 h treatment, lysis buffer was resuspended on the hydrogel in order to collect all the cellular contents. Cell fractions were sedimented by centrifugation at 13000 g for 20 min at 4°C, and supernatant collected. 10 µg per lane of protein extract were solubilized in loading buffer (Invitrogen), 10% DTT (Invitrogen) and heated for 10 minutes at 70°C. Proteins were resolved in 3-8% precast gels (Tris-Acetate NuPAGE, Invitrogen) and then transferred on PVDF membranes (Invitrogen) under a potential difference of 45V, 400mA for 6 h. Membranes were blocked with 5% nonfat dry milk (Bio-Rad) in TBST (TBS, 0.05% Tween 20) and then probed with primary antibodies for dystrophin (Abcam), myosin heavy chain II (Sigma-Aldrich) and β-actin (Sigma-Aldrich), and then with the proper HRP–conjugated secondary antibodies: goat anti-rabbit antibody (Invitrogen) and goat anti-mouse antibody (BioRad). Proteins were visualized by enhanced chemiluminescence (Invitrogen) and dystrophin content was quantified by densitometry using ImageJ software (US National Institutes of Health). For each culture condition, we quantified the intensity of dystrophin and myosin heavy chain bands and normalized them by the housekeeping protein, β-actin.

2.4 Immunofluorescence

Primary antibodies used in this study were against myosin heavy chain II (Sigma-Aldrich) and dystrophin (Abcam). A standard immunohistochemistry protocol was used[20]. Nuclei were counterstained with DAPI (Sigma Aldrich) and samples were mounted with Elvanols, and viewed under a fluorescence confocal microscope (Leica, Germany).

Results

3.1 Assay validation

As recently demonstrated[20, 21], human primary myoblasts (both Dys^+ and Dys^-) differentiated optimally in our system and gave rise to fully differentiated myotubes. Sarcomeric striations of myosin heavy chain (MHC) are visible (Fig. 2A) and dystrophin is expressed and located at the membrane (Fig. 2C). Also pericytes differentiate in our system: we obtained myotubes striated for MHC (Fig. 2B) and expressing membrane localized dystrophin (Fig. 2D).

The expression and accumulation of dystrophin was then analized through western blot. First of all we verified that the culture of Dys^+ cells performed in our micro-engineered model maintain the same ratio between dystrophin and MHC of cultures performed in standard multiwell (48 wells) for both human primary myoblasts and human pericytes (Fig. 2E). The results showed that our micro-engineered model induces a differentiation consistent with standard culture substrate and moreover it increases the expression of dystrophin (Fig. 2E). In order to determine the lower ratio of Dys^+ and Dys^- cells with a detectable expression of dystrophin, we performed co-cultures of Dys^+ and Dys^- human primary myoblasts at different ratio: 1:1, 1:2 and 1:9 respectively. We quantified the production of dystrophin and MHC as the intensity of western blot bands. Figure 2F shows a representative western blot. The results are reported in figure 2G. As expected, the production of dystrophin is directly proportional to the number of Dys^+ cells in culture. Based on these results, we decided to use the 1:9 ratio since the dystrophin band is still detectable.

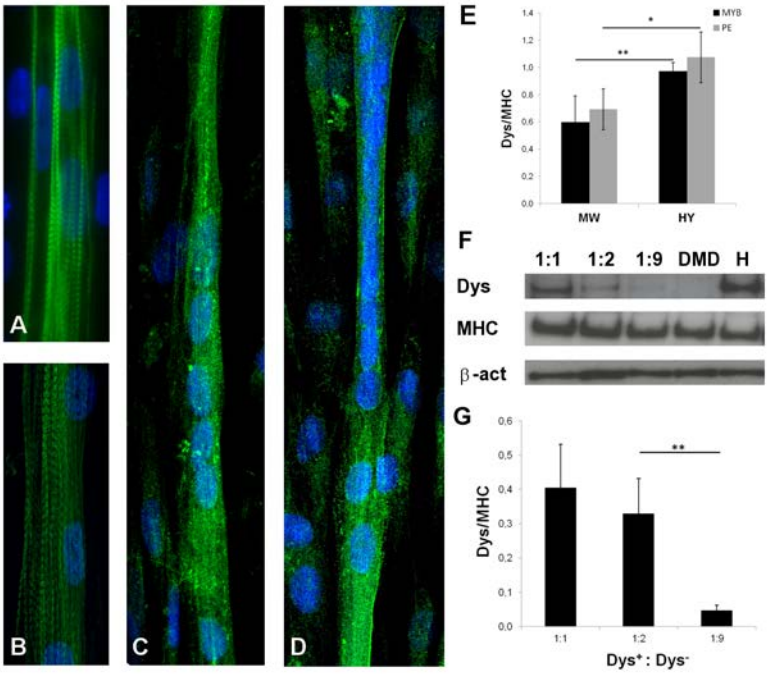

Figure. 2. *Assay validation. A-D: functional maturation of human primary myoblasts (A, C) and human pericytes (B, D) was confirmed through immunofluorescence against MHC (A,B) and Dystrophin (C, D). E: Graph representing the ratio between the band intensity of dystrophin and MHC in Dys^+ primary myoblasts (MYB) and Dys^+ human pericytes (PE). The culture were performed in standard multiwell (MW) and onto the micro-engineered skeletal muscle chip (HY). F: a representative western blot of the co-culture of primary myoblasts. Samples: 1:1, 1:2, 1:9 are the ratio of Dys^+ and Dys^- myoblasts, DMD are Dys^- primary myoblasts (affected by DMD), H are Dys^+ primary myoblasts (from healthy donor). G: quantification of the bands intensity. *: p-value < 0.05; **: p-value < 0.01.*

3.2 Dystrophin accumulation

We analyzed dystrophin expression by Dys^+ myoblasts and pericytes, when co-cultured with Dys^- primary myoblasts in a 1:9 ratio, through western blot analysis (Fig. 3A). The graph in figure 3B reports the percentage of dystrophin restoration versus MHC intensity. The percentage of dystrophin restoration is defined as the intensity of dystrophin in the co-culture normalized by the intensity of dystrophin in a sample entirely composed of Dys^+ cells. Dystrophin restoration is represented as a function of MHC expression because this represents the differentiation degree of the culture. Being dystrophin expression strictly correlated to the differentiation degree of the culture, we observed that, despite the differentiation timing was kept constant (8 days) the cultures reached different levels of differentiation. Therefore, in order to compare different samples, dystrophin restoration is reported in function of MHC expression. The results showed that dystrophin restoration is always higher within pericytes co-cultures than primary myoblasts co-cultures (Fig. 3B).

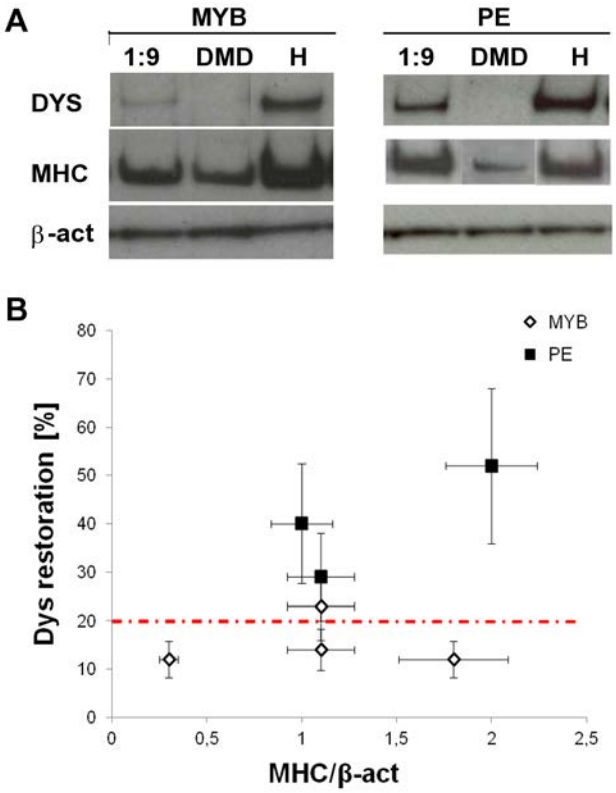

Figure 3. *Dystrophin accumulation. A: representative western blot of the co-culture experiments of primary Dys^+ and Dys^- myoblasts (MYB) and Dys^+ pericytes (PE) and Dys^- primary myoblasts. B: quantification of the percentage of dystrophin restoration as function of MHC expression.*

3.3 Dystrophin expression domain on the myotube surface

In terms of dystrophin localization, immunofluorescence analysis indicated that Dys^+ myoblasts, co-cultured with Dys^- myoblasts (at 1:9 ratio), gave rise to myotubes where dystrophin was expressed in defined portion of the myotube (Fig. 4A, B).

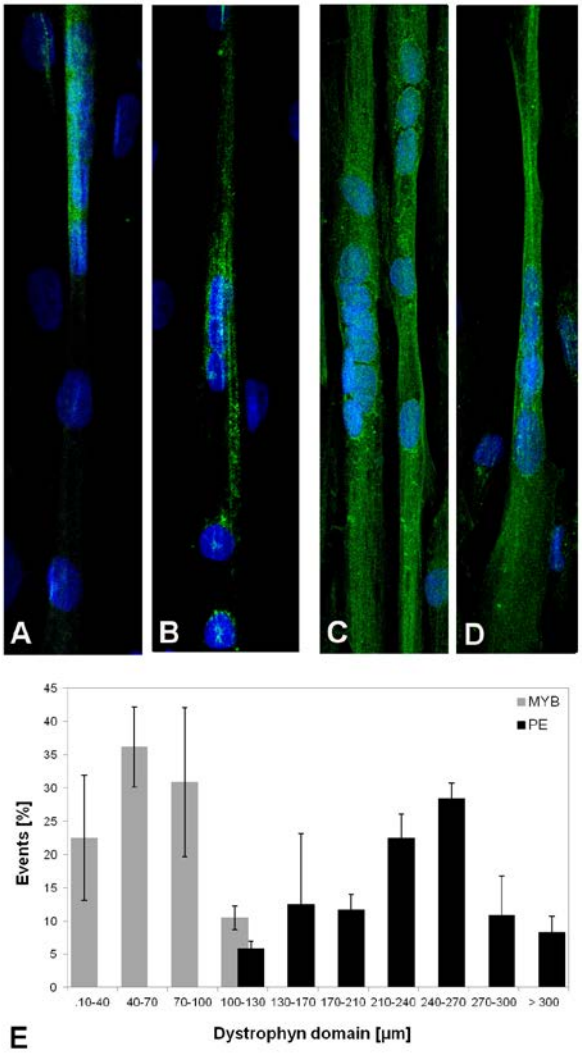

Figure 4. *Dystrophin restoration domain. A-D: immunofluorescence against dystrophin in the 1:9 co-culture of primary Dys^+ and Dys^- myoblasts (A, B) and 1:9 co-culture of Dys^+ pericytes and Dys^- primary myoblasts (C, D). E: quantification of dystrophin domain length.*

On the contrary, Dys^+ pericytes under similar conditions gave rise to myotubes expressing dystrophin for the majority of their length: the protein was expressed almost along the entire myotube (Fig. 4C, D). We analyzed the length of the myotube surface expressing dystrophin, that we named dystrophin domain. The length of each domain was calculated and each event was classified in groups, depending on their increasing length. The distribution is depicted in figure 4E. The dystrophin restoration domain sustained by myoblasts had an average length of 40-100 µm, while pericytes nuclei contributed to restore dystrophin for 210-240 µm.

It is worth to underline that we analyzed the number of nuclei per myotube in the dystrophin domain intervals, in order to avoid that a longer dystrophin domain could be due to a higher number of nuclei per myotube (Fig. 1S). We observed that the average number of nuclei per myotube was comparable in myoblasts and pericyte co-cultures.

Discussion

Being this process so complex, reproducing *in vitro* all the phases could be very challenging. However, these phases may be dissected in separate steps, for each of which an in vitro assay may be developed as a predictive tool of the corresponding *in vivo* performance. For example, Boiden chambers coated with endothelium, under various experimental conditions, may mimic crossing of the blood vessel *in vivo* (Giannotta et al., in revision). However, how a pericyte nucleus (or of other myogenic progenitors) contributes to dystrophin synthesis and consequently, which is the minimal ratio of delivered/survived and fused cells versus resident myofiber nuclei needed to rise dystrophin level above the 20% threshold, is a fundamental question in this context[22].

This study shows that human pericytes restore dystrophin expression and distribution in an *in vitro* model of human DMD skeletal muscle. Unexpectedly they do so more efficiently than human skeletal myoblasts.

The *in vitro* model of human skeletal muscle used in this work is a versatile tool for studying human skeletal muscle proliferation and differentiation. Recently, it has been demonstrated that human wild type and DMD myoblasts can differentiate optimally in this model thanks to the mechanical and topological stimuli exerted[20, 21]. In addition, dystrophin is expressed at significant levels and could be detected by immunofluorescence analysis[20]. These two main characteristics, being based on human DMD myoblasts and being able to induce dystrophin expression *in vitro*, makes it a suitable *in vitro* model for studying human skeletal muscle physiology and physiopathology. In this work it has been exploited for studying the ability of pericytes of restoring dystrophin expression in hybrid myotubes formed with an excess of dystrophic myoblasts.

First of all we verified that pericytes differentiate optimally in our micro-engineered model (Fig. 2). We observed that the substrate stiffness (15 kPa) and topology (parallel lanes) induced the differentiation of pericytes to functional myotubes (sarcomeric striation of MHC) expressing dystrophin. Indeed the culture in our model on chip induced a higher expression of dystrophin if compared to the standard culture on dish: the ratio between dystrophin and myosin heavy chain is higher in the colture performed in our microengineered model than the one performed onto standard multwell (48) (Fig. 2E). An

additional advantage of using our model on chip is the ordered topology of myotubes. In our model, myotubes grow only onto the micro-patterned area and are all oriented along the main direction of the patterning. Therefore, such an organization of the sample allows to easily quantify the dystrophin expression domain, which would be much more difficult in a standard culture of myotubes, where they are randomly oriented.

This study is based on the co-culture of human Dys^- and Dys^+ myogenic cells (primary myoblasts and pericytes). The first issue we had to face was how to dissect the two cell populations. One of the standard procedure, when one of the two population is murine, is based on the nuclei staining with Hoechst 33258: human has a diffuse staining, while mouse has punctate nuclei[23]. In this case, being all the cells used human, this procedure could not be adopted. We tested a number of standard methodologies used (Fig. 2S), but they all failed for different reasons. Marking one cell population with Hoechst (Fig 2S, A) resulted in a reduced cell viability after 5 days of culture and a premature culture deterioration and myotube detachment. This methodology remains a good procedure when short term experiments are performed. Human myoblasts were then infected with an adenovirus carrying the Green Fluorescent Protein (Fig 2S, B). Even though the fluorescent signal was good, the infection efficiency was quite low (around 50%). Therefore, we decided to use a lentivirus encoding for a nuclear LacZ. In this case the efficiency was high (90%), but the β-galactosidase was translocated to all the nuclei inside the myotube. Being our experiments quite long (10-12 days), we observed two categories of myotubes: myotubes with all positive nuclei and myotubes with all negative nuclei. In few cases we observed a gradient of staining (Fig 2S, C), but this was not sufficient to dissect the populations and to predict the number of nuclei per populations inside the mixed myotubes. We also tried to mark our myogenic cells with lipophilic tracers (Dil and DiO). In this case, the efficiency was around 80% and we were able to dissect the mixed myotubes (colored in orange, 50% of the total myotubes) (Fig. 2S, D-E), but it was impossible to maintain the staining and performing immunofluorescence against dystrophin for measuring its domain.

Since all the methodologies tested for cell staining had a particular drawback for our purpose, we decided to perform the experiments of co-culture without staining the cells.

Human pericytes[9, 13] are a promising cell source for DMD therapy because they overcome some of the limitations associated with myoblast intra-muscular injections[8]. In particular they can be delivered through intra-arterial injections since they cross the endothelium and migrate extensively in the interstitial space, show long-term survival and partially restore muscle structure and function in dystrophic mice and dogs[11, 12], beside contributing to the muscle satellite cell pool[8]. Here we tested the ability of pericytes to restore dystrophin

expression, in terms of protein accumulation and distribution along the surface of myotubes derived from DMD patients, using a micro-engineered DMD model.

Interesting, three different batches of human pericytes showed the ability to restore a significant level of dystrophin, which was analyzed by immunofluorescence and western blot.

In terms of dystrophin accumulation, pericytes restoration of dystrophin was higher than the theoretical 20% of control needed to protect muscle fibers from exercise-induced damage[22], provided that a 1:9 ratio was achieved *in vitro*.

The domain of dystrophin restoration due to healthy pericytes nuclei spanned almost along the entire myotube (with an average domain length of 240 μm). An intrinsic advantage of using our model on chip is the ordered topology of myotubes. In our model, myotubes grow only onto the micro-patterned area and are all oriented along the main direction of the patterning. Therefore, such an organization of the sample allows to easily quantify the dystrophin expression domain, which would be much more difficult in a standard culture of myotubes.

The pericytes used in this study are actually used in a phase I/II clinical trial based on intra-arterial delivery of pericytes, currently ongoing in children affected by Duchene Muscular Dystrophy at the San Raffaele Hospital in Milan (EudraCT no. 2011-000176-33).

In any cell therapy protocol, the preparation of donor cells to be injected require their manipulation *ex vivo* and it is widely known how this step could be crucial for the obtainment of good results. In this scenario, we hypothesize that our microscaled *in vitro* model could be used as a quality control test of donor cell batches and could help the prediction of the clinical outcomes. In this respect it is interesting to note that preliminary results from the trial (Cossu et al. in preparation) indicated the expression of donor dystrophin, albeit at a very low level, when donor DNA, analyzed by satellite micro-chimerism, was approximately 1% of total DNA in the biopsy on the patient with highest engraftment.

Another important aspect to consider is the very large number of variables that may be tested to enhance the efficacy of cell therapy, such as for example, pre-treatment of donor cells and/or of host muscle cells with molecules that may enhance differentiation, protein synthesis or fusion. Obviously it would be impossible to test all these variables in patients and pre-clinical experimental studies on animal models, beside being expensive and time consuming, may not reveal subtle differences between mouse and human cells[24, 25]. Our model could be used as an *in vitro* standard for testing the extent of dystrophin restoration in parallel to pre-clinical and before clinical studies.

In conclusion, we demonstrate that clinical trial on chip, conducted on microscaled engineered human tissues could be a valuable support during pre-clinical phases or clinical trials.

Acknowledgments

This work was supported by Telethon GGP08140 and AFM 15462 and 16028 to NE; Optistem FP7 IP 223098 and ERC 233263 to GC. ES was supported by University of Padova (DIRPRGR10), SZ by Città della Speranza.

Disclosure:

The authors declare no potential conflicts of interest.

References

1. Hoffman EP, Brown RH, Kunkel LM. Dystrophin: The protein product of the duchenne muscular dystrophy locus. **CELL** 1987;51(6):919928.
2. Emery AE. The muscular dystrophies. **THE LANCET** 2002;359(9307):687–695.
3. Benedetti S, Hoshiya H, Tedesco FS. Repair or replace? Exploiting novel gene and cell therapy strategies for muscular dystrophies. **FEBS J.** 2013;280(17):4263–4280.
4. Goyenvalle A, Seto JT, Davies KE, et al. Therapeutic approaches to muscular dystrophy. **HUM. MOL. GENET.** 2011;20(R1):R69–78.
5. Goemans NM, Tulinius M, Akker JT van den, et al. Systemic Administration of PRO051 in Duchenne's Muscular Dystrophy. **N. ENGL. J. MED.** 2011;364(16):1513–1522.
6. Cirak S, Arechavala-Gomeza V, Guglieri M, et al. Exon skipping and dystrophin restoration in patients with Duchenne muscular dystrophy after systemic phosphorodiamidate morpholino oligomer treatment: an open-label, phase 2, dose-escalation study. **LANCET** 2011;378(9791):595–605.
7. Anthony K, Cirak S, Torelli S, et al. Dystrophin quantification and clinical correlations in Becker muscular dystrophy: implications for clinical trials. **BRAIN** 2011;134:3544–3556.
8. Tedesco FS, Hoshiya H, D'Antona G, et al. Stem Cell-Mediated Transfer of a Human Artificial Chromosome Ameliorates Muscular Dystrophy. **SCI. TRANSL. MED.** 2011;3(96).
9. Dellavalle A, Maroli G, Covarello D, et al. Pericytes resident in postnatal skeletal muscle differentiate into muscle fibres and generate satellite cells. **NAT COMMUN** 2011;2:499.

10. Cappellari O, Cossu G. Pericytes in Development and Pathology of Skeletal Muscle. **CIRC. RES.** 2013;113(3):341–347.
11. Sampaolesi M, Torrente Y, Innocenzi A, et al. Cell therapy of alpha-sarcoglycan null dystrophic mice through intra-arterial delivery of mesoangioblasts. **SCIENCE** 2003;301(5632):487–492.
12. Sampaolesi M, Blot S, D'Antona G, et al. Mesoangioblast stem cells ameliorate muscle function in dystrophic dogs. **NATURE** 2006;444(7119):574–579.
13. Dellavalle A, Sampaolesi M, Tonlorenzi R, et al. Pericytes of human skeletal muscle are myogenic precursors distinct from satellite cells. **NAT. CELL BIOL.** 2007;9(3):255–267.
14. Stolpe A van de, Toonder J den. Workshop meeting report Organs-on-Chips: human disease models. **LAB. CHIP** 2013. Available at: http://dx.doi.org/10.1039/C3LC50248A.
15. Liang P, Lan F, Lee AS, et al. Drug Screening Using a Library of Human Induced Pluripotent Stem Cell–Derived Cardiomyocytes Reveals Disease-Specific Patterns of Cardiotoxicity. **CIRCULATION** 2013;127(16):1677–1691.
16. Engle SJ, Puppala D. Integrating Human Pluripotent Stem Cells into Drug Development. **CELL STEM CELL** 2013;12(6):669–677.
17. Lesko LJ, Schmidt S. Individualization of Drug Therapy: History, Present State, and Opportunities for the Future. **CLIN PHARMACOL THER** 2012;92(4):458–466.
18. Tedesco FS, Gerli M, Perani L, et al. Transplantation of genetically corrected human iPSC-derived progenitors in mice with limb-girdle muscular dystrophy. **SCI. TRANSL. MED.** 2012;4(140):140ra89.
19. Huh D, Torisawa Y, Hamilton GA, et al. Microengineered physiological biomimicry: Organs-on-Chips. **LAB. CHIP** 2012;12(12):2156–2164.
20. Serena E, Zatti S, Reghelin E, et al. Soft substrates drive optimal differentiation of human healthy and dystrophic myotubes. **INTEGR. BIOL. QUANT. BIOSCI. NANO MACRO** 2010;2(4):193–201.
21. Zatti S, Zoso A, Serena E, et al. Micropatterning Topology on Soft Substrates Affects Myoblast Proliferation and Differentiation. **LANGMUIR** 2012;28(5):2718–2726.
22. Putten M van, Hulsker M, Nadarajah VD, et al. The Effects of Low Levels of Dystrophin on Mouse Muscle Function and Pathology. **PLOS ONE** 2012;7(2):e31937.
23. Pomerantz JH, Mukherjee S, Palermo AT, et al. Reprogramming to a muscle fate by fusion recapitulates differentiation. **J. CELL SCI.** 2009;122(Pt 7):1045–1053.
24. Willmann R, Luca A De, Benatar M, et al. Enhancing translation: Guidelines for standard pre-clinical experiments in mdx mice. **NEUROMUSCUL. DISORD.** 2012;22(1):43–49.

25. Meng J, Muntoni F, Morgan JE. Stem cells to treat muscular dystrophies – Where are we? **NEUROMUSCUL. DISORD.** 2011;21(1):4–12.

Supplementary Information

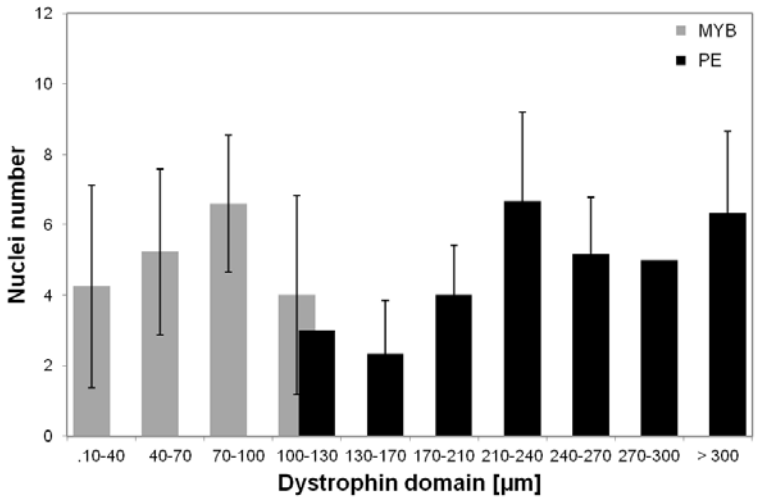

Figure 1S. *Nuclei distribution. Quantification of nuclei distribution as function of dystrophin domain length.*

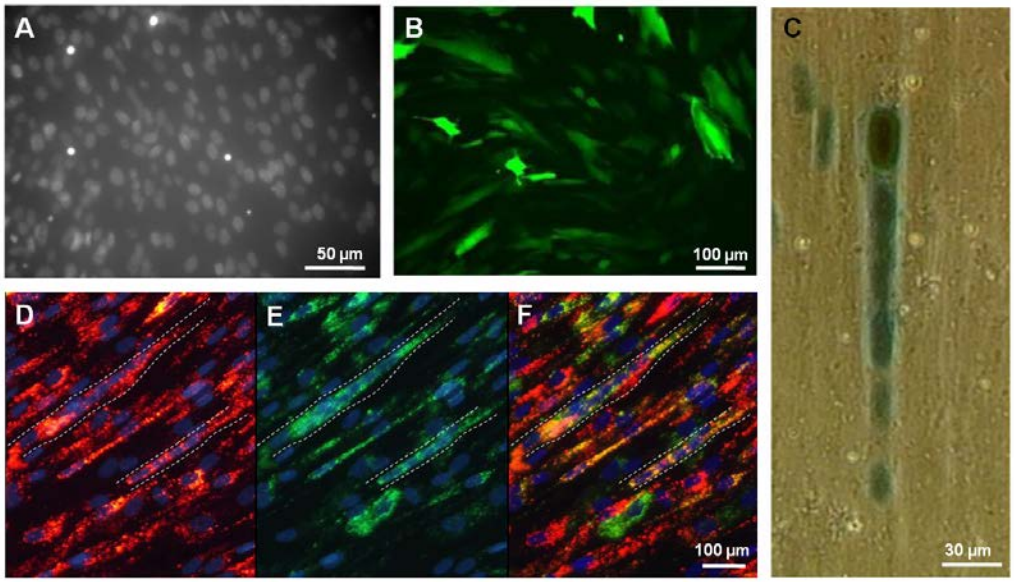

Figure 2S. *Cell population (Dys^- and Dys^+) staining. A: hoechst staining of living myoblasts. B: infection with a GFP adenovirus. C: infection with a LacZ lentivirus. D-F: staining with lipophilic tracers DiI (red, Dys^-) and DiO (green, Dys^+).*

Appendix D

Determination of glucose flux in live myoblasts by microfluidic nanosensing and mathematical modeling

Alessandro Zambon[†a,b], *Alice Zoso*[†a,b], *Camilla Luni* [a,b], *Wolf B. Frommer*[c] *and Nicola Elvassore*[*a,b]

[a] Department of Industrial Engineering, University of Padova, Padova, Italy.

[b] Venetian Institute of Molecular Medicine (VIMM), Padova, Italy.

[c] Department of Plant Biology, Carnegie Institution for Science, Stanford, CA, USA

[*] Author to whom correspondence should be addressed.

E-mail: nicola.elvassore@unipd.it; Fax: +39 049 827-5461; Tel: +39 049 827-5469

[†] These authors contributed equally to this work.

Integrative Biology
In press
DOI: 10.1039/c3ib40204e

Abstract

Glucose is the main energy source for cells in an organism and its blood concentration is tightly regulated in healthy individuals. However, impaired blood glucose control has been found in diseases such as metabolic syndrome and diabetes, and anomalous glucose utilization in cancer tissues. Dissecting the dynamics of the different phenomena involved in glucose handling (intracellular mass transport, membrane diffusion, and intracellular phosphorylation) is very relevant to identify which mechanisms are disrupted under disease conditions. In this work, we developed an effective methodology for quantitatively analyzing these phenomena in living cells. A measurement of steady-state glucose uptake is, by itself, insufficient to determine the dynamics of intracellular glucose. For this purpose, we integrated two types of measurements: cytosolic glucose concentration at the single-cell level, obtained using a cytosolic FRET nanosensor, and cell population glucose uptake, obtained without perturbing culture conditions using a microfluidic perfusion system. Microfluidics enabled accurate temporal stimulation of cells through cyclic pulses of glucose concentration at defined flow rates. We found that both, glucose uptake and phosphorylation, are linearly dependent on glucose concentration in the physiologic range. Mathematical modeling enabled precise determination of the kinetic constants of membrane transport (0.27 s^{-1}) and intracellular phosphorylation (2.01 s^{-1}).

Insight, innovation, integration

Quantitatively studying cellular glucose handling is very relevant for better understanding alterations implicated in diseases, like diabetes and cancer. Although of critical importance, an investigation of glucose kinetics under physiological conditions is still lacking. Here, we performed a quantitative dissection of the mechanisms that involve glucose uptake and metabolism in a culture of cells from skeletal muscle, one of the primary tissues responsible for glucose uptake in the body. We accurately controlled the extracellular microenvironment performing experiments within a microfluidic culture system. Data were analyzed through a mathematical model for quantification. Combining experimental technology and modeling enabled precise determination of rates of glucose diffusion across cell membrane and intracellular phosphorylation, and their dependence on external glucose concentration under physiologic conditions and under perturbation.

Introduction

Glucose is the primary energy source for cells in an organism and its blood concentration is tightly regulated in healthy individuals (3.9-6.1 mmol/L)[1,2]. Impaired blood glucose control has been found in diseases such as metabolic syndrome and diabetes, with serious consequences for patients[3,4]. Furthermore, alterations in glucose flux has been implicated in cancer development through the so-called Warburg effect[5].

In a cell culture there are three different phenomena involved in glucose handling: intracellular mass transport, diffusion through plasma membrane, and intracellular phosphorylation. Dissecting their dynamics is very important for identifying compromised mechanisms at the single-cell level relevant for disease conditions.

Intracellular mass transport represents the movement of glucose in the culture medium by diffusion and, in case of a perfused system, also by convection. This process is dependent on the geometry and operative conditions of the experimental setup used, however computational modeling can easily describe the glucose concentration field in different systems by solving its microscopic mass balance, coupled with fluid dynamic simulations in case of perfused systems[6].

Diffusion through plasma membrane brings intracellular glucose into the cells through glucose transporters (GLUTs, SGLTS and SWEETs). Multiple GLUT isoforms have been discovered whose membrane expression is highly regulated[7], either through hormonal control (for example, by insulin) or by intracellular mechanisms such as glycosylation[8,9]. Glucose transport across the cell membrane is conventionally studied *in vitro* using glucose analogs. The most commonly used are radioactive hexoses, such as [^{14}C] 2-deoxy-D-glucose[10] and [^{18}F] fluoro-2-deoxy-D-glucose[11]. Besides the criticality of working with radioactivity, radiolabeled analogs present some limitations, such as lack of spatio-temporal resolution and the inability to measure glucose uptake in viable cell cultures[12]. To avoid these shortcomings, non-metabolizable and metabolizable fluorescence-tagged glucose analogs were developed, the most common being 6- and 2-(N-(7-Nitrobenz-2-oxa-1,3-diazol-4-yl)amino)-6-Deoxyglucose (6-NBDG and 2-NBDG)[13,14]. Compared to radioisotopes fluorescently labeled analogs provide high spatial and temporal resolution, with fluorescence detectable at the single cell level within seconds[12]. However, a common limitation to both isotope and fluorescent analogs is that they are not transported by GLUTs and metabolized by hexokinase with the same kinetics as glucose[12], and they can be toxic even at low doses[15]. More recently nanosensors were developed for intracellular glucose imaging in live cells at single-cell resolution[16]. They are based on the interaction of intracellular D-glucose with a molecular probe that, upon glucose binding, undergoes a

conformational rearrangement detectable by Förster resonance energy transfer (FRET) between two spectral GFP variants. FRET is a direct proxy for the cytosolic glucose concentration at steady state[17]. While non-steady-state FRET changes can be correlated to changes in cytosolic glucose concentration only if the nanosensor kinetics is faster than that of intracellular glucose processes. If this condition is not met, a dynamic use of the nanosensor is precluded.

After import into the cell, glucose is phosphorylated by hexokinases. Multiple isoforms of this enzyme exist in different tissues[18]. Hexokinase kinetics has been studied after enzyme purification mainly by spectrophotometric techniques[19,20,21]. One study measured hexokinase rate of glucose phosphorylation within the complexity of cytoplasmic environment[22]. However, in this study nanosensor kinetics is assumed to be faster than hexokinase rate.

A comprehensive investigation to simultaneously dissect intracellular glucose transport, its diffusion through plasma membrane, and its intracellular phosphorylation in a quantitative manner is still missing. These three processes occur sequentially, and at steady-state their rates are the same and equal to the rate of the slowest of the three steps. Thus, measuring the uptake of glucose by cells at steady-state gives information on the overall speed of the process, but does not allow the identification of the dynamics of each of the three steps individually. A deeper study is needed for a quantitative analysis of these processes and of the impairments occurring in pathological conditions.

Here, we performed a dissection of the dynamics of the three processes involved in glucose acquisition in a myoblast cell culture. We took advantage of different experimental and computational techniques for the study of mass transport and myoblast kinetics of glucose uptake and phosphorylation. We coupled the detection of cytosolic glucose concentration via FRET-based nanosensors at the single-cell level with the enzymatic measurement of glucose uptake of a cell population, performed with minimal culture perturbation. We performed the experiments within a microfluidic culture system to accurately control the extracellular environment and in particular glucose concentration in the immediate vicinity of cell membrane. The small volumes of medium used also increased the signal-to-noise ratio of measurements because a small glucose uptake by the cells produced a large concentration difference in the culture medium. Experimental data were analyzed making use of mathematical modeling to derive the kinetic constants of each glucose-related process.

Results and discussion

Experimental strategy

Dissecting the dynamics of glucose intracellular mass transport, diffusion through plasma membrane, and intracellular phosphorylation in a quantitative manner is not feasible by measuring steady-state glucose uptake or glucose intracellular concentration alone[22]. A more thorough analysis is needed to characterize each of these processes. We used mathematical modeling to theoretically determine which measurements are required to quantify each rate. The model we developed is multi-scale and describes the glucose concentration field in the whole culture system, the cell population glucose uptake and the single-cell processes of glucose handling. It is based on standard techniques of fluid dynamic modeling and glucose mass balances. We found that, by coupling the two measurements of steady-state glucose uptake and cytosolic glucose concentration, it is possible to fully quantify the kinetics of each of the three processes involved in glucose handling.

Based on this theoretical result, we set up a microfluidic experimental system for accurately performing the two measurements, steady-state glucose uptake and cytosolic glucose concentration (Figure 1). The microfluidic chip allowed a tight control of glucose concentration thanks to the perfusion in laminar flow conditions and an accurate temporal stimulation of the cells obtained by coupling the chip with an automated liquid handling apparatus. Each chip included three culture chambers to perform experiments in triplicate and was made of transparent PDMS to perform fluorescence microscopy on line.

To determine the overall glucose uptake in each cell culture chamber, we carried out steady-state experiments at defined inlet glucose concentrations and measured glucose concentration at the outlet (Figure 2). Uptake was then calculated from the overall mass balance on the culture system (Eq. (9)). Thanks to the low flow rates used (12.5 nL/min) and the very high surface-to-volume ratio of the culture chamber (Table I), the difference of glucose concentration between inlet and outlet had a significant signal-to-noise ratio, because a small flux of glucose into the cells resulted in a large concentration variation in the culture medium.

To obtain the second type of measurement, cytosolic glucose concentration in individual cells, the response of the intracellular FRET-based nanosensor FLIPglu-600μΔ13V[17] was detected online by microscopy (Figure 3). A high flow rate (4 μL/min) was used in these experiments in order to have a glucose concentration on the cell surface approximately equal to its concentration at the inlet of the culture system, i.e. the glucose assimilated by cells was negligible compared to the amount of glucose entering the system. These

measurements were taken both at steady state and under fast dynamic changes of inlet glucose concentration. We used a multi-inlet system to switch between different glucose concentrations entering the culture chamber with high temporal accuracy by means of pneumatic valves integrated on chip (Figure 1). For example it can be easily used to generate a pulse or an approximately linear ramp of concentrations.

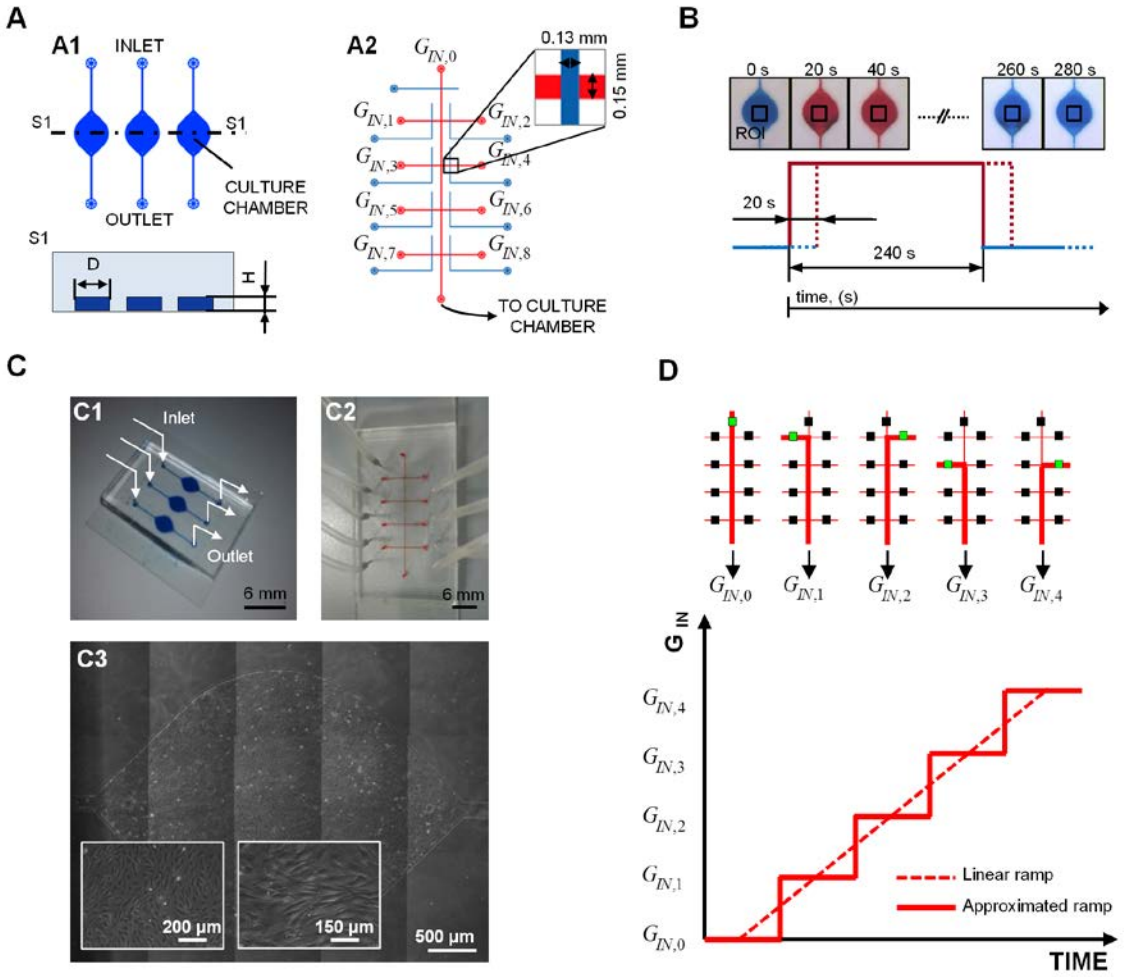

Figure 1. *Experimental setup. (**A**) A1) Top view and section of the microfluidic cell culture chambers. A2) Top view of the multi-inlet system for FRET experiments. Blue lines: microfluidic channels used to pneumatically control the valve system. Red lines: flow channels connecting external medium reservoirs at different glucose concentrations ($G_{IN,i}$ with $i = 1...9$) to the inlet of a culture chamber. Enlargement shows the detail of a pneumatic valve. (B) Analysis of the delay between a change in input conditions and the actual change of medium composition in the culture chamber, using dyes of different colors, at 4-µL/min flow rate. ROI: region of interest. (**C**) C1) and C2) Pictures of the experimental setup schematically represented in A). The culture chambers and the flow channels in the multi-inlet system were filled with blue and red dyes, respectively. C3) Images of the culture chamber after seeding of myoblasts, at different enlargements. (**D**) Example of the functionality of the multi-inlet system for reproducing an approximately linear ramp of glucose concentration at the inlet of the culture chamber. In the upper part, the system is schematically depicted with green and black squares representing open and closed valves, respectively.*

Validation of glucose uptake measurements

We verified the sensitivity of our system for glucose uptake measurements and optimized parameters for imaging and perfusion. Myoblasts were seeded within the microfluidic chambers and perfusion started after cell adhesion. We studied how sensitive the measurements of glucose concentration at the outlet of the culture chamber were to different flow-rate regimes. As flow rate is inversely correlated to the residence time of medium in the culture chamber, we expected the measurements to be less sensitive at high flow rates when glucose outlet concentration was expected not to be significantly different from the inlet concentration.

First, we applied a step change in flow rate from 0.025 to 0.5 μL/min, collected the medium continuously at the outlet of the culture chambers, and analyzed it enzymatically every 0.6-μL volume eluted (Figure 2B). Results showed high accuracy: average data variability was approximately 30% both for samples from different culture chambers and for samples collected at different time points at steady-state. At the low flow rate, glucose concentration at the outlet was significantly different from that of the control, represented by a culture chamber where no cells were seeded. On the contrary, at 0.5 μL/min the steady-state outlet concentration was approximately the same as for the control, and the signal-to-noise ratio too small for an accurate derivation of the uptake rate.

As the time needed to collect a 0.6-μL sample is inversely proportional to the flow rate (Figure 2B, inset), then flow rate also affects the maximum time resolution of the measurement. For example, at 0.025 μL/min each sampling was performed every 24 min, while at 0.5 μL/min every 1.2 min. Thus, working at low flow rates increases measurement sensitivity, but at the expenses of time resolution.

From this experiment we also determined the time needed to reach a steady-state condition to be approximately that needed for eluting 2-μL volume (Figure 2B). This result was also confirmed by fluid dynamic simulations (see Supporting Information). In the next steady-state measurements presented, we always collected samples after 3-μL volumes (as an excess of 2 μL) were eluted following a flow rate change.

To determine the optimal flow rate to use, a second experiment was performed measuring steady-state outlet glucose concentration for six different flow rates ranging between 0.0125 and 0.5 μL/min (Figure 2C). The experimental results confirmed that the smaller is the flow rate, the larger is the glucose concentration difference between inlet and outlet, and the higher is glucose uptake measurement sensitivity. However, lower flow rates imply longer times for sample collection and less temporal resolution during dynamic experiments. As a trade-off between these two requirements we decided to perform next

experiments of glucose uptake measurement at a flow rate of 0.05 µL/min.

As single-cell glucose uptake is the measurement usually reported in the literature, we calculated its mean value in the culture chamber as the ratio of the overall uptake, calculated by Eq. (9), to the number of cells in the culture chamber (Figure 2D). For the same inlet glucose concentration and high flow rates, uptake by the average cell was approximately independent from the flow rate. The flow rate can be considered high when glucose gets to cell surface more rapidly than it is consumed. The single-cell uptake we measured (~30 fmol min^{-1} per cell) is of the same order of magnitude of a previous study on myoblasts[23], where it was obtained from radioactivity measurements after addition of ^{14}C(U)deoxy-D-glucose. Assuming a total protein content of 120±18 pg/cell (Table I), the uptake from data in Kotliar et al.[23] was 17±3 fmol min^{-1} per cell).

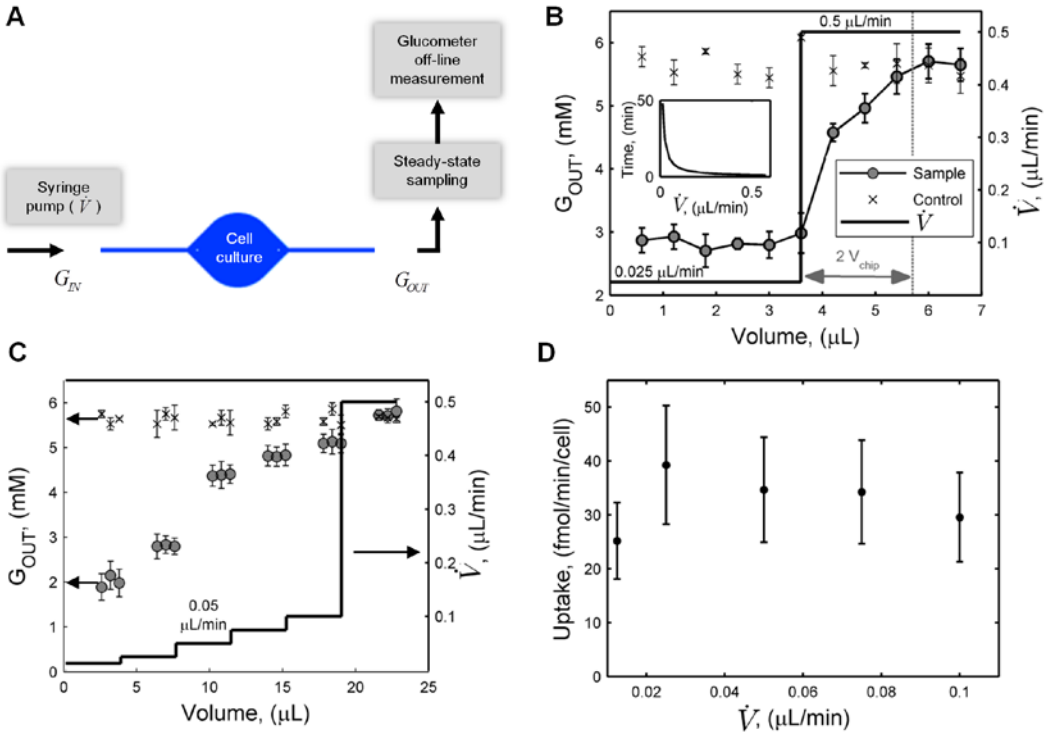

Figure 2. *Effect of flow rate on glucose uptake measurements. (**A**) Schematic representation of glucose uptake experiments. (**B**) Experimental measurements of outlet glucose concentration after a step change in flow rate as a function of the eluted volume. Sampling was performed continuously (medium was analyzed every 0.6-µL volume eluted). Control data are taken from a chamber having the same inlet conditions as the sample chamber, but no cells inside.* V_{chip} *is the total volume, including culture chamber and microfluidic channels (approximately 1 µL). Error bars represent standard deviation (n=3). Inset: computational simulation of the duration of sampling as a function of volumetric flow rate. (**C**) Experimental steady-state measurements of outlet glucose concentration at increasing flow rates, as a function of the eluted volume. Control experiments were performed as in B). Error bars indicate standard deviation of 3 repeated measurements from the same culture chamber. (**D**) Mean single-cell glucose uptake rate,* U/N_c*, in the culture chamber as a function of flow rate, calculated from data in C).* G_{IN} *was equal to 5.6±0.3 mM.*

Validation of dynamic monitoring of cytosolic glucose concentration

We next validated the suitability of our experimental system for cytosolic glucose detection by the FRET-based nanosensor FLIPglu-600μΔ13V. Myoblasts were seeded within the microfluidic chamber and transfected with the nanosensor plasmid. We used a high flow rate (4μL/min) in these experiments so that glucose concentration on cell membrane, G_m, was approximately equal to its concentration in the inlet, G_{IN}. We performed dynamic stimulations of cells alternating glucose-free and 1.5-mM concentration buffer solution, using the multi-inlet system (Figure 3A). Each concentration was kept constant for 4 min during repeated pulses (Figure 3C). Using dyes of different colors, we verified a delay of approximately 20 s between a change of valve opening in the multi-inlet system and the actual change of medium composition in the cell culture chamber, at the flow rate used (Figure 1C). The square-shaped pulse was fairly conserved (Figure 1C).

We performed live cell imaging for FRET detection (Figure 3B), and analyzed the images, as previously reported[17], to obtain the FRET index r (Figure 3C). A decrease in this index represents an increase in cytosolic glucose concentration. The results show the accuracy of our measurements, with a consistent return to the FRET index baseline after each stimulation pulse. After 4 min of stimulus, FRET signal approximately reaches a new steady state.

In this work we used FRET results at steady-state to determine cytosolic glucose concentration. For using the nanosensor to determine non-steady-state concentrations, the nanosensor-glucose binding needs to be faster than the other intracellular processes involving glucose (membrane transport, phosphorylation, and maybe others), so that a quasi-steady-state approximation holds and online FRET detection is directly correlated to cytosol glucose concentration. However, we will show later that this condition is not satisfied in our system.

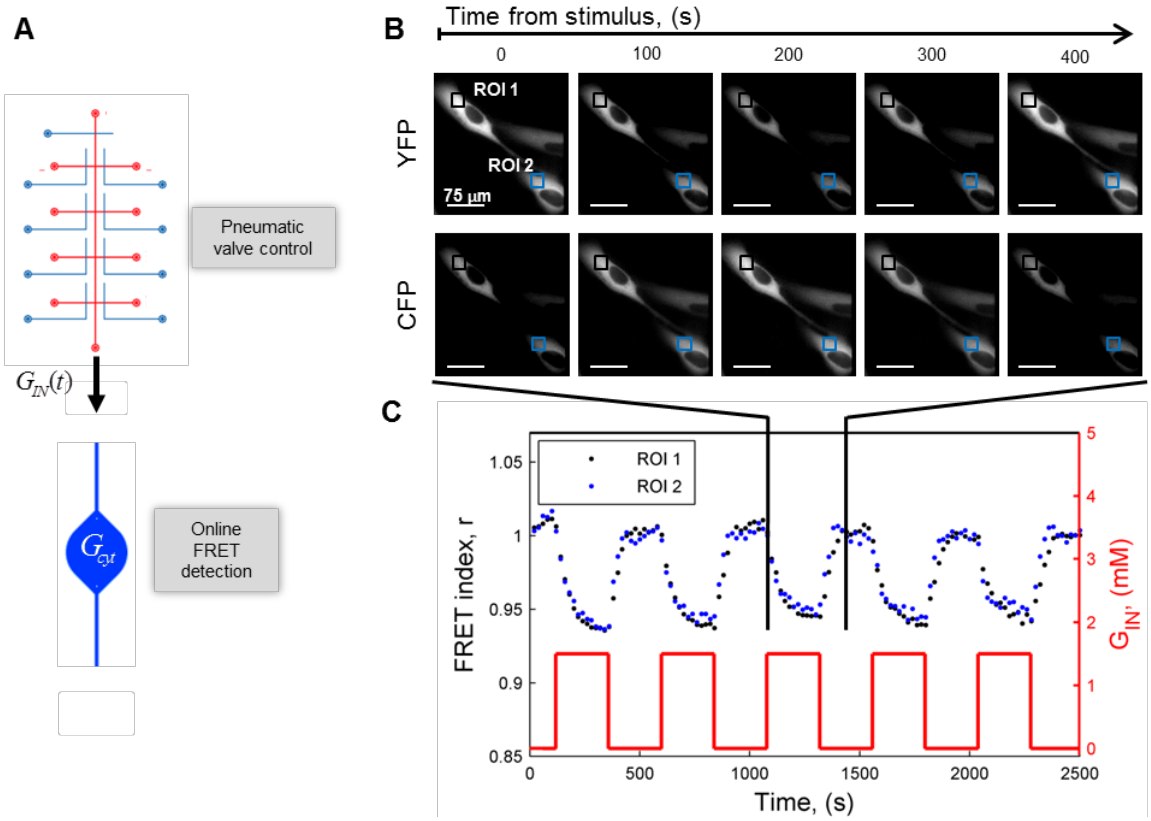

Figure 3. *Dynamic measurements of intracellular glucose concentration via FRET nanosensor. (**A**) Schematic representation of FRET experiments. (**B**) Sequence of images, obtained by fluorescence microscopy, of cyan (CFP) and yellow (YFP) fluorescent signals during pulse perfusion at 1.5 mM glucose concentration. (**C**) Normalized baseline-corrected FRET index, r, during an experiment of 4-min cyclic pulses of 1.5-mM glucose concentration. Blue and black dots refer to the two regions of interest (ROIs) shown in A).*

Dissection of myoblast glucose handling mechanisms

We studied how glucose uptake rate changes as a function of extracellular glucose concentration in the physiological range of concentrations (3-13 mM). To this aim, we measured the uptake for different conditions at the inlet of the culture chamber, keeping the flow rate constant and equal to 0.05 µL/min. Experimental data showed a linear relationship between inlet and outlet glucose concentration, with the latter being about 74% of the former (Figure 4A).

In order to better understand fluid dynamics and glucose mass transport within the microfluidic chip, we developed a 3-dimensional (3D) mathematical model to simulate the experimental operative conditions. In particular, we aimed at investigating the spatial heterogeneity within the culture chamber and the actual glucose concentration in the cell microenvironment, i.e. immediately outside of the cell membrane.

The model described glucose uptake as a consumption flux at the bottom of the culture chamber, whose rate was assumed proportional to glucose concentration at this surface. Under this assumption, the numerical simulation reproduced the linearity of the experimental data ($G_{OUT} = 74\% \cdot G_{IN}$), as shown in Figure 4A.

Model results also highlighted that, at the low flow rate used (0.05 μL/min), the average glucose concentration outside cell membrane, G_m , is reduced to 84% of its concentration at the inlet (Figure 4B). However, this result is specific for the setup geometry we used.

By our 3D model we simulated the glucose concentration profile within the culture chamber. As shown in Figure 4C, a cell near the outlet is exposed to a concentration of glucose that is 27% lower compared to a cell located near the inlet. On the other hand, the concentration gradient in the z-direction is very small (Figure 4C and Supporting Information). Thus, spatial heterogeneity is mainly due to the progressive consumption of glucose by cells located upstream during the 14 min taken by medium to convectively flow from inlet to outlet. The measured overall glucose uptake is an average over a spatially heterogeneous cell population. However, as glucose uptake was described as a linear function of concentration, it is reasonable to assume that the overall uptake is the same as if all the cells were exposed to the average of medium composition shown in Figure 4B.

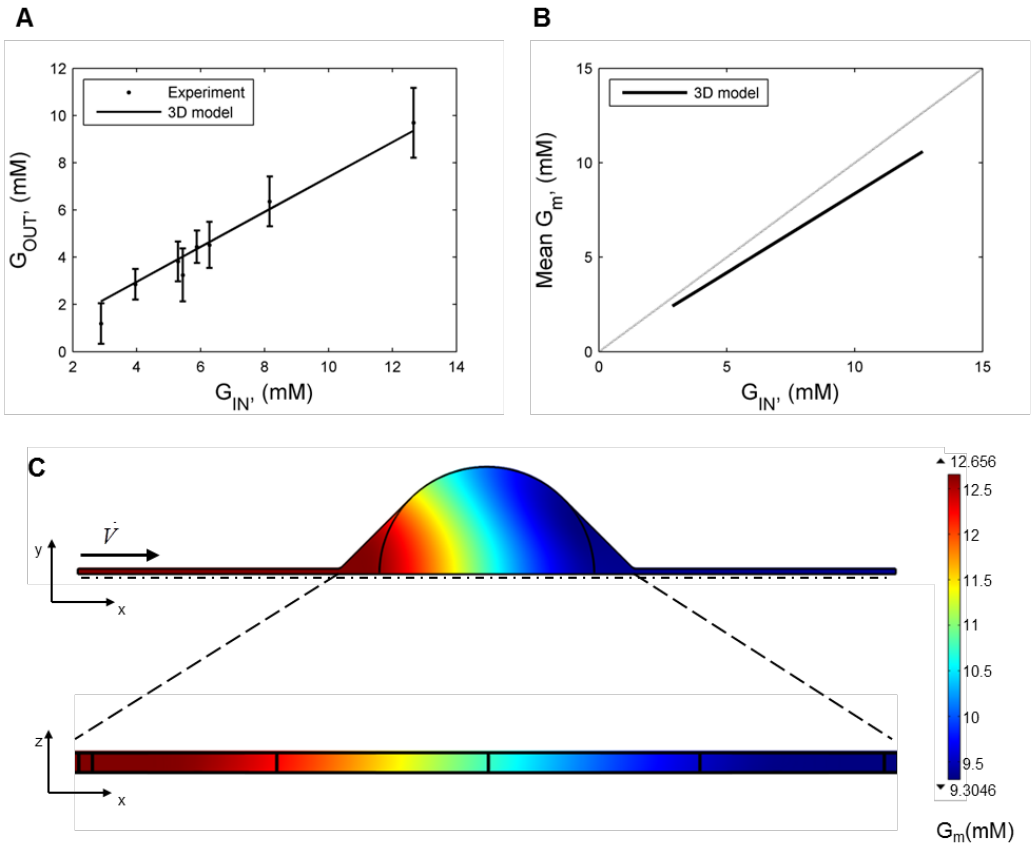

Figure 4. *Results from glucose uptake experiments and simulations.* ***(A)*** *Data of steady-state glucose concentration at the outlet of the culture chamber, obtained from off-line enzymatic measurements, as a function of different inlet glucose concentrations. Error bars: standard deviations (n=3). Solid line: results simulated by the 3-dimensional computational model after fitting parameter* k_U. ***(B)*** *Computational estimation of the mean glucose concentration at cell surface within the culture chamber, calculated by the 3-dimensional model. Linear fit slope: 0.84. Gray line:* $G_m = G_{IN}$. ***(C)*** *Simulation of the glucose concentration profile at steady-state at the bottom of the culture chamber (top) and in the vertical symmetry plane (bottom) for* G_{IN} *equal to 12.7 mM. Flow rate was 0.05 µL/min.*

Next, we performed FRET-based nanosensor experiments to determine cytosolic glucose concentration under different inlet conditions. Flow rate was fixed at approximately 4 µL/min, high enough for the assumption $G_m \approx G_{IN}$, as demonstrated by data in Figure 2C (medium residence time in the chamber was only 11 s).

We applied 4-min pulses of increasing glucose concentrations (0.5-5 mM), separated by 4 min of glucose-free inlet condition (Figure 5A). As expected, the FRET index had larger amplitude of oscillation for pulses of higher glucose concentration. Measurement noise was relevant at low concentrations, but the sensor response showed a good signal-to-noise ratio for concentrations larger than 1 mM. By approximating FRET response at the end of each pulse as a steady state, first we obtained a nanosensor saturation curve (see Supporting Information) and then derived steady-state cytosolic glucose concentration by Eq. (3) as a

function of inlet concentration (Figure 5B). We experimentally found the following linear relationship:

$$G_{cyt} = 0.12 \cdot G_m \qquad (1)$$

that is characteristic of myoblasts stimulated with glucose concentrations up to 5 mM (and maybe even higher), and is independent from the specific experimental setup (system geometry, flow rate).

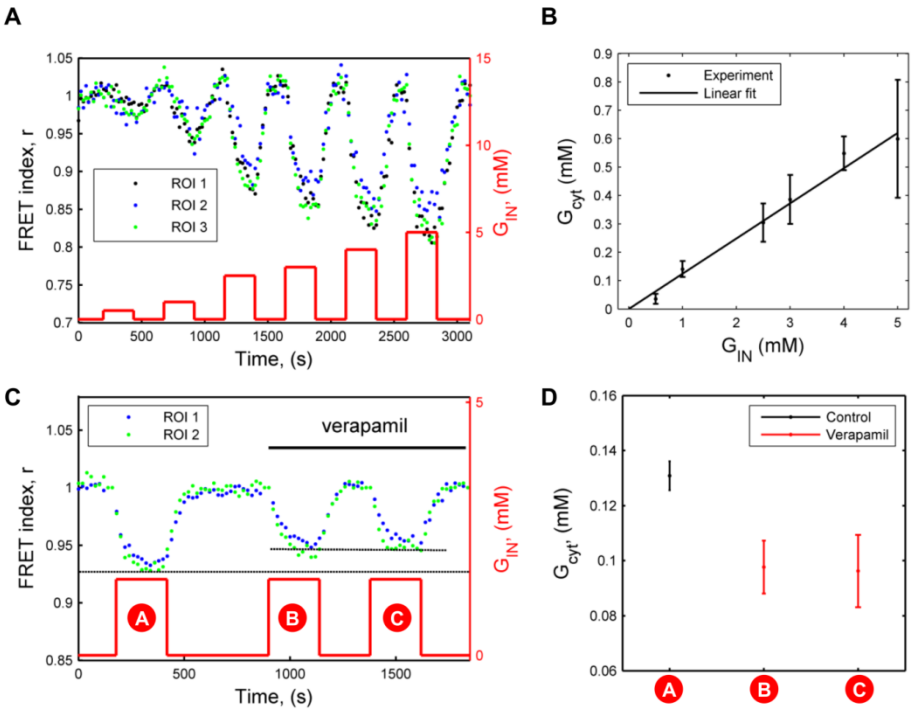

Figure 5. *Effect of glucose concentration on FRET nanosensor response. (**A**) Normalized baseline-corrected FRET index, r, as a function of time during repeated pulses of increasing inlet glucose concentrations (0.5, 1, 2.5, 3, 4, and 5 mM). Black, blue and green dots refer to the signal from 3 different cells. (**B**) Relationship between steady-state cytosolic and inlet glucose concentrations, derived from data in A). Linear fit slope: 0.12. (**C**) Effect of verapamil on FRET nanosensor response. Repeated pulses of inlet glucose concentration (1.5 mM), in presence or absence of verapamil (150 μM), as indicated. Blue and green dots refer to the signal from 2 different cells. (**D**) Decrease of steady-state cytosolic glucose concentration, for* $G_{IN} = 1.5\ mM$ *, in presence of the inhibitor (p-value<0.05), calculated from the data in C. Flow rate was 4 μL/min.*

Perturbing the system with the inhibitor verapamil (150 μM), known to affect glucose transport[24], we obtained a reduction in cytosolic glucose concentration of about 26%, reducing the constant in (Eq. (1)) to 0.065 (Figure 5C and D). This result is consistent with a 30% decrease in glucose uptake obtained in L929 fibroblasts using radiolabeled 2-deoxyglucose[24], and shows how impairments can be precisely detected by our system. We also verified the reversibility of this inhibitory mechanism (see Supporting Information).

The linearity of Eq. (1) is confirmed also by the results obtained from a single-cell balance equation at steady state (Eq. (8)). This simple analytical model was developed assuming a first-order intracellular glucose phosphorylation (Eq. (6)), with kinetic constant k_g. Eq. (8) shows that steady-state G_{cyt} is also dependent on another kinetic constant, $k_m^{'}$, that characterizes the rate of transport through cell membrane.

As previously mentioned, the steady-state measurements of glucose uptake and cytosolic glucose concentration need to be coupled in order to quantitatively dissect the contribution of the two phenomena of glucose transport through cell membrane and glucose phosphorylation, i.e. to determine $k_m^{'}$ and k_g, whose values are reported in Table I. Specifically, Eqs. (8) and (11) were simultaneously solved, the former assuming $G_m \approx G_{IN}$ and the latter using G_m from Figure 4B.

The characteristic times (equal to the reciprocal of the kinetic constants) of glucose transport and phosphorylation are 3.7 s and 0.5 s, respectively. Thus, the latter process is 7.4 times faster than the former, making transport the limiting step of glucose handling process, as already well-known.

While hexokinase 1 (HK1) is the main isoform in human skeletal muscle, hexokinase 2 (HK2) is prevalent in mouse[25]. The Michaelis-Menten kinetics of HK2 has been studied in the literature after purification: Michaelis-Menten constant, K_m, is equal to 0.3 mM and its specific activity to 0.17 U/mg[26], which corresponds to a $V_{\max}$ of 0.57 mM/s. When glucose concentration is lower than K_m, the enzymatic conversion rate can be approximated by a linear expression with proportionality constant $V_{\max} / K_m$, equal to 1.9 s^{-1}. This value is very close to the k_g value we obtained experimentally (2.01 s^{-1}), however the approximation $G_{cyt} << K_m$ does not hold for the whole range of G_{IN} concentrations we used, as shown in Figure 5B.

These results are not contradictory. If in the cellular context the value of K_m increases, then the inequality $G_{cyt} << K_m$ holds and phosphorylation occurs as a 1st-order reaction. To preserve the value of the ratio $V_{\max} / K_m$, a parallel increase in $V_{\max}$ is required. As a speculation, we propose in the Supporting Information an example of a simple dynamics, based on the Briggs-Haldane derivation of the Michaelis-Menten equation, that could support this hypothesis. However, multiple other mechanisms could be equally plausible considering the intracellular molecular crowding.

Our results suggest care in extending *in vitro* kinetics to the cellular context and provide a means to experimentally measure precise metabolic fluxes within the cellular environment.

The direct detection of glucose uptake in a microfluidic system offers accuracy at high time resolution and minimal disruption of culture conditions. Furthermore, to the best of our knowledge, we described the first determination of hexokinase phosphorylation rate in living cells under physiological conditions. Our results are particularly relevant in the context of studies on glucose handling processes, involved in the development of dramatic diseases, such as diabetes and cancer, and not restricted to the particular cell system we analyzed.

From a technological point of view, we also investigated the kinetics of the FRET-based nanosensor used in this study, first theoretically and then experimentally. This is particularly important for using the sensor for dynamic real time measurements. In Figure 6A we present the FRET index data shown in Figure 5A, overlapping the results during the first 100 s of each G_{IN} pulse. As expected, data show a faster response during cellular uptake at higher glucose concentrations. We fitted each curve by an exponential function to obtain the time constant of the nanosensor, τ, which is the same for each curve and equal to 67 s. We confirmed experimentally this result as reported in the Supporting Information. Thus, the binding of glucose to the nanosensor is a very slow process compared to both glucose transport through cell membrane and phosphorylation. As previously mentioned, this means that the FRET-based nanosensor does not give information about the transient cytosolic glucose concentration directly. However, knowing the kinetic constants $k_m^{'}$ and k_g, derived by the procedure above, transient G_{cyt} can be calculated mathematically by Eq. (7). Figure 6B shows the results from computational simulations reproducing the experimental conditions of Figure 6A. The dynamics of cytosolic glucose concentration after a change in the intracellular one is much faster than the nanosensor response. This aspect is particularly relevant and affects the dynamic use of this nanosensor without the combination of other external measurements.

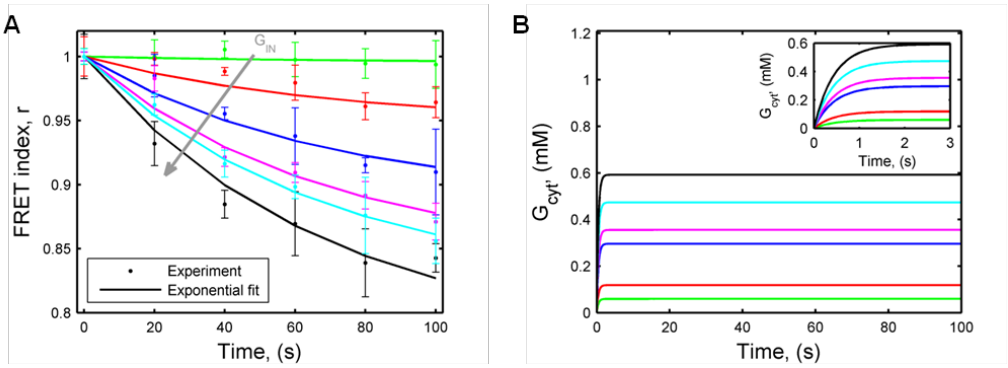

Figure 6. *Analysis of non-steady-state FRET data. (**A**) Transients of FRET nanosensor response at different inlet glucose concentrations (0.5, 1, 2.5, 3, 4, and 5 mM). Data were derived from experimental results in Figure 5A. Time 0 represents the beginning of pulses at different glucose concentrations. Curves were overlapped and fitted by the exponential function:* $A_i + (1 - A_i) \cdot \exp(-t/\tau)$*, where* A_i $(i = 1...6)$ *are constants dependent on* G_{IN} *and* τ *is the nanosensor time constant, equal to 67 s. Error bars: standard deviation of 3 ROIs. (**B**) Simulation of cytosolic glucose transient by Eq. (7) under the same conditions of A). An enlargement is shown in the inset.*

Materials and methods

Single-layer microfluidic chip fabrication

The microfluidic chip containing the cell culture chambers was fabricated according to standard photolithographic techniques[27]. Briefly, the silicon substrate was spin-coated with the negative photoresist SU8-2100 (MicroChem, USA) to obtain a 100-µm thickness of resist layer. After soft baking, UV exposure, post-exposure baking, and development in SU-8 Developer (MicroChem), the mold was hard baked up to 433 K and then cooled to room temperature. Polydimethylsiloxane (PDMS) (Sylgard, Dow Corning, USA) was used for replica molding in the ratio 10:1 (base:cure agent). The mold was treated with chlorotrimethylsilane (Sigma-Aldrich, Italy) vapor for 15 min before casting. The input/output holes on the PDMS chip were made using a 20G needle punch (Small Parts, USA). The PDMS chip was bonded by plasma treatment (Harrick Plasma, USA) onto a 25x60x0.1-mm borosilicate glass cover slip (Menzel Glaser, Germany). Medium reservoirs were built at the inlet and outlet of the chip by adding an additional layer of PDMS. Specifically, holes were made with a 3-mm diameter Biopsy Punch (Integra LifeSciences, USA) in two 25x10x3-mm PDMS slices, and then bonded by plasma treatment on top of the main chip in correspondence to the input/output holes.

Two-layer microfluidic chip fabrication

The microfluidic chip containing the multi-inlet system required two molds for its fabrication to obtain a two-layer PDMS chip[28]. The former had 25-µm round channels

(round mold), obtained from SPR 220-7 (Dow Corning) after reflow during the hard bake time. The latter had 25-µm square channels (square mold) obtained from SU-8 2025 (MicroChem). PDMS was spun on the square mold to obtain a 50-µm thickness layer using a spin coater (Laurell Technologies, USA), and poured on the round mold to make a thick layer (4-5 mm). The thicker PDMS chip was bonded and aligned under a microscope onto the thin one, at the end of the curing phase. The final two-layer chip was bound on a 25x75x1-mm microscope borosilicate glass slide (Menzel Glaser).

Myoblast cell line

C2C12 (ATCC, Italy), an immortalized murine myoblast cell line, were maintained on tissue culture Petri dishes in low-glucose Dulbecco's Modified Eagle Medium (DMEM) (Sigma-Aldrich), supplemented with 10% fetal bovine serum (FBS) (Life Technologies, Italy), and 1% penicillin-streptomycin (pen-strep) solution (Life Technologies). Before confluence, cells were passaged with Trypsin-EDTA 0.05% (Life Technologies) and seeded into the microfluidic chip. Cells were maintained in a humidified incubator at 37°C with 5% CO_2.

Cell culture within the microfluidic chip

Prior to cell seeding, microfluidic channels and cell culture chambers within the chip were filled with 4°C-cold Matrigel® (Becton-Dickinson, USA) 5% in DMEM, incubated at room temperature for at least 1 hour, and washed with DMEM. A cell suspension was then introduced in the microfluidic chambers in order to obtain a seeding density of 250 cell/mm^2. After 1-hour incubation at 37°C and 5% CO_2, culture medium was added drop by drop into the reservoirs to prevent evaporation in the culture chamber and the whole culture system was placed in the incubator. Medium changes were performed every 24 h, by adding fresh medium in the inlet reservoir and aspirating from the outlet using a vacuum pipette. Myoblast differentiation into myotubes occurred spontaneously once myoblasts reached confluence.

Immunofluorescence analyses.

Myoblast differentiation was verified by immunofluorescence analysis for Myosin Heavy Chain II (MHC II), as previously described[29]. Briefly, C2C12 myotubes were fixed with 2% PFA (Sigma-Aldrich) for 7 min, permeabilized with 0.5% Triton X-100 (Sigma-Aldrich) and blocked in 2% horse serum (Life Technologies) for 45 min at room temperature. Mouse monoclonal primary antibody against MHC II (Sigma-Aldrich) was applied for 1 h at 37 °C, followed by incubation with the Alexa488 fluorescence-conjugated anti-mouse IgG secondary antibody (Life Technologies) for 45 min at 37°C. Nuclei were counterstained with

Hoechst (Life Technologies) and samples maintained in PBS during fluorescence microscopy analysis.

Glucose uptake measurements

DMEM having 3- to 13-mM glucose concentrations was obtained by mixing 25-mM glucose and glucose-free DMEM media (Life Technologies) in different ratios. DMEM was then supplemented with 10% FBS and 1% pen-strep, and conditioned overnight in the incubator. Using a sterile plastic syringe (Becton-Dickinson), conditioned medium was used to wash four 0.02" ID Tygon® tubes (Cole-Palmer, USA). Each tube was then connected at one end to a 100-µL Hamilton syringe (Hamilton, USA) pre-loaded with conditioned medium, and at the other end to the microfluidic chip inlet through a 21G stainless-steel needle (Small Parts). Hamilton syringes were set up on a syringe pump (Harvard Apparatus, USA) and perfusion started at flow rates in the range 0.0125-0.5 µL/min. At the outlets of the microfluidic chambers, needles were inserted to facilitate medium collection at different time points. Medium samples of 0.6-µL volume were analyzed off-line with FreeStyle Lite® glucometer and strips (Abbott Diabetes Care, Italy) to measure glucose concentration G_{OUT}.

Cell transfections

Plasmid pcDNA3.1-FLIPglu-600µΔ13V, previously developed in our lab[17], was amplified and purified by GenElute™ HP Plasmid MaxiPrep Kit (Sigma-Aldrich). At the time of transfection, two solutions were prepared: (1) 0.2 µg DNA in 25 µL Opti-MEM® (Life Technologies), and (2) 1.5 µL Lipofectamine in 25 µL Opti-MEM. They both were incubated for 5 min at room temperature, mixed together and incubated for another 20 min at room temperature. The final transfection solution was then prepared adding 100 µL of Opti-MEM to the previous mixed solution. Part of this transfection solution was used to suspend the cells to be seeded at a concentration of 5000 cell/µL into the microfluidic chip. Cells adhered to the surface in about 30 min. The remaining solution was used to change the transfection solution within the chip every hour until the end of transfection (5 h). Then, culture medium was injected into the chip.

FRET image acquisition and analysis

Imaging was performed 24-48 h after transfection at the inverted microscope IX81 (Olympus, Italy) with a 40X/1.30 oil immersion objective (Olympus). The microscope was equipped with a CCD camera (SIS F-View), an illumination system MT20 (Olympus), and a beam-splitter optical device (Multispec Microimager; Optical Insights). Dual emission intensity ratio was simultaneously recorded using cellR 2.0 software (Olympus) after both

excitation at 430/25 and 500/20 for the two emission filters (470/30 CFP and 535/30 for YFP). Images were acquired within the linear detection range of the camera at intervals of 20 s for up to 1 hour. Exposure time was set to 200 ms. All experiments were carried out at room temperature.

Acquired FRET images were analyzed as previously reported[17], with spectral bleed-through (SBT) and baseline correction using polynomial fit. The analysis produced the normalized baseline-corrected FRET index, r.

FRET experiments

During FRET image acquisition, perfusion through the cell culture chamber was performed at 4 μL/min. Cells were imaged in DPBS with calcium and magnesium 1X (Life Technologies) with added different glucose concentrations (Sigma-Aldrich). A microfluidic multi-inlet system was placed upstream of the culture chamber and connected by a vertical 5-cm long PEEK tube, having inner diameter of 65 μm (IDEX, USA), to produce the pressure-driven flow. This system allowed switching between up to 9 different glucose concentrations during an experiment by controlling valve opening and closing via LabView software (National Instruments, Italy). Cyclic pulses of different glucose concentrations were alternated with glucose-free infusion every 4 min.

Determination of cytosolic glucose concentration

The normalized baseline-corrected FRET index, r, was used to calculate glucose saturation, S, of FRET nanosensor by the following expression:

$$S = 1 - \frac{r - r_{\min}}{r_{\max} - r_{\min}}, \qquad (2)$$

where $r_{\min}$ represents FRET index under glucose-free conditions, and $r_{\max}$ the index under high glucose concentrations at sensor saturation. Steady-state cytosolic glucose concentration, $G_{cyt,ss}$, is then obtained using the glucose dissociation constant, K_d, equal to 0.59 mM from previous nanosensor calibration[17]:

$$G_{cyt,ss} = \frac{K_d \cdot S}{1 - S}. \qquad (3)$$

Three-dimensional mathematical model

A 3D mathematical model was developed to describe fluid dynamics and mass transport in the experimental system. The system geometry included the cell culture chamber and the inlet and outlet microfluidic channels. Geometric dimensions matched those of the experimental setup. Because of the system symmetrical geometry, only one half of it was

simulated. The velocity field in the microfluidic channel was obtained solving the continuity equation and the equation of motion for an incompressible Newtonian fluid. The glucose concentration field was obtained by solving its equation of continuity. Glucose uptake by the cell layer at the bottom of the culture chamber was included in the model as a flux boundary condition, i.e. by an outward homogeneous glucose flux proportional to glucose concentration on the surface. The proportionality constant, k_U, was obtained by least-square regression of glucose uptake measurements and equal to $3 \cdot 10^{-8}$ m/s. The mean value of medium concentration in the vicinity of the cells, G_m, was calculated by numerical integration of glucose concentration on the bottom surface of cell culture chamber. The model was implemented in Comsol Multiphysics (COMSOL, Sweden) using a relative tolerance of 10^{-6} for the solution. Coarsening and refining the mesh space grid ensured that the results were independent of the spatial discretization.

Single-cell model

An analytical model was also developed in the form of a single-cell balance equation, including the flow of glucose across the cell membrane, F_m, and that of glucose intracellular consumption through glycolysis, F_g:

$$V_c \frac{dG_{cyt}}{dt} = F_m - F_g , \qquad (4)$$

where G_{cyt} represents glucose concentration in the cytoplasm, t is time, and V_c represents the intracellular volume where glucose is phosphorylated. We assumed V_c equal to the cytosolic volume, as studies on hexokinase exclude a nuclear localization for this enzyme under normal conditions [18,30]. At steady-state, the term on the left hand side of (4) is null.
The first flow rate on the right hand side is expressed as:

$$F_m = k_m \cdot S_c \cdot \left(G_m - G_{cyt}\right), \qquad (5)$$

where k_m is the overall mass transfer coefficient and S_c represents the cell surface. The second flow rate, due to glucose phosphorylation by hexokinase enzyme, is given by the following expression:

$$F_g = k_g \cdot V_c \cdot G_{cyt} , \qquad (6)$$

where k_g is the reaction kinetic constant.

After substitution of Eqs. (5) and (6), cytosolic glucose concentration, G_{cyt}, after a step change from 0 to G_{IN}, is obtained by Eq. (4):

$$G_{cyt}(t) = \frac{k_m^{'}}{k_m^{'} + k_g} \cdot \left(1 - \exp\left(-\left(k_m^{'} + k_g\right) \cdot t\right)\right) \cdot G_{IN} , \qquad (7)$$

where $k_m^{'} = k_m \cdot S_c / V_c$; and steady-state glucose concentration, $G_{cyt,ss}$, is then:

$$G_{cyt,ss} = \frac{k_m^{'}}{k_m^{'} + k_g} \cdot G_m \,. \qquad (8)$$

Overall mass balance

A macroscopic mass balance was performed considering the whole culture chamber as the system of interest. The overall glucose uptake, U , by the cell population is given by the following expression:

$$U = \dot{V} \cdot (G_{IN} - G_{OUT}) \,, \qquad (9)$$

where $\dot{V}$ is medium flow rate, G_{IN} and G_{OUT} are glucose concentrations at the inlet and outlet of the chamber, respectively. At steady state, flow rates are equals and these equalities hold:

$$U = N_c \cdot F_m = N_c \cdot F_g \,, \qquad (10)$$

where N_c represents the number of cells in the culture chamber. Combining Eqs. (5), (6) and (10), the following expression is obtained:

$$U = \left(\frac{1}{k_m^{'}} + \frac{1}{k_g} \right)^{-1} \cdot N_c \cdot V_c \cdot G_m \,. \qquad (11)$$

Conclusions

We developed a methodology for quantitatively dissecting the kinetics of glucose intracellular transport, single-cell uptake and phosphorylation kinetics in live myoblasts. We took advantage of multiple technologies: a microfluidic system that enhances cell microenvironment dynamic control and measurement sensitivity, a FRET-based nanosensor that measures cytosolic glucose in live cells with high spatial resolution, and mathematical modeling to assist data interpretation.

We used this procedure to analyze glucose metabolism in myoblasts, accurately determining single-cell kinetics of glucose flow through cell membrane and phosphorylation. In particular, we found the following results in myoblasts under physiological glucose concentrations: (1) steady-state cytosolic glucose concentration is only 12% of the intracellular concentration in the immediate vicinity of cell membrane; (2) intracellular glucose phosphorylation is 7.4 times faster than glucose transport through cell membrane; (3) the characteristic times of transport and phosphorylation are 3.7 s and 0.5 s, respectively; (4) the time required for a cell to reach a new steady state after a change in

extracellular glucose concentration is approximately 2 s; (5) within the intracellular context hexokinase has a 1st-order kinetics also at higher glucose concentrations compared to what was previously known from studies performed with the purified enzyme.

We also found that FRET-based nanosensor FLIPglu-600μΔ13V can be used for dynamic cytosolic measurements only indirectly via mathematical modeling, as its kinetics is much slower than those of cellular glucose handling processes. However, through mathematical modeling, it can be successfully used for very accurate measurements of intracellular kinetics under physiological conditions, once its measurement is coupled with the detection of glucose uptake.

A very relevant perspective of this work is the extension of glucose-related processes dissection to different biological systems involved in metabolic impairments. In particular, live myotubes are phenotypically more similar to skeletal muscle *in vivo*, compared to myoblasts. We were able to efficiently differentiate myoblasts within the microfluidic culture chamber, obtaining myotubes showing a mature sarcomeric organization (Figure 7). Currently, direct transfection of myotubes with the FRET nanosensor resulted too inefficient for reliable measurements. However, transfecting them using a different vector for constitutive expression, such as a lentivirus encoding the nanosensor, could overcome this limitation and extend the applicability of the methodology.

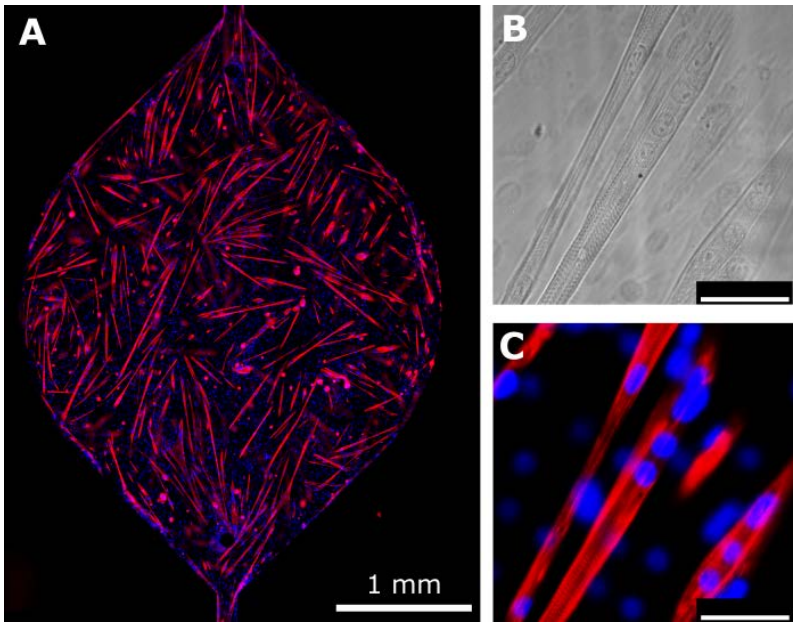

Figure 7. *Differentiated myotubes within the microfluidic culture chamber. (**A**) Immunofluorescence analysis of myotubes derived from murine myoblasts after 7 days of differentiation. Red: myosin heavy chain II, blue: Hoechst for nuclei. (**B-C**) Enlargement of myotubes in (A), bright field and fluorescence images highlighting the sarcomeric structure. Scale bar: 50 μm.*

Acknowledgement

This work was supported by Progetti di Eccellenza CaRiPaRo and the European Foundation for the Study of Diabetes, WBF was supported by funds from the Carnegie Institution.

Notes and references

Electronic Supplementary Information (ESI) available

1. B. M. Frier, *Diabetologia*, 2009, **52**, 31–34.
2. M. Laakso, *Diabetes*, 1999, **48**, 937–942.
3. P. E. Cryer, S. N. Davis, and H. Shamoon, *Diabetes Care*, 2003, **26**, 1902–1912.
4. A. P. Rolo and C. M. Palmeira, *Toxicol. Appl. Pharmacol.*, 2006, **212**, 167–178.
5. J. Kim and C. V. Dang, *Cancer Res.*, 2006, **66**, 8927–8930.
6. R. B. Bird, W. E. Stewart, and E. N. Lightfoot, *Transport Phenomena*, John Wiley & Sons, 2007.
7. B. Thorens and M. Mueckler, *Am. J. Physiol. - Endocrinol. Metab.*, 2010, **298**, E141–E145.
8. K. Ohtsubo, M. Z. Chen, J. M. Olefsky, and J. D. Marth, *Nat. Med.*, 2011, **17**, 1067–1075.
9. C. Luni, J. D. Marth, and F. J. Doyle, *PLoS ONE*, 2012, **7**, e53130.
10. L. Sokoloff, M. Reivich, C. Kennedy, M. H. D. Rosiers, C. S. Patlak, K. D. Pettigrew, O. Sakurada, and M. Shinohara, *J. Neurochem.*, 1977, **28**, 897–916.
11. F. Turkheimer, R. M. Moresco, G. Lucignani, L. Sokoloff, F. Fazio, and K. Schmidt, *J. Cereb. Blood Flow Metab.*, 1994, **14**, 406–422.
12. W. H. Kim, J. Lee, D.-W. Jung, and D. R. Williams, *Sensors*, 2012, **12**, 5005–5027.
13. L. Speizer, R. Haugland, and H. Kutchai, *Biochim. Biophys. Acta BBA - Biomembr.*, 1985, **815**, 75–84.
14. K. Yoshioka, H. Takahashi, T. Homma, M. Saito, K.-B. Oh, Y. Nemoto, and H. Matsuoka, *Biochim. Biophys. Acta BBA - Gen. Subj.*, 1996, **1289**, 5–9.
15. M. Kurtoglu, J. C. Maher, and T. J. Lampidis, *Antioxid. Redox Signal.*, 2007, **9**, 1383–1390.
16. M. Fehr, S. Lalonde, I. Lager, M. W. Wolff, and W. B. Frommer, *J. Biol. Chem.*, 2003, **278**, 19127–19133.
17. B.-H. Hou, H. Takanaga, G. Grossmann, L.-Q. Chen, X.-Q. Qu, A. M. Jones, S. Lalonde, O. Schweissgut, W. Wiechert, and W. B. Frommer, *Nat. Protoc.*, 2011, **6**, 1818–1833.
18. J. E. Wilson, *J. Exp. Biol.*, 2003, **206**, 2049–2057.

19. J. D. Lueck and H. J. Fromm, *J. Biol. Chem.*, 1974, **249**, 1341–1347.

20. W. T. Jenkins and C. C. Thompson, *Anal. Biochem.*, 1989, **177**, 396–401.

21. S. Rodríguez-Enríquez, A. Marín-Hernández, J. C. Gallardo-Pérez, and R. Moreno-Sánchez, *J. Cell. Physiol.*, 2009, **221**, 552–559.

22. C. X. Bittner, A. Loaiza, I. Ruminot, V. Larenas, T. Sotelo-Hitschfeld, R. Gutiérrez, A. Córdova, R. Valdebenito, W. B. Frommer, and L. F. Barros, *Front. Neuroenergetics*, 2010, **2**, 26.

23. N. Kotliar and P. F. Pilch, *Mol. Endocrinol.*, 1992, **6**, 337–345.

24. L. L. Louters, N. Stehouwer, J. Rekman, A. Tidball, A. Cok, and C. P. Holstege, *J. Med. Toxicol.*, 2010, **6**, 100–105.

25. J. E. Wilson, in *Reviews of Physiology, Biochemistry and Pharmacology, Volume 126*, Springer Berlin Heidelberg, Berlin, Heidelberg, 1995, vol. 126, pp. 65–198.

26. R. L. Printz, S. Koch, L. R. Potter, R. M. O'Doherty, J. J. Tiesinga, S. Moritz, and D. K. Granner, *J. Biol. Chem.*, 1993, **268**, 5209–5219.

27. J. C. McDonald and G. M. Whitesides, *Acc. Chem. Res.*, 2002, **35**, 491–499.

28. J. Melin and S. R. Quake, *Annu. Rev. Biophys. Biomol. Struct.*, 2007, **36**, 213–231.

29. S. Zatti, A. Zoso, E. Serena, C. Luni, E. Cimetta, and N. Elvassore, *Langmuir ACS J. Surf. Colloids*, 2012, **28**, 2718–2726.

30. S. John, J. N. Weiss and B. Ribalet, PLoS One, 2011,6(3), e17674.

Electronic Supplementary Information (ESI)

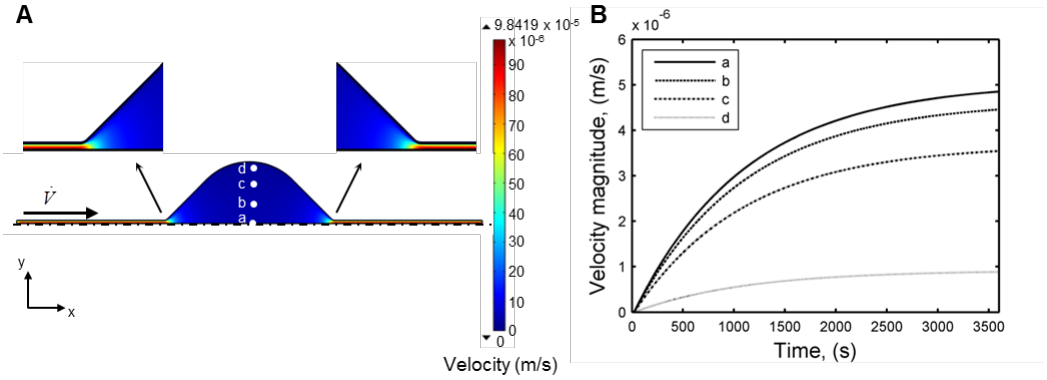

Figure S1. *Fluid dynamics study using the developed 3D model. (**A**) Simulation of the velocity field at steady state in the median plane (z = H/2) of the culture chamber. Flow rate was 0.05 µL/min. (**B**) Velocity magnitude during the step change in flow rate from 0 to 0.05 µL/min. a, b, c, and d, refer to the positions indicated in A).*

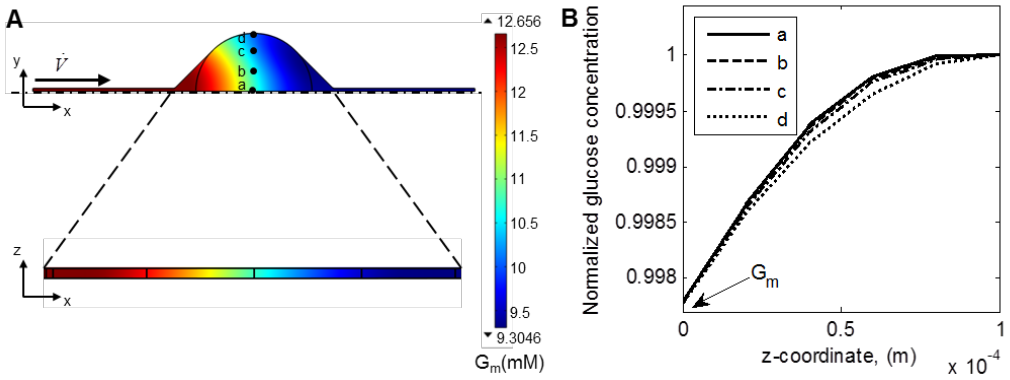

Figure S2. *Study of the concentration profile within the microfluidic chip simulated by the developed 3D model. (**A**) Same as Figure 4C, with indicated the position of points a, b, c, d plotted in B). (**B**) Glucose concentration along the z-direction at positions indicated in A). Concentration was normalized by the concentration at the top of the channel (z = H) in each position.*

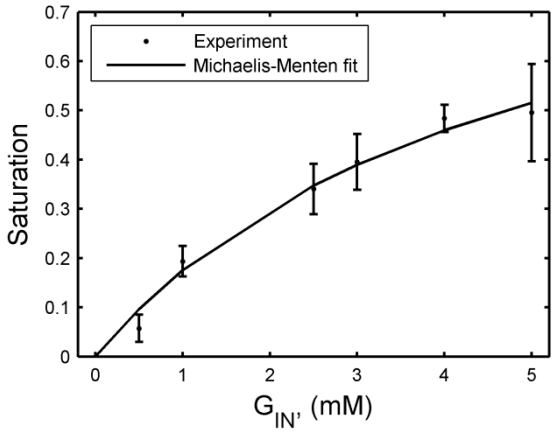

Figure S3. *FRET-based nanosensor saturation curve. Saturation was calculated by Eq. (2) from the steady-state FRET data presented in Figure 5A. Solid line represents the results of least-square data fitting by a Michaelis-Menten-like equation.*

Potential hexokinase enzymatic rate modification in the intracellular environment

We considered the classical elementary steps of an enzymatic reaction:

$$S + E \underset{k_{-1}}{\overset{k_1}{\rightleftarrows}} ES \xrightarrow{k_2} P$$

where S represents glucose, E hexokinase enzyme, ES the enzyme-substrate complex, and P glucose-6-phosphate. Mass-action kinetic parameters are indicated as k_1, k_{-1}, and k_2

.

The Briggs-Haldane derivation of Michaelis-Menten equation assumes ES concentration is at quasi-steady state, i.e. in mathematical terms:

$$k_1[E][S] \approx (k_{-1} + k_2)[ES] \qquad \text{(S12)}$$

where square brackets represent concentrations. Following this approximation the well-known Michaelis-Menten equation is obtained:

$$\frac{d[P]}{dt} = \frac{V_{\max}[S]}{K_m + [S]}, \qquad \text{(S13)}$$

where the values of parameters K_m and $V_{\max}$ are related to the mass-action constants by the following expressions:

$$K_m = \frac{k_{-1} + k_2}{k_1}, \qquad \text{(S14)}$$

and

$$V_{\max} = k_2 [E]_0, \qquad \text{(S15)}$$

where $[E]_0$ is the total (constant) enzyme concentration in its bound and unbound states.

From Eqs. (S14) and (S15), the ratio of $V_{\max}$ to K_m is given by the following relationship:

$$\frac{V_{\max}}{K_m} = \frac{k_2 [E]_0}{\frac{k_{-1} + k_2}{k_1}}. \qquad \text{(S16)}$$

Under the feasible assumption that $k_{-1} \gg k_2$, Eq. (S16) becomes:

$$\frac{V_{\max}}{K_m} \approx \frac{k_2 [E]_0}{\frac{k_2}{k_1}} = k_1 [E]_0. \qquad \text{(S17)}$$

Eq. (S17) shows that under the two simple assumptions above, it is possible to have a linear relationship between $V_{\max}$ and K_m. Assuming that, compared to *in vitro* enzymatic experiments, the intracellular environment favors the production of glucose-6-phosphate by speeding up the reaction described by parameter k_2, this would imply an increase in $V_{\max}$ and K_m, without affecting their ratio.

Analysis of FRET-based nanosensor characteristic time

We performed further experiments using the FRET-based nanosensor to verify the accuracy of its time constant that we obtained. In particular, we stimulated the cells with approximately linear ramps of glucose concentration at increasing rate (Figure S4 A). According to the model developed, once the rise in glucose concentration is faster than the rate of nanosensor response, the nanosensor responds at its maximum rate and its half-time for saturation ($t_{1/2}$) is not affected by a further increase in the speed of the ramp any more (Figure S4 B).

The experimental results we obtained confirm this theoretical prediction. In particular, Figure S4 F shows that experimental results are in agreement with model simulations. Below about 10^0 min, the nanosensor characteristic time, the half-time for saturation remains approximately constant.

One would say that other resistances could be present that prevent nanosensor access to glucose as it is intracellular. However, we obtained the characteristic time of glucose uptake by myoblasts in culture, equal to 3.7 s, through repeated enzymatic assays of medium out flowing from the culture chamber, in a microfluidic culture system that enhanced the signal-to-noise-ratio. As the process of glucose transport through cell membrane is much faster than the interaction of glucose with the nanosensor, it is possible to analyze the kinetics of the nanosensor within the cell, because the cell membrane transport is essentially not affecting the measurement.

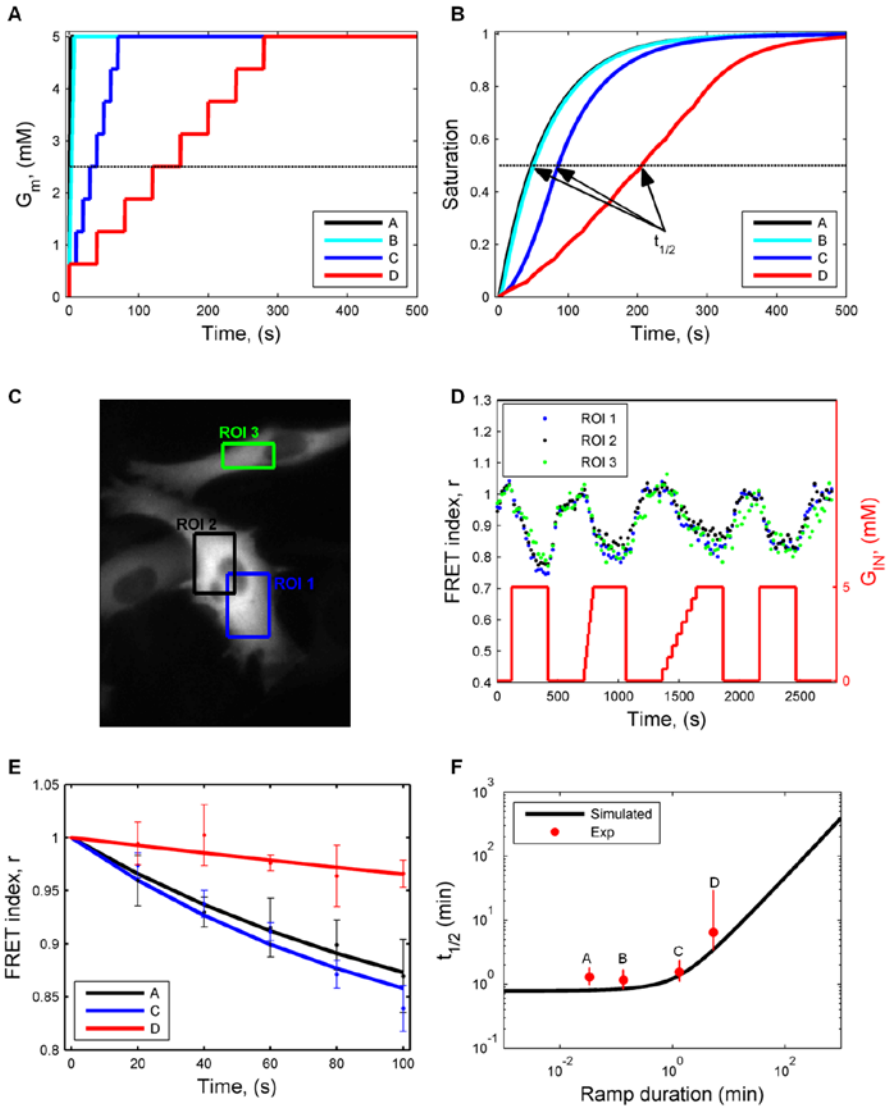

Figure S4. *Study of FRET-based nanosensor time constant. (**A**) Simulated approximately linear ramps of glucose concentration of increasing rate. The step approximation mimics the inflow from the multi-inlet system into the culture chamber. (**B**) Model predictions of the nanosensor response to the stimuli described in (A). (**C**) Image of YFP fluorescence and indication of the ROIs analyzed in (D) and (E). (**D**) Experimental data of FRET-based nanosensor response to the glucose concentration profile indicated. (**E**) Analysis of the transient of FRET index decay following an increase in glucose concentration as shown in (D). Error bars indicate the standard deviation calculated from the 3 ROIs. (**F**) Comparison between the half-time for sensor saturation obtained by experimental data and model simulations. The experiment was repeated twice.*

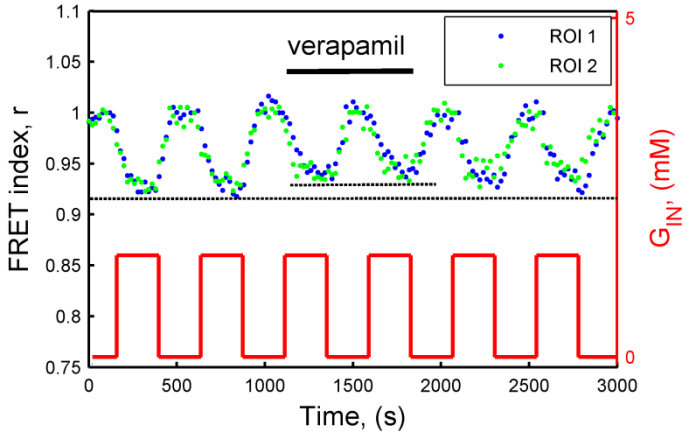

Figure S5. *Effect of verapamil stimulation on cell response to glucose. Normalized baseline-corrected FRET index, r, as a function of time during repeated pulses of 1.5-mM glucose concentration, in presence or absence of glucose transport inhibitor, verapamil (150 μM). Removal of verapamil after 2 glucose pulses shows the inhibitory effect is reversible. Blue and green dots refer to the signal from 2 different cells. Flow rate was 4 μL/min.*

Appendix E

Methods and Experimental Protocols

E.1 Cell culture protocols

E.1.1 C2C12 proliferation and differentiation

C2C12 is an immortalized cell line of murine myoblasts. Protocol for cells expansion was described by Zatti et al. (Appendix B) and adapted for the culture in the microfluidic chip as described by Zambon et al. in Appendix D.

Briefly, C2C12 are expanded in 10 mm dishes tissue culture (Becton-Dickinson) with proliferation medium composed by Dulbecco Modified Eagle's Medium (DMEM, Sigma-Aldrich), supplied with 10% Fetal Bovine Serum (FBS, Life Technologies), and 1% Penicillin-Streptomycin mix (Life Technologies). Before cells reach confluence, they are trypsinized with Trypsin-EDTA 0.05% (Life Technologies) and re-plated either in new dishes or into the microfluidic chip.

Before cell seeding, microfluidic chip are sterilized by autoclave processing. After sterilization, chips are moved into a 35 mm Petri dish under sterile hood and injected with cold Matrigel® (Becton-Dickinson), 2.5% in DMEM; the chip is kept at room temperature for at least 1 hour. The Matrigel® coating is then removed by washing microfluidic chamber with proliferation medium. A cells suspension is then prepared in order to obtain a cell seeding density of 200 cell/mm^2 and injected in the chip. The bottom of the dish is covered with 1 ml of PBS 1X, in order to maintain proper humidity. The cells are kept in incubator at 37°C, 5% CO^2 for 3 to 5 hours, until they adhered to the bottom glass of the chip. After their adhesion, medium is changed every 12 hours by the help of lateral reservoir well placed on the top of inlet/outlet channels. Medium is changed by adding new medium in the lateral wells and rapidly perfusing it inside the chambers with the help of a vacuum pipette.

Differentiation of C2C12 into myotubes in the chip is achieved spontaneously, after 4 to 5 days from seeding. To help differentiation, medium at this point is replaced every 24 h with same procedure reported for proliferation. Myotubes are visible after 7 days from seeding.

E.1.2 Human Skeletal Muscle Cells extraction, expansion and differentiation

Human primary myoblasts were isolated from skeletal muscle biopsies derived from patient undergoing surgery. Human myoblasts isolation was performed in the laboratory of Dr. Karim Bouzakri (University of Genève) following methods reported in (Bouzakri et al., 2003).

Briefly, human skeletal muscle biopsy is maintained, right after explant, in 20 ml of physiological solution at +4 °C for 2 hours, to permit blood coagulation. The biopsy is then processed under sterile hood with scalpels, in order to isolate single muscle fibers from connective, adipose and blood vessel tissues. The isolated fibers is then maintained in a solution 0.05% Trypsin-EDTA at 37°C for 3 hours in order to extract single cell myoblasts precursors. Surnatant trypsin with floating myoblasts is then moved in a new tube adding an equal amount of Fetal Calf Serum (FCS, Life Technologies) in order to stop its action and avoid cells disruption. The solution of FCS and trypsin is centrifuged at 200 g for 5 min. The pellet is resuspended in 10 ml of Skeletal Muscle Cell Basal Medium (PromoCell) and pre-plated in a Petri dish in order to facilitate fibroblasts adhesion. After 2 h, the medium is collected and plated in a 25 mm^2 tissue-culture flask: primary human myoblasts are visible after 7 days of culture. When myoblasts start to grow, medium is changed every 2-3 days and before they reach confluence, they can be passed by trypsinization with Trypsin-EDTA 0.05%.

Cell seeding into the microfluidic chip follows the same procedure described for C2C12 in A.1.1. Differentiation of human myoblasts in myotubes into the microfluidic chip was achieved by switching the Basal medium with Differentiating Medium composed by DMEM, 2% Horse Serum (HS, Life Technologies) once cells reach confluence. At this stage, medium is changed every 24 h. Well differentiated human myotubes are obtained after 5 to 8 days in differentiating medium.

E.2 *Ex vivo* adipose tissue culture

E.2.1 Biopsy preparation

Biopsies of omental adipose tissue are kindly provided from prof. Avogaro from Policlinic Hospital, right after surgery. Protocol for their *in vitro* culture, was adapted from [3]. Before

processing, they are maintained in 5 ml of DMEM 5 mM glucose (Life Technologies), for no more than 3 h at room temperature. Under sterile hood, biopsy is put in a 100 mm Petri dish, wash with PBS 1X and cut in 4 mm diameter, 1 mm high slides with the help of sterile punch and scalpel. Each slice is then placed in a tube filled with 100 uL DMEM pre-weight, and then weight again in order to calculated each slice mass. Biopsy samples are finally put in a 48well plate with 300 µl of DMEM for at least 12 hours before performing dynamic culture, in order to permit sample adaptation.

E.2.2 Biopsy integration within the platform and culture

DMEM 4 mM glucose is previously conditioned in incubator (37°C, 5% CO2, 95% relative humidity) into a Petri dish, for at least 2 hour. Then medium is loaded in 4 sterile plastic syringes, 3 ml volume (Becton-Dickinson). After the medium loading, inlet Tygon® tubes are then connected to the syringe; medium is then flown inside the tubes. Syringes are set up on the syringe pump (Harvard Apparatus). Helped by sterile tweezers, inlet ends are connected to the microfluidic chip, and the syringe pump is started at 10 µl/min flow rate. Tubes are connected to an empty microfluidic chip. It is conditioned at 1 µl/min for at least 4 hours in order to wash out PDMS residual and avoid cytotoxicity. Flow perfusion is decreased or stopped during biopsy insertion. Chambers are filled with at least 3 biopsy slides for experiments, one slide for one chamber, by choosing ones with the same weight.
Sealing is ensured covered with biocompatible sterile PMMA and PDMS cup. One microfluidic chamber is kept empty as control for glucose concentration measurements. Microfluidic platform system is finally put in the incubator for the culture. Pumps are set at a flow rate of 25 nl/min. At the end of the cultures, adipose tissue biopsies can be either frozen for further histological analyses or tested for vitality through MTT test.

E.3 Tissue on a chip characterization

E.3.1 Immunofluorescence

Myoblasts and myotubes cultured in the microfluidic chip can be analyzed by immunofluorescence analyses for the expression of myogenic markers (e.g. Desmin, Myosin Heavy Chain II MHC II). Firsts, cells are fixed with paraformaldehyde (PFA, Sigma-Aldrich), 4% in PBS 1X (Life-Technologies) for 15 min. After washes with PBS, cells are treated with Tryton (Sigma-Aldrich) 0.25% in PBS for 8 min and blocked with scomplemented HS 2% in PBS. Follows incubation with proper primary and secondary antibodies diluted in BSA (Sigma-Aldrich), 3% in PBS. More specifically, mouse monoclonal primary antibody against

Myosin Heavy Chain II (MHC, Sigma-Aldrich) or mouse monoclonal primary antibody against Desmin (DAKO) was applied for 1 h at 37 °C, while the Alexa488 fluorescence-conjugated anti-Mouse IgG secondary antibody (Invitrogen) was applied for 45 min at 37 °C. Nuclei were finally counterstained with DAPI (Sigma-Aldrich) or Hoechst (Life Technologies).

E.3.2 Immunoblotting

Microfluidic cultures are treated ice-cold with 12 µl of lysis buffer: 5% DOC in TBS supplemented with Complete EDTA-free protease inhibitor cocktail (Roche) and anti-phosphatases cocktails (Simga-Aldrich). Lysis buffer is directly injected in the microfluidic channel in order to detach and lysate myotubes from the microfluidic channel. All the lysate volume is collected; cell fractions are sedimented by centrifugation at 13000 g for 20 min at 4°C, and supernatant collected and store at -80 °C. All the supernatant volume is solubilized in loading buffer (Invitrogen), 10% DTT (Invitrogen) and heated for 10 minutes at 70°C. Proteins are then resolved in 4-12% precast gels (Tris-Acetate NuPAGE, Invitrogen) and transferred on PVDF membranes (Invitrogen) under a potential difference of 45V, 400mA for 2 h. Membranes are blocked with 5% nonfat dry milk (Bio-Rad) in TBST (TBS, 0.05% Tween 20) for 1 h and probed with proper primary antibodies specific for phospho-Akt (Ser 473), Akt, Phospho-AS160 (Thr 642), AS160 (all from Cell Signaling) and GAPDH (Abcam) and then with the proper HRP–conjugated secondary antibodies: goat anti-rabbit antibody (Invitrogen) and goat anti-mouse antibody (BioRad). Proteins are visualized by enhanced chemiluminescence (Invitrogen) and protein content is quantified by densitometry using ImageJ software (US National Institutes of Health). For each culture condition, we quantified the intensity of phosphorylated form of Akt and AS160 and normalized them by the basal protein quantification.

E.3.3 Hematoxylin & Eosin stain

Adipose tissue slides after microfluidic culture can be removed from chip and further analyzed. Once culture is over, adipose tissue samples are embedded in OCT®, rapidly passed in liquid nitrogen and stocked at -80°C. Each sample is cryosectioned into 20 to 40 um thick slices. Cryosections are cut onto poly-L-lysine coated glass microscope slides (SuperFrost® Menzel-Glazer) and slides store at -80°C.

Hematoxylin and Eosin (H&E) is an hystochemical analysis that permit to visualize cytoplasm in orange/red and nuclei in violet/blue. Briefly, slides with adipose tissue cryosections are kept at room temperature for 10 min approximately. Then slides are passed in Hematoxylin (Sigma-Aldrich) for 2 min, followed by a rinse with running tap

water for 15 min. Slides are finally passed in Eosin (Sigma-Aldrich) for 2 min and dehydrated with three consecutive passages in increasing concentration of ethanol: EtOH 80% for 1 min, EtOH 96% for 3 min, absolute EtOH for 5 min. At the end of the process, slides are mounted with mounting medium HI-MO (Lab-Optica).

E.3.4 MTT

MTT test permits to evaluate adipose tissue viability. 1 ml of MTT (Sigma-Aldrich), 0.5 mg/mL in PBS, is added to samples and incubated for 3 h at 37°C. Solution is then removed and an equal amount of 10% DMSO (Sigma-Aldrich) in isopropanol (Sigma-Aldrich) is added. DMSO/isopropanol solution is incubated at 37°C and maintained until complete dissolution of the violet salt formed by the MTT. Surnatant is finally removed and its absorbance is read at 580 nm.

E.4 Microscaled technologies manufacturing

E.4.1 Microfluidic chip fabrication

The prototype chip used mostly in this dissertation consists of one layer of PDMS bonded via plasma treatment to a glass slide.

To reproduce the chip design previously prepared molds are used. A mold is produced with photoresist-based photolithographic techniques that can be found in Methods section of Appendix D.

First, every mold is treated with Chlorotrimethylsilane (Sigma Aldrich) vapor for 10 min at room temperature. Uncured PDMS (Sylgard, Dow Corning; 10:1 elastomer:crosslinker ratio) is then pour onto the mold to a thickness of 3 to 5 mm. PDMS is then cured on the molds by baking at 60°C for 45 min. After curing, the layer is take out the mold and inlet and outlet channels are created using a 20G round hole cutter (Technical Innovations Inc., Brazoria, Texas). Then, PDMS layer can be bound to a coverglass slide: bond is achieved by plasma treatment (Harrick) for 33 sec at 70W. After the bonding, the final chip is baked at 80°C overnight to promote the plasma bounding and the full crosslink of PDMS. Thereafter, reservoirs made of a PDMS layer punched with a 3-mm punch are bounded on the top of inlet channels via Plasma treatment again. Also in this case, follows an overnight baking at 80°C. Once last bake is over, microfluidic chip can be sterilized with autoclave processing.

E.4.2 Integration of micropattern in a microfluidic chip

A pattern with the desired geometry can be reproduce inside the microfluidic cell culture chambers through a technique based on photo-patterning of linear acrylamide.

Finalized microfluidic channels are rinsed with isopropanol and distilled water and treated with a 0.1 M NaOH solution for 1 h. A 0.3% solution of 3-acryloxypropil methacrylate (Acros) in ethanol and 5% v/v acetic acid is used to treat oxidized glass surface inside each microfluidic channel. After 5 minutes, channels are rinsed twice with ethanol and filled with an acrylamide solution (8% v/v acrylamide (Sigma-Aldrich), 50 mM HEPES, 10% v/v methanol solution with 35 mg/ml Irgacure 2959 (Ciba)). Microfluidic chip are placed over a transparent photomask with a micrometric black opaque pattern and exposed for 2 minutes with a 50 W collimated UV-lamp (Dymax Bluewave 50W). Channels are finally rinsed with distilled water twice and sterilized under UV-light for 20 min minimum. Follows coating of glass surface with the desired adhesion proteins. Proteins are able to coat only the part of glass that are not masked with acrylamide: in this way, cells will adhere following the pattern determined by the acrylamide.